UC San Diego
UC San Diego Electronic Theses and Dissertations

Title
Nitrogen Cycling in the Euphotic Zone of the California Current

Permalink
https://escholarship.org/uc/item/1298v2jn

Author
Stephens, Brandon

Publication Date
2018

Peer reviewed|Thesis/dissertation

eScholarship.org Powered by the California Digital Library
University of California

UNIVERSITY OF CALIFORNIA, SAN DIEGO

Nitrogen Cycling in the Euphotic Zone of the California Current

A dissertation submitted in partial satisfaction of the
requirements for the degree Doctor of Philosophy

in

Oceanography

by

Brandon Michael Stephens

Committee in charge:

Professor Lihini I. Aluwihare, Chair
Professor Katherine A. Barbeau
Professor Michael R. Landry
Professor Todd R. Martz
Professor Jonathan B. Shurin

2018

Copyright

Brandon Michael Stephens, 2018

All rights reserved.

The Dissertation of Brandon Michael Stephens is approved, and it is acceptable in quality and form for publication on microfilm and electronically:

Chair

University of California, San Diego

2018

DEDICATION

For my children and for whatever they may dream

EPIGRAPH

この世は無常だからこそ素晴らしいのです

The most precious thing in life is its uncertainty

Yoshida Kenkō (1284 - 1350)

TABLE OF CONTENTS

LIST OF ABBREVIATIONS

NPP	net primary production
NPGO	North Pacific Gyre Oscillation
ENSO	El Nino Southern Oscillation
TOC	total organic carbon
ΔTOC	added total organic carbon over baseline concentrations
DOC	dissolved organic carbon
DOM	dissolved organic matter
POC	particulate organic carbon
PON	particulate organic nitrogen
POM	particulate organic matter
Chl-a	chlorophyll-a
MLD	mixed layer depth
CalCOFI	California Cooperative Oceanic Fisheries Investigations
CCS	California Current System
CCE-LTER	California Current Ecosystem-Long-term Ecological Research
EBCS	eastern boundary current system
PAR	photosynthetically active radiation
EZ	euphotic zone
P_{New}	potential new production
P_{TOC}	TOC production
NCP	net carbon production
Cp	*Calanus pacificus* copepod
f-ratio	ratio of new production to net primary production
e-ratio	ratio of export production to net primary production

LIST OF SYMBOLS

$\delta^{13}C$	per mil (‰) deviation of $^{13}C/^{12}C$ from Pee Dee Belemnite
$\delta^{15}N$	per mil (‰) deviation of $^{15}N/^{14}N$ from air
σ_{θ}	potential density of seawater (kg m^{-3})
ε_p	nitrate uptake fractionation factor by phytoplankton
f_w	contribution (%) of nitrifcation to nitrate in euphotic zone
N2	ocean stratification

LIST OF FIGURES

CHAPTER I

CHAPTER II

CHAPTER III

CHAPTER IV

LIST OF TABLES

CHAPTER II

CHAPTER III

CHAPTER IV

ACKNOWLEDGEMENTS

I’d like to thank, first and foremost, my dissertation adviser Lihini Aluwihare. I entered SIO with wild expectations of discovering the origins of dissolved organic matter, much in the way she had done in her dissertation. And along the way we began to broaden the scope of my research focus such that I now leave with a much broader understanding of organic and nutrient cycling in the oceans than I could have imagined. For each of my dissertation chapters, Lihini shared essential insight into approaching the unknowns of the California Current. And I can’t count how many times I felt as though I was struggling and failing as a student, but in the end I feel stronger in my ability to communicate the science because of how Lihini had challenged me. And it is in this regard that Lihini has been more than a dissertation adviser, she recognizes the challenges that each student faces and she helps them to grow as scientists. And for that I am deeply indebted to Lihini.

This work is largely dedicated to my family, who has only been supportive as I’ve become reclusive these past few years. My wife, Yaling, and children, Matthew and Eliana, have always supported my excursions to sea and weekend/evening stop-ins to the lab to check on things. And this is dedicated to my parents, Annette and Mike, who had also always supported my interests growing up: from science experiments on tadpole exposure to fertilizer in middle school, to visits to oceanography undergraduate institutions, to studies abroad. My father’s passing a couple of years ago was sudden and work-life became difficult to balance but his positive presence and attitude on life will be something that lives on and continues to inspire. Other members of both my own and

Yaling’s family have also only been but encouraging; Yaling’s sisters staying with us after Matthew was born 3 years ago made it easier to continue with the science.

I would also like to thank current and former labmates of the Aluwihare lab. Lab members of the past (Ian, Nellie, Jenan, Magali and Neal) always had an open door when I was getting oriented to the area, the science in the lab and questions in general. And Magali and Neal in particular were awesome friends when I was struggling with life crises and challenges with research; they taking me out of the office was crucial when I reached the lowest points of this journey. More recent lab members (Sara, Margot, Irina and Daniel) have been great to get to know and work with in the lab and field. They have provided support in collecting and running samples and have provided encouragement and feedback in the final years of my time at SIO.

Other friends at SIO that I have made along the way have been great to get to know and share experiences with inside and out of SIO. Angel, my co-chief scientist on a student cruise, is like the rock that cannot be shaken and for that I have been inspired. Lauren, Kiefer and Belli, you guys have great hearts and I will forever commiserate with you in our tendency toward isolating tiny fecal pellets. Michael, we spent quite a lot of time outside of SIO and in different parts of the world and I have enjoyed your culinary insights. Members of the Ohman and Landry labs have been awesome to work with at sea over the years, many of you also provided support or data while at sea or on land.

Researchers, post-docs and faculty have been of extraordinary value and it’s difficult to express all of the ways that each has been useful in my training and interpretation of data. Members of the faculty like (and including members of my committee) Dave Checkley, Farooq Azam, Brice Semmens, Greg Mitchell, Peter Franks, Art Miller, Bruce Cornuelle, Dan Rudnick have all at some point taken time to sit with me in their offices. And I am especially indebted to researchers Ralf Goericke, Mati Kahru, Arianne Verdy, Matt Mazloff, for using so much of your time to develop research ideas and interpret data. I have also learned so much from SIO post-docs Wilson Mendoza, Julie Dinasquet and Fanny Chenillat and hope that some of our collaborative interactions and research will lead to publications at some point.

Faculty from outside of SIO have also given a significant fraction of their time to help analyze samples and give feedback on interpretations of data and for their time I am also greatly appreciative. Scott Wankel was essential for at least one of the dissertation chapters perhaps two of them. Mike Beman helped to both give advice and to help run samples that will be of great use in interpreting data. Alyson Santoro also provided insight and welcomed me to her lab to prepare samples, the data from which we hope to interpret in the future.

Chapter II significantly benefited from study design and framework conceived by Lihini Aluwihare and the analysis was carried out by the dissertation author. This chapter benefited from analyses of TOC and POC collected and analyzed by Magali Porrachia, Shonna Dovel, Megan Roadman and Bruce Deck, where funding was provided in part by the NSF and NOAA joint-funded CalCOFI and CCE-LTER Programs. Additional data presented here was made publicly available by the CCE and CalCOFI programs, where data were made available with support from James Conners, James Wilkinson and David Wolgast. This chapter also benefited from useful discussions of statistical analysis approaches with Norm Nelson, Brice Semmens and Jason Tan. Mati Kahru provided useful advice about estimating and averaging satellite-based net primary production for the California Current System. Ralf Goericke provided useful feedback on the presentation and discussion of data in earlier versions of this chapter. The physical model for the California Current presented here was made publicly accessible by Bruce Cornuelle, Matt Mazloff and Ariane Verdy.

Chapter III significantly benefited from correspondences with Scott Wankel, primarily regarding use of the nitrification model from which most of the conclusions were drawn here. This chapter also benefited from conversations with J. Michael Beman, Carly Buchwald and Alyson Santoro regarding estimations of nitrification and use of stable isotopes in nitrification studies. Isolation of 16s community composition was made possible by Andy Allen and Ariel Rabines. Lihini Aluwihare and Sara Rivera collected a subset of the samples presented here. Margot White analyzed a subset of the nitrate isotope samples presented here. A subset of the CalCOFI nitrate isotope samples presented here were also analyzed by Patrick Rafter and Daniel Sigman. Sinking POM isotope samples were made possible by Michael Stukel and analyzed by Bruce Deck. Funding for POM isotopes, 16s composition and nitrate isotopes were in part supported by funding from CCE Program and an SIO Graduate Student Excellence Research Award.

Many of the nitrate samples presented **Chapter IV** were also presented in **Chapter III** and so similar appreciation is extended to Scott Wankel, Andy Allen, Ariel Rabines, Lihini Aluwihare, Sara Rivera, Margot White, Patrick Rafter, Daniel Sigman, Michael Stukel and Bruce Deck. 18s-V4 community composition for one cruise were graciously made available by Ali Friebott and Michael Landry. Fecal pellet collection experiments were carried out with assistance from Belli Vallencia and Michael Landry. Assistance isolating *Calanus pacificus* copepods was provided by Belli Vallencia, Liz Heatherington and Mark Ohman. Kathy Barbeau provided useful guidance regarding the use of Si* to estimate iron limitation. Funding for POM isotopes, 18s composition and nitrate isotopes were in part supported by funding from CCE Program and an SIO Graduate Student Excellence Research Award.

VITA

2004	Bachelor of Science, University of Minnesota
2004-2005	Laboratory Assistant, USDA-Agriculture Research Service
2005-2006	English Teacher, Taipei, Taiwan
2006-2008	Research and Teaching Assistant, University of Minnesota, Duluth
2008	Master of Science, University of Minnesota, Duluth
2009-2010	Project Assistant, Cook County Soil and Water Conservation District
2010-2012	Science Assistant, National Science Foundation
2012-2018	Research and Teaching Assistant, University of California, San Diego
2018	Doctor of Philosophy, University of California, San Diego

PUBLICATIONS

1) Stephens BM, Porrachia M, Dovel S, Roadman M, Goericke R, Aluwihare LI, *Stocks and dynamics of organic carbon in the California Current Ecosystem Region.* Global Biogeochemical Cycles (In prep).
2) Ball GI, Noble PJ, Stephens BM, Higgins A, Mensing SA, Aluwihare LI. *A lignin, diatom, and pollen record spanning the Pleistocene-Holocene transition at Fallen Leaf Lake, Sierra Nevada, California, USA.* Geological Society of America Special Issue (In Press).
3) Petras D, Koester I, Da Silva R, Stephens BM, Haas AF, Nelson CE, Kelly LW, Aluwihare LI, Dorrestein PC, *High-resolution liquid chromatography tandem mass spectrometry enables large scale molecular characterization of dissolved organic matter.* Frontiers in Marine Science 2017; 4.
4) Arakawa NK, Aluwihare LI, Simpson AJ, Soong R, Stephens BM, Lane-Coplan D, *Carotenoids are the likely precursor of a significant fraction of marine dissolved organic matter.* Science Advances 2017; 3: e16002976.
5) Stukel MR et al., *Mesoscale ocean fronts enhance carbon export due to gravitational sinking and subduction*. PNAS 2017; 1609435114.
6) Burd AB et al., *Terrestrial and marine perspectives on modeling organic matter degradation pathways*. Global Change Biology 2015; gcb.12987.
7) Stephens BM, Minor EC. *DOM characteristics along the continuum from river to reservoir: a comparison of freshwater and saline transects.* Aquatic Sciences 2010; 72(4): 403-417.
8) Minor EC, Stephens BM. *Dissolved organic matter characteristics within the Lake Superior watershed.* Organic Geochemistry 2008; 39: 1489-1501.
9) Ochser TE, Stephens BM, Koskinen WC, Kookana RS. *Sorption of a hydrophilic pesticide: effects of soil water content.* Soil Science Society of America Journal 2006; 70: 1991-1997.
10) Koskinen WC, Ochsner TE, Stephens BM, Kookana RS. *Sorption of isoxaflutole, a diketonitrile degradate (DKN), and dicamba in unsaturated soil.* Environmental Science and Health B 2006; 41: 1071-1083.

ABSTRACT OF THE DISSERTATION

Nitrogen Cycling in the Euphotic Zone of the California Current

by

Brandon Michael Stephens

Doctor of Philosophy in Oceanography

University of California, San Diego, 2018

Professor Lihini I. Aluwihare, Chair

Deep ocean nitrate supply to the surface euphotic zone of the California Current Ecosystem (CCE) increases rates of productivity and leads to an overall increase in the fixed repository of dissolved and particulate organic matter (DOM and POM, respectively). **Chapter II** demonstrates that DOM production, in carbon units, can represent 12 ± 8% of nitrate-based production during low production periods and up to 28 ± 15% during highly productive periods. DOM can also accumulate in the surface CCE during post-bloom, surface stratified or iron-limited conditions, and therefore can represent a potentially exportable reservoir when subsequently subducted from the surface ocean. DOM production rates are comparable to regional sinking particle export rates, the combination of which matches net oxygen production rates as estimated in previous studies. While **Chapters I** and **II** demonstrate that deep ocean nitrate concentrations track patterns of surface productivity in the CCE, **Chapter III** tests whether all nitrate used in the surface ocean is derived from the dark ocean via upwelling. Stable isotopes of nitrate estimate that 6 - 36% of nitrate uptake is generated by nitrification occurring within the euphotic zone of the CCE. Rates of euphotic zone nitrification spanned 4 - 103 nmol L^{-1} d^{-1}, rates of which extend to the surface ocean. A strong correlation between euphotic zone nitrification and nitrite concentrations led to the inference that either increased POM substrate or reduced phytoplankton abundance to be determinants of nitrification. Use of nitrate stable isotopes in **Chapter IV** demonstrates that surface nitrate utilization was enhanced at inshore CCE stations during the 2014 warm anomaly. The effect of utilization was detected as an isotopic enrichment in sinking and suspended POM and *Calanus pacificus* copepods. Nitrate sourced from the remnant mixed layer depth supports the food web, and was a source that was at times decoupled from deeper (200 - 400 m) nitrate. A relatively low 3.0 ± 0.5‰ nitrate uptake isotope effect corresponded with phytoplankton communities dominated by chlorophytes and flagellates. Data from **Chapter IV** support hypotheses that isotopes of upper ocean N reservoirs in the CCE will primarily reflect surface ocean nitrate dynamics.

Chapter I

Introduction

1. Production in Eastern Boundary Current Systems

The oceans are responsible for roughly half the global net primary production (NPP) [*Field et al.*, 1998], rates of which range from below detection limits in the open ocean to over 400 mmol C m^{-2} d^{-1} in more productive regions [*Falkowski et al.*, 2003]. High latitudes and coastal areas tend to be some of the more productive regions in the oceans (Figure 1.1). Among the coastal systems, eastern boundary current systems (EBCSs; circled in Figure 1.1) are an important site of surface ocean NPP, providing 20% of the world's fish catch while representing <1% of the ocean's surface area [*Chavez* and *Messié*, 2009].

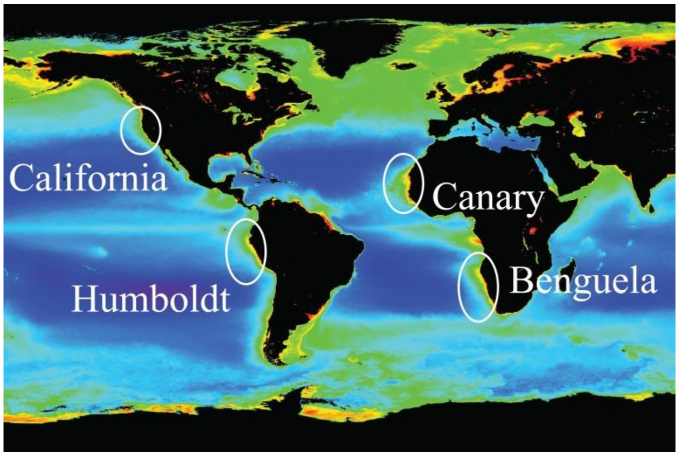

Figure 1.1. *Satellite-based estimate of mean surface ocean chlorophyll (1997-2003) contrast regions of increased autotrophic biomass indicated by green to red colors and low biomass in blue. Circled are four primary eastern boundary current systems (EBCSs). Image courtesy of NASA at https://oceancolor.gsfc.nasa.gov.*

EBCSs differ in their extent of NPP, the rates of which depend primarily on the rate of nitrate supply to the surface ocean [*Messié et al.*, 2009; *Messié* and *Chavez*, 2015] (Figure 1.2). The total quantity of nitrate supply in the more productive EBCSs is related to upwelled volume, which in turn is influenced by a combination of open-ocean wind stress curl and wind-driven coastal upwelling processes [*Carr* and *Kearns*, 2003; *Di Lorenzo et al.*, 2008]. While surface ocean winds induce upwelling [*Bakun* and *Nelson*, 1991], the total upwelled volume compared across EBCSs is a better predictor of NPP and nitrate supply [*Messié et al.*, 2009; *Messié* and *Chavez*, 2015]. This influence is particularly evident when comparing among EBCSs, where the California Current has some of the highest surface wind speeds of EBCSs yet exhibits the lowest NPP, nitrate supply and upwelled volume (Figure 1.2).

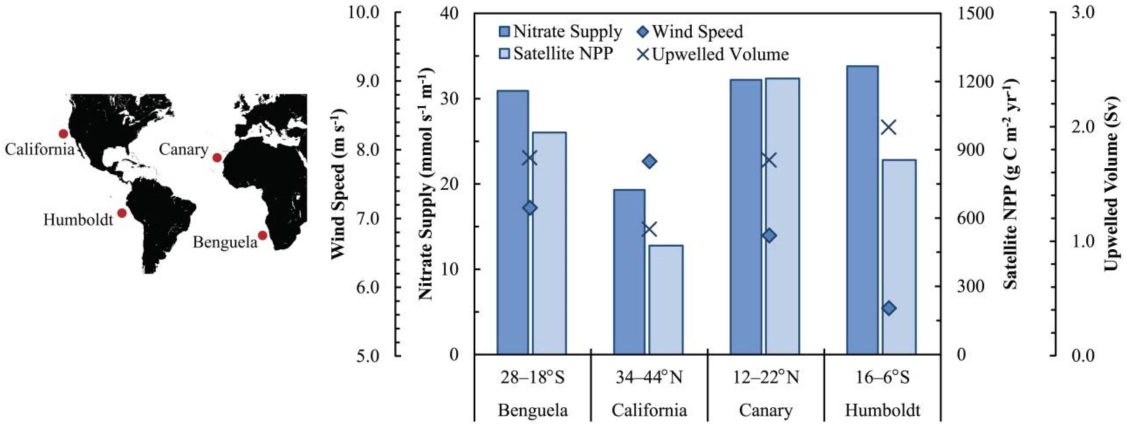

Figure 1.2. *Annual average satellite-estimated net primary production (NPP) in eastern boundary current systems is directly related to upwelling-driven nitrate supply (data from* [*Messié et al.*, 2009]*).*

EBCSs located closer to the equator (i.e., < ±30° latitude) exhibit greater upwelled volumes due to an increase in Coriolis parameter and the extent of wind stress curl [*Rykaczewski* and *Checkley*, 2008; *Chavez* and *Messié*, 2009]. Aside from differences in total upwelled volume, the extent of lateral transport can also have an inhibitory effect on production, particularly when the lateral transport rates exceed nutrient uptake by phytoplankton [*Messié* and *Chavez*, 2015]. And so a combination of transport and strong eddy activity can explain most of the reduction in NPP for the California Current relative to other EBCSs [*Gruber et al.*, 2011; *Lachkar* and *Gruber*, 2011, 2012], though additional factors like increased iron limitation can also distinguish the California Current [*Messié* and *Chavez*, 2015].

The California Current System (CCS) is an equatorward flowing water mass originating in the eastern North Pacific sub-arctic around 50° N extending down to 15 - 25° N [*Checkley* and *Barth*, 2009]. Production in the CCS exhibits a seasonal cycle due to an increase in alongshore winds, which typically peak in May - June in the southern CCS (near 33 - 36° N) and in June - July in the northern CCS (near 39 - 45° N) [*Bograd et al.*, 2009]. The strength of the CCS and the associated magnitude of nitrate supply can also vary over inter-annual to decadal scales [*Chavez et al.*, 2003; *Di Lorenzo et al.*, 2008].

2. Nutrient Supply and Organic Export

Determining the spatial and temporal coupling between nutrient delivery and carbon export is vital for predicting the fate of atmospheric CO_2 and the cycling of other major elements [*Falkowski et al.*, 1998; *Siegel et al.*, 2016]. In EBCSs, the primary limiting nutrient, nitrate, is supplied from outside of the euphotic zone and so in this sense it is referred to as a "new" nutrient [*Dugdale* and *Goering*, 1967; *Messié et al.*, 2009]. If the uptake rate is similar to rate of nitrate supply, the production supported by this nutrient can be referred to as "new production," and the *f*-ratio has been introduced to identify that fraction of primary production that is supported by external nutrient inputs [*Dugdale* and *Goering*, 1967; *Eppley* and *Peterson*, 1979; *Falkowski et al.*, 2003]. The concept of new production has been useful for examining the balance between inputs of new nutrients and export production [*Eppley* and *Peterson*, 1979; *Falkowski et al.*, 2003]. For systems to be in steady state the *f*-ratio and the *e*-ratio (the fraction of primary production that is exported as sinking organic matter) must be in balance; however, demonstrating this for a given ecosystem requires balancing supply and export processes over appropriate length and spatial scales.

In the CCS, the primary routes of nitrogen export have been identified as (1) nitrate transport due to incomplete utilization followed by subduction [*Messié* and *Chavez*, 2015], (2) sinking and non-sinking particles [*Stukel et al.*, 2011, 2017], (3) migrating zooplankton [*Steinberg* and *Landry*, 2017] and (4) mesopelagic fishes [*Davison et al.*, 2013]. Incomplete nitrate utilization and subsequent export via subduction was recently estimated as 15% on average of nitrate supply [*Messié* and *Chavez*, 2015]. The combined rates of sinking and predator-mediated export in productive waters of the coastal CCS, can account for 25 to 50% of the uptake of new nitrogen. The lateral transport and subsequent export of non-sinking organic matter in the central CCS has be estimated to be between 11% of nitrate supply [*Pennington et al.*, 2010] and of similar magnitude to sinking export [*Stukel et al.*, 2017]. Though direct measurements of non-sinking contributions to export in the CCS beyond this are limited, the broad contributions of a laterally transported non-sinking organic reservoir has also been implicated by use as a passive tracer in biogeochemical ocean models [*Plattner et al.*, 2005; *Gruber et al.*, 2011; *Letscher et al.*, 2013; *Nagai et al.*, 2015].

The various fates of primary production are shown in Figure 1.3. Non-sinking reservoirs are identified as particulate and dissolved organic carbon (POC and DOC) and amorphous aggregates. These accumulated reservoirs could contribute to sinking flux through aggregation but export is more likely through physical processes such as subduction, mixing of isopycnals, and, in the CCS, upwelling and downwelling events [*Siegel et al.*, 2016]. However, the long-lived background reservoir of these accumulated pools [*Druffel et al.*, 1992] and their complexity make it challenging to accurately quantify their contribution to export.

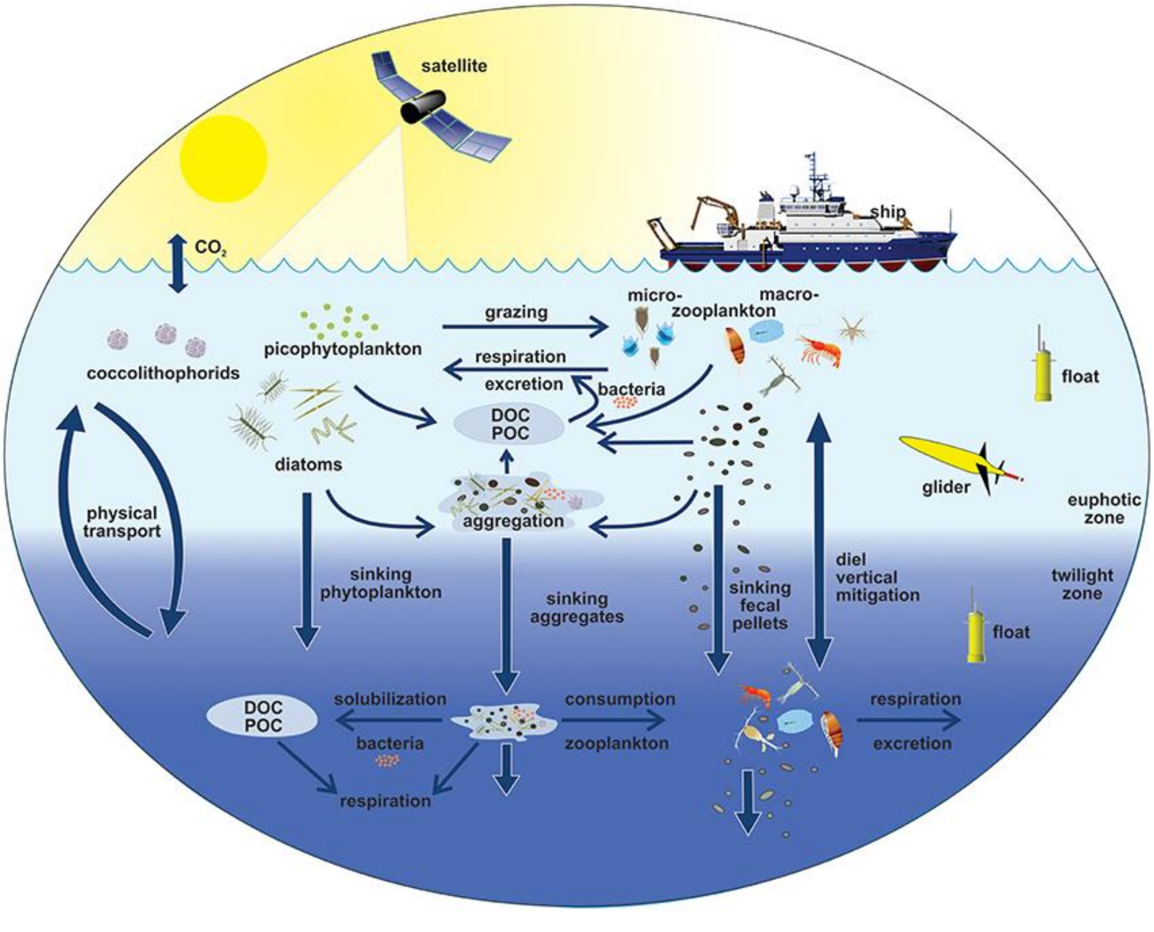

Figure 1.3. *Fates of primary production in the ocean from Siegel et al. (2016).*

Studies that have attempted to quantify the role of these reservoirs in carbon export have estimated that ~ 20% of marine new (or net community) production is channeled through the non-sinking organic reservoir [*Carlson et al.*, 1998; *Hansell* and *Carlson*, 1998; *Abell et al.*, 2000; *Romera-Castillo et al.*, 2016], roughly half of which persists on the order of 5 to 10 years [*Letscher et al.*, 2013, 2015]. However, processes influencing the surface accumulation and ultimate export of non-sinking organic matter can differ significantly across different oceanic ecosystems [*Carlson* and *Hansell*, 2014]. For instance, non-sinking organic matter produced by a picophytoplankton community had accumulated in the oligotrophic Sargasso Sea where up to half of this reservoir was exported below the euphotic zone by convective overturn [*Carlson et al.*, 1994], whereas low non-sinking organic matter accumulation in the nutrient-rich Ross Sea was attributed to the low release of organics by the dominant phytoplankton species *Phaeocystis sp.* [*Carlson et al.*, 1998, 2000]. A study within the Santa Barbara Channel, located within the southern CCS, showed consistently higher organic matter partitioning under post-bloom, nutrient limited conditions when compared to bloom conditions [*Halewood et al.*, 2012], which implicated post-bloom conditions as contributing disproportionately to the exportable non-sinking reservoir. In short, determining the relative partitioning of non-sinking organic matter from new production informs studies of carbon export as well as studies that examine food web connections to higher trophic levels (e.g., via the microbial loop; [*Ducklow*, 1994; *Fuhrman*, 1999; *Azam* and *Malfatti*, 2007]). For these reasons, NASA's large-scale EXPORTS science plan identified accumulated, non-sinking carbon reservoirs as a research priority for studies aimed at accurately quantifying carbon export and assessing the sensitivity of export rates to climate variability [*Siegel et al.*, 2016].

3. Nitrate Regeneration in the Oceans

In the CCS, nitrate is primarily delivered by wind stress curl-driven coastal upwelling or Ekman pumping (e.g., [*Rykaczewski* and *Checkley*, 2008; *Messié* and *Chavez*, 2015]). Model formulations use nitrate concentrations at the base of the euphotic zone and upwelling rates to parameterize the extent of new production [*Messié* and *Chavez*, 2015]. However, some studies have shown that nitrification in the euphotic zone and just below it can contribute nitrate [*Ward*, 2005]. Consumption of nitrogen biomass and detritus by heterotrophic organisms – commonly referred to as secondary production – results in the release of ammonia, most of which is ultimately re-incorporated into phytoplankton biomass or heterotrophic microbes [*Ward*, 1987, 2005; *Smith et al.*, 2014a]. However, some of this ammonia is also utilized by autotrophic bacteria and archaea responsible for the process of nitrification (e.g., [*Ward et al.*, 1982; *Beman et al.*, 2008]), which is the combined oxidation of ammonia into nitrite and nitrite into nitrate [*Ward*, 2008]. Most early nitrification studies found that nitrification was peaked below the 1% PAR level [*Ward et al.*, 1982; *Ward*, 1985]. However, appreciable ammonia oxidation rates of 5 to 30 nmol N L^{-1} d^{-1} have been detected extending up to the surface ocean [*Ward*, 2005; *Smith et al.*, 2014a]. In such cases, the relative contribution of euphotic zone nitrification to the surface nitrate reservoir becomes relevant in terms of its impact on formulations of new production.

In the central California Current, euphotic zone nitrification represented an average of 15 to 20% of the surface nitrate reservoir incorporated by phytoplankton [*Wankel et al.*, 2007; *Santoro et al.*, 2010]. Yet, the frequency of nitrification and the biogeochemical processes that influence its magnitude in the euphotic zone are not well understood. For instance, nitrification rates have sometimes been correlated to substrate quantity [*Ward*, 1985], while other studies have suggested that competition between phytoplankton and nitrifiers for ammonia uptake exerts a primary control on where nitrification takes place [*Smith et al.*, 2014a]. Thus, to obtain a more complete picture of nitrate cycling in the surface ocean of the CCS, factors that control the extent of euphotic zone nitrification must be more accurately parameterized.

4. Nitrate Utilization Influences on the Food Web and Export

As discussed previously, nitrate is the primary limiting nutrient in the CCS [*Messié et al.*, 2009; *Chavez et al.*, 2011]. An analysis of the temporal variability in the satellite-based NPP and surface chlorophyll is correlated to the nitrate concentration at the 26.0 kg m^{-3} isopycnal and captures this dependency (Figure 1.4). Nitrate concentrations upwelling into the euphotic zone may decrease in the future due to increased upper ocean stratification [*Chavez et al.*, 2011] or increased denitrification in source waters of the California Undercurrent [*Deutsch et al.*, 2014; *Tems et al.*, 2015], which flows poleward along the slope between 200 - 600 m. Alternatively, a decrease in meridional transport could increase the nitrate concentration of intermediate waters that transport nitrate into the CCS [*Rykaczewski* and *Dunne*, 2010]. In addition, increased wind stress could increase seasonal coastal upwelling, which would increase the rate of nitrate delivery into the euphotic zone [*Bakun et al.*, 2015]. To predict ecosystem responses to future perturbations in the euphotic zone nitrate inventory of the CCS many have turned to examine past variations in nitrate supply. These studies have employed nitrogen isotopes ($\delta^{15}N$) of archived samples (sediments or zooplankton) as a proxy for nutrient availability or nutrient source (e.g., [*Rau et al.*, 1998; *Ohman et al.*, 2012; *Deutsch et al.*, 2014; *Tems et al.*, 2015].

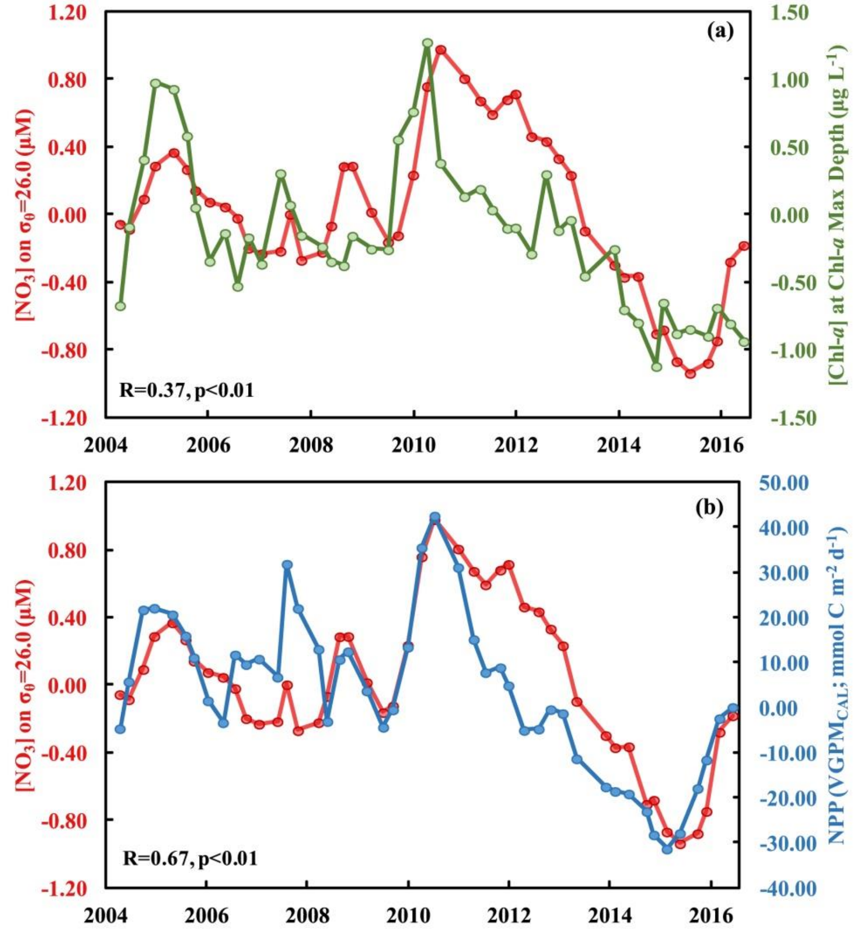

Figure 1.4. *CCS nearshore mean nitrate concentration ($[NO_3^-]$) for potential density 26.0 kg m^{-3} is compared with chlorophyll-a concentration ([Chl-a]) at the chlorophyll-a maximum depths (a) and satellite-based estimate of net primary production following VGPM-CAL formulation (b). Values represent seasonally-corrected anomalies and smoothed using a 6-month running average over 2004-2016. From the* dissertation *author's Chapter II, Figure S2.5.*

Nitrogen isotopes can be a useful tracer to balance the flow of nitrogen within ecosystems [*Fry*, 2006]. For example, the $\delta^{15}N$ signature of N pools can vary due to the interaction of the inorganic reservoir with biota. For instance, enzymatic processes favor the lighter isotope ^{14}N, which fractionates the relative abundance of $^{15}N/^{14}N$ in biomass relative to the inorganic nitrogen source. For the same reason, inorganic nitrogen produced as a result of catabolic processes in cells is also often depleted in $\delta^{15}N$ relative to the source [*Checkley* and *Miller*, 1989]. Two processes can increase the isotope signature of euphotic zone biomass in oxygenated water columns. First of all, if the stable isotope signature of source nitrate ($^{15}N_{NO3}$) changes then this can be expressed in the biomass that is produced from that nitrate. For this signature to be recorded in archived sediments, for example, nitrate utilization must go to completion at that site. The second process is related to nitrate utilization; as nitrate in the euphotic zone is consumed, the remaining $\delta^{15}N_{NO3}$ becomes enriched [*Sigman et al.*, 2010]. Thus, if nitrate consumption does not go to completion (because of greater nitrate flux to that site or because nutrient consumption is limited by some other process), then the $\delta^{15}N$ signature of the archive will primarily reveal changes in nitrate utilization.

To ground truth the $\delta^{15}N$ relationship between CCS N reservoirs it is necessary to (1) provide direct estimates of $\delta^{15}N_{NO3}$ [*Miyake* and *Wada*, 1967], (2) examine the isotope effects associated with both assimilation [*Needoba et al.*, 2003] and trophic transfer [*Wada et al.*, 1987] and (3) determine which processes are responsible for observed variations in $\delta^{15}N$. Previous studies identified relatively enriched $\delta^{15}N_{NO3}$ (7 - 8‰) for deep waters of the coastal CCS consistent with the influence of poleward flowing California Undercurrent with a source in the tropics [*Liu* and *Kaplan*, 1989; *Altabet et al.*, 1999], but it has been proposed that this signature has changed [*Deutsch et al.*, 2014].

The few studies that have used nitrate assimilation fractionation factors to model the isotopic behavior of various N reservoirs in the CCS have used a value between 3 to 8‰ [*Altabet et al.*, 1999; *Deutsch et al.*, 2014]. Modern studies have also attempted to examine $\delta^{15}N_{NO3}$ in the CCS by directly measuring sinking POM or examining the $\delta^{15}N$ of sessile, particle feeders (e.g., mussels) [*Altabet et al.*, 1999; *Vokhshoori* and *McCarthy*, 2014]. Additionally, $\delta^{15}N$ of CCS zooplankton collected over 1950 - 2000 was used to infer changes in surface nitrate utilization [*Rau et al.*, 2003; *Ohman et al.*, 2012]. However, whether changes in the food web $\delta^{15}N$ enrichment are due to nitrate availability or due to changes in the $\delta^{15}N$ nitrate source remains an important question in estimating the flow of nitrate through the CCS.

5. Organization of the Dissertation

The following dissertation chapters discuss specific biogeochemical processes as they relate to and are impacted by nitrogen cycling in the CCS. This work was made possible by the invaluable long-term time series of biogeochemical parameters measured by the California Current Cooperative Oceanic Fisheries Investigation (CalCOFI) survey cruises and supported by the California Current Ecosystem (CCE) Long-Term Ecological Research (LTER) program.

Chapter II addresses the topic of non-sinking organic carbon production as a fraction of nitrate supply. The primary goal to this chapter was to first provide an estimate of new production for the CalCOFI grid between 2008 and 2010. For this work thousands of data points were used to provide a robust assessment of new production variability across the grid. In order to do this, nitrate concentration measurements made by CalCOFI were employed in a modified formulation of the new production calculation. The second step was to quantify the amount of new production that was partitioned into the non-sinking organic matter reservoir. The components of this reservoir ranged from both DOC and POC in inshore environments to primarily DOC in offshore environments.

Chapter II represents the most spatially comprehensive assessment of new production partitioning into non-sinking reservoirs available for field measurements spanning a relatively continuous (i.e., quarterly) time record. The non-sinking reservoir accumulated on long enough timescales to be relevant for export and contributed a similar proportion as sinking export [*Stukel et al.*, 2011]. To examine the physical and biological controls on this partitioning, the diverse measurements made by the CalCOFI program were coupled with a multiple regression analysis approach to identify potential influences on the non-sinking reservoir. Productive periods led to a greater proportion (e.g., 28 ± 15% of new production) and quantity of organic matter accumulation (10 to 20 μM C above baseline conditions), an increase that often persisted during post-bloom and surface stratified conditions. Overall, this chapter contributes new knowledge on the temporal variability of non-sinking organic matter production and provided new constraints on the amount of new production that could be partitioned into this reservoir and was available for export.

Chapter III addresses the topic of nitrification in the euphotic zone of the CCS. Using a nitrate stable isotope model developed by [*Wankel et al.*, 2007], nitrification in the euphotic zone was estimated to contribute between 6 and 36% of the surface nitrate reservoir. Rates of nitrification required for this process ranged from 4 to 103 nmol L^{-1} d^{-}

^{1} and integrated euphotic zone nitrification was 0.1 to 2.0 mmol N m^{-2} d^{-1}. These ranges were similar to direct measurements of ammonia oxidation rates in on-deck incubations (e.g., [*Ward et al.*, 1982; *Santoro et al.*, 2010; *Smith et al.*, 2016]).

Nitrification contributions in the euphotic zone were positively correlated with nitrite concentrations, which suggested that substrate quantity may have exerted a control on the rate of nitrification as previously hypothesized for the northern CCS [*Ward*, 1985]. To investigate this topic further, data from the long-term CalCOFI time series were used in a multiple linear correlation analysis. This analysis found that both particulate organic nitrogen concentrations and possible competition with phytoplankton exerted a control on nitrite accumulation in the CCS. Together, the data presented in **Chapter III** found that nitrification contributed nitrate to the euphotic zone and should be considered when discussing new and export production. These data also represent the first natural abundance isotope-based estimates of euphotic zone nitrification in the CCE-LTER and CalCOFI domains.

Chapter IV addresses the use of nitrogen isotope dynamics in the CCE to study nitrate sources and cycling. Sampling was primarily conducted during the warm anomaly CCE-LTER Process Cruises of 2014 and 2016. Analysis of nitrate, suspended POM, sinking POM and copepod δ^{15}N data showed that the extent of nitrate utilization in the surface ocean exerted a strong control on δ^{15}N expressed in various organic N reservoirs. The correspondence was strongest for sinking POM, which suggested that sinking POM was primarily affected by changes to the nitrate reservoir thereby implicating sinking export to be an immediate and local reflection of New Production. Suspended POM showed variability that could be attributed to both the longer residence time of this reservoir in the surface ocean compared with sinking POM and the incorporation of isotopically depleted nitrogen, such as amino acids or ammonium, into suspended particles at certain locations. A comparison with zooplankton $\delta^{15}N$ and their fecal pellets suggested that sinking export is largely a balance between the isotope effect of nitrate uptake by phytoplankton and trophic enrichment by primary consumers.

The evidence presented in **Chapter IV** strongly supports the conclusion that the observed $\delta^{15}N$ enrichment detected across the food web resulted from enhanced nitrate utilization of a smaller nitrate pool during the 2014 - 2016 anomalously warm periods. However, by spring of 2016 upwelling had resumed in the inshore stations and lower nitrate utilization at these locations was observed compared to prior El Niño-neutral conditions, likely a result of enhanced grazing pressure on the phytoplankton community. Despite use of archived $\delta^{15}N$ samples from the CCS as proxies for variations in the local nitrate inventory, this is the first study to directly examine the propagation of nitrate $\delta^{15}N$ into the various organic matter reservoirs of the surface ocean.

REFERENCES

Abell, J., Emerson, S., and Renaud, P. (2000). Distributions of TOP, TON and TOC in the North Pacific subtropical gyre: Implications for nutrient supply in the surface ocean and remineralization in the upper thermocline. *Journal of Marine Research*, *58*(2), 203–222.

Altabet, M. A., Pilskaln, C., Thunell, R., Pride, C., Sigman, D., Chavez, F., and Francois, R. (1999). The nitrogen isotope biogeochemistry of sinking particles from the margin of the eastern North Pacific. *Deep-Sea Research Part I: Oceanographic Research Papers*, *46*(4), 655–679.

Azam, F., and Malfatti, F. (2007). Microbial structuring of marine ecosystems. *Nature Reviews Microbiology*, *5*(10), 782–791.

Bakun, A., and Nelson, C. S. (1991). The seasonal cycle of wind-stress curl in subtropical eastern boundary current regions. *Journal of Physical Oceanography*, *21*(12), 1815–1834.

Bakun, A., Black, B. A., Bograd, S. J., García-Reyes, M., Miller, A. J., Rykaczewski, R. R., and Sydeman, W. J. (2015). Anticipated Effects of Climate Change on Coastal Upwelling Ecosystems. *Current Climate Change Reports*, *1*(2), 85–93.

Beman, J. M., Popp, B. N., and Francis, C. A. (2008). Molecular and biogeochemical evidence for ammonia oxidation by marine Crenarchaeota in the Gulf of California. *ISME Journal*, *2*(4), 429–441.

Bograd, S. J., Schroeder, I., Sarkar, N., Qiu, X., Sydeman, W. J., and Schwing, F. B. (2009). Phenology of coastal upwelling in the California Current. *Geophysical Research Letters*, *36*(1), L01602.

Carlson, C. A., and Hansell, D. A. (2014). DOM Sources, Sinks, Reactivity, and Budgets. In *Biogeochemistry of Marine Dissolved Organic Matter: Second Edition* (pp. 65–126).

Carlson, C. A., Ducklow, H. W., and Michaels, A. F. (1994). Annual flux of dissolved organic carbon from the euphotic zone in the northwestern Sargasso Sea. *Nature*, *371*, 405–408.

Carlson, C. A., Ducklow, H. W., Hansell, D. A., and Smith, W. O. (1998). Organic carbon partitioning during spring phytoplankton blooms in the Ross Sea polynya and the Sargasso Sea. *Limnology and Oceanography*, *43*(3), 375–386.

Carlson, C. A., Hansell, D. A., Peltzer, E. T., and Smith, W. O. (2000). Stocks and dynamics of dissolved and particulate organic matter in the southern Ross Sea, Antarctica. *Deep Sea Research Part II: Topical Studies in Oceanography*, *47*(15–16), 3201–3225.

Carr, M. E., and Kearns, E. J. (2003). Production regimes in four Eastern Boundary Current systems. *Deep-Sea Research Part II: Topical Studies in Oceanography*, *50*(22–26), 3199–3221.

Chavez, F. P., and Messié, M. (2009). A comparison of Eastern Boundary Upwelling Ecosystems. *Progress in Oceanography*, *83*(1–4), 80–96.

Chavez, F. P., Ryan, J., Lluch-Cota, S. E., and Ñiquen, C. M. (2003). Climate: From anchovies to sardines and back: Multidecadal change in the Pacific Ocean. *Science*, *299*(5604), 217–221.

Chavez, F. P., Messié, M., and Pennington, J. T. (2011). Marine Primary Production in Relation to Climate Variability and Change. *Annual Review of Marine Science*, *3*(1), 227–260.

Checkley, D. M., and Barth, J. A. (2009). Patterns and processes in the California Current System. *Progress in Oceanography*, *83*(1–4), 49–64.

Checkley, D. M., and Miller, C. A. (1989). Nitrogen isotope fractionation by oceanic zooplankton. *Deep Sea Research Part A, Oceanographic Research Papers*, *36*(10), 1449–1456.

Davison, P. C., Checkley, D. M., Koslow, J. A., and Barlow, J. (2013). Carbon export mediated by mesopelagic fishes in the northeast Pacific Ocean. *Progress in Oceanography*, *116*, 14–30.

Deutsch, C., Berelson, W., Thunell, R., Weber, T., Tems, C., McManus, J., Crusius, J., Ito, T., Baumgartner, T., Ferreira, V., Mey, J., and Van Geen, A. (2014). Centennial changes in North Pacific anoxia linked to tropical trade winds. *Science*, *345*(6197), 665–668.

Druffel, E. R. M., Williams, P. M., Bauer, J. E., and Ertel, J. R. (1992). Cycling of Dissolved and Particulate Organic Matter in the Open Ocean. *Journal of Geophysical Research*, *97659*(15), 639–15.

Ducklow, H. W. (1994). Modeling the microbial food web. *Microbial Ecology*, *28*(2), 303–319.

Dugdale, R. C., and Goering, J. J. (1967). Uptake of New and Regenerated Forms of Nitrogen in Primary Productivity. *Limnology and Oceanography*, *12*(2), 196–206.

Eppley, R. W., and Peterson, B. J. (1979). Particulate organic matter flux and planktonic new production in the deep ocean. *Nature*, *282*(5740), 677–680.

Falkowski, P. G., Laws, E. A., Barber, R. T., and Murray, J. W. (2003). Phytoplankton and Their Role in Primary, New, and Export Production. In *Ocean Biogeochemistry* (pp. 99–121). Berlin, Heidelberg: Springer Berlin Heidelberg.

Falkowski, P. G., Barber, R. T., and Smetacek, V. (1998). Biogeochemical controls and feedbacks on ocean primary production. *Science*, *281*(5374), 200–206.

Field, C. B., Behrenfeld, M. J., Randerson, J. T., and Falkowski, P. (1998). Primary production of the biosphere: Integrating terrestrial and oceanic components. *Science*, *281*(5374), 237–240.

Fry, B. (2006). *Stable isotope ecology*. *Stable Isotope Ecology*. New York, NY: Springer New York.

Fuhrman, J. A. (1999). Marine viruses and their biogeochemical and ecological effects. *Nature*, *399*(6736), 541–548.

Gruber, N., Lachkar, Z., Frenzel, H., Marchesiello, P., Münnich, M., McWilliams, J. C., Nagai, T., and Plattner, G.-K. (2011). Eddy-induced reduction of biological production in eastern boundary upwelling systems. *Nature Geoscience*, *4*(11), 787–792.

Halewood, E. R., Carlson, C. A., Brzezinski, M. A., Reed, D. C., and Goodman, J. (2012). Annual cycle of organic matter partitioning and its availability to bacteria across the Santa Barbara Channel continental shelf. *Aquatic Microbial Ecology, 67*(3), 189–209.

Hansell, D. A., and Carlson, C. A. (1998). Net community production of dissolved organic carbon. *Global Biogeochemical Cycles*, *12*(3), 443–453.

Lachkar, Z., and Gruber, N. (2011). What controls biological production in coastal upwelling systems? Insights from a comparative modeling study. *Biogeosciences*, *8*(10), 2961–2976.

Lachkar, Z., and Gruber, N. (2012). A comparative study of biological production in eastern boundary upwelling systems using an artificial neural network. *Biogeosciences*, *9*(1), 293–308.

Letscher, R. T., Hansell, D. A., Carlson, C. A., Lumpkin, R., and Knapp, A. N. (2013). Dissolved organic nitrogen in the global surface ocean: Distribution and fate. *Global Biogeochemical Cycles*, *27*(1), 141–153.

Letscher, R. T., Moore, J. K., Teng, Y. C., and Primeau, F. W. (2015). Variable C : N : P stoichiometry of dissolved organic matter cycling in the Community Earth System Model. *Biogeosciences*, *12*(1), 209–221.

Liu, K., and Kaplan, I. R. (1989). The eastern tropical Pacific as a source of 15N-enriched nitrate in seawater off southern California. *Limnology and Oceanography*, *34*(5), 820–830.

Di Lorenzo, E., Schneider, N., Cobb, K. M., Franks, P. J. S., Chhak, K., Miller, A. J., McWilliams, J. C., Bograd, S. J., Arango, H., Curchitser, E., Powell, T. M., and Rivière, P. (2008). North Pacific Gyre Oscillation links ocean climate and ecosystem change. *Geophysical Research Letters*, *35*(8).

Messié, M., Ledesma, J., Kolber, D. D., Michisaki, R. P., Foley, D. G., and Chavez, F. P. (2009). Potential new production estimates in four eastern boundary upwelling ecosystems. *Progress in Oceanography*, *83*(1–4), 151–158.

Messié, M., and Chavez, F. P. (2015). Seasonal regulation of primary production in eastern boundary upwelling systems. *Progress in Oceanography*, *134*, 1–18.

Miyake, Y., and Wada, E. (1967). The Abundance Ratio of 15N/14N in Marine Environments. *Records of Oceanographic Works in Japan*, *9*(1), 37–53.

Nagai, T., Gruber, N., Frenzel, H., Lachkar, Z., McWilliams, J. C., and Plattner, G. K. (2015). Dominant role of eddies and filaments in the offshore transport of carbon and nutrients in the California Current System. *Journal of Geophysical Research: Oceans*, *120*(8), 5318–5341.

Needoba, J. A., Waser, N. A., Harrison, P. J., and Calvert, S. E. (2003). Nitrogen isotope fractionation in 12 species of marine phytoplankton during growth on nitrate. *Marine Ecology Progress Series*, *255*, 81–91.

Ohman, M. D., Rau, G. H., and Hull, P. M. (2012). Multi-decadal variations in stable N isotopes of California Current zooplankton. *Deep-Sea Research Part I: Oceanographic Research Papers*, *60*, 46–55.

Pennington, J. T., Friederich, G. E., Castro, C. G., Collins, C. A., Evans, W. W., and Chavez, F. P. (2010). The Northern and Central California Coastal Upwelling System. In K.-K. Liu, L. Atkinson, R. Quinones, & L. Talaue-McManus (Eds.), *Carbon and Nutrient Fluxes in Continental Margins* (pp. 29–44). Springer Science & Business Media.

Plattner, G.-K., Gruber, N., Frenzel, H., and McWilliams, J. C. (2005). Decoupling marine export production from new production. *Geophysical Research Letters*, *32*(11), L11612.

Rau, G. H., Low, C., and Chavez, F. P. (1998). Suspended particle nitrogen delta 15 N versus nitrate ultilization: observations in Monterey Bay, CA. *Deep-Sea Research*, *45*(8 / 9), 1603.

Rau, G. H., Ohman, M. D., and Pierrot-Bults, A. (2003). Linking nitrogen dynamics to climate variability off central California: A 51 year record based on 15N/14N in CalCOFI zooplankton. *Deep-Sea Research Part II: Topical Studies in Oceanography*, *50*(14–16), 2431–2447.

Romera-Castillo, C., Letscher, R. T., and Hansell, D. A. (2016). New nutrients exert fundamental control on dissolved organic carbon accumulation in the surface Atlantic Ocean. *Proceedings of the National Academy of Sciences*, 201605344.

Rykaczewski, R. R., and Checkley, D. M. (2008). Influence of ocean winds on the pelagic ecosystem in upwelling regions. *Proceedings of the National Academy of Sciences*, *105*(6), 1965–1970.

Rykaczewski, R. R., and Dunne, J. P. (2010). Enhanced nutrient supply to the California Current

Ecosystem with global warming and increased stratification in an earth system model. *Geophysical Research Letters*, *37*(21).

Santoro, A. E., Casciotti, K. L., and Francis, C. A. (2010). Activity, abundance and diversity of nitrifying archaea and bacteria in the central California Current. *Environmental Microbiology*, *12*(7), 1989–2006.

Siegel, D. A., Buesseler, K. O., Behrenfeld, M. J., Benitez-Nelson, C. R., Boss, E., Brzezinski, M. A., Burd, A., Carlson, C. A., D'Asaro, E. A., Doney, S. C., Perry, M. J., Stanley, R. H. R., and Steinberg, D. K. (2016). Prediction of the Export and Fate of Global Ocean Net Primary Production: The EXPORTS Science Plan. *Frontiers in Marine Science*, *3*(March), 1–10.

Sigman, D. M., Karsh, K. L., and Casciotti, K. L. (2010). Nitrogen Isotopes in the Ocean. In *Encyclopedia of Ocean Sciences* (pp. 40–54).

Smith, J. M., Chavez, F. P., and Francis, C. A. (2014). Ammonium uptake by phytoplankton regulates nitrification in the sunlit ocean. *PLoS ONE*, *9*(9).

Smith, J. M., Damashek, J., Chavez, F. P., and Francis, C. A. (2016). Factors influencing nitrification rates and the abundance and transcriptional activity of ammonia-oxidizing microorganisms in the dark northeast Pacific Ocean. *Limnology and Oceanography*, *61*(2), 596–609.

Steinberg, D. K., and Landry, M. R. (2017). Zooplankton and the Ocean Carbon Cycle. *Annual Review of Marine Science*, *9*(1), 413–444.

Stukel, M. R., Landry, M. R., Benitez-Nelson, C. R., and Goericke, R. (2011). Trophic cycling and carbon export relationships in the California Current Ecosystem. *Limnology and Oceanography*, *56*(5), 1866–1878.

Stukel, M. R., Aluwihare, L. I., Barbeau, K. A., Chekalyuk, A. M., Goericke, R., Miller, A. J., Ohman, M. D., Ruacho, A., Song, H., Stephens, B. M., and Landry, M. R. (2017). Mesoscale ocean fronts enhance carbon export due to gravitational sinking and subduction. *Proceedings of the National Academy of Sciences*, *114*(6), 1252–1257.

Tems, C. E., Berelson, W. M., and Prokopenko, M. G. (2015). Particulate δ15N in laminated marine sediments as a proxy for mixing between the California Undercurrent and the California Current: A proof of concept. *Geophysical Research Letters*, *42*(2), 419–427.

Vokhshoori, N. L., and McCarthy, M. D. (2014). Compound-specific δ15N amino acid measurements in littoral mussels in the California upwelling ecosystem: A new approach to generating baseline δ15N isoscapes for coastal ecosystems. *PLoS ONE*, *9*(6).

Wada, E., Terazaki, M., Kabaya, Y., and Nemoto, T. (1987). 15N and 13C abundances in the Antartic Ocean with emphasis on the biogeochemical structure of the food web. *Deep Sea Research Part A, Oceanographic Research Papers*, *34*(5–6), 829–841.

Wankel, S. D., Kendall, C., Pennington, J. T., Chavez, F. P., and Paytan, A. (2007). Nitrification in the euphotic zone as evidenced by nitrate dual isotopic composition: Observations from Monterey Bay, California. *Global Biogeochemical Cycles*, *21*(2).

Ward, B. B. (1985). Light and substrate concentration relationships with marine ammonium assimilation and oxidation rates. *Marine Chemistry*, *16*(4), 301–316.

Ward, B. B. (1987). Nitrogen transformations in the Southern California Bight. *Deep Sea Research Part A, Oceanographic Research Papers*, *34*(5–6), 785–805.

Ward, B. B. (2005). Temporal variability in nitrification rates and related biogeochemical factors in Monterey Bay, California, USA. *Marine Ecology Progress Series*, *292*, 97–109.

Ward, B. B. (2008). Nitrification in Marine Systems. In *Nitrogen in the Marine Environment* (pp. 199–261).

Ward, B. B., Olson, R. J., and Perry, M. J. (1982). Microbial nitrification rates in the primary nitrite maximum off southern California. *Deep Sea Research Part A, Oceanographic Research Papers*, *29*(2), 247–255.

Chapter II

Stocks and Dynamics of Organic Carbon in the California Current Ecosystem Region

Abstract

Productive eastern boundary upwelling systems such as the California Current Ecosystem (CCE) are important for supporting both local and remote food webs. Several studies have reported on the temporal and spatial variability of primary production and gravitational export in the CCE. However, few studies have quantified the partitioning of net primary and new production into non-sinking reservoirs of organic matter. Non-sinking reservoirs, defined here as dissolved organic matter (DOM) and suspended particulate organic matter (POM), are available for lateral export to locations remote from their sites of production. This study tested the hypothesis that non-sinking detrital reservoirs constitute a sink for new production in the CCE. Non-sinking organic matter was quantified as total organic carbon (TOC) concentration, which included all of dissolved organic carbon (DOC) and some suspended particulate organic carbon (POC) in samples collected by the California Cooperative Oceanic Fisheries Investigation (CalCOFI) survey between 2008 and 2010. Overall, calculated TOC production (P_{TOC}) varied between 0.16 - 0.56 and 0.08 - 0.26 as a fraction of either potential new production (P_{New}) or satellite-based net primary production (NPP), respectively. In the most productive, inshore region P_{TOC}:NPP was similar to reported mean sinking export ratios (‘*e*-ratio’), and so, TOC represented a quantitatively significant reservoir for fixed carbon in the CCE. Throughout the CCE domain the sum of P_{TOC}:NPP and the *e*-ratio was similar to prior estimates of oxygen based *e*-ratio (0.16 - 0.24). These data identified TOC as an important repository of net and new production that was available for export from the inshore region of the CCE into the California Current.

1. Introduction

Under steady state conditions the export of organic matter from the surface ocean is expected to be equivalent to ‘new production’ [*Eppley* and *Peterson*, 1979; *Laws et al.*, 2000]. A prominent mechanism of export includes processed sinking particulate organic carbon (POC), and is comprised of intact phytoplankton cells, zooplankton and planktivorous fish fecal pellets, as well as remnants of zooplankton themselves [*Eppley* and *Peterson*, 1979]. In the California Current Ecosystem (CCE), enhanced Ekman transport and mesoscale variability can spatially and temporally decouple new and export production due to lateral offshore transport of inorganic nutrients and organic species such as biomass and detrital organic matter [*Landry et al.*, 1997; *Hales et al.*, 2005; *Plattner et al.*, 2005; *Stukel et al.*, 2011, 2013]. Modeling efforts based in the California Current have further shown that eddy-induced subduction of inorganic and organic nitrogen into the upper thermocline can reduce near-shore production at the site of upwelling but fertilize communities at the edge of the gyre [*Gruber et al.*, 2011; *Letscher et al.*, 2013].

Small particles that are suspended in seawater (~1-70 μm, [*Abramson et al.*, 2010]) are isotopically and chemically distinct from fast sinking particles typically associated with vertical export [*Altabet*, 1988; *Druffel et al.*, 1992; *Abramson et al.*, 2010]. This suspended POM can represent a significant fraction of the carbon and nitrogen accumulating in coastal environments following periods of upwelling [*Hill* and *Wheeler*, 2002; *Walker* and *McCarthy*, 2012]. Dissolved organic matter (DOM) contributes the highest concentration of organic carbon to the water column in most oceanic environments [*Hill* and *Wheeler*, 2002; *Halewood et al.*, 2012; *Walker* and *McCarthy*, 2012; *Wear et al.*, 2015] and may aggregate to form suspended POM. Both DOM and suspended POM are treated here as separate and distinct from fast sinking particles but both have been shown to participate in lateral export following subduction and advection [*Abell et al.*, 2000; *Carlson et al.*, 2004; *Duarte et al.*, 2013; *Letscher et al.*, 2013, 2016; *Siegel et al.*, 2014; *Omand et al.*, 2015]. In temperate regions of high convective overturn, the subduction of non-sinking organic matter (OM) has been shown to account for as much carbon export as the sinking organic matter flux [*Carlson et al.*, 1994]. In situ measurements and models suggest that non-sinking OM can exceed 25% of total export production from the surface ocean [*Hansell* and *Carlson*, 1998; *Najjar et al.*, 2007; *Stukel et al.*, 2017], and support up to 67% of apparent oxygen utilization (AOU) in the mesopelagic [*Emerson*, 2014]. Assessing the magnitude of new and primary production that is channeled into non-sinking organic carbon could reconcile the observed regional decoupling of new and export production in the CCE.

In this study, we calculated seasonal new production (P_{New}) and TOC production (P_{TOC}) for four hydrographically distinct regions of the southern CCE. These calculations relied on measured concentrations of nitrate and total organic carbon (TOC) from samples collected between 2008 and 2010 on quarterly California Cooperative Oceanic Fisheries Investigations (CalCOFI) survey cruises. The relative partitioning of P_{New} and satellite-based net primary production (NPP) into the TOC reservoir was calculated and compared to regional rates of sinking POC flux to examine the relevance of non-sinking OM as a sink of newly fixed carbon. Variations in the ratio of P_{TOC} to P_{New} and NPP were further examined in the context of available biological and physical data to identify potential mechanisms that contributed to the production and accumulation of non-sinking OM across the CCE during the study period. Overall, the accumulations of TOC across the domain could help to balance previously identified offsets between new production and sinking export production in the California coastal environment [*Plattner et al.*, 2005; *Gruber et al.*, 2011; *Stukel et al.*, 2011, 2017].

2. Materials and Methods

2.1. Study Region and Sampling Period

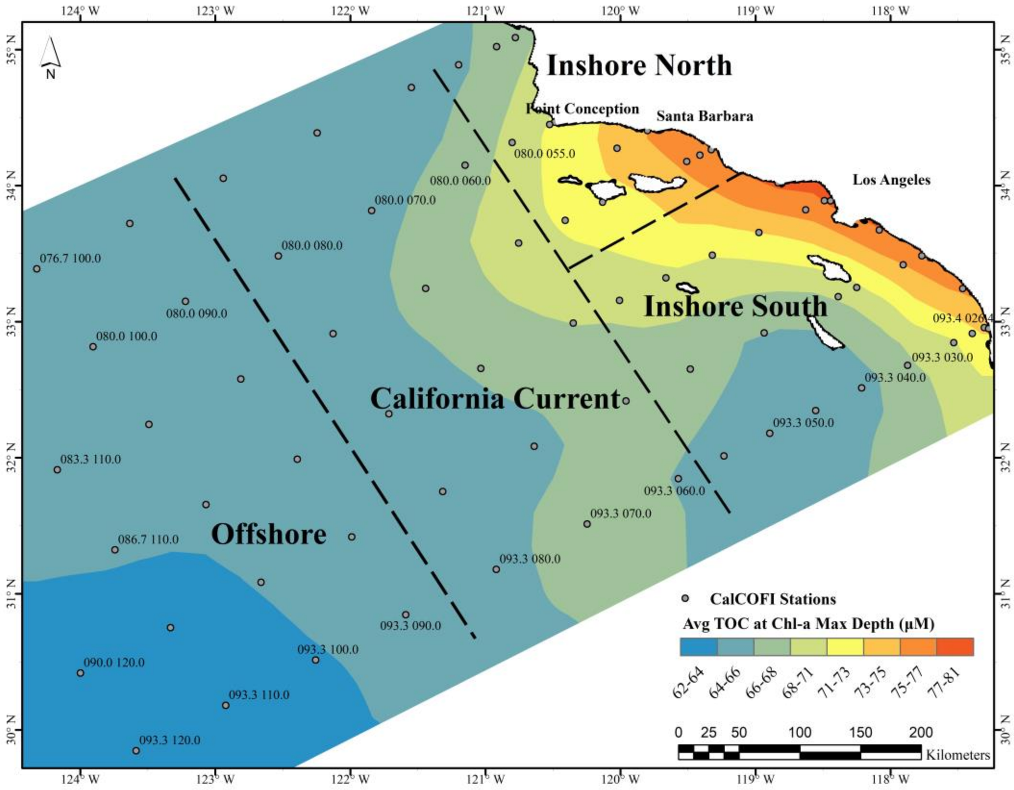

Figure 2.1. *Sampling locations in the CalCOFI domain. Colors depict the annual mean [TOC] (µM C) at the chlorophyll-a maximum (Chl-a Max) depth across the CCE. Greater [TOC] are observed in coastal upwelling dominated sites. CCE-CalCOFI subregions discussed in the text are identified in the figure as Inshore North (Chl-a Max depth of 14 ± 4m), Inshore South (22 ± 6m), California Current (33 ± 6m) and Offshore (62 ± 12m).*

Datasets discussed in this study were generated primarily from samples collected between 2008 and 2010 on quarterly CalCOFI cruises augmented by the CCE Long Term Ecological Research (LTER) program. Total organic carbon (TOC) and suspended particulate organic carbon (POC) samples were collected from up to twenty depths between 0 and 550 m for TOC and from 0 to 100 m for suspended POC. Hydrographic data and biological and inorganic chemical parameters were available for all relevant depths for ~77 stations during these survey cruises (Figure 2.1). In addition, we estimated net primary production (NPP) from satellite data for the same time period.

Samples were collected on CalCOFI cruises from April 2008 (i.e., cruise 200804), August 2008 (200808), October 2008 (200810), January, July and November 2009 (200901, 200907, 200911), and January, April, and August 2010 (201001, 201004 and 201008). In total, 5,213 TOC and 1,966 POC samples were analyzed for this study. For ease of data analysis and discussion, sample collection locations within the typical CalCOFI sampling grid are designated as Inshore North (13 stations), Inshore South (28), California Current (18), and Offshore (18) regions [*Munro et al.*, 2013; *Taylor et al.*, 2015] (Figure 2.1). Mean [TOC] distributions for the Chl-*a* max depth by station and line suggest these designations appropriately differentiate regional influences on [TOC] (Figure 2.1). Generally, the California Current region represents the transition between the oligotrophic Offshore and eutrophic Inshore and loosely tracks the path of the California Current along the shelf break. However, the California Current meanders and does not always adhere to the above definition of fixed station location. Southern Inshore typically differs in surface circulation patterns depending on time of year but generally receives more surface water from the south (i.e., from Baja California) and the North Pacific Subtropical Gyre than the Northern Inshore region [*Hayward* and *Venrick*, 1998].

2.2. Hydrographic and Biogeochemical Analysis

As part of the ongoing CalCOFI program, continuous measurements of pressure, temperature, and conductivity were made from surface to 515m, bottom depth permitting, via shipboard CTD (Sea-Bird Electronics, Inc., Bellevue, WA, USA). Standard nutrient and hydrographic samples were collected via rosette casts at twenty standard depths. Measured variables include salinity (Practical Salinity Scale, UNESCO 1981), dissolved oxygen, phosphate, nitrate, nitrite, ammonium, silicate and chlorophyll a (see www.calcofi.org for analytical protocols). Chl-a was measured via fluorescence on acetone extracts of POM [*Goericke*, 2002; *Taylor et al.*, 2015]. Nutrients were analyzed shipboard by continuous-flow analysis within 2-16 h of sample collection. Nitrite and nitrate are measured concurrently using a colorimetric assay on a cadmium reduction coil (after [*Armstrong et al.*, 1967] with modification). Accuracy of nitrate measured by this method is ±0.05 µM, as determined by the quality of standards.

2.3. TOC Analysis

Seawater for [TOC] analysis was collected into combusted 40-mL borosilicate vials and sealed using acid-washed vial caps with septa that had not been previously pierced. Seawater was immediately acidified to pH 2, where 40 mL of seawater received 2 drops (~200 µL) of trace metal grade 12N HCl (Fisher Scientific). Acidified samples were stored at room temperature in the dark until analyzed via high-temperature combustion on a Shimadzu 500 V-CSN/TNM-1 (Shimadzu Corp, Kyoto, Japan) that was modified from the manufacturer's design.

We used combustion tubes containing 0.5 cm of glass fiber above and below the Pt catalyst beads to improve peak shape (C. Carlson pers. comm.). Combustion columns were pre-conditioned on 40-100 injections of filtered (0.2 μm) seawater until the baseline of measured carbon was stable. Columns and catalyst were generally changed every 120-150 samples. A magnesium perchlorate water-trap was placed prior to the halogen trap and changed daily. CO_2-free carrier gas was used to pre-condition the column and ultra-high purity grade O_2 gas was delivered to the instrument as the carrier gas during sample analysis.

Each acidified TOC sample was sparged for two minutes and measured following high-temperature combustion at 680˚ C. During analysis, five 100 μL injections are made from a single sample reservoir and samples were reanalyzed when the %CV of the best 3 injections was >5%. TOC measurements were calibrated using an 8-point calibration curve between 10 and 100 μM C of potassium phthalate in Milli-Q water. Milli-Q water and deep sea reference water were analyzed every 10 samples. Reference standards were obtained from NSF-supported deep Florida Strait (Batch 6FS – 2006; Dennis Hansell, RSMAS, University of Miami). Reference standards measured here typically ranged between 41 and 44 μM C. If reference standard measurements were outside the expected range then TOC samples were reanalyzed. The reference standards were measured within a mean CV of 2.7%, which typically corresponded to an average TOC range of ±1.2 μM C. The expected concentration range for Batch reference materials is provided at http://www.rsmas.miami.edu/groups/biogeochem/. Further details of sample analysis details and data verification protocols here can be found at cce.lternet.edu/research.

The relationship between TOC and density below the surface Ekman layer was examined to identify any outliers in the dataset, and this served as a final quality check of each data point. This relationship is remarkably predictable in subsurface waters (i.e., >250 m), and so, samples that produced data points that strayed greater than one standard deviation from the best-fit TOC:potential density relationship were reanalyzed to test whether the measured [TOC] was reproduced.

As others have noted (e.g., [*Hansell et al.*, 1997]), the small volume of the TOC measurement preferentially selects for the more homogeneously distributed dissolved organic carbon (DOC) reservoir. As discussed in the results, when suspended POC concentrations ([POC]) are higher during bloom conditions, [TOC] will also be influenced by [POC]. Our TOC measurement does not capture the sinking POC present during sampling (and any aggregation and settling after TOC sample collection is not included in the measurement). As such, our [TOC] measurement excludes fast sinking organic carbon, consistently quantifies DOC, and sometimes includes suspended POC. As these are all operational definitions it is not possible to completely separate each fraction.

2.4. POC Analysis

Suspended [POC] and [PON] were determined on one- to two-liters of seawater filtered through 25 mm pre-combusted (450˚ C, 6h) Whatman GF/F filters. Inorganic carbon was removed by acidifying the filters with HCl vapor, followed by oven drying, overnight. One half of the filter was used for PON and POC analysis on a Costech Elemental Analyzer (Costech Analytical Technologies, Valencia, CA, USA) according to standard protocols (see http://cce.lternet.edu/data/methods-manual).

2.5. Satellite-Estimated Net Primary Production

The low temporal and spatial resolution of shipboard ^{14}C-based measurements of NPP restricted the size of the TOC dataset that was available to compare to various indices of production. Thus, we turned to satellite-based estimates of NPP to achieve the spatial coverage that matched our TOC dataset. Satellite-based estimates of NPP were calculated using a transformed vertically generalized production model (VGPM) for the California Current region (termed VGPM-CAL) after [*Kahru et al.*, 2009]. The VGPM model estimates NPP using detected surface chlorophyll, photosynthetically active radiation and temperature as well as estimates of euphotic zone depth and photosynthetic efficiency [*Behrenfeld* and *Falkowski*, 1997]. Briefly, monthly average VGPM data were obtained at 10 km-grid spacing from Oregon State's Ocean Productivity website (http://www.science.oregonstate.edu/ocean.productivity/). Values were converted from the standard VGPM product to VGPM-CAL using the following formula: 10^log(VGPM-0.1924). The average of eight spatial estimates within a 20 km square and within ±15 d of CalCOFI station sampling locations and times was used to estimate the average satellite-based NPP value. Satellite-based estimates of NPP scale well with other methods of estimating primary producer biomass (e.g., [Chl-*a*] at Chl-a max depths; r^2=0.53 and p<0.001).

2.6. Δ[TOC] and Δ[POC]

Both DOC and POC include long-lived fractions that are unlikely to vary with indices of primary production [*Druffel et al.*, 1992]. Thus we attempted to calculate “new” additions to the TOC and POC reservoir above background concentrations (i.e., Δ[TOC] and Δ[POC]) in order to examine variations linked to biological activity. First, [TOC] and [POC] were binned into 0.25 kg m^{-3} potential density (σ_θ) intervals across the entire CalCOFI grid. Second, the minimum 10th percentile value of all measured [TOC] or [POC] within a density interval was identified, which resulted in a single density-based profile (Figure S2.1) that was designated as the background TOC or POC profile. We used the minimum 10th percentile value and not the minimum measured value to avoid biasing the background profile with outliers. Such an approach also accommodated the analytical error of our measurements. On average, the minimum 10th percentile value represented in the 11th (± 5) lowest [TOC] observation per isopycnal. To compute density interval-specific Δ[TOC] and Δ[POC] at each CalCOFI station the minimum TOC or POC profile was subtracted from the measured profile. Studies at other locations computed this parameter using seasonal DOC profiles that constrained background concentrations (e.g., Sargasso and Ross Seas; [*Carlson et al.*, 1994; *Carlson et al.*, 1998]). However, the CCE region is subject to high meso- and microscale eddy activity, which means that the *seasonal* resetting of surface ocean organic carbon concentrations is inconsistently detected. Seasonal Δ[TOC] and Δ[POC] for each subregion (Figure S2.2) are seasonal compilations (in terms of median and range) of values within the surface σ_θ

< 26.0 kg m^{-3}. We determined the spread surrounding Δ[TOC] according to the following formulation:

$$\boldsymbol{\Delta TOC_{error}} = \left(\left([\boldsymbol{TOC}] * \left(\frac{\%\boldsymbol{CV}}{\boldsymbol{100}}\right)\right)^{\boldsymbol{2}} + (\boldsymbol{\Delta TOC_{20th\,Perc}} - \boldsymbol{\Delta TOC_{10th\,Perc}})^{\boldsymbol{2}}\right)^{\boldsymbol{1/2}} \tag{1}$$

The range (i.e., denoted by “±”) in Δ[TOC] encountered regionally or seasonally is determined as the 10th and 90th percentile values (e.g., Figure S2.2). The error for the 10th and 90th percentile Δ[TOC] values were propagated using the coefficient of variation (CV) per measured sample and the CV for the region and season-specific 10th percentile value.

2.7. BECCO Model Velocities

The Biogeochemistry Estimation of the California Current (BECCO) model currently under development at SIO (http://sose.ucsd.edu/CASE/) has been used here to estimate vertical and horizontal velocities for 2008-2010. The BECCO model has a 1/16 of a degree (~7 km) resolution and has 72 vertical depths of varying thickness. 5-d averages for those model locations within a 40 km radius of the relevant CalCOFI station were used to estimate vertical velocities. Validation of BECCO model velocities has been reported by *Todd et al.* (2011, 2012).

2.8. Principal Components Analysis

To provide statistically significant estimates of TOC production and new production it was necessary to divide the vast dataset into spatial subsets, as was done above. However, the complex hydrography within a CalCOFI subregion can blur signatures of ecological and biogeochemical processes. As such, consistent patterns in [TOC] variability were further examined by identifying other measurements that exhibited a significant correlation with [TOC]. The dominant variables driving [TOC] in each CalCOFI sub-region were first identified using a stepwise multiple regression analysis using Minitab (v17.1.0). For regression analysis, surface mean values were first calculated from individual profiles of 18 variables available through CalCOFI to be compared to surface mean [TOC]. Properties for each profile were averaged over σ_θ<26.0 kg m^3, where 26.0 kg m^{-3} is defined as the depth of the pycnocline based on *Jacox et al.* [2016]. In addition to the 18 near-surface variables available from the CalCOFI database, eddy kinetic energy [*Kelly et al.*, 1998] and NPP were calculated separately using satellite data (See Table S2.1 for a list of variables tested). All twenty variables were then transformed by taking the cube root to improve dataset normality across all variables.

For each subregion a subset of four predictor variables resulted in minimum derived Mallows' Cp values [*Mallows*, 1973] relative to the number of predictors selected across the region. For instance for the Inshore North region, surface mean [Chl-*a*], AOU, buoyancy frequency (0 over 200m; [*Smith* and *Ferrari*, 2009]) and surface mean spiciness [*Munk*, 1981] were the best predictor variables, which indicated that indices of surface stratification, upwelling and phytoplankton productivity were correlated with [TOC] in this region. Overall, the combination of predictor variables explained 66% and 57% of the variance in TOC for the Northern and Southern Inshore regions, respectively. However, less of the variance in the California Current (32%) and Offshore (15%) regions was explained by the 4 best region-specific predictor variables. Table S2.1 provides a list of the predictor variables selected for each sub-region and Text S2.1 includes a brief description of the physical, ecological and biogeochemical significance of the selected variables.

Minitab was used again to perform a Principal Components Analysis (PCA) for each subregion on the identified combination of cube-root normalized four variables and [TOC] (Matlab (vR2013a) produced similar data separations by PCA and was used to produce biplots in Figure S2.3). Such an analysis separated sampling locations on a biplot based on their physical/biological signatures. The combined variance explained by the first two components ranged from 65 to 77% for all sub-regions. Results of the PCA are primarily analyzed here in terms of how stations separated across PC biplot space, where samples appeared to separate reasonably well by quadrants of the biplot (see Text S2.2 for a brief description of PCA quadrants). Stations for the same cruise (season) that fell into a particular quadrant were also averaged to provide a mean PCA-based quadrant value for each cruise. Any quadrant could have up to 9, cruise-specific, mean values for each property (9 is the total number of cruises in this study). Such an approach reduced data complexity from 5,032 [TOC] data points to 121 values (e.g., Figure 2.4) facilitating identification of broad ecosystem patterns associated with changes in [TOC].

2.9. Statistical Evaluation of Best Fit Lines

Figures generated in the following analysis include linear and logarithmic best fit lines using Sigma Plot (v10.0). The best fit lines include ±95% confidence intervals to illustrate the number of observations that fall within statistical significance of the prediction lines. All model best fit lines were determined using a Model II formulation using Matlab Code provided by Ed Peltzer (MBARI; www.mbari.org).

2.10. New Production

Phytoplankton production in the Southern California Bight region is primarily limited by nitrate [*Eppley* and *Peterson*, 1979; *Eppley et al.*, 1979], and in the southern CCE vertical transport is the major source of nitrate delivered to the euphotic zone [*Messié et al.*, 2009; *Pennington et al.*, 2010]. Therefore, potential new production (P_{New}) can be estimated from the vertical gradient in nitrate and the vertical advection rates determined from a regional model. Vertical diffusivity is only important during particular seasons and is a small component of the total vertical flux [*Olivieri* and *Chavez,* 2000; *Pennington et al.*, 2010; *Todd et al.*, 2012].

The concentration of nitrate ($[NO_3^-]$) at the base of the nitracline was designated the upwelling $[NO_3^-]$. This study defined nitracline depth differently from previous studies (e.g., [*Hansell* and *Carlson*, 1998; *Pennington et al.*, 2010; *Haskell et al.*, 2016; *Romera-Castillo et al.*, 2016]). For instance, the CalCOFI domain defines the nitracline depth as the depth where $[NO_3^-]$ reaches a value of 1 μM (e.g. [*Bjorkstedt et al.*, 2010]), but to calculate potential new production we defined it as the "depth of first nitrate use." In the CCE, $[NO_3^-]$ is consistently predictable using the highly conserved relationship of temperature and nitrate in the range of temperatures <14.5° C [*Lucas et al.*, 2011]. As such, our designation of nitracline was determined as the deepest depth where observed nitrate was 2.5±0.5 μM lower than the $[NO_3^-]$ predicted by the temperature versus nitrate relationship. That is, we assumed that biological uptake was occurring at depths where $[NO_3^-]$ fell below the predicted value by 2.5 ± 0.5 μM or more. The magnitude of this departure for each profile was restricted by sampling resolution. Our defined nitracline depth often corresponded with the deepest depth where CTD-detected fluorescence increased over background values (Figure S2.4), consistent with the assumption that autotrophic production was responsible for the observed departure in $[NO_3^-]$ from the predicted value. The mean isopycnal surface for our nitracline estimate was 25.6±0.5 kg m^{-3}. Over the long term, the seasonal inshore mean $[NO_3^-]$ at the pycnocline (26.0 kg m^{-3}; [*Jacox et al.*, 2016]), was correlated with [Chl-*a*] at the depth of the Chl-*a* maximum ($R=0.37$, $p<0.001$) and satellite estimates of NPP ($R=0.67$, $p<0.001$; Figure S2.5).

Potential new production within the euphotic zone (P_{New}) was calculated according to Equation (2). For this formulation, the euphotic zone was designated as the region of the water column shallower than the depth of first nitrate use. To calculate the mean $[NO_3^-]$ in the euphotic zone (i.e., $[NO_3^-]_{EZ}$) we only considered non-zero concentrations in the region shallower than the depth of first-use, or as defined here, the nitracline depth. This $[NO_3^-]_{EZ}$ was then subtracted from the nitrate concentration at the nitracline depth ($[NO_3^-]_{first}$) to estimate $[NO_3^-]$ that had been utilized in the euphotic zone. Finally, to convert utilized $[NO_3^-]$ to a nitrate removal rate the vertical advection rate for each depth profile was taken from the BECCO model. This provided upwelling velocities within ±10 m of the nitracline depth and within ±10 d surrounding the CalCOFI cruise sampling date. 20-d average velocities represent the typical event length observed at the CCE-2 mooring for the chemically- (and biologically-) relevant species nitrate, oxygen and pCO_2 [*Martz et al.*, 2014], and is a slightly longer time scale than the

7.5 d of biomass turnover used to estimate nitrate-based production used elsewhere (e.g., [*Aksnes* and *Ohman*, 2009]). For reference, the CCE-2 mooring is positioned on the shelf break off Point Conception along Line 080.0 of the CalCOFI domain. The removal rate was subsequently converted to carbon equivalents using published C:N ratios [*Martiny et al.*, 2013].

$$\boldsymbol{P_{New}} = \left(\overline{[\boldsymbol{NO_3}]}_{\boldsymbol{first}} - \overline{[\boldsymbol{NO_3}]}_{\boldsymbol{EZ}}\right) * \boldsymbol{\overline{w}_{Deep}} * \boldsymbol{C:N} \tag{2}$$

In the above equation $\overline{w}_{Deep}$ (m d^{-1}) refers to the mean vertical transport within ±10m of the nitracline depth, $[NO_3^-]_{first}$ (μM) refers to the concentration of nitrate at the nitracline depth, and $\overline{[NO_3]}_{EZ}$ refers to mean nitrate concentrations (μM) in the euphotic zone (the region between the nitracline and up to shallowest depth with observable $[NO_3^-] > 0$ μM). Two different C:N values were chosen to represent the different CCE sub-regions. The Offshore and California Current communities of the CCE are typically comprised of small cyanobacteria, in particular Prochlorococcus [*Taylor et al.*, 2015]. These communities are expected to be similar to those gyre communities for which [*Martiny et al.*, 2013] determined a C:N of 195:28 (~7:1). The Inshore communities are typical of nutrient-rich upwelling zones with C:N of 137:18 (7.6:1). In formulating Equation (2) it was also assumed that nitrate supplied to the euphotic zone with a BECCO model-derived 20-d average vertical velocity was channeled into primary production at this same rate (i.e., utilization rate) [*Messié et al.*, 2009; *Pennington et al.*, 2010; *Romera-Castillo et al.*, 2016].

Other processes such as nitrification can influence observed $[NO_3^-]$ in the euphotic zone (e.g., [*Santoro et al.*, 2010]) and physical processes other than vertical advection can also supply nitrate to the euphotic zone. Vertical advection was most often an order of magnitude greater than mean eddy diffusivity in the CCE [*Gelpi* and *Norris*, 2008; *Todd et al.*, 2012]. However, when winds are reduced, particularly inside the Southern California Bight, diapycnal diffusion of nitrate can sometimes be the dominant vertical supply route [*Haskell et al.*, 2016]. Nonetheless, in the absence of robust diffusion estimates for each profile, we only consider vertical advection in this formulation of nitrate-based production.

For Equation (2) to yield a meaningful utilization rate, each location with a [NO_3^-] profile had to be characterized by a positive vertical advection rate (i.e., upwelling) and a clearly distinguishable nitracline depth, as defined above. Of the 646 depth profiles that had both [NO_3^-] and [TOC], 282 satisfied both conditions necessary for calculating P_{New} using Equation (2).

2.11. TOC Production and P_{TOC}:P_{New} Partitioning

Potential TOC production (P_{TOC}) was estimated using a method similar to P_{New} as described above. [TOC] at the depth of first NO_3^- use was subtracted from the mean "euphotic zone" $[TOC]_{EZ}$ (note that TOC is produced in the euphotic zone while nitrate is consumed). The TOC production rate (mmol C m^{-2} d^{-1}) was calculated by multiplying the excess [TOC] in the euphotic zone by the average upwelling velocity used in equation (2). The fraction of potential new production that was partitioned into TOC was expressed as P_{TOC}:P_{New} and was determined as a profile specific value. To be consistent with P_{New}, calculated $[TOC]_{EZ}$ did not include measured [TOC] at depths where [NO_3] was zero even though there was measurable TOC. Any TOC present in surface waters where nitrate was zero was considered to be surface "accumulating" TOC. Including these depths in the P_{TOC} calculation significantly impacted sampling locations with a stratified water column, such as those in the Offshore region, where P_{TOC} could increase by as much as 20-30%.

2.12. Important Differences Between Datasets

When the goal was to examine stocks and dynamics of [TOC] and [POC], which served to inform how variations in P_{TOC}:P_{New} could be impacted by TOC dynamics, data from all 646 stations were used. These datasets were used to calculate density binned TOC and POC accumulations (i.e., Δ[TOC] (n= 5,032) and Δ[POC] (n=1,966)) by subtracting measured concentrations from a background profile generated from the 10th percentile minimum values of either the [TOC] or [POC] dataset. When we sought to identify the physical and biological parameters that best explained [TOC] variability in each region we calculated mean surface zone properties (σ_θ<26.0 kg m^{-3}) for each station during each cruise ($[TOC]_{Surface}$ and $\Delta[TOC]_{Surface}$). In this case, mean surface properties were examined by stepwise multiple regression followed by PCA to visualize ecologically relevant correlations that could be driving the variability in surface [TOC]. The PCA was divided by sub-region, and both PCA quadrant-specific means (Table S2.2 and Figure 2.2) and cruise specific means (Figures 2.3 and 2.4) within a PCA quadrant, were calculated for comparative analysis (see Figure S2.6 for a schematic of the averaging methods used here). Finally, P_{TOC} was determined for each profile by subtracting nitracline [TOC] from mean euphotic zone [TOC], where mean euphotic zone [TOC] excluded any TOC values at depths where [NO_3^-] was zero (this was done to stay consistent with the P_{New} calculation). The two estimates of added TOC (the euphotic zone [TOC] difference used for P_{TOC} and Δ[TOC]) were different from one another and varied with region and season (Figure S2.8).

3. Results

3.1. Profiles and Regional Trends

[TOC] for the southern CCE between 2008 and 2010 were 36.0 - 210.5 µM C (n=5,032) over depths 0 - 3550 m and potential densities (σ_θ) 22.5 - 27.8 kg m^{-3}. Increases in [TOC] were typically associated with enhanced [Chl-*a*] (>1.0 µg L^{-1}; Figure 2.2). In Inshore regions of the CCE, springtime shoaling of denser isopycnals (σ_θ: 25.5-26.0 kg m^{-3}) increased nutrient concentrations in the euphotic zone and led to [Chl-*a*] in excess of 1.0 µg L^{-1} and [TOC] in excess of 70 µM C (Figure 2.2). During the summer, surface waters warmed and their potential density and surface [Chl-*a*] decreased (σ_θ<25.0 kg m^{-3}; [Chl-*a*] <1.0 µg L^{-1}), yet [TOC] sometimes persisted at elevated levels. [TOC] in excess of the upwelling concentration of ~50 µM C reflected either recent "addition" to the reservoir by primary production or a persisting pool of TOC from recent biological activity [*Carlson et al.*, 1994]. Along a specific isopycnal, median [TOC] at inshore sites exceeded offshore values by 3 - 10 µM (Figure 2.2). The Inshore North region exhibited the greatest additions, which were likely linked to persistent moderate upwelling at this location throughout the year [*Huyer*, 1983].

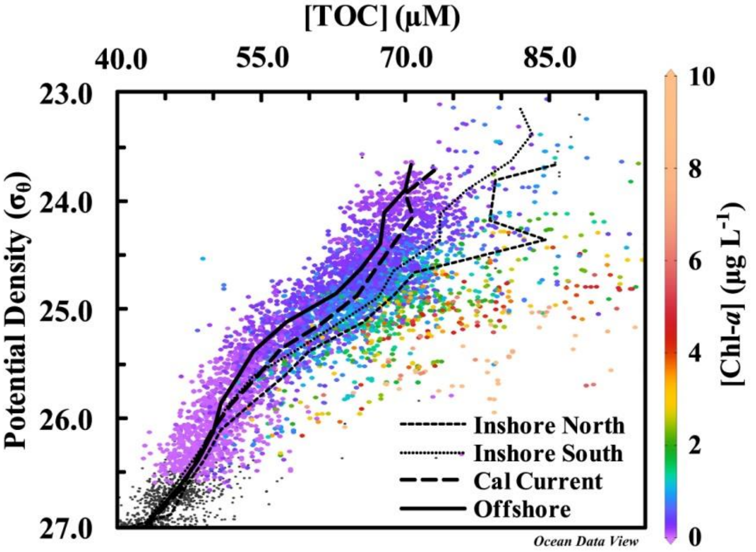

Figure 2.2. *Colored dots represent individual samples with associated [Chl-a]. Profiles for each region represent median [TOC] for 0.25 kg m^{-3} density bins (interpolated black lines). Data points where [Chl-a] >1.0 µg L^{-1} are often associated with denser isopycnals (25.0 - 26.0 kg m^{-3}) shoaling into the surface euphotic zone. Data points where [Chl-a] <0.5 µg L^{-1} and TOC = 60-75 µM C are associated with warmer, less dense (<24.5 kg m^{-3}) summer and fall stratified waters. Black dots have no associated [Chl-a] measure.*

Throughout the water column [TOC] was most strongly correlated with potential temperature (r^2=0.66, p<0.0001, n=5,032). As expected, [TOC] was also significantly correlated with log-transformed depth (r^2=0.58, p<0.0001) and other chemical variables whose concentrations change with depth, such as [O_2] (r^2=0.56, p<0.0001) and [PO_4] (r^2=0.62, p<0.0001). These correlations point to the strong physical control on [TOC] profiles in this hydrographically complex region.

At the pycnocline (i.e., $\sigma_\theta \approx 26.0$ kg m^{-3}) [TOC] was 50.0 - 55.0 µM C (Figure 2.2), and these concentrations were sometimes observed in surface waters during an upwelling event. In upwelling waters, TOC was primarily DOC (i.e., [DOC] ≈ [TOC]). In fact, throughout much of the Inshore South, California Current, and Offshore subregions [TOC] measurements primarily reflected [DOC]. For example, there was consistent overlap of surface measured [TOC] with surface [DOC] from the Santa Barbara Channel (SBC; [*Wear et al.*, 2015]) (Figure S2.7a). Additionally, [DOC] collected in 2013 for CLIVAR line P02 (east of longitude 139.0 W) had similar values to [TOC] by depth (Figure S2.7a). During bloom conditions when Inshore regions had suspended POC concentrations ([POC]) in excess of ~5.0 µM C, [TOC] was influenced by [POC] (Figure S2.7; see also Text S2.3 for further discussion). Other studies in productive regions have made similar observations (e.g., [*Carlson et al.*, 1998]).

3.2. Insights into Regional TOC Variability

To identify key parameters that best explained the variance in surface [TOC] we carried out a stepwise multiple regression analysis using a suite of mean surface water properties (σ_θ<26.0 kg m^{-3}). In each sub-region four variables related to water column stability and primary production most effectively correlated with surface [TOC] (see Text S2.1 for a description of the variables used for each subregion and Figure S2.3 for PCA biplots). The combination of those four variables and [TOC] were then used in a PCA to further separate out the subregional datasets into unique conditions. Each of the five variables contributed to PC1 and PC2 of the PCA and so the resulting distribution of points in the PCA biplot is a reflection of the combined contribution of those variables. However, there were many stations where selected variables were all relatively close to mean conditions and those points fell toward the middle of PCA biplot space. In other words, PCA could not always separate the stations for each subregion into distinct and easily identifiable clusters. To avoid biasing the analysis by removing stations that fell toward the center of the PCA biplot, we designated all sampling locations that fell into each quadrant in the PCA biplot as a ‘cluster’. As such, each sub-region had four different clusters/quadrants representing a range of surface [TOC] and [Chl-*a*] conditions (Figure 2.3).

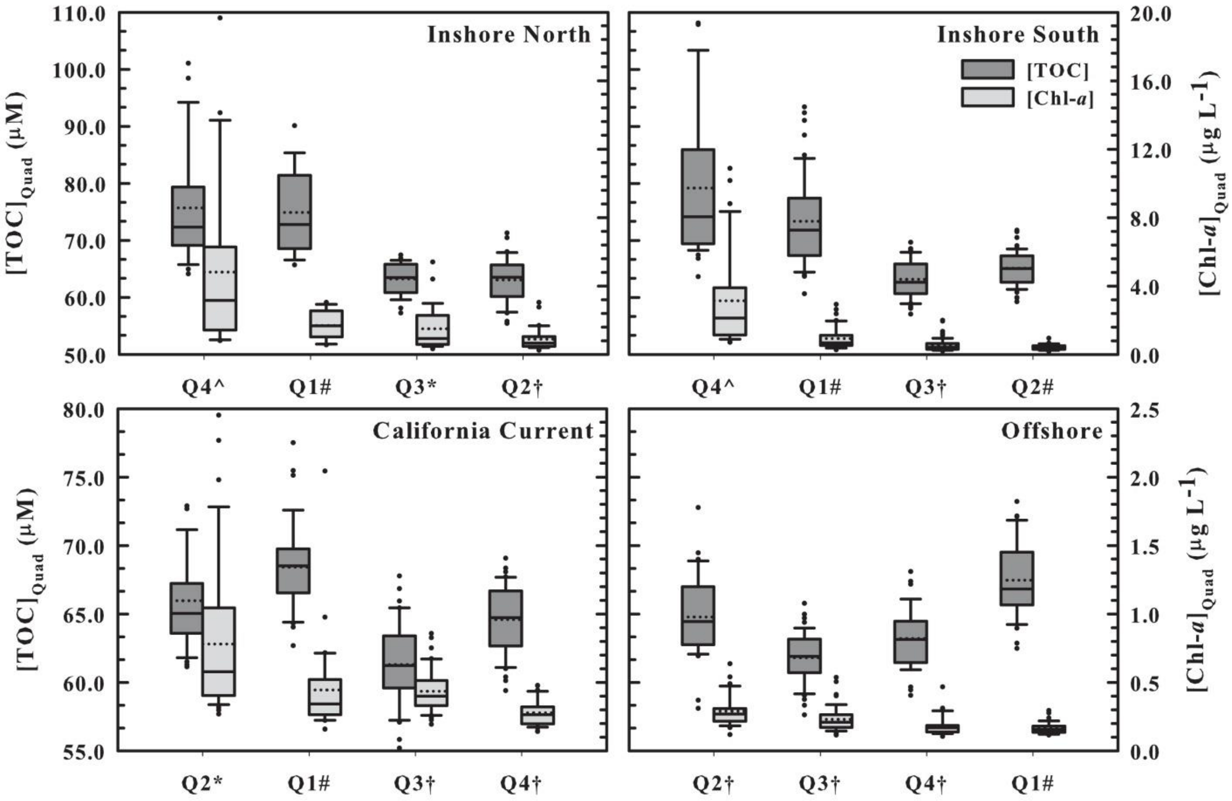

Figure 2.3. *Principal components divided stations in each subregion into four “Quadrants.” Q1-4 refers to each quadrant of the PCA biplot and are ordered here by decreasing mean quadrant [Chl-a]. PCA was performed for each region using surface [TOC], and a combination of 4 other variables that best explained the variance in [TOC]. See methods and results sections for further details on determinations of each quadrant designation and Table S2.2 for mean values for each quadrant. Inside the box plots, the solid and dotted lines are the median and mean, respectively. The edges of the box plots represent the 25th and 75th percentiles, and outside the box plots the whiskers are the 10th and 90th percentile values. The dots identify “outliers”. Note change in scales between Inshore (top panels) and Offshore (bottom panels).*

In the Inshore North and South regions, stations with elevated mean quadrant-specific [TOC] values, 75.7 ± 10.1 μM and 79.2 ± 13.7 μM, respectively, were associated with sampling locations that had high [Chl-*a*] (Figure 2.3) and also high net primary production. The highest [TOC] stations were typically closest to shore (<20 km from shore). However, [Chl-*a*] alone did not explain the observed differences in surface mean [TOC]. For example, some sampling locations, in the Inshore South (n=55 out of 207), clustered based on relatively high [TOC] (73.4 ± 7.8 μM) but low [Chl-*a*] (0.93 ± 0.06 μg L^{-1}; Figure 2.3). Other factors that impacted [TOC] at these sampling locations can be inferred by examining PC biplots.

To remove the influence of background [TOC] (50 - 55 μM C) and examine only variations in added [TOC] we considered the relationship between Δ[TOC] and other parameters that explained [TOC] variance in PCA biplots (Δ[TOC] was calculated as described in Section 2.6). To simplify the PCA we calculated surface mean values, and the same was done for Δ[TOC] (e.g., mean of all Δ[TOC] values above the pycnocline at each sampling location). To further simplify the comparison, a cruise-specific mean value of surface mean Δ[TOC] was determined for sampling locations that fell within each quadrant of a PCA biplot. As expected, Δ[TOC] values increased with increasing [Chl-*a*] (Δ[TOC] = 6.5(ln[Chl-*a*]) + 11.1; r^2=0.64, p<0.001; Figure 2.4a and Table S2.2); and ΔPOC, calculated in a similar manner, and ΔTOC were highly correlated across the region (r^2=0.80, p<0.001) (Figure 2.S9). Based on the relationship to [Chl-*a*], a 'Bloom' classification (Figure 2.4) was assigned to quadrants in Inshore biplots containing sampling locations with the highest Δ[TOC] (20 - 35μM) and highest [Chl-*a*] (Figure 2.4a).

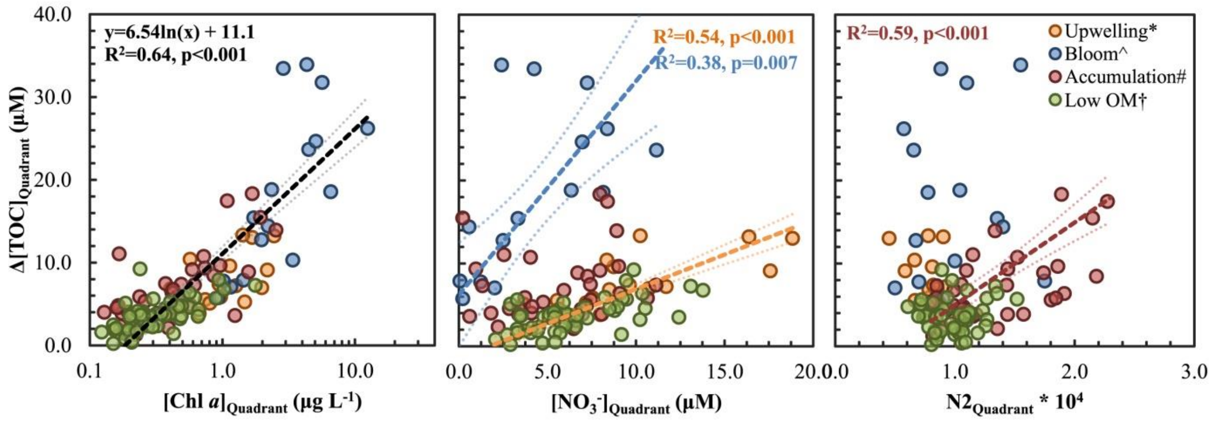

Figure 2.4. *Each point represents a cruise mean for identified Quadrants (see Quadrant description in methods and results sections). The "Upwelling" condition was designated for the California Current (Q2) and Inshore North (Q3). "Bloom" conditions were designated for the Inshore North (Q4) and South (Q4). "Accumulation" conditions were designated for Q1 of all subregions. And "Low OM" conditions were identified for Inshore North and South and California Current and Offshore: Quads 2, 3, 3 and 4. The thinner dotted lines outside of Model II best fit lines represent the ±95% confidence intervals.*

In the Inshore North and California Current region several sampling locations clustered together in each PCA biplot that had medium [Chl-*a*] and Δ[TOC] (10 - 15μM) but high [NO_3^-] (Figure 2.4a and 2.4b). Quadrants where these sampling locations were found were designated as 'Upwelling' conditions. In the California Current region the Upwelling quadrant was characterized by higher [Chl-*a*] and higher wind speed (Figure S2.3 biplots) indicating that upwelling was likely mediated by wind stress curl [*Rykaczewski* and *Checkley*, 2008]. Finally, some sampling locations had moderate Δ[TOC] but were primarily differentiated by high buoyancy frequency (N2) (Figure S2.3), which indicated stratified conditions. Elevated Δ[TOC] (5 - 15μM) at these sampling sites may have resulted from post-production accumulation of TOC. Quadrants containing these sampling locations were assigned an "Accumulation" designation. The

Δ[POC] varied in a similar manner (Table S2.2), contributing significantly to Δ[TOC] during bloom conditions (in a related dataset ~51 ± 22% of TOC could be detected as DOC, when [POC] > 5μM, see TextS2).

3.3. New production and TOC production

Sampling locations that were classified as "Bloom" had the highest P_{New} estimates, where mean P_{New} was 139.0 ± 71.7 mmol C m^{-2} d^{-1} (Table S2.2). In contrast, mean P_{New} for the "low [TOC]" in the Offshore region was 4.7 ± 2.2 mmol C m^{-2} d^{-1}. Corresponding mean P_{TOC} values for these two conditions were 43.8 ± 37.7 mmol C m^{-2} d^{-1} and 0.8 ± 0.5 mmol C m^{-2} d^{-1}, respectively (Table S2.2). Variations in P_{New} across the region primarily reflected changes in model-derived upwelling velocities (r^2=0.83) that converted NO_3^- removal to P_{New} (Figure S2.10a). Theses velocities varied over several orders of magnitude (e.g., 0.01 to 1.0 m d^{-1}). Upwelling influenced P_{TOC} in a similar way (not shown).

The P_{New} and P_{TOC} calculation was restricted to profiles where the depth of first NO_3 use could be identified and upwelling (i.e., positive vertical advection) conditions were documented at the time of sampling (i.e., 282 profiles out of 646 sampled during the time series). In the Inshore region several profiles were omitted because they were too shallow to establish an accurate depth of first NO_3^- utilization (97 out of 328 Inshore profiles). To test whether omitting these stations affected the P_{TOC} calculation we used $[NO_3^-]$ at a fixed depth of 60 m to replace $[NO_3^-]_{first}$ [*Messié et al.*, 2009]. Calculations of P_{New} by the fixed 60 m method both increased and decreased relative to all methods and so on average P_{New} was similar between the two methods; however, P_{TOC} increased by

13% on average (Figure S2.11). This resulted in the inshore ratio of P_{TOC}:P_{New} being slightly impacted (increasing by ~3% on average). Additionally, some locations were omitted in the California Current and Offshore regions (116 of 318) because they had net downwelling conditions at the time of CalCOFI sampling. To test the impact of excluding these sampling locations, both average [Chl-*a*] at the chlorophyll max depth and satellite-based NPP for each cruise in the offshore region were compared with and without stations that were omitted in the P_{New} estimate. If the regional mean value for these parameters was under(over) estimated by omitting stations then it would be logical to assume that P_{New} was also impacted. However, cruise-specific [Chl-*a*] values were overestimated by only ~3% when stations experiencing net downwelling at the time of sampling were omitted. Finally, a relatively small number of Inshore profiles (*n*=13 or 4% of inshore stations) were omitted because there was no measurable gradient in [NO_3^-] within the euphotic zone (i.e., no change in [NO_3^-]).

3.5.1. Satellite-based Net Primary Production, the *f*-ratio, and carbon partitioning

The relationship of P_{New} to net primary production (NPP), or the '*f*-ratio'[*Eppley et al.*, 1979], was examined using satellite-based NPP. Bottle incubation data for primary production are available for a handful of sampling locations during each cruise, but satellite NPP achieved the broader spatial coverage appropriate for comparing to [NO_3^-] and TOC datasets. Across all regions of the CCE, P_{New} was significantly correlated (r^2=0.60, p<0.001) with satellite-based NPP (Figure S2.10b), and the *f*-ratio (P_{New}:NPP), decreased from 0.53 ± 0.23 Inshore to 0.37 ± 0.31 Offshore (Figure S2.12). Across the domain, P_{New}:NPP was a spatially-averaged 0.44 ± 0.30, where the spatial averaging was performed in order to adjust the sub-regional average $P_{New:}$NPP values to reflect the areal contribution of each sub-region to the entire CalCOFI domain.

When spatially-averaged over the CalCOFI region P_{TOC}:NPP was 0.06 ± 0.04, and P_{TOC}:P_{New} was 0.15 ± 0.07. When separated by subregion and PCA space, P_{TOC}:NPP and P_{TOC}:P_{New} had values of 0.04 ± 0.02 and 0.12 ± 0.06 for the least productive oligotrophic Offshore region and up to 0.16 ± 0.08 and 0.28 ± 0.15 for coastal "Bloom" conditions (Table S2.2, Figures S2.13a and S2.13b). The variability in these ratios for any given "ecosystem" condition was linked in part to the mean euphotic zone [TOC], which exhibited greater regional variability than either mean euphotic zone [NO_3^-] or the upwelling [TOC] and [NO_3^-] determined at the nitracline depth (i.e., depth of first NO_3^- use).

4. Discussion

Thousands of total organic carbon concentration ([TOC]) and nitrate concentration ([NO_3^-]) measurements from the southern California Current Ecosystem (CCE) region were used to examine the variable partitioning of net primary production (NPP) and new production (P_{New}) into non-sinking reservoirs of detrital organic matter over a 2.5 year period (2008 - 2010). This analysis provided the most comprehensive dataset of its kind for the region to date and is a valuable resource for models that attempt to examine carbon partitioning in the CCE.

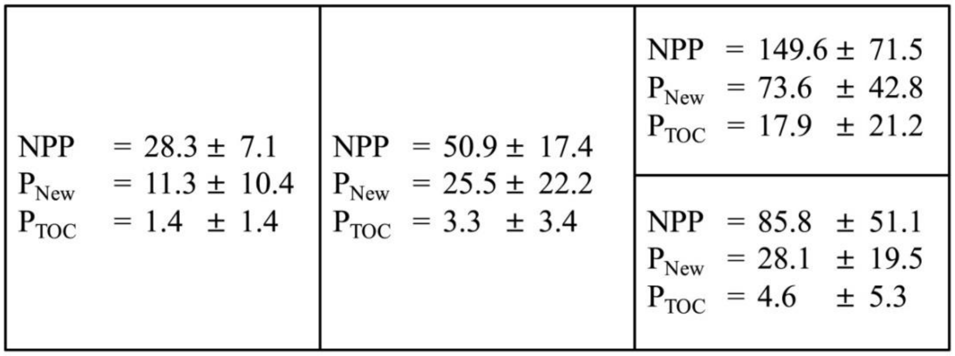

NPP = 28.3 ± 7.1 P_{New} = 11.3 ± 10.4 P_{TOC} = 1.4 ± 1.4	NPP = 50.9 ± 17.4 P_{New} = 25.5 ± 22.2 P_{TOC} = 3.3 ± 3.4	NPP = 149.6 ± 71.5 P_{New} = 73.6 ± 42.8 P_{TOC} = 17.9 ± 21.2
		NPP = 85.8 ± 51.1 P_{New} = 28.1 ± 19.5 P_{TOC} = 4.6 ± 5.3

Figure 2.5. *Annual average production values for the 4 subregions in this study. Subregions are arranged from left to right: Offshore, California Current, Inshore North and Inshore South. Errors represent the sum of seasonal squared errors.*

4.1. Net Primary Production and Potential New Production in the CCE

To calculate new production we formulated a method that took advantage of the large CalCOFI dataset of [NO_3^-] measurements. Although our approach differed from previous studies, our results are in broad agreement with published work. For example, P_{New} in the Inshore North region varied from a high of 118.2 ± 72.2 mmol C m^{-2} d^{-1} during the two spring cruises to a low of 51.7 ± 15.9 mmol C m^{-2} d^{-1} during the two fall cruises (Figure S2.14). Averaged over the 9 seasons, P_{New} was 73.6 ± 42.8 mmol C m^{-2} d^{-1} (Figure 2.5) and was similar to a previous estimate for the central CCE (<150 km from the coast) of 74 ± 9 mmol C m^{-2} d^{-1} [*Messié et al.*, 2009]. The larger deviation in the present CalCOFI dataset (±42.8 mmol C m^{-2} d^{-1}) reflects greater variability in direct water column-based measurements as opposed to seasonal satellite-based production estimates. In the Inshore South, P_{New} was 57.3 ± 34.2 mmol C m^{-2} d^{-1} during spring cruises (Figure S2.14) and 28.1 ± 19.5 mmol C m^{-2} d^{-1} averaged seasonally (Figure 2.5). For the more productive Inshore South CalCOFI station (086.7 035.0), P_{New} was 134.3 and 113.9 mmol C m^{-2} d^{-1} during spring 2008 and 2010, respectively. This is a similar rate to estimates at the nearby San Pedro Ocean Time series (SPOT), during spring times of 2013 – 2014 (83 ± 42 to 103 ± 55 mmol C m^{-2} d^{-1}) based on similar nitrate removal estimates but with more direct measures of vertical advection/diffusion velocities [*Haskell et al.,* 2016]. For comparison, the Peru and Benguela eastern boundary current systems exhibit mean P_{New} values of 120 ± 4 mmol C m^{-2} d^{-1} [*Messié et al.*, 2009].

Our spatially averaged P_{New} was 26.6 ± 21 mmol C m^{-2} d^{-1} across the CalCOFI domain and nearly identical to previous long-term (1984-1997) new production estimates (27.2 ± 13 mmol C m^{-2} d^{-1} [*Roemmich*, 1989; *Bograd et al.*, 2001]). Overall, the general agreement with different methods lends confidence to our approach.

The annual mean *f*-ratio for the Central CCE has been estimated to be between 0.59 and 0.66 [*Messié et al.*, 2009; *Pennington et al.*, 2010], which is similar to the *f*-ratio for the southern CCE (0.58 and 0.69) during productive periods [*Eppley et al.*, 1979; *Munro et al.*, 2013]). For comparison, our highest *f*-ratios (P_{New} to satellite-based NPP) were 0.58 ± 0.10 during "Bloom" periods in the Inshore North region and 0.59 ± 0.46 during "Upwelling" (wind-stress curl) periods in the California Current region (Table S2.2). Enhanced *f*-ratios estimated during bloom and upwelling conditions (as identified by PCA) are greater than seasonal mean estimates for all subregions (e.g., spring *f*-ratios of 0.53 ± 0.14 and 0.45 ± 0.26 for the Inshore North and California Current, respectively), suggesting that the PCA approach isolated conditions where nitrate made a greater contribution to net primary production. We note that previous estimates were made from much smaller datasets, which likely explains the smaller range reported in these studies. Even within our sub-regions we observed considerable variability in ecosystem conditions (e.g., deviations in Table S2.2) in a matter consistent with the complex hydrography of the region, which can advect and redistribute biomass and chlorophyll along and across shore [*Haury et al.*, 1986; *Olivieri* and *Chavez*, 2000; *Barth et al.*, 2002; *Chenillat et al.*, 2015].

4.2. TOC Cycling in the CCE

The high *f*-ratio of 0.58 ± 0.10 during "Bloom" periods in the Inshore North accompanied high [TOC] and [Chl-*a*] (Figures 2.3 and 2.4) in the region, which supported the new, nitrate-driven production of [TOC]. Other upwelling regions show a similar relationship between nutrient supply and TOC or DOC production, such as the Equatorial Pacific Ocean [*Peltzer* and *Hayward*, 1996], Iberian Peninsula [*Álvarez-Salgado et al.*, 2001], Ross Sea [*Carlson et al.*, 2000], eastern North Pacific Ocean off Oregon [*Hill and Wheeler*, *2002*], East China Sea [*Ogawa* and *Tanoue*, 2003], Oyashio Current [*Hasegawa et al.*, 2010], and Santa Barbara Channel [*Halewood et al.*, 2012; *Wear et al.*, 2015]. In the southern CCE, bottle incubation studies that have measured DOC and suspended POC production during phytoplankton grow out experiments have also confirmed the partitioning of new production into detrital reservoirs [*Halewood et al.*, 2012; *Wear et al.*, 2015]. In the current dataset, Δ[TOC] was positively correlated with diatom and dinoflagellate (both heterotrophic and autotrophic) abundances during "Bloom" conditions (data not shown). These organisms dominated the >20 µm size fraction, which constituted 50 - 70% of total [Chl-*a*] at these locations ([*Goericke*, 2011]). Extracellular release of DOM by these large phytoplankton (e.g., [*Fogg*, 1983; *Teira et al.*, 2001]), sloppy feeding by grazers on these larger cells [*Lampert*, 1978; *Saba* *et al, 2011*], cell lysis [*Breitbart*, 2012; *Bidle 2015*], and other processes [*Carlson and Hansell*, 2014] likely contributed high [TOC] and Δ[TOC] to Inshore regions

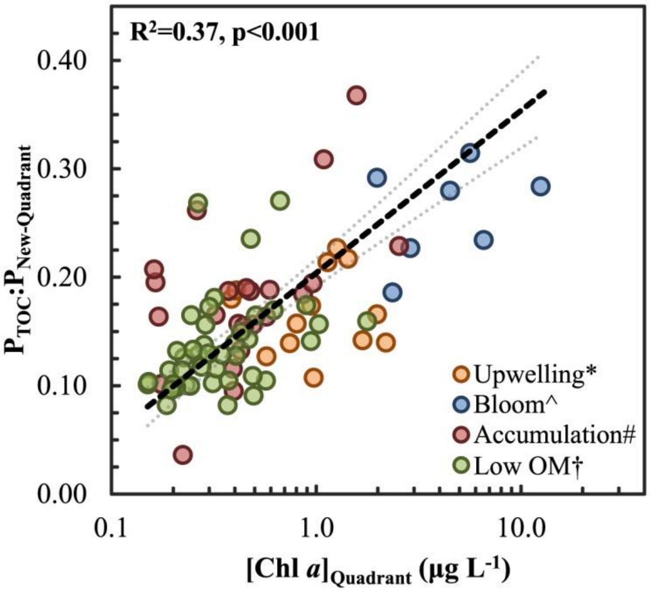

Figure 2.6. *Partitioning of potential net TOC production from P_{New} tends to be greater (P_{TOC}:P_{New}>0.25) for more productive conditions based on [Chl-a]>1.0 µg L^{-1}. Each point represents a unique cruise and condition as noted in Figure 2.4 and the Model II regression fit is applied across all shown data points (n=86; y=0.07ln(x)+0.20; r^2=0.37). Thinner dotted lines outside of natural log best fit line represent the ±95% confidence intervals.*

Across the southern CCE study region, P_{TOC} normalized to P_{New} increased significantly with increasing [Chl-*a*] (r^2=0.37, p<0.001, Figure 2.6), and this trend was driven primarily by changes in [TOC]. Increased production of TOC during bloom conditions has been documented in several locations, including a coastal upwelling system in the eastern North Atlantic (42 vs. 15 mmol C m^{-2} d^{-1} during post-bloom periods; [*Álvarez-Salgado et al.*, 2001]). Enhanced partitioning of net and new production into DOC has also been documented for spring blooms in the oligotrophic

Sargasso Sea (DOC was 0.59-0.70 of NCP) [*Hansell* and *Carlson,* 1998], during coastal upwelling off the Iberian Peninsula (DOC was 0.20 of NPP) [*Álvarez-Salgado et al.*, 2001], and spring blooms in the western North Atlantic (DOC was 0.17 of NCP) [*Romera-Castillo et al.*, 2016].

The ratio of P_{TOC}:P_{New} varied from 0.12 ± 0.08 to 0.28 ± 0.15 between low production locations in the oligotrophic gyre and coastal bloom locations in the Inshore North. Both Inshore North Bloom (0.28 ± 0.15) and mean springtime P_{TOC}:P_{New} of 0.24 ± 0.15 were significantly (Mann Whitney, $p<0.01$) elevated over other PCA-based conditions and seasons. Springtime mean (2013-2014) partitioning of DOC:NCP was also significantly elevated (~0.28) at SPOT (decreasing to ~0.08 in the fall) [*Haskell et al.*, 2016], compared with P_{TOC}:P_{New} estimates of 0.16 and 0.23 for CalCOFI station 086.7 0.35.0, during spring 2008 and 2010, respectively.

The PCA-based approach also appeared to distinguish some of the sampling locations as "TOC accumulation" sites (23% of total stations) based on a decoupling of [TOC] and [Chl-*a*]. At these locations, surface Δ[TOC] could increase to between 5 - 15 μM; DOC additions of similar magnitude, 10 - 12 μM, have also been reported for the Santa Barbara Channel region during warm stratified and post-bloom conditions [*Halewood et al.*, 2012; *Wear et al.*, 2015]. Other coastal regions, such as throughout the Mediterranean [*Romera-Castillo et al.*, 2013; *Santinelli et al.*, 2013] and Ross Seas [*Carlson et al.*, 1998; *Carlson et al.*, 2000] show similar DOC accumulations (10 - 20 μM C) during post-bloom, stratified conditions.

Higher P_{TOC}:P_{New} was consistently observed for bloom conditions in the Inshore (>0.25; Figure 2.6 and Table S2.2), TOC "accumulation" sites sometimes exhibited moderate P_{TOC}:P_{New} as well (Figure 2.6). When sampling locations were highly stratified, such as those observed during the summer cruise of 2009, we observed P_{TOC}:P_{New} of 0.22 and 0.35 at "accumulation" locations in the Inshore North and South regions, respectively. These findings are more consistent with bottle-based DOC exocellular release (PER) experiments near the Santa Barbara basin, which have shown consistently higher TOC partitioning under post-bloom, nutrient limited conditions compared to bloom conditions [*Halewood et al.*, 2012].

Micronutrient limitation of heterotrophic bacteria that degrade DOC could also result in TOC accumulation [*Kirchman et al.*, 2000]. Excess silicic acid relative to [NO_3^-] (Si_{ex} after [*Sarmiento et al.,* 2004] as modified by *King and Barbeau,* 2011]) has been used as a proxy for iron limitation in surface waters, where Si_{ex} is the difference between measured silicic acid concentrations and [NO_3^-] in the euphotic zone when the upwelling ratio of the two macronutrients is ~1. The silica:nitrate uptake ratio is expected to be 1 for diatom dominated ecosystems, and so, Si_{ex} is expected to be ≥ 0. When $Si_{ex}<0.0$, excess [NO_3^-] is present in the euphotic zone, and iron limitation is inferred [*Hutchins and Bruland,* 1998], [*King* and *Barbeau,* 2011]. About 13% of the ~646 profiles identified for the 2008-2010 CalCOFI time series had mean surface $Si_{ex}<0.0$, which was consistent with iron limitation of phytoplankton production, and by extension, limitation of heterotrophic bacterial production. Several of the profiles characterized as iron-limited were encountered in the Inshore South (50 - 100 km from shore) during summer and fall, and these locations may be perennially iron-limited during these seasons (e.g., [*King* and *Barbeau*, 2011]). These sites were characterized by surface [TOC] >65 μM, [Chl-*a*] <1.0 μg L^{-1}, and moderate P_{TOC}:P_{New} of 0.20 ± 0.11. Relatively low [Chl-*a*] indicated that

TOC production was muted, and so, moderate P_{TOC}:P_{New} may have resulted from iron limitation of TOC consumption by heterotrophic bacteria and not from enhanced TOC production. Most of the identified iron-limited stations also had low bacteria counts ($<5x10^5$ cells mL^{-1}). We cannot rule out the possibility that Fe-stressed phytoplankton increased their partitioning of New Production into TOC as well.

Overall, we observed that surface mean [TOC] can become elevated (e.g., 70 - 90 μM) during coastal bloom conditions in the CCE corresponding to P_{TOC}:P_{New} ratios of 0.20 - 0.40. Some locations exhibit elevated [TOC] but low [Chl-*a*], signaling post-production accumulation of TOC. A subset of these locations can be characterized by conditions consistent with iron limitation. However, low bacteria counts and micronutrient limitation are not always linked to TOC accumulation. In general, elevated P_{TOC}:P_{New} represents partitioning of new production into TOC, but if [Chl-*a*] is used as a proxy of active production then some sampling sites with moderate P_{TOC}:P_{New} may have artificially elevated P_{TOC} due to TOC accumulation.

4.3. P_{TOC} Contributions to Export and New Production

Non-sinking reservoirs of organic carbon – specifically DOC and suspended POC – can contribute to carbon export through mechanisms such as subduction and/or biological repackaging [*Siegel et al.*, 2016; *DeVries and Weber*, 2017]. Based on imbalances between new production estimates and gravitational export measurements, previous studies based in the CCE have identified additional pathways that redistribute nutrients and/or organic carbon [*Plattner et al.*, 2005; *Gruber et al.*, 2011; *Stukel et al.*, 2011, 2017; *Nagai et al.*, 2015]. In this context, P_{TOC} determined by the current study could represent “potentially exportable TOC”, given sufficiently long enough turnover times [*Hansell*, 2013]. The annual P_{TOC}:NPP, ranging from 0.19 ± 0.09 in the Inshore North to 0.02 ± 0.01for the Offshore oligotrophic gyre (Figure 2.6), differs from the pattern in sinking export (relative to NPP), which increases from 0.10 ± 0.03 in the Inshore to 0.18 ± 0.10 in the oligotrophic gyre [*Stukel et al.*, 2011, 2013].

If all P_{TOC} is exportable, then combined P_{TOC} and sinking export flux, each normalized to NPP, should approximate the ‘*ef*-ratio’ [*Laws et al.*, 2000], where the ‘*ef*-ratio’ represents the ratio of total export (gravitational and other forms) to primary production. Thorium-based gravitational export flux datasets were compiled to provide representative average gravitational fluxes for each subregion (i.e., May 2006, April 2007 and October 2008 [*Stukel et al.*, 2011, 2013], and 2013-2014 [*Haskell et al.*, 2016]) and combined with P_{TOC} (all normalized to NPP) to determine the ‘*ef*-ratio’ as defined above. The calculated ‘*ef*-ratio’ varies from 0.16 to 0.24 across the grid, consistently falling below the *f*-ratio calculated from potential new production ($P_{New;}$ estimated by this study) and satellite NPP (Figure 2.7). However, this *ef*-ratio approximates the fraction of net carbon (community) production estimated from net oxygen production (NOP) to gross oxygen production (GOP) measurements [*Munro et al*., 2013] in all but the Offshore region (Figure 2.7).

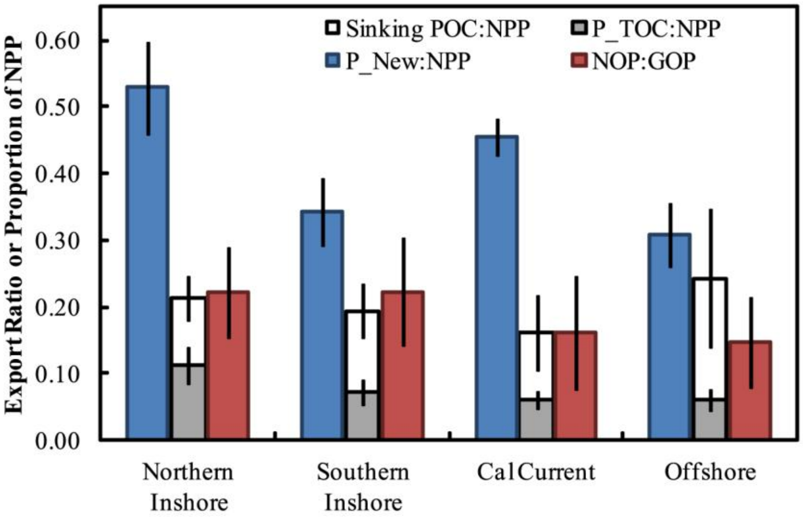

Figure 2.7. *The combination of sinking POC* [*Stukel et al.*, 2011, 2013] *and TOC production* (P_{TOC}) *is similar to net carbon production (NCP) estimated as net oxygen production:gross oxygen production (NOP:GOP)* [*Munro et al.*, 2013] *for coastal regions. Values of new production* (P_{New}), P_{TOC} *and sinking export are expressed as a ratio relative to satellite derived net primary production (NPP) to normalize across methodology and temporal offsets. Error bars represent the standard deviation.* P_{New}*:NPP and* P_{TOC}*:NPP were calculated using seasonal means over 2008-2010. NCP is the annual mean of that reported for 2005-2008 in* [*Munro et al.*, 2013]. *Sinking POC for Southern Inshore estimated are from* [*Haskell et al.*, 2016] *for 2013-2014 at San Pedro Ocean Time Series, and mean estimates for other regions are from* [*Stukel et al.*, 2011, 2013] *over 2006-2008.*

Clearly, P_{New} normalized to satellite estimated NPP (i.e., *f*-ratio) exceeds export production (Figure 2.7) estimated as either the "*ef* ratio" or NOP:GOP, across the southern CCE regions. For the system to remain at steady-state over the long-term the overall *ef*-ratio must balance the *f*-ratio. One way this may be achieved is if the *ef*-ratio exceeds the *f*-ratio offshore as nutrient rich waters are being laterally advected (e.g., [*Plattner et al.*, 2005; *Stukel et al.*, 2011]). Although we did not observe such a reversal of ratios offshore, the scale over which offshore nutrient transport can occur has been shown to be much greater than the area over which these measurements are made

[*Gruber et al.*, 2011; *Nagai et al.*, 2015]. Also, if some fraction of the upwelled NO_3^- is subducted before being converted to biomass, this may explain observations of higher *f*-ratios but lower oxygen based measurements of net community production as well as the "*ef-ratio*" (Figure 2.7). One caveat is that only satellite NPP, [NO_3^-], and [TOC] are available for the same dataset, and the spatial and temporal coverage of that dataset is far higher than gravitational export and NOP:GOP datasets.

Suspended particulate organic carbon additions (ΔPOC) are similar to ΔTOC in Inshore regions and contribute to approximately 33 - 50% of ΔTOC Inshore (Figure S2.7 and Text S2.3). Including ΔPOC in the *ef*-ratio calculations increases the P_{TOC}:NPP ratio Inshore by 2 - 4%. Assuming that the contributions of ΔPOC to ΔTOC in the California Current and Offshore regions did not exceed that of Inshore regions, the contribution of ΔPOC to P_{TOC}:NPP is 0.5 - 2.0%. Updating the *ef*-ratio to include ΔPOC in the comparison to *f*-ratio this brings the cross-shore supply and export more into balance, particularly if the *f*-ratio is indeed overestimated Offshore. Including ΔPOC in P_{TOC} calculations also keeps mean P_{TOC}:NPP within the error bars of NOP:GOP.

4.3. Cross-Shore [TOC]

Biogeochemical models invoke the non-sinking organic matter reservoir as a mechanism for transporting nutrients and carbon from coastal California Current regions to the ocean's interior [*Gruber et al.*, 2011; *Letscher et al.*, 2013]. To test the possible importance of this process lateral TOC transport was estimated by considering this pool to be a passive tracer [*Letscher et al.*, 2013], where gradients in [TOC] between adjacent regions were assumed to result from transport and not other processes. Surface currents of the CCE are dominated by alongshore transport of 5 - 12 km d^{-1} but simultaneous cross-shore transport can also average 0.5 km d^{-1} [*Todd et al.*, 2011]. Using BECCO model lateral velocities and a simple box model approach [*Peltzer* and *Hayward*, 1996], we found areal integrated cross-shore TOC export from the Inshore North region could be on the order of 10 ± 7 mmol C m^{-2} d^{-1} during more productive upwelling conditions. Such estimates are similar to those for lateral export away from sites of production in the Equatorial upwelling region of the eastern tropical Pacific Ocean [*Peltzer* and *Hayward*, 1996]. The lateral export from the Northern Inshore represents ~50% of mean Northern Inshore P_{TOC} estimates. If even half of this non-sinking reservoir persists on the order of 6-12 months (i.e., semi-labile DOM; [*Hansell*, 2013]) then coastal TOC can be effectively transported to TOC-depleted regions like that of the California Current (50 - 100 km). Future modeling efforts based in the CCE should incorporate TOC transport and TOC turnover rates to better constrain potential lateral transport of inshore primary production.

5. Summary and Conclusions

The surface production and accumulation of total organic carbon (P_{TOC}) in the California Current Ecosystem (CCE) correlates with indicators of primary production (e.g., [Chl-*a*]). To provide a broader context, calculated P_{TOC} was compared with estimated potential new production (P_{New}) and satellite-based production (NPP), and it was found that P_{TOC}:P_{New} ranged from 0.12 ± 0.08 to 0.28 ± 0.15 and P_{TOC}:NPP ranged from 0.04 ± 0.02 to 0.28 ± 0.15 between the lowest productive periods in the oligotrophic gyre and the highly productive periods in the Inshore North regions, respectively.

Additionally, our calculations found that on average P_{TOC} represented a quantitatively important reservoir of reduced carbon in the CCE. For instance, P_{TOC}:NPP (mean of 0.11 ± 0.03) could equal the *e*-ratio (mean of 0.10 ± 0.03) in coastal regions but was less than the gravitational flux in the offshore (0.06 ± 0.02 vs. 0.18 ± 0.10). Together, P_{TOC} and gravitational export or the "*ef*-ratio," approximated net community production in the CCE as estimated by a previous study [*Munro et al.*, 2013], but fell short of P_{New}.

The addition of TOC (Δ[TOC]) under Inshore bloom conditions was sometimes 5 to 10-fold (up to 30 μM) that of base conditions and likely included a significant contribution (e.g., up to 50%) from suspended [POC] (i.e., Δ[TOC] did not approximate Δ[DOC] under these conditions). Post-bloom TOC accumulation was detected in some cases, and it was anticipated that this TOC could be passively 'exported' from sites of production. A simple estimate of cross-shore transport from the Inshore North to the adjacent California Current region indicated that TOC transport could be up to 10 mmol C m^{-2} d^{-1}, representing about half of mean P_{TOC} in the Inshore North region.

Ultimately, this dataset allowed us to examine the role of non-sinking organic matter in carbon export, in line with a priority that was recently designated by the EXPORTS Science Plan [*Siegel et al.*, 2016]. To further enhance our understanding of the role of TOC as a repository of fixed carbon, we attempted to derive the flux of TOC produced as a fraction of new production. Such a parameter is also important for numerical models that are attempting to resolve the net effects of biological processes in the region. By modifying existing regional models to incorporate the proposed TOC partitioning coefficients (as a function of P_{New} and NPP), we can test the accuracy of these coefficients by observing whether these models reproduce [TOC] distributions encountered across the CCE. Together, the data and derived products discussed in this paper fill an important knowledge gap that brings us closer to a more accurate parameterization of the role of TOC as a pathway for carbon export and accumulation in the California Current [*Nagai et al.*, 2015].

APPENDIX

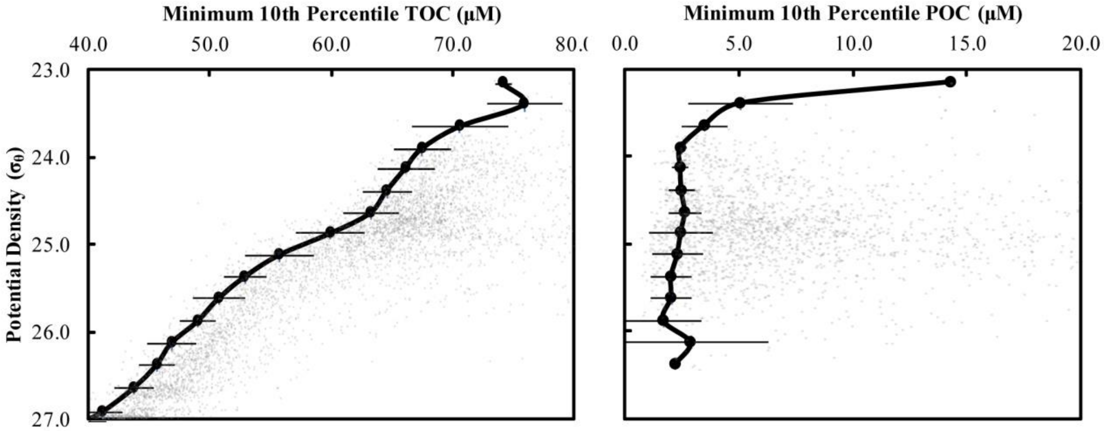

Figure S2.1. *Minimum 10th percentile [TOC] and [POC] values (figures a and b). We use the difference of observed [TOC] and [POC] from the minimum values grouped into 0.25 kg* m^{-3} *isopycnal bins to estimate ΔTOC and ΔPOC, respectively. Calculations are based on the assumption that the minimum concentrations observed for a given isopycnal represent background conditions and the ΔTOC and ΔPOC represent "additional" organic carbon over background.*

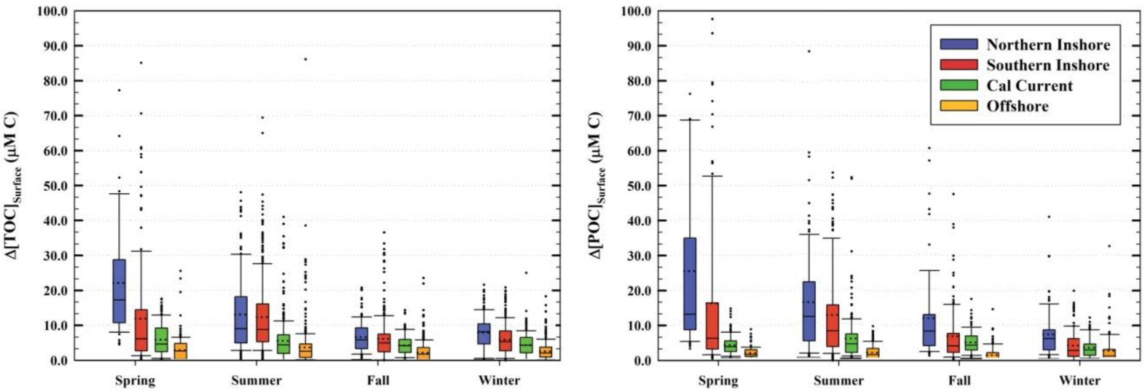

Figure S2.2. *Seasonal differences in* $\Delta[TOC]_{Surface}$ *and* $\Delta[POC]_{Surface}$ *are only significant for the Inshore regions (p<0.001, Mann-Whitney). Data presented here represent measures for potential densities <26.0 kg* m^{-3}*. Each dot represents a single* $\Delta[TOC]_{Surface}$ *measure (and* $\Delta[POC]_{Surface}$*) as estimated using* $[TOC]_{obs} - [TOC]_{min}$*, where* $[TOC]_{min}$ *represents the minimum* 10^{th} *percentile [TOC] value by isopycnal bin as shown in Figure S2.2 above. Inside the box plots the solid line is the median and dotted line the mean. Outside the box plots, the whiskers are the* 10^{th} *and* 90^{th} *percentile values and the dots "outliers".*

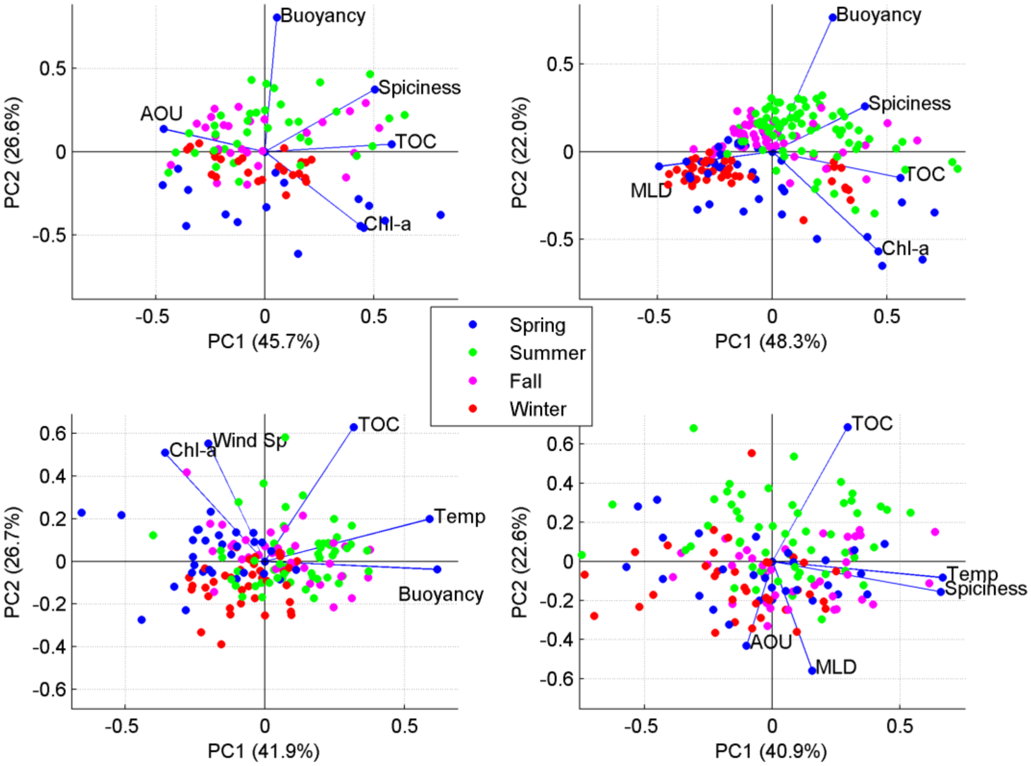

Figure S2.3. *Biplots of regional ecosystem "condition" isolation. Starting at the top left working clockwise, biplots are for Inshore North (a), Inshore South (b), California Current (c) and Offshore (d) regions. Noted in each sector are the names identified for each condition, and colors represent seasons as noted in the legend. The lines originating from the center of each biplot are the loadings of each variable used in the component analysis, where the combination of variables was first selected using stepwise multiple regression (see Sec 2.8 and 3.5).*

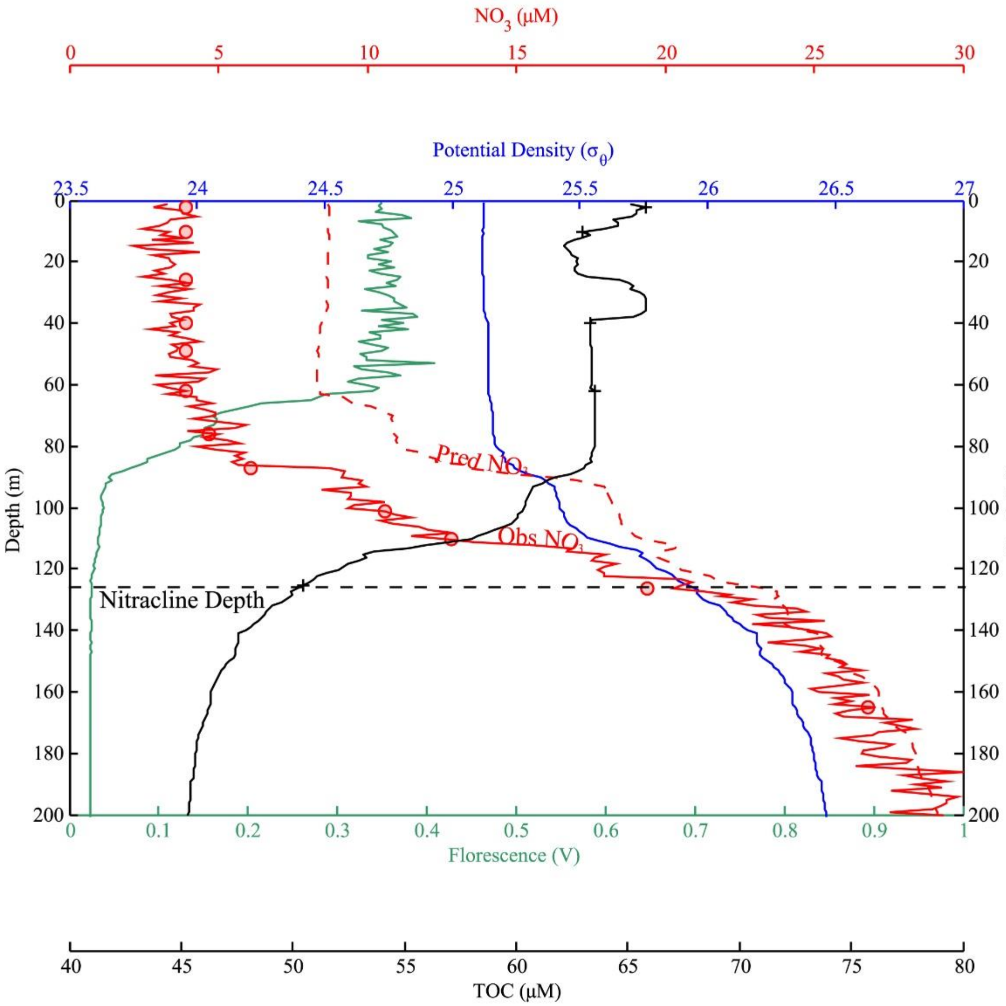

Figure S2.4. *An example figure of how the depth of first nitrate utilization ($[NO_3^-]_{First}$) is determined. Typically, the $[NO_3^-]_{First}$ depth corresponded to the deepest depths of florescence increase over sub-euphotic zone values. The $[NO_3^-]_{First}$ depth is estimated as the depth where the difference between temp:NO_3 predicted $[NO_3^-]$ and observed $[NO_3^-]$ was greater than 2µM. The mean $[NO_3^-]$ and [TOC] from that point to where $[NO_3^-]=0.0$ µM are taken to be mean euphotic zone $[NO_3^-]$ and [TOC]. The upwelling velocity is estimated from BECCO model velocities for depths around the nitracline depth and sampling date.*

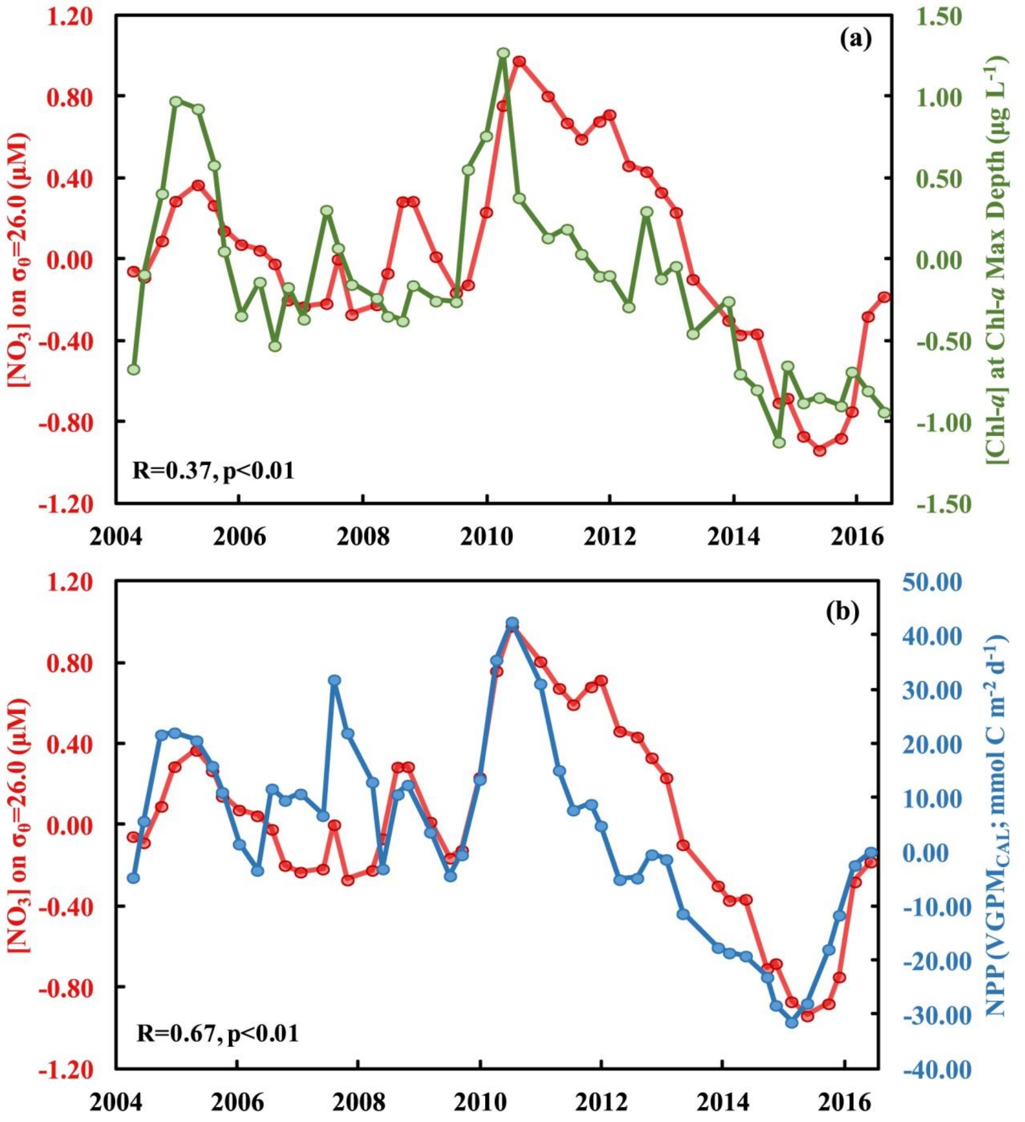

Figure S2.5. *CCE Inshore mean [NO_3^-] for potential density 26.0 kg m^{-3}, [Chl-a] at the Chlorophyll-a maximum depths (a) and satellite-based estimate of net primary production following VGMP-CAL formulation (b). Values represent seasonally-corrected anomalies and smoothed using a 6-month running average over 2004-2016. A Durbin-Watson test for autocorrelation found the errors in Chl-a and NPP to be positively autocorrelated with NO_3. So both trends were adjusted for autocorrelation using the Cochrane-Orcutt procedure, which still resulted in significant relationships ($p<0.01$). Trends suggest a coherence between base euphotic zone [NO_3^-] and primary production detected at the ocean's surface skin (0m) by satellite and below the surface (0-30m) as [Chl-a]. Additionally, a regression of mean [Chl-a] from (a) and satellite-based estimates of NPP from (b) above is significant ($r^2=0.53$, $p<0.001$), suggesting that both measures capture similar trends in primary producers.*

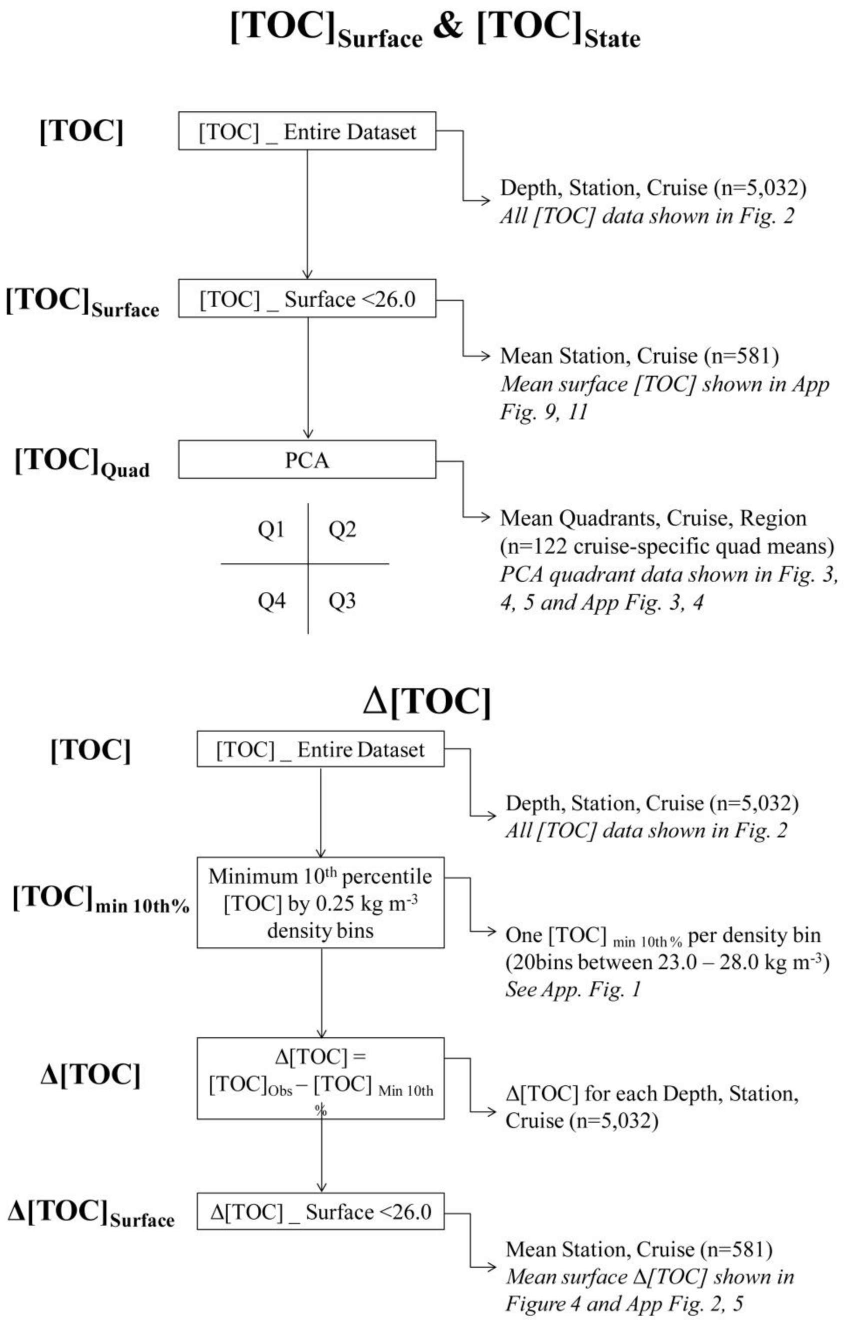

Figure S2.6. *Schematic of determining mean [TOC] and ΔTOC. Bolded abbreviations on the left are referred to in the text and figures (e.g., $[TOC]_{surface}$, $[TOC]_{Quad}$). Notes on the right indicate the number of data points used to determine the mean value for the associated data (e.g., $\Delta[TOC]_{Surface}$ n = 581) and the figures where these values were used.*

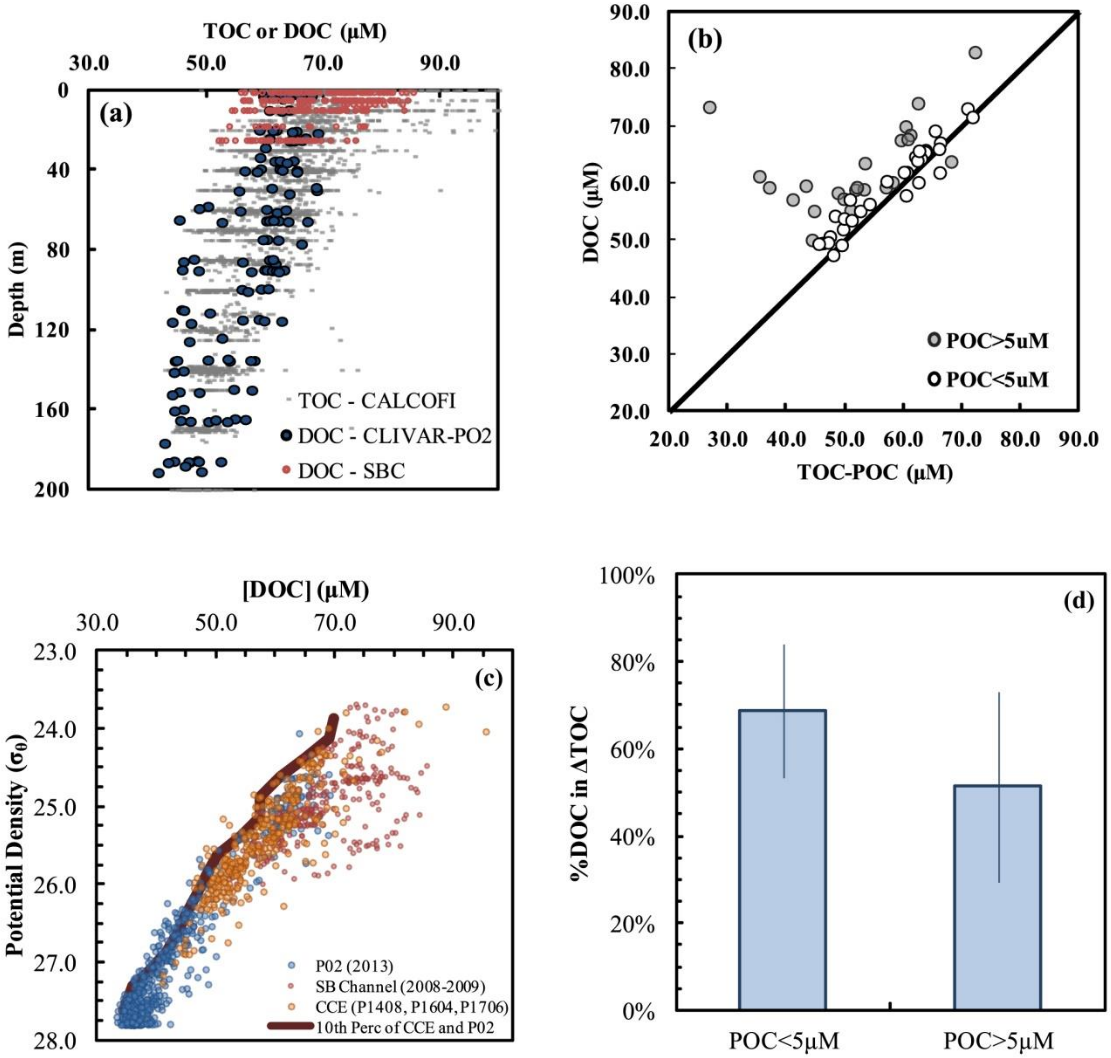

Figure S2.7. *Comparison of [TOC] with [DOC] measured for the Santa Barbara Channel (red) and CLIVAR line P02 (east of 139W; blue) demonstrate that [TOC] often fall on the same gradient of [DOC], particularly falling within the same minimum concentrations (a). Comparison of [TOC], [DOC] and [POC] for simultaneous collection of water (CCE-LTER cruises P1408 and P1604; n=44), demonstrate that when [POC] is high the difference between [TOC] and [DOC] strongly underestimates the contribution of [POC] (b). A minimum* 10^{th} *percentile analysis of all [DOC] available for the eastern North Pacific found that the CCE and P02 [DOC] data represent the CalCOFI region well (c). Using this minimum [DOC] profile we estimated Δ[DOC] for the CCE region where we have a corresponding [TOC]. Dividing Δ[DOC] by Δ[TOC] we find that when [POC] >5 µM Δ[DOC] can represent 29-73% (51% on average) of Δ[TOC] (d). See Text S1 for further details.*

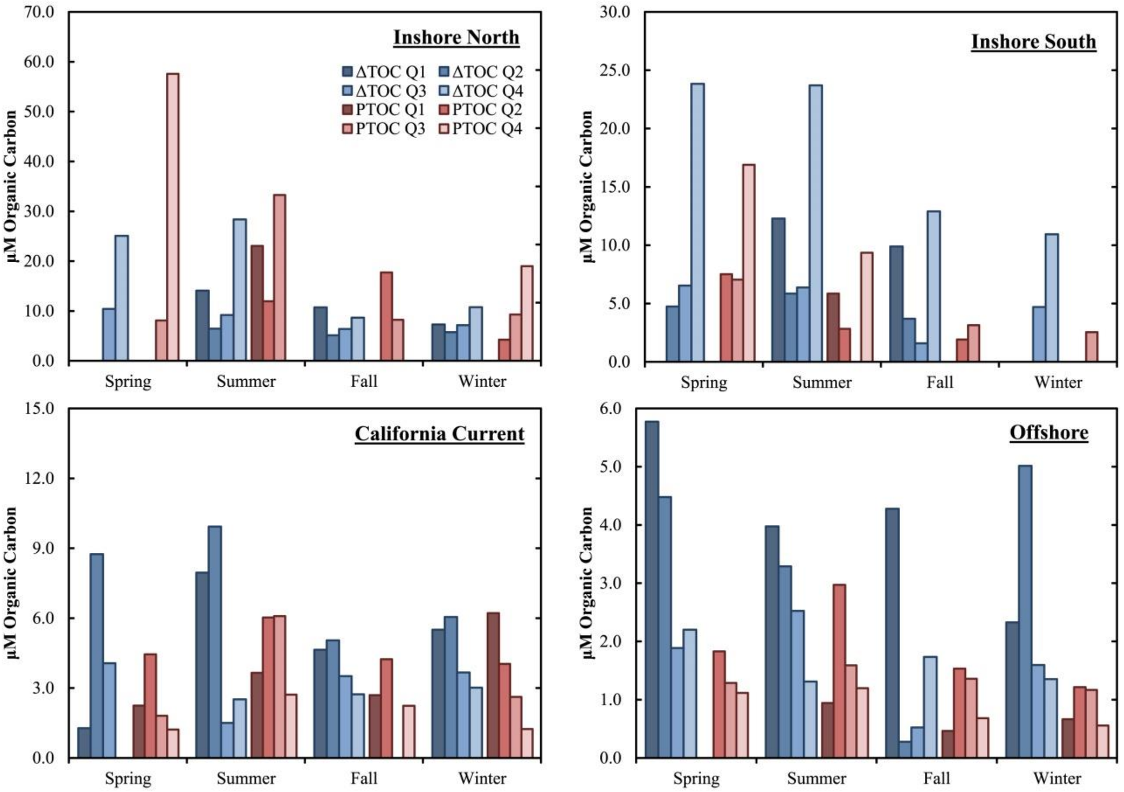

Figure S2.8. *Seasonal quadrant mean surface ΔTOC (blue) are compared with seasonal quadrant mean [TOC] values used in calculating* P_{TOC} *(red). Colors go from dark (Q1) to light (Q4) shading to distinguish among quadrant seasonal means. First, this set of figures demonstrates that the patterns in ΔTOC generally follow those of the [TOC] value used to calculate* P_{TOC}*. However, direct comparison between the two measures finds that the [TOC] used for* P_{TOC} *often exceeds ΔTOC by 1.5 times Inshore but is half that of ΔTOC Offshore. Second, this figure while not cruise-specific, helps to demonstrate that all seasons can appear in all four quadrants and that a range of ΔTOC values can be found for any given season in any sub-region.*

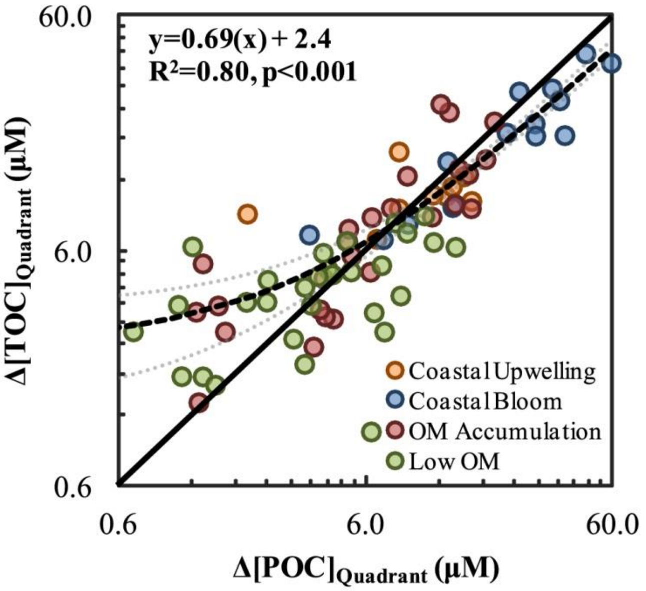

Figure S2.9. *Cruise quadrant mean surface (σ_θ<26.0 kg m^{-3}) Δ[TOC]$_{Quadrant}$ is significantly correlated with mean Δ[POC]$_{Quadrant}$ across all regions (r^2 = 0.69, p<0.001, n=117). Δ[POC] more often to exceeds Δ[TOC]$_{Quadrant}$ during productive periods in the Inshore and is less than Δ[TOC]$_{Quadrant}$ during low OM periods suggesting a difference in phase partitioning. Each dot represents an average value for a given quadrant for each cruise, where available.*

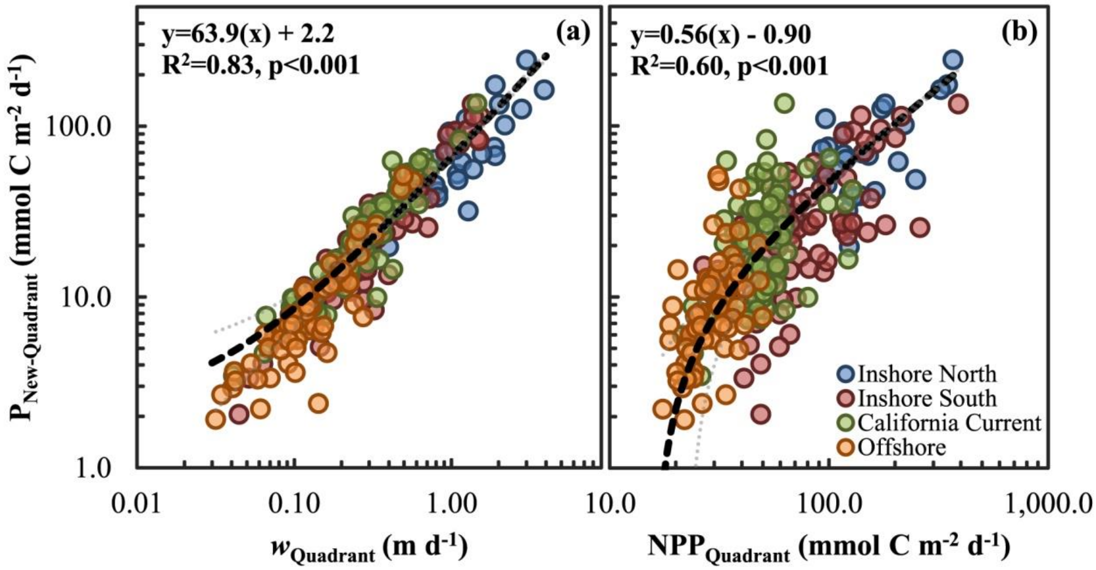

Figure S2.10. *Potential new production (P_{New}) is more strongly correlated with the vertical velocity (a; r^2=0.83) used to calculate the P_{New} rate but is also positively correlated with NPP (b; r^2=0.60). Satellite NPP is estimated using the VGPM-CAL algorithm and represents a monthly and spatial 50 km^2 average.*

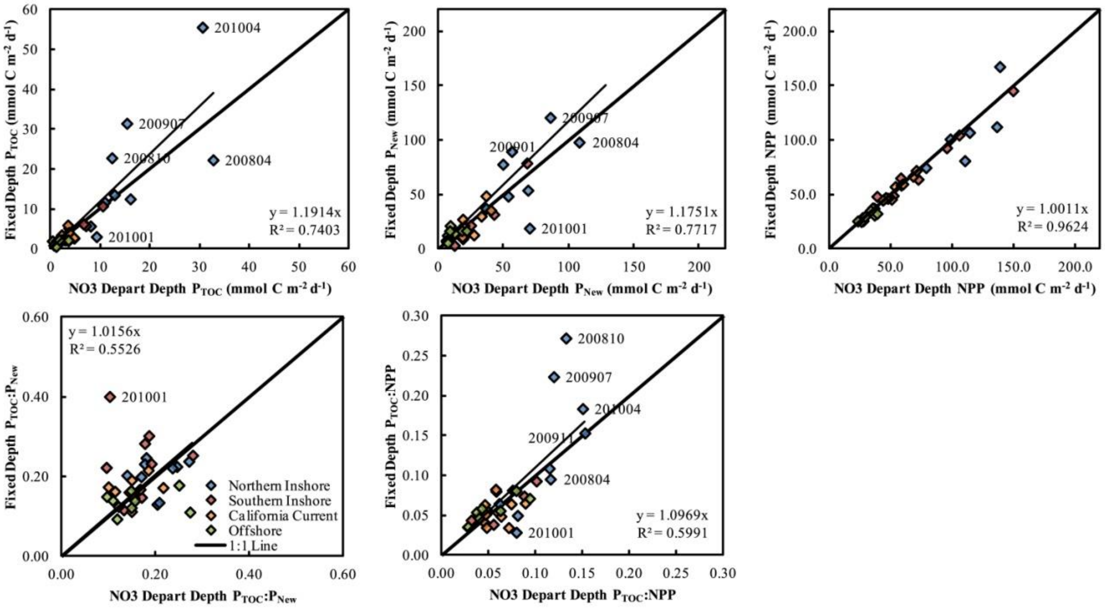

Figure S2.11. *Our study makes use of establishing a deep water nitrate:temperature relationship for each profile. And there are some stations where we do not obtain a relationship because the profile is too shallow, for instance. Usually the stations excluded are closest to shore and therefore associated with the greatest [Chl-a], [TOC], etc. There were 90 inshore profiles excluded based solely on being too shallow out of ~300 total profiles for this region. So we compare here the effect of excluding these stations by selecting a fixed deep depth from which to calculate surface [NO3] drawdown and [TOC] addition (similar to [Romera-Castillo et al., 2016]). The fixed depth was 60m inshore, 100m for the California Current and 150m for the Offshore region, roughly corresponding to the bottom of the wind-driven Ekman layer. This depth is similar to the average nitrate:temp departure depth but there is quite a bit of variability ±20m for all subregions, consistently deepening in winter months in the inshore regions. This analysis shows that TP and NP are likely underestimated by 18-19% for the Northern Inshore region by excluding the shallow stations but the net effect on TP:NP and TP:NPP is more muted. However the fact that mean NPP satellite estimates do not differ by excluding the shallow stations suggests that we are capturing broad spatial features captured by surface ocean color.*

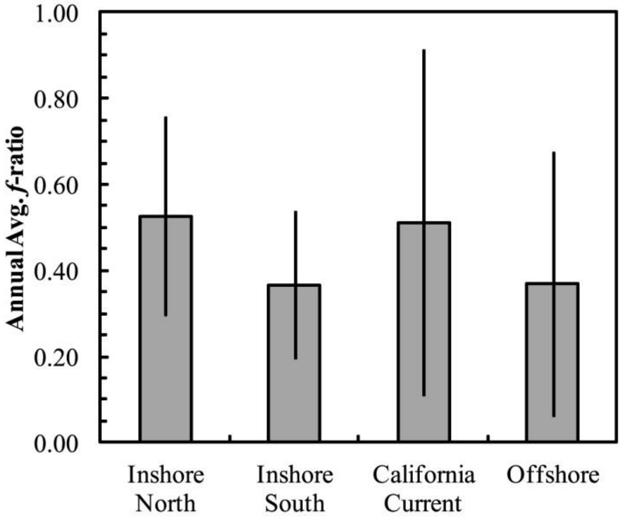

Figure S2.12. *Mean regional f-ratios follow patterns previously described for the southern CCE region (e.g.,*[*Harrison et al.*, 1987]*).*

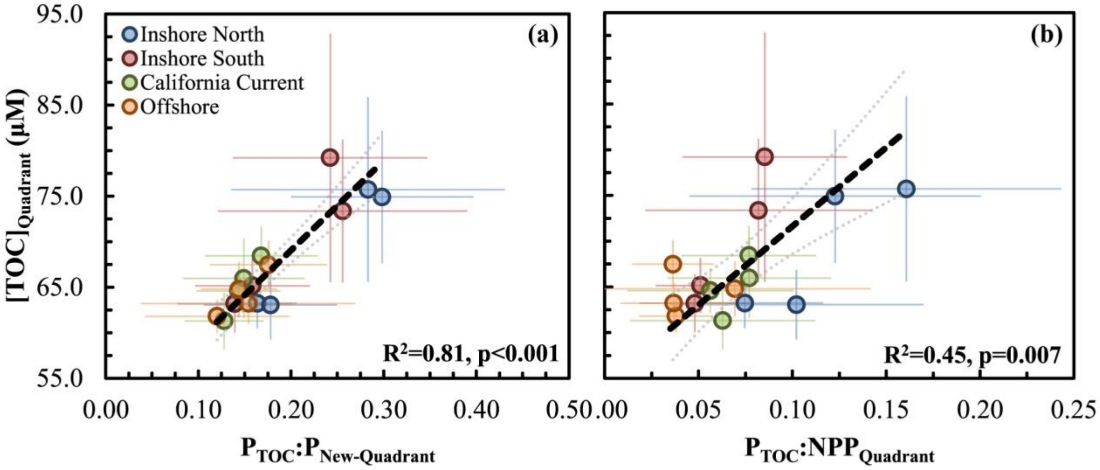

Figure S2.13. *"Quadrant" mean P_{TOC}:P_{New} is correlated (r^2=0.81; $p<0.001$) with quadrant mean euphotic zone $[TOC]_{Quadrant}$ across regions (a). The correlation of mean euphotic zone $[TOC]_{Quadrant}$ with P_{TOC}:NPP (b) is weaker but still significant (r^2=0.45; p=0.007),, where NPP is based on satellite estimates. Partitioning of production into TOC (P_{TOC}:P_{New} and P_{TOC}:NPP) tends to be greater for conditions of high productivity (i.e., 'Coastal Bloom') and post-production TOC accumulation (i.e., 'OM accumulation'). The data points and standard deviations used to produce this figure can be found in Table S2.2.*

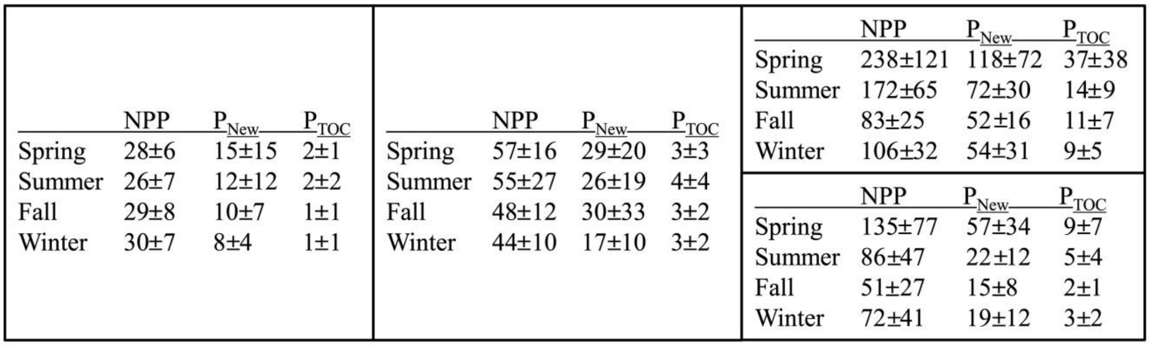

	NPP	P_{New}	P_{TOC}
Spring	28±6	15±15	2±1
Summer	26±7	12±12	2±2
Fall	29±8	10±7	1±1
Winter	30±7	8±4	1±1

	NPP	P_{New}	P_{TOC}
Spring	57±16	29±20	3±3
Summer	55±27	26±19	4±4
Fall	48±12	30±33	3±2
Winter	44±10	17±10	3±2

	NPP	P_{New}	P_{TOC}
Spring	238±121	118±72	37±38
Summer	172±65	72±30	14±9
Fall	83±25	52±16	11±7
Winter	106±32	54±31	9±5

	NPP	P_{New}	P_{TOC}
Spring	135±77	57±34	9±7
Summer	86±47	22±12	5±4
Fall	51±27	15±8	2±1
Winter	72±41	19±12	3±2

Figure S2.14. *Seasonal mean (±1σ) net primary, new and TOC production (NPP, P_{New} and P_{TOC}, respectively) values by region. Working from left to right these regions are Offshore, California Current and Inshore North (top) and South (bottom). NPP are satellite-based estimates.*

Table S2.1. Variables used in stepwise regression.

Buoyancy Frequency (N2)
Dynamic Height (m)
Eddy Kinetic Energy ($cm^2\ s^{-2}$)
Satellite NPP (mmol C $m^{-2}\ d^{-1}$)
Integrated Chl a (mg m^{-2})
Wind Speed (knots)
Distance from coast (naut miles)
Mixed Layer Depth (m)
Avg Temp $\sigma_\theta<26.0$ (deg C)
Avg Chl a $\sigma_\theta<26.0$ ($\mu g\ L^{-1}$)
Avg Chl a:Phaeo $\sigma_\theta<26$
Avg AOU $\sigma_\theta<26.0$ (μM)
Avg [NO3] $\sigma_\theta<26.0$ (μM)
Avg [NH4] $\sigma_\theta<26.0$ (μM)
Avg N* $\sigma_\theta<26.0$ (μM)
Avg Si-ex $\sigma_\theta<26.0$ (μM)
1% PAR depth (m)
Spiciness $\sigma_\theta<26.0$ (kg m^{-3})
Nitracline [NO3] from P_{New} (μM)
Chl a Max Depth (m)

Table S2.2. Mean chemical, biological and physical properties of CCE regional states (see Methods for PCA-estimated quadrant determinations). The “⁑” inside the table indicates variables used for region-specific PCA. Symbols next to the Quadrant names refer to groups used in Figures 2.4 and 2.6: *Upwelling, ^Bloom, #Accumulation and †Low OM.

Region	Quadrant	N2 *10^4	Dyn Ht (m)	EKE (cm^2 s^{-2})	Satellite NPP (mmol C m^{-2} d^{-1})	Integ. Chl-a (mg m^{-2})	Integ. ^{14}C NPP (mmol C m^{-2} d^{-1})	Wind Speed (knots)	Distance from coast (naut miles)	MLD (m)
Inshore North	Bloom Q4^	0.78±0.31⁑	0.75±0.03	46±53	196±112	155±178	146±186	12±8	-8±15	17±13
	OM Accum Q1#	1.69±0.46⁑	0.83±0.02	34±30	149±78	80±53	97±28	11±7	-14±19	12±6
	Upwelling Q3*	0.75±0.20⁑	-	59±67	123±49	115±110	52±25	13±8	-21±19	35±18
	Low OM Q2†	1.27±0.28⁑	0.84±0.03	27±20	105±50	57±27	62±28	14±6	-26±20	19±9
Inshore South	Bloom Q4^	1.15±0.38⁑	0.83±0.01	123±130	150±70	106±139	121±98	7±7	-10±21	8±4⁑
	OM Accum Q1#	2.03±0.39⁑	0.86±0.05	64±65	73±32	51±27	70±38	6±4	-32±35	9±6⁑
	S. Offshore Wi/Sp Q3†	0.94±0.16⁑	0.87±0.05	46±41	76±52	44±19	36±15	12±9	-54±37	36±12⁑
	S. Offshore Su/Fa Q2#	1.59±0.27⁑	0.89±0.05	42±38	61±37	37±12	42±15	7±6	-46±34	20±10⁑
Cal Current	Wind Curl Prod Q2*	0.76±0.12⁑	0.86±0.05	82±98	63±25	70±51	34±21	21±7⁑	-105±46	40±18
	OM Accum/High TOC Q1#	1.00±0.11⁑	0.89±0.05	110±102	47±15	42±22	23±13	15±6⁑	-145±41	33±15
	Cal Curr Mix Q3†	0.78±0.12⁑	0.88±0.05	139±134	53±13	41±11	29±9	11±5⁑	-118±51	38±21
	OM Accum/Mod TOC Q4†	1.00±0.11⁑	0.92±0.05	126±117	43±16	31±7	30±8	10±5⁑	-156±41	35±18
Offshore	Cal Curr - Su/Fa Q2†	0.99±0.16	0.95±0.04	128±89	32±6	34±9	18±7	11±6	-228±42	27±16
	Cal Curr - Wi/Sp Q3†	0.89±0.14	0.97±0.04	137±172	31±8	30±8	20±5	11±7	-256±66	56±20
	Gyre - Mix Q4†	0.95±0.15	1.00±0.05	108±115	25±6	25±5	13±6	13±7	-286±62	59±20
	Gyre - Su Strat Q1#	1.07±0.12	1.02±0.04	91±71	23±4	24±4	14±4	13±7	-300±45	43±23

Table S2.2 continued. Mean chemical, biological and physical properties of CCE regional states (see Methods for PCA-estimated quadrant determinations). The "⁑" inside the table indicates variables used for region-specific PCA. Symbols next to the Quadrant names refer to groups used in Figures 2.4 and 2.6: *Upwelling, ^Bloom, #Accumulation and †Low OM.

Region	**Quadrant**	**%Chl-a >1 µm**	**Avg Temp $\sigma_\theta<26.0$ (deg C)**	**Avg [Chl-*a*] $\sigma_\theta<26.0$ (µg L^{-1})**	**Avg [Phaeo] $\sigma_\theta<26.0$ (µg L^{-1})**	**Avg Chla: Phaeo $\sigma_\theta<26.0$**	**Avg [POC] $\sigma_\theta<26.0$ (µM)**	**Avg [PON] $\sigma_\theta<26.0$ (µM)**	**Avg POC: PON $\sigma_\theta<26.0$**	**Avg [TOC] $\sigma_\theta<26.0$ (µM)**
Inshore North	**Bloom Q4^**	*70±19*	*13.1±1.5*	*4.81±4.72⁑*	*1.1±1.4*	*7.1±8.3*	*24.7±15.4*	*3.8±2.4*	*6.5±1.0*	*75.7±10.1⁑*
	OM Accum Q1#	*54±31*	*14.2±1.8*	*1.69±0.84⁑*	*0.5±0.2*	*3.9±2.4*	*18.3±10.9*	*2.6±1.3*	*6.8±1.0*	*74.9±7.3⁑*
	Upwelling Q3*	*52±24*	*11.8±0.9*	*1.50±1.25⁑*	*0.5±0.4*	*3.4±3.2*	*10.1±5.0*	*1.7±0.8*	*6.1±0.6*	*63.2±2.8⁑*
	Low OM Q2†	*34±15*	*12.3±0.6*	*0.89±0.65⁑*	*0.3±0.1*	*2.7±1.6*	*9.9±3.9*	*1.5±0.6*	*6.5±0.9*	*63.0±3.8⁑*
Inshore South	**Bloom Q4^**	*61±14*	*13.8±1.5*	*3.14±2.69⁑*	*0.7±0.3*	*5.9±10*	*23.9±15.6*	*3.4±2.0*	*6.7±0.8*	*79.2±13.7⁑*
	OM Accum Q1#	*46±24*	*13.8±1.4*	*0.93±0.60⁑*	*0.3±0.2*	*3.6±4.0*	*13.9±7.9*	*2.0±1.0*	*7.0±1.3*	*73.4±7.8⁑*
	S. Offshore Wi/Sp Q3†	*40±20*	*12.5±0.6*	*0.54±0.37⁑*	*0.2±0.1*	*2.1±0.8*	*6.1±3.0*	*1.0±0.5*	*6.2±0.7*	*63.2±3.2⁑*
	S. Offshore Su/Fa Q2#	*32±12*	*13.0±0.5*	*0.40±0.15⁑*	*0.2±0.1*	*2.1±0.6*	*6.8±2.7*	*1.1±0.4*	*6.4±0.8*	*65.1±3.0⁑*
Cal Current	**Wind Curl Prod Q2***	*39±18*	*12.1±0.6⁑*	*0.78±0.55⁑*	*0.3±0.2*	*3.0±1.7*	*9.3±5.1*	*1.5±0.7*	*6.3±1.1*	*66.0±4.4⁑*
	OM Accum/High TOC Q1#	*36±25*	*13.2±0.5⁑*	*0.44±0.33⁑*	*0.2±0.1*	*2.3±0.4*	*7.6±4.3*	*1.2±0.6*	*6.6±1.3*	*68.4±3.3⁑*
	Cal Curr Mix Q3†	*28±6*	*11.9±0.4⁑*	*0.44±0.16⁑*	*0.2±0.1*	*2.4±0.9*	*6.7±2.7*	*1.2±0.6*	*6.0±1.1*	*61.3±3.1⁑*
	OM Accum/Mod TOC Q4†	*24±4*	*12.8±0.4⁑*	*0.28±0.09⁑*	*0.1±0.0*	*2.1±0.4*	*5.5±2.3*	*0.9±0.4*	*6.5±1.6*	*64.6±2.4⁑*
Offshore	**Cal Curr - Su/Fa Q2†**	*26±5*	*12.6±0.4⁑*	*0.29±0.11⁑*	*0.1±0.0*	*2.7±1.2*	*6.3±2.3*	*1.0±0.4*	*6.3±0.6*	*64.8±3.0⁑*
	Cal Curr - Wi/Sp Q3†	*22±6*	*12.8±0.4⁑*	*0.23±0.09⁑*	*0.1±0.0*	*2.3±0.7*	*4.0±1.7*	*0.7±0.3*	*6.1±1.0*	*61.8±1.8⁑*
	Gyre - Mix Q4†	*17±3*	*13.7±0.4⁑*	*0.18±0.07⁑*	*0.1±0.0*	*2.3±0.6*	*2.8±1.0*	*0.5±0.3*	*6.2±1.5*	*63.2±2.2⁑*
	Gyre - Su Strat Q1#	*19±5*	*13.7±0.4⁑*	*0.16±0.04⁑*	*0.1±0.0*	*2.7±0.7*	*3.1±1.5*	*0.5±0.2*	*7.6±6.5*	*67.5±2.6⁑*

Table S2.2 continued. Mean chemical, biological and physical properties of CCE regional states (see Methods for PCA-estimated quadrant determinations). The "⁑" inside the table indicates variables used for region-specific PCA. Symbols next to the Quadrant names refer to groups used in Figures 2.4 and 2.6: *Upwelling, ^Bloom, #Accumulation and †Low OM.

Region	**Quadrant**	**AOU $\sigma_\theta<26.0$ (μM)**	**O_2 Sat $\sigma_\theta<26.0$ (%)**	**Avg $[NO_3^-]$ $\sigma_\theta<26.0$ (μM)**	**Avg $[NH_4^+]$ $\sigma_\theta<26.0$ (μM)**	**Avg $[NO_2^-]$ $\sigma_\theta<26.0$ (μM)**	**Avg $[PO_4^{3-}]$ $\sigma_\theta<26.0$ (μM)**	**Avg N* $\sigma_\theta<26.0$ (μM)**	**Avg $[SiO_3^{2-}]$ $\sigma_\theta<26.0$ (μM)**	**Avg Si-ex $\sigma_\theta<26.0$ (μM)**
Inshore North	**Bloom Q4^**	*4.7±22.2*⁑	*98.9±9.6*	*5.6±4.3*	*0.56±0.35*	*0.20±0.08*	*0.74±0.28*	*-3.6±1.9*	*6.7±3.4*	*1.4±1.7*
	OM Accum Q1#	*16.4±27.9*⁑	*95.4±10.3*	*5.7±4.0*	*0.30±0.33*	*0.10±0.07*	*0.67±0.27*	*-2.9±1.2*	*6.8±3.5*	*1.8±1.2*
	Upwelling Q3*	*49.1±22.8*⁑	*81.5±8.0*	*11.4±4.7*	*0.18±0.20*	*0.16±0.07*	*1.12±0.29*	*-3.6±1.2*	*12.4±4.8*	*1.0±0.9*
	Low OM Q2†	*51.2±17.8*⁑	*81.5±6.8*	*10.3±2.6*	*0.15±0.14*	*0.13±0.07*	*1.03±0.17*	*-3.3±1.0*	*10.9±2.4*	*0.5±1.1*
Inshore South	**Bloom Q4^**	*4.4±30.6*	*99.2±11.6*	*4.2±4.3*	*0.27±0.24*	*0.12±0.08*	*0.61±0.27*	*-2.7±0.9*	*6.3±3.8*	*2.1±1.6*
	OM Accum Q1#	*22.0±29.7*	*93.1±11.3*	*7.1±3.9*	*0.23±0.34*	*0.10±0.06*	*0.77±0.26*	*-2.6±0.8*	*7.9±3.2*	*1.0±1.1*
	S. Offshore Wi/Sp Q3†	*40.1±13.5*	*85.4±5.1*	*7.8±2.3*	*0.19±0.52*	*0.08±0.07*	*0.87±0.13*	*-3.2±1.0*	*8.6±1.7*	*0.8±1.1*
	S. Offshore Su/Fa Q2#	*38.9±13.7*	*86.0±5.0*	*8.3±2.1*	*0.09±0.09*	*0.08±0.07*	*0.88±0.13*	*-2.8±0.6*	*8.6±1.9*	*0.3±0.8*
Cal Current	**Wind Curl Prod Q2***	*27.4±13.1*	*90.2±4.9*	*7.7±2.9*	*0.16±0.13*	*0.10±0.06*	*0.87±0.20*	*-3.3±1.4*	*8.5±2.9*	*0.8±1.7*
	OM Accum/High TOC Q1#	*27.2±13.1*	*90.2±4.0*	*7.0±1.9*	*0.12±0.11*	*0.08±0.04*	*0.80±0.11*	*-2.9±1.0*	*7.5±1.5*	*0.4±0.7*
	Cal Curr Mix Q3†	*26.4±10.9*	*90.5±4.2*	*7.4±2.6*	*0.11±0.10*	*0.11±0.05*	*0.84±0.17*	*-3.1±1.2*	*8.3±2.3*	*1.0±0.7*
	OM Accum/Mod TOC Q4†	*22.9±8.1*	*92.0±2.9*	*6.2±2.0*	*0.07±0.07*	*0.07±0.04*	*0.75±0.13*	*-3.0±1.0*	*6.9±1.7*	*0.8±0.6*
Offshore	**Cal Curr - Su/Fa Q2†**	*14.3±7.9*⁑	*94.5±3.0*	*4.9±1.6*	*0.11±0.11*	*0.06±0.04*	*0.68±0.11*	*-3.1±1.4*	*5.9±1.3*	*1.1±0.6*
	Cal Curr - Wi/Sp Q3†	*17.7±6.4*⁑	*94.0±2.1*	*4.3±1.1*	*0.04±0.03*	*0.03±0.02*	*0.63±0.07*	*-2.9±1.2*	*5.4±0.9*	*1.1±0.6*
	Gyre - Mix Q4†	*16.5±6.1*⁑	*94.1±2.3*	*3.9±1.7*	*0.04±0.07*	*0.03±0.02*	*0.59±0.12*	*-2.6±0.9*	*5.1±1.4*	*1.2±0.6*
	Gyre - Su Strat Q1#	*11.5±4.5*⁑	*96.0±1.7*	*3.4±1.4*	*0.05±0.06*	*0.03±0.02*	*0.55±0.10*	*-2.5±0.9*	*4.8±1.1*	*1.4±0.7*

Table S2.2 continued. Mean chemical, biological and physical properties of CCE regional states (see Methods for PCA-estimated quadrant determinations). The “⁑” inside the table indicates variables used for region-specific PCA. Symbols next to the Quadrant names refer to groups used in Figures 2.4 and 2.6: *Upwelling, ^Bloom, #Accumulation and †Low OM.

Region	Quadrant	Nitracline $[NO_3^-]$ (µM)	Avg Euph zone $[NO_3^-]$ (µM)	P_{New} (mmol C m^{-2} d^{-1})	Nitracline Depth (m)	P_{TOC} (mmol C m^{-2} d^{-1})	P_{TOC}:P_{New}	P_{TOC}:NPP	*f*-ratio
Inshore North	**Bloom Q4^**	*15.4±8.7*	*4.7±5.3*	*139±71.1*	*30.7±23.1*	*43.8±37.7*	*0.28±0.15*	*0.16±0.08*	*0.58±0.10*
	OM Accum Q1#	*15.7±9.0*	*7.4±6.1*	*65.4±5.2*	*55.5±35.4*	*19.8±8.0*	*0.30±0.10*	*0.12±0.08*	*0.39±0.13*
	Upwelling Q3*	*19.7±3.9*	*10.0±5.4*	*58.0±31.4*	*83.5±33.6*	*9.6±7.1*	*0.16±0.04*	*0.07±0.04*	*0.51±0.27*
	Low OM Q2†	*22.4±4.5*	*10.9±6.1*	*60.8±24.0*	*89.6±49.6*	*11.1±7.2*	*0.18±0.07*	*0.10±0.07*	*0.54±0.23*
Inshore South	**Bloom Q4^**	*17.1±8.1*	*3.2±5.1*	*59.6±32.5*	*43.1±28.1*	*13.7±7.6*	*0.24±0.10*	*0.09±0.04*	*0.40±0.23*
	OM Accum Q1#	*19.2±5.4*	*9.4±6.1*	*21.6±9.0*	*82.2±40.1*	*5.8±4.4*	*0.26±0.13*	*0.08±0.06*	*0.34±0.16*
	S. Offshore Wi/Sp Q3†	*19.8±4.0*	*9.8±4.1*	*32.7±29.2*	*98.9±36.9*	*4.1±4.3*	*0.14±0.06*	*0.05±0.03*	*0.37±0.20*
	S. Offshore Su/Fa Q2#	*20.6±4.2*	*11.3±4*	*26.2±25.9*	*101.6±33.8*	*4.0±4.4*	*0.16±0.06*	*0.05±0.02*	*0.37±0.19*
Cal Current	**Wind Curl Prod Q2***	*19.7±4.0*	*7.4±3.4*	*34.3±26.7*	*94.2±27.3*	*4.8±3.3*	*0.15±0.07*	*0.08±0.04*	*0.59±0.46*
	OM Accum/High TOC Q1#	*19.7±3.4*	*8.0±3.8*	*23.9±15.4*	*108.3±37.4*	*3.5±1.8*	*0.17±0.06*	*0.08±0.04*	*0.54±0.42*
	Cal Curr Mix Q3†	*20.3±3.5*	*8.9±2.8*	*25.0±18.5*	*109.1±31.7*	*3.2±2.7*	*0.13±0.04*	*0.06±0.05*	*0.49±0.32*
	OM Accum/Mod TOC Q4†	*19.0±4.2*	*8.7±3.1*	*14.0±13.3*	*122.7±29.9*	*2.1±2.2*	*0.14±0.05*	*0.06±0.04*	*0.38±0.28*
Offshore	**Cal Curr - Su/Fa Q2†**	*17.5±4.2*	*6.9±2.8*	*17.7±14.7*	*134.6±35.4*	*2.3±2.4*	*0.14±0.04*	*0.07±0.07*	*0.53±0.45*
	Cal Curr - Wi/Sp Q3†	*19.0±3.3*	*8.4±3.3*	*10.1±4.5*	*151.4±26.4*	*1.3±0.8*	*0.12±0.08*	*0.04±0.02*	*0.30±0.12*
	Gyre - Mix Q4†	*18.5±3.5*	*8.6±3.9*	*6.6±3.4*	*153.6±29.3*	*0.8±0.6*	*0.15±0.12*	*0.04±0.03*	*0.28±0.17*
	Gyre - Su Strat Q1#	*17.2±4.7*	*7.5±3.9*	*4.7±2.2*	*154.9±28.6*	*0.8±0.5*	*0.18±0.06*	*0.04±0.02*	*0.21±0.10*

Table S2.2 continued. Mean chemical, biological and physical properties of CCE regional states (see Methods for PCA-estimated quadrant determinations). The “⁑” inside the table indicates variables used for region-specific PCA. Symbols next to the Quadrant names refer to groups used in Figures 2.4 and 2.6: *Upwelling, ^Bloom, #Accumulation and †Low OM.

Region	**Quadrant**	**w (m d^{-1})**	**1% PAR depth (m)**	**Spiciness σ_θ<26.0 (kg m^{-3})**	**Chl-a Max depth (m)**	**Δ[TOC] σ_θ<26.0 (µM)**	**Δ[POC] σ_θ<26.0 (µM)**
Inshore North	**Bloom Q4^**	*1.60±1.07*	*19.9±12.2*	*0.58±0.20*⁑	*13.2±11.8*	*18.9±10.1*	*22.1±16.5*
	OM Accum Q1#	*0.16±0.55*	*19.6±7.8*	*0.81±0.35*⁑	*16.6±7.7*	*12.7±6.3*	*16.6±10.1*
	Upwelling Q3*	*0.52±0.95*	*36.0±22.4*	*0.29±0.12*⁑	*17.1±15.6*	*8.1±3.7*	*8.0±5.6*
	Low OM Q2†	*0.16±0.82*	*33.9±18.6*	*0.42±0.11*⁑	*16.2±8.9*	*5.8±2.7*	*7.7±3.9*
Inshore South	**Bloom Q4^**	*0.78±0.39*	*30.9±26.3*	*0.67±0.27*⁑	*11.9±6.0*	*18.7±12.5*	*23.3±19.3*
	OM Accum Q1#	*0.17±0.24*	*33.1±15.1*	*0.70±0.33*⁑	*21.9±10.5*	*11.8±7.1*	*11.6±8.3*
	S. Offshore Wi/Sp Q3†	*0.28±0.44*	*32.9±11.7*	*0.42±0.11*⁑	*24.2±13.3*	*5.4±3.1*	*4.0±3.1*
	S. Offshore Su/Fa Q2#	*0.08±0.45*	*41.9±17.6*	*0.53±0.12*⁑	*34.1±10.9*	*4.6±2.4*	*4.5±2.8*
Cal Current	**Wind Curl Prod Q2***	*0.15±0.53*	*39.8±13.8*	*0.27±0.18*	*23.0±11.8*	*7.7±4.8*	*6.8±5.2*
	OM Accum/High TOC Q1#	*0.02±0.29*	*56.9±73.4*	*0.51±0.20*	*36.9±16.6*	*6.5±3.6*	*5.0±4.0*
	Cal Curr Mix Q3†	*0.10±0.35*	*40.2±18.2*	*0.16±0.12*	*23.2±16.7*	*4.1±2.5*	*4.0±2.5*
	OM Accum/Mod TOC Q4†	*0.00±0.26*	*45.1±22.5*	*0.34±0.15*	*43.0±15.3*	*3.0±1.3*	*3.1±2.3*
Offshore	**Cal Curr - Su/Fa Q2†**	*0.06±0.26*	*45.6±22.4*	*0.20±0.12*⁑	*43.0±16.7*	*4.1±2.3*	*4.0±2.2*
	Cal Curr - Wi/Sp Q3†	*-0.04±0.29*	*56.0±25.1*	*0.27±0.12*⁑	*54.3±19.5*	*2.1±1.4*	*1.9±1.6*
	Gyre - Mix Q4†	*0.02±0.10*	*117.5±116.6*	*0.55±0.14*⁑	*71.0±19.5*	*2.5±1.9*	*1.0±0.9*
	Gyre - Su Strat Q1#	*-0.03±0.11*	*63.2±22.6*	*0.52±0.14*⁑	*75.4±18*	*4.5±2.9*	*1.7±1.5*

Supplemental Text S2.1. Top Variables Correlated with Surface [TOC] by Stepwise Regression

To test for the variables that were most strongly correlated with surface [TOC] a stepwise multiple regression analysis was performed. Twenty available parameters were tested (see Table S2.1) for each sub-region. The combination of variables selected had minimized the Mallow's Cp values while also minimizing the total number of variables. In this case, a combination of four variables was the most appropriate across the sub-region to regress against surface [TOC].

In the Northern Inshore region, surface mean [Chl-*a*] and apparent oxygen utilization (AOU), buoyancy frequency (0 over 200m; [*Smith* and *Ferrari*, 2009]) and surface mean spiciness [*Munk*, 1981] led to the strongest correlation (r^2=0.66) with surface [TOC]. In the Southern Inshore region mean surface [TOC] was strongly correlated (r^2=0.57) with [Chl-*a*], spiciness, buoyancy frequency and mixed layer depth (MLD). In the California Current and Offshore regions, the strength of correlations decreased (r^2=0.32 and r^2=0.15, respectively) and predictors shifted to temperature (most important), [Chl-*a*], buoyancy frequency, and wind speed for the California Current and spiciness, MLD, AOU and temperature Offshore.

The above selected variables have physical and biogeochemical relevance to TOC cycling in the southern CCE study region. For instance, spiciness has been used in the CCE to identify warm and salty waters transported into the CCE region from the Northern Equatorial Pacific (e.g., [*Todd et al.*, 2012]), and so we can use this variable to distinguish among water masses within a given sub-region. Buoyancy frequency is a measure of surface water stratification, which is important not only for reduced nutrient transport and phytoplankton growth (and therefore organic matter production) but also for mixing of subsurface waters into the surface that might contain reduced carbon concentrations. Finally, AOU can be a useful variable to distinguish between periods of oxygen production and consumption, where a negative AOU value can indicate oxygen supersaturation during production and a high positive value can be indicative of upwelling of deep waters into the surface ocean.

Text S2.2. PCA-based Quadrants

Quadrants in each PCA biplot were designated “Q1” through “Q4” (Figure S2.3). The designation of Q1 to Q4 was subregion specific and linked to biplot location, with positive PC1 and PC2 space designated as Q1, and remaining quadrant designations increased in a counterclockwise direction. Mean values for different properties were first examined in aggregate and used to categorize each quadrant into a general ecosystem condition (e.g., “high production”). Q1 Inshore North had quite different ecosystem characteristics from Q1 Offshore because the PCA was separated by subregion. The complex hydrography and mesoscale variability that is typical of the CCE prevented consistent, clear seasonal and/or spatial separation for every cruise for every region. However, the Inshore North region generally followed a seasonal progression while Inshore South and California Current regions followed more patterns associated with production and distance from shore (see Table S2.2). Quadrant specific mean [TOC] were significantly different (Mann-Whitney, $p<0.01$) in the California Current region yet smaller in magnitude than the significant differences observed among the Inshore regions.

Text S2.3. DOC and POC Contributions to TOC

Samples collected simultaneously for [TOC], [DOC] (TOC filtered through a pre-combusted Whatman GF/F filter), and [POC] on recent CCE-LTER process cruises (P1408 and P1604) within the Northern Inshore (near CalCOFI stations 080.0 055.0) demonstrated that when [POC]>5.0µM, [TOC] - [POC] < [DOC] (Figure S2.7b), indicating that subtracting [POC] from [TOC] does not accurately estimate [DOC]. [DOC] is always included in the [TOC] measurement (i.e., as a subset of TOC), but even at higher suspended [POC] concentrations, the [TOC] measurement does not quantitatively capture [POC] (i.e., [POC] intersects with [TOC] but is not a subset of [TOC]).

To further constrain the contribution of DOC to [TOC] we performed a minimum 10th percentile analysis of available [DOC] for the eastern North Pacific. This minimum [DOC] profile was most representative by use of P02 and CCE datasets (n=854) and takes on nearly identical minimum concentrations as compared to the minimum 10th percentile profile for [TOC] (see Profiles in Figures S2.1 and S2.7c). Then for cruises where we had overlapping [TOC], [DOC] and [POC] we estimated the Δ[DOC] values (n=32). This Δ[DOC] was finally divided by Δ[TOC] to estimate the contribution of added DOC to the added TOC reservoir. From this we find that when [POC] is >5 µM that DOC contributes 51 ± 22% to the ΔTOC reservoir and increases to 69 ± 15% when [POC] < 5 µM (Figure S2.7d). Again, we do not use [POC] to estimate proportional contributions to [TOC] given the slight offsets shown in Fig S7b. Instead we make use of concurrently collected samples and assume minimum contamination during sample filtration (as tested by (1) connecting combusted GF/F directly to Niskin bottle spout and (2) gentle filtration was used in the ship’s lab).

REFERENCES

Abell, J., Emerson, S., and Renaud, P. (2000). Distributions of TOP, TON and TOC in the North Pacific subtropical gyre: Implications for nutrient supply in the surface ocean and remineralization in the upper thermocline. *Journal of Marine Research*, *58*(2), 203–222.

Abramson, L., Lee, C., Liu, Z., Wakeham, S., and Szlosek, J. (2010). Exchange between suspended and sinking particles in the northwest Mediterranean as inferred from the organic composition of in situ pump and sediment trap samples. *Limnology and Oceanography*, *55*(2), 725–739.

Aksnes, D. L., and Ohman, M. D. (2009). Multi-decadal shoaling of the euphotic zone in the southern sector of the California Current System. *Limnology and Oceanography*, *54*(4), 1272–1281.

Altabet, M. A. (1988). Variations in nitrogen isotopic composition between sinking and suspended particles: implications for nitrogen cycling and particle transformation in the open ocean. *Deep Sea Research Part A, Oceanographic Research Papers*, *35*(4), 535–554.

Álvarez-Salgado, X. A., Gago, J., Míguez, B. M., and Pérez, F. F. (2001). Net ecosystem production of dissolved organic carbon in a coastal upwelling system: The Ría de Vigo, Iberian margin of the North Atlantic. *Limnology and Oceanography*, *46*(1), 135–146.

Armstrong, F. A. J., Stearns, C. R., and Strickland, J. D. H. (1967). The measurement of upwelling and subsequent biological process by means of the Technicon Autoanalyzer® and associated equipment. *Deep Sea Research and Oceanographic Abstracts*, *14*(3), 381–389.

Barth, J. A., Cowles, T. J., Kosro, P. M., Shearman, R. K., Huyer, A., and Smith, R. L. (2002). Injection of carbon from the shelf to offshore beneath the euphotic zone in the California Current. *Journal of Geophysical Research*, *107*(C6), 3057.

Behrenfeld, M. J., and Falkowski, P. G. (1997). Photosynthetic rates derived from satellite-based chlorophyll concentration. *Limnology and Oceanography*, *42*(1), 1–20.

Bjorkstedt, E. P., Goericke, R., McClatchie, S., Weber, E., Watson, W., Lo, N. C. H., Peterson, B., Emmett, B., Peterson, J., Durazo, R., Gaxiola-Castro, G., Chavez, F., Pennington, J. T., Munger, L. M. (2010). State of the California Current 2009-2010: Regional variation persists through transistion from La Niña to El Niño (and back?). *California Cooperative Oceanic Fisheries Investigations Report*, *51*, 39–69.

Bograd, S. J., Chereskin, T. K., and Roemmich, D. (2001). Transport of mass, heat, salt, and nutrients in the southern California Current System: Annual cycle and interannual variability. *Journal of Geophysical Research: Oceans*, *106*(C5), 9255–9275.

Breitbart, M. (2012). Marine Viruses: Truth or Dare. *Annual Review of Marine Science*, *4*(1), 425–448.

Carlson, C. A., and Hansell, D. A. (2014). DOM Sources, Sinks, Reactivity, and Budgets. In *Biogeochemistry of Marine Dissolved Organic Matter: Second Edition* (pp. 65–126).

Carlson, C. A., Ducklow, H. W., and Michaels, A. F. (1994). Annual flux of dissolved organic carbon from the euphotic zone in the northwestern Sargasso Sea. *Nature*, *371*, 405–408.

Carlson, C. A., Ducklow, H. W., Hansell, D. A., and Smith, W. O. (1998). Organic carbon partitioning during spring phytoplankton blooms in the Ross Sea polynya and the Sargasso Sea. *Limnology and Oceanography*, *43*(3), 375–386.

Carlson, C. A., Hansell, D. A., Peltzer, E. T., and Smith, W. O. (2000). Stocks and dynamics of dissolved and particulate organic matter in the southern Ross Sea, Antarctica. *Deep Sea Research Part II:*

Topical Studies in Oceanography, *47*(15–16), 3201–3225.

Carlson, C. A., Giovannoni, S. J., Hansell, D. A., Goldberg, S. J., Parsons, R., and Vergin, K. (2004). Interactions among dissolved organic carbon, microbial processes, and community structure in the mesopelagic zone of the northwestern Sargasso Sea. *Limnology and Oceanography*, *49*(4), 1073–1083.

Chenillat, F., Franks, P. J. S., Rivière, P., Capet, X., Grima, N., and Blanke, B. (2015). Plankton dynamics in a cyclonic eddy in the Southern California Current System. *Journal of Geophysical Research: Oceans*, *120*(8), 5566–5588.

DeVries, T., and Weber, T. (2017). The export and fate of organic matter in the ocean: New constraints from combining satellite and oceanographic tracer observations. *Global Biogeochemical Cycles*, *31*(3), 535–555.

Druffel, E. R. M., Williams, P. M., Bauer, J. E., and Ertel, J. R. (1992). Cycling of Dissolved and Particulate Organic Matter in the Open Ocean. *Journal of Geophysical Research*, *97659*(15), 639–15.

Duarte, C. M., Regaudie-de-Gioux, A., Arrieta, J. M., Delgado-Huertas, A., and Agustí, S. (2013). The Oligotrophic Ocean Is Heterotrophic. *Annual Review of Marine Science*, *5*(1), 551–569.

Emerson, S. (2014). Annual net community production and the biological carbon flux in the ocean. *Global Biogeochemical Cycles*, *28*(1), 14–28.

Eppley, R. W., Renger, E. H., and Harrison, W. G. (1979). Nitrate and phytoplankton production in southern California coastal waters. *Limnology and Oceanography*, *24*(3), 483–494.

Eppley, R. W., and Peterson, B. J. (1979). Particulate organic matter flux and planktonic new production in the deep ocean. *Nature*, *282*(5740), 677–680.

Fogg, G. E. (1983). The Ecological Significance of Extracellular Products of Phytoplankton Photosynthesis. *Botanica Marina*, *26*(1), 3–14.

Gelpi, C. G., and Norris, K. E. (2008). Seasonal temperature dynamics of the upper ocean in the Southern California Bight. *Journal of Geophysical Research*, *113*, 1–18.

Goericke, R. (2002). Top-down control of phytoplankton biomass and community structure in the monsoonal Arabian Sea. *Limnology and Oceanography*, *47*(5), 1307–1323.

Goericke, R. (2011). The Size Structure of Marine Phytoplankton— What Are the Rules? *CalCOFI Rep*, *52*, 198–204.

Gruber, N., Lachkar, Z., Frenzel, H., Marchesiello, P., Münnich, M., McWilliams, J. C., Nagai, T., and Plattner, G.-K. (2011). Eddy-induced reduction of biological production in eastern boundary upwelling systems. *Nature Geoscience*, *4*(11), 787–792.

Hales, B., Takahashi, T., and Bandstra, L. (2005). Atmospheric CO2 uptake by a coastal upwelling system. *Global Biogeochemical Cycles*, *19*(1), 1–11.

Halewood, E. R., Carlson, C. A., Brzezinski, M. A., Reed, D. C., and Goodman, J. (2012). Annual cycle of organic matter partitioning and its availability to bacteria across the Santa Barbara Channel continental shelf. *Aquatic Microbial Ecology*, *67*(3), 189–209.

Hansell, D. A. (2013). Recalcitrant Dissolved Organic Carbon Fractions. *Annual Review of Marine Science*, *5*(1), 421–445.

Hansell, D. A., Bates, N. R., and Carlson, C. A. (1997). Predominance of vertical loss of carbon from surface waters of the equatorial Pacific Ocean. *Nature*.

Hansell, D. A., and Carlson, C. A. (1998). Net community production of dissolved organic carbon. *Global Biogeochemical Cycles*, *12*(3), 443–453.

Harrison, W. G., Platt, T., and Lewis, M. R. (1987). f-Ratio and its relation to ambient nitrate concentration in coastal waters. *Journal of Plankton Research*, *9*(l), 235–248.

Hasegawa, T., Kasai, H., Ono, T., Tsuda, A., and Ogawa, H. (2010). Dynamics of dissolved and particulate organic matter during the spring bloom in the Oyashio region of the western subarctic Pacific Ocean. *Aquatic Microbial Ecology*, *60*(2), 127–138.

Haskell, W. Z., Prokopenko, M. G., Hammond, D. E., Stanley, R. H. R., Berelson, W. M., Baronas, J. J., Fleming, J. C., and Aluwihare, L. I. (2016). An organic carbon budget for coastal Southern California determined by estimates of vertical nutrient flux, net community production and export. *Deep-Sea Research Part I: Oceanographic Research Papers*, *116*, 49–76.

Haury, L. R., Simpson, J. J., Pelxez, J., Koblinsky, C. J., and Wiesenhahn, D. (1986). Biological Consequences of a Recurrent Eddy off Point Conception. *Journal of Geophysical Research*, *91956*(15), 937–12.

Hayward, T., and Venrick, E. (1998). Nearsurface pattern in the cal current coupling between physical and biologial structure.pdf. *Deep Sea Research Part II: Topical Studies in Oceanography*, *45*, 1617–1638.

Hill, J. K., and Wheeler, P. A. (2002). Organic carbon and nitrogen in the northern California current system: Comparison of offshore, river plume, and coastally upwelled waters. *Progress in Oceanography*, *53*(2–4), 369–387.

Huyer, A. (1983). Coastal upwelling in the California current system. *Progress in Oceanography*.

Jacox, M. G., Hazen, E. L., and Bograd, S. J. (2016a). Optimal Environmental Conditions and Anomalous Ecosystem Responses: Constraining Bottom-up Controls of Phytoplankton Biomass in the California Current System. *Scientific Reports*, *6*(June), 27612.

Jacox, M. G., Hazen, E. L., Zaba, K. D., Rudnick, D. L., Edwards, C. A., Moore, A. M., and Bograd, S. J. (2016b). Impacts of the 2015–2016 El Niño on the California Current System: Early assessment and comparison to past events. *Geophysical Research Letters*, *43*(13), 7072–7080.

Kahru, M., Kudela, R., Manzano-Sarabia, M., and Mitchell, B. G. (2009). Trends in primary production in the California Current detected with satellite data. *Journal of Geophysical Research: Oceans*, *114*(2).

Kelly, K. A., Beardsley, R. C., Limeburner, R., Brink, K. H., Paduan, J. D., and Chereskin, T. K. (1998). Variability of the near-surface eddy kinetic energy in the California Current based on altimetric, drifter, and moored current data. *Journal of Geophysical Research*, *103*(C6), 13067.

King, A. L., and Barbeau, K. A. (2011). Dissolved iron and macronutrient distributions in the southern California Current System. *Journal of Geophysical Research: Oceans*, *116*(3).

Kirchman, D. L., Meon, B., Cottrell, M. T., Hutchins, D. a., Weeks, D., and Bruland, K. W. (2000). Carbon versus iron limitation of bacterial growth in the California upwelling regime. *Limnology and Oceanography*, *45*(8), 1681–1688.

Lampert, W. (1978). Release of dissolved organic carbon by grazing zooplankton. *Limnology and Oceanography*, *23*(4), 831–834.

Landry, M. R., Barber, R. T., Bidigare, R., Chai, F., Coale, K. H., Dam, H. G., Lewis, M. R., Lindley, S. T., Mccarthy, J. J., and Roman, M. R. (1997). Iron and grazing constraints on primary production in the central equatorial Pacific: An EqPac synthesis. *Limnology and Oceanography*, *42*(3), 405–418.

Laws, E. A., Falkowski, P. G., Smith, W. O., Ducklow, H., and McCarthy, J. J. (2000). Temperature effects on export production in the open ocean. *Global Biogeochemical Cycles*, *14*(4), 1231–1246.

Letscher, R. T., Hansell, D. A., Carlson, C. A., Lumpkin, R., and Knapp, A. N. (2013). Dissolved organic nitrogen in the global surface ocean: Distribution and fate. *Global Biogeochemical Cycles*, *27*(1), 141–153.

Letscher, R. T., Primeau, F., and Moore, J. K. (2016). Nutrient budgets in the subtropical ocean gyres dominated by lateral transport. *Nature Geoscience*, *9*(11), 815–819.

Lucas, A. J., Dupont, C. L., Tai, V., Largier, J. L., Palenik, B., and Franks, P. J. S. (2011). The green ribbon: Multiscale physical control of phytoplankton productivity and community structure over a narrow continental shelf. *Limnology and Oceanography*, *56*(2), 611–626.

Mallows, C. L. (1973). Some Comments on Cp. *Technometrics*, *15*(4), 661.

Martiny, A. C., Pham, C. T. A., Primeau, F. W., Vrugt, J. A., Moore, J. K., Levin, S. A., and Lomas, M. W. (2013). Strong latitudinal patterns in the elemental ratios of marine plankton and organic matter. *Nature Geoscience*, *6*(4), 279–283.

Martz, T. R., Send, U., Ohman, M. D., Takeshita, Y., Bresnahan, P., Kim, H. J., and Nam, S. (2014). Dynamic variability of biogeochemical ratios in the Southern California Current System. *Geophysical Research Letters*, *41*(7), 2496–2501.

Messié, M., Ledesma, J., Kolber, D. D., Michisaki, R. P., Foley, D. G., and Chavez, F. P. (2009). Potential new production estimates in four eastern boundary upwelling ecosystems. *Progress in Oceanography*, *83*(1–4), 151–158.

Munk, W. (1981). Internal Waves and Small-Scale Processes. In *Evolution of physical oceanography* (pp. 264–291).

Munro, D. R., Quay, P. D., Juranek, L. W., and Goericke, R. (2013). Biological production rates off the Southern California coast estimated from triple O 2 isotopes and O 2 : Ar gas ratios. *Limnol. Oceanogr.*, *58*(4), 1312–1328.

Nagai, T., Gruber, N., Frenzel, H., Lachkar, Z., McWilliams, J. C., and Plattner, G. K. (2015). Dominant role of eddies and filaments in the offshore transport of carbon and nutrients in the California Current System. *Journal of Geophysical Research: Oceans*, *120*(8), 5318–5341.

Najjar, R. G., Jin, X., Louanchi, F., Aumont, O., Caldeira, K., Doney, S. C., Dutay, J. C., Follows, M., Gruber, N., Joos, F., Lindsay, K., Maier-Reimer, E., Matear, R. J., Yool, A. (2007). Impact of circulation on export production, dissolved organic matter, and dissolved oxygen in the ocean: Results from Phase II of the Ocean Carbon-cycle Model Intercomparison Project (OCMIP-2). *Global Biogeochemical Cycles*, *21*(3).

Ogawa, H., and Tanoue, E. (2003). Dissolved organic matter in oceanic waters. *Journal of Oceanography*, *59*(2), 129–147.

Olivieri, R. a, and Chavez, F. P. (2000). A model of plankton dynamics for the coastal upwelling system of Monterey Bay, California. *Deep Sea Research Part II: Topical Studies in Oceanography*, *47*(5–6), 1077–1106.

Omand, M. M., D'Asaro, E. A., Lee, C. M., Perry, M. J., Briggs, N., Cetinić, I., and Mahadevan, A. (2015). Eddy-driven subduction exports particulate organic carbon from the spring bloom. *Science*, *348*(6231), 222–225.

Peltzer, E. T., and Hayward, N. A. (1996). Spatial and temporal variability of total organic carbon along 140°W in the equatorial Pacific Ocean in 1992. *Deep Sea Research Part II: Topical Studies in Oceanography*, *43*(4–6), 1155–1180.

Pennington, J. T., Friederich, G. E., Castro, C. G., Collins, C. A., Evans, W. W., and Chavez, F. P. (2010). The Northern and Central California Coastal Upwelling System. In K.-K. Liu, L. Atkinson, R. Quinones, & L. Talaue-McManus (Eds.), *Carbon and Nutrient Fluxes in Continental Margins* (pp. 29–44). Springer Science & Business Media.

Plattner, G.-K., Gruber, N., Frenzel, H., and McWilliams, J. C. (2005). Decoupling marine export production from new production. *Geophysical Research Letters*, *32*(11), L11612.

Roemmich, D. (1989). Mean transport of mass, heat, salt and nutrients in southern California coastal waters: implications for primary production and nutrient cycling. *Deep-Sea Research*, *36*(9), 1359–1378.

Romera-Castillo, C., Letscher, R. T., and Hansell, D. A. (2016). New nutrients exert fundamental control on dissolved organic carbon accumulation in the surface Atlantic Ocean. *Proceedings of the National Academy of Sciences*, 201605344.

Romera-Castillo, C., Alvarez-Salgado, X., Gali, M., Gasol, J. M., and Marrase, C. (2013). Combined effect of light exposure and microbial activity on distinct dissolved organic matter pools. A seasonal field study in an oligotrophic coastal system (Blanes Bay, NW Mediterranean). *Marine Chemistry*, *148*, 44–51.

Rykaczewski, R. R., and Checkley, D. M. (2008). Influence of ocean winds on the pelagic ecosystem in upwelling regions. *Proceedings of the National Academy of Sciences*, *105*(6), 1965–1970.

Santinelli, C., Hansell, D. A., and Ribera d'Alcalà, M. (2013). Influence of stratification on marine dissolved organic carbon (DOC) dynamics: The Mediterranean Sea case. *Progress in Oceanography*, *119*, 68–77.

Santoro, A. E., Casciotti, K. L., and Francis, C. A. (2010). Activity, abundance and diversity of nitrifying archaea and bacteria in the central California Current. *Environmental Microbiology*, *12*(7), 1989–2006.

Siegel, D. A., Buesseler, K. O., Doney, S. C., Sailley, S. F., Behrenfeld, M. J., and Boyd, P. W. (2014). Global assessment of ocean carbon export by combining satellite observations and food-web models. *Global Biogeochemical Cycles*, *28*(3), 181–196.

Siegel, D. A., Buesseler, K. O., Behrenfeld, M. J., Benitez-Nelson, C. R., Boss, E., Brzezinski, M. A., Burd, A., Carlson, C. A., D'Asaro, E. A., Doney, S. C., Perry, M. J., Stanley, R. H. R., and Steinberg, D. K. (2016). Prediction of the Export and Fate of Global Ocean Net Primary Production: The EXPORTS Science Plan. *Frontiers in Marine Science*, *3*(March), 1–10.

Smith, K. S., and Ferrari, R. (2009). The production and dissipation of compensated thermohaline variance by mesoscale stirring. *Journal of Physical Oceanography*, *39*(10), 2477–2501.

Stukel, M. R., Landry, M. R., Benitez-Nelson, C. R., and Goericke, R. (2011). Trophic cycling and carbon export relationships in the California Current Ecosystem. *Limnology and Oceanography*, *56*(5), 1866–1878.

Stukel, M. R., Ohman, M. D., Benitez-Nelson, C. R., and Landry, M. R. (2013). Contributions of mesozooplankton to vertical carbon export in a coastal upwelling system. *Marine Ecology Progress Series*, *491*, 47–65.

Stukel, M. R., Aluwihare, L. I., Barbeau, K. A., Chekalyuk, A. M., Goericke, R., Miller, A. J., Ohman, M. D., Ruacho, A., Song, H., Stephens, B. M., and Landry, M. R. (2017). Mesoscale ocean fronts enhance carbon export due to gravitational sinking and subduction. *Proceedings of the National Academy of Sciences*, *114*(6), 1252–1257.

Taylor, A. G., Landry, M. R., Selph, K. E., and Wokuluk, J. J. (2015). Temporal and spatial patterns of microbial community biomass and composition in the Southern California Current Ecosystem. *Deep Sea Research Part II: Topical Studies in Oceanography*, *112*, 117–128.

Teira, E., Pazo, M. J., Serret, P., and Fernandez, E. (2001). Dissolved Organic Carbon Production by Microbial Populations in the Atlantic Ocean. *Limnology and Oceanography*, *46*(6), 1370–1377.

Todd, R. E., Rudnick, D. L., Mazloff, M. R., Davis, R. E., and Cornuelle, B. D. (2011). Poleward flows in the southern California Current System: Glider observations and numerical simulation. *Journal of Geophysical Research: Oceans*, *116*(2).

Todd, R. E., Rudnick, D. L., Mazloff, M. R., Cornuelle, B. D., and Davis, R. E. (2012). Thermohaline structure in the California Current System: Observations and modeling of spice variance. *Journal of Geophysical Research: Oceans*, *117*(2).

Walker, B. D., and McCarthy, M. D. (2012). Elemental and isotopic characterization of dissolved and particulate organic matter in a unique California upwelling system: Importance of size and composition in the export of labile material. *Limnology and Oceanography*, *57*(6), 1757–1774.

Wear, E. K., Carlson, C. A., James, A. K., Brzezinski, M. A., Windecker, L. A., and Nelson, C. E. (2015). Synchronous shifts in dissolved organic carbon bioavailability and bacterial community responses over the course of an upwelling-driven phytoplankton bloom. *Limnology and Oceanography*, *60*(2), 657–677.

Chapter III

Euphotic Zone Nitrification in the California Current Ecosystem

Abstract

The transformation of nitrogen species through nitrification is essential for closing the nitrogen budget in the environment. Nitrification can occur throughout the water column in aquatic environments, including in the euphotic zone, where its contribution to the nitrate inventory can complicate estimates of new production. Nitrate derived from local euphotic zone nitrification can be identified by its natural abundances of $\delta^{15}N$ and $\delta^{18}O$. In this study, the N and O isotope signature of nitrate was used in an existing model framework to quantify nitrate contributed by euphotic zone nitrification in the southern California Current Ecosystem (CCE) during two anomalously warm years. Model data estimated that between 6% and 36% of the euphotic zone nitrate reservoir was derived from nitrification. A simple vertical advection model that divided the euphotic zone into three different light regimes showed that 20 - 50% of the nitrified nitrate was advected from low light depths (0.1 to 1% surface PAR) while the remaining contribution was produced in relatively high light regimes. Nitrification contributions in the euphotic zone were positively correlated with $[NO_2^-]$ at the primary nitrite max depths. Nitrite is an essential substrate for the last step of nitrification, suggesting that nitrite accumulation signals greater nitrification in the euphotic zone of the CCE. Using the long-term California Cooperative Oceanic Fisheries Investigation (CalCOFI) survey record (2004 - 2016), a multiple linear regression analysis found that $[NO_2^-]$ likely increased due either to reduced phytoplankton competition for nitrite or to increased supply of organic substrate.

1. Introduction

Nitrification is an essential process in the regeneration of nitrate [*Ward*, 2008]. In strong upwelling regions the nitrate present in the euphotic zone largely enters into the surface ocean as a 'new' nutrient (e.g., [*Chavez et al.*, 1989; *Messié et al.*, 2009]), produced by nitrification in the dark ocean. However, under stratified conditions, nitrification in the euphotic zone can be an important source of nitrate within the surface ocean (e.g., [*Lipschultz*, 2001; *Yool et al.*, 2007]). In situ observations and global models have estimated that >30% of the surface nitrate reservoir can be derived from local nitrification (e.g., [*Yool et al.*, 2007; *Santoro et al.*, 2010; *Beman et al.*, 2012]).

Aerobic nitrification typically proceeds as a two-step process, mediated first by ammonia oxidizing *Thaumarchaeota* (referred to here as ammonia oxidizing *Archaea*, or AOA) and to a lesser extent, ammonia oxidizing bacteria (AOB) [*Ward* and *Carlucci*, 1985; *Könneke et al.*, 2005; *Schleper et al.*, 2005; *Mincer et al.*, 2007; *Santoro et al.*, 2010], and subsequently by nitrite oxidizing bacteria (NOB, e.g., [*Watson* and *Waterbury*, 1971; *Ward* and *Carlucci*, 1985; *Lücker et al.*, 2013]). Recent studies have also identified bacteria within the common marine genus *Nitrospira* that are capable of oxidizing both ammonia and nitrite to ultimately produce nitrate [*Daims et al.*, 2015, 2016]. Nitrification rates often measured as ammonia oxidation tend to peak (up to 60 - 100 nmol N L^{-1} d^{-1}) just below the 1% PAR and/or primary nitrite maximum depths [*Ward*, 2005, 2008; *Santoro et al.*, 2010]. Although nitrification rates can be correlated with nitrifier abundance [*Smith et al.*, 2014b], data from the California Current have shown that nitrification rates can peak at a slightly shallower depth than the abundances of phylogenetic and functional gene markers for nitrifiers (typically AOA and NOB) [*Smith et al.*, 2016].

The nitrogen (N) and oxygen (O) stable isotopic signature of nitrate, $\delta^{15}N$ and $\delta^{18}O$, have also been used to estimate the contribution of nitrification to the surface nitrate reservoir of the central CCE (e.g., [*Wankel et al.*, 2007]). Culture studies have indicated that the isotopes of nitrate exhibit concurrent enrichment in $\delta^{15}N_{NO3}$ and $\delta^{18}O_{NO3}$ in a 1:1 ratio, during uptake by phytoplankton (e.g., [*Granger et al.*, 2004]). A similar relationship for nitrate uptake in surface waters is expected. However, the addition of oxygen (and its associated isotopic signature) from water into the surface nitrate reservoir during nitrification results in a departure from the expected 1:1 relationship relative to the upwelled nitrate signature [*Wankel et al.*, 2007]. The imprint of nitrification on nitrate, in this case, can be detected and quantified based on this isotopic departure. Such a method is attractive because it provides a temporally integrated estimate of nitrification not offered by the bottle incubation methods that are typically used to assess nitrification rates. However, models are necessary to quantify nitrification from stable isotope measurements of nitrate, and these models incorporate several constants associated with the biological transformation of various nitrogen reservoirs that are difficult to constrain (e.g., isotope fractionation factors; [*Ward,* 2008]).

In the current study, we build on this existing nitrate stable isotope model [*Wankel et al.*, 2007] to quantify euphotic zone nitrification in the central CCE. Our study was conducted in the southern CCE during two cruises, one that sampled the recent North

Pacific warm pool anomaly of 2014 - 2015 and a second that examined the El Niño of 2015 - 2016. Results suggest that nitrification contributed between 6% and 36% of euphotic zone nitrate. Nitrification was positively correlated with nitrite concentrations at the primary nitrite max depths, which offered an opportunity to approximate past variations in nitrification using long-term nitrite records from the CalCOFI time series. Such an analysis suggests that potential changes in nitrification are linked to observed variations in nitrite concentrations are correlated with particulate organic nitrogen concentrations and phytoplankton abundance.

2. Materials and Methods

2.1. Study Location

The present study was located in the southern California Current region of the eastern North Pacific Ocean. Sample locations typically extended from within 20 km of Point Conception, a site of persistent upwelling, to as far as 350 km from shore (Figure 3.1). Samples for this study were collected during CCE-Long Term Ecological Research (LTER) process cruises P1408 and P1604, which took place during August 8 to September 9, 2014 and April 22 to May 10, 2016, respectively. Samples were collected daily from noontime casts via Niskin bottles during coordinated experimental activities called “Cycles”. Each Cycle lasted between 2 to 4 days and a drifter array with a subsurface drogue centered around 15 m enabled the ship to nominally follow the same water mass throughout the Cycle. Depth profiles extended from the surface to the 0.01% light level, typically <150 - 200 m, and at least one sample was collected from >200 m for each Cycle.

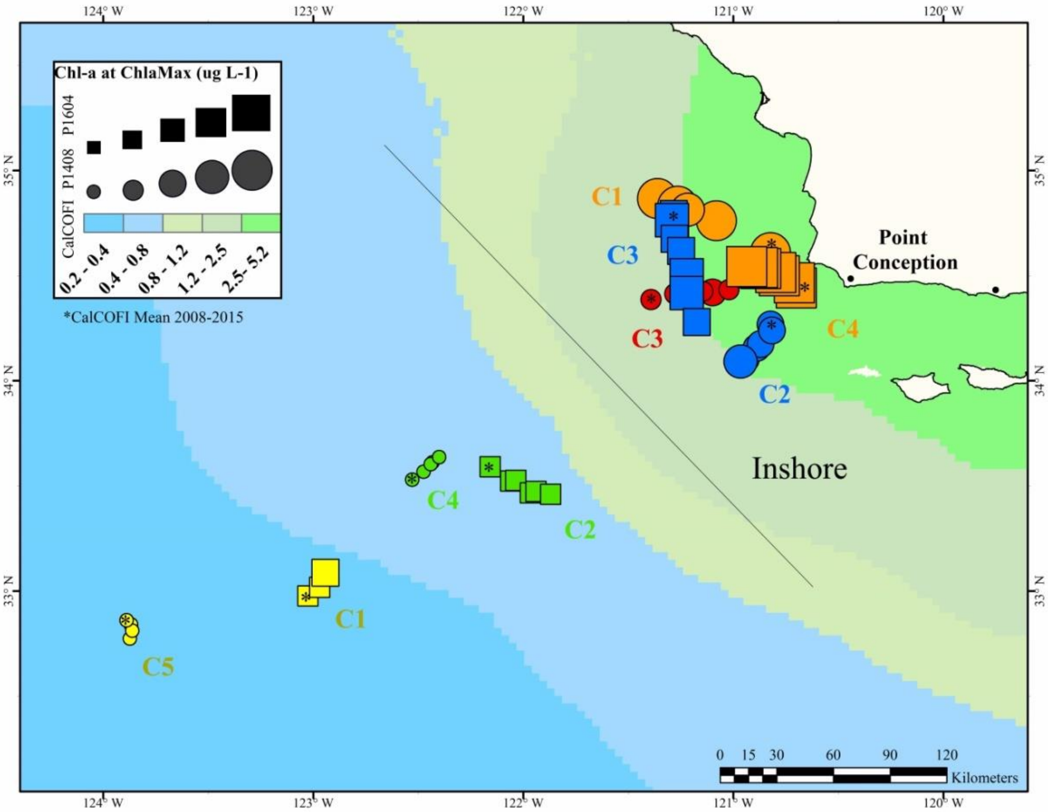

Figure 3.1. *Map of individual Cycles (C1, C2, etc.) for P1408 (circles) and P1604 (squares) cruises. Background blue-green colors coarsely delineate regions by chlorophyll-a (Chl-a) concentrations based on the long-term interpolated CalCOFI mean Chl-a concentrations over 2008-2015 at the Chl-a maximum depth. The size of each Cycle symbol is scaled to Chl-a concentrations. Cycle colors are conserved throughout the document. An asterisk inside a Cycle symbol marks the starting location for each Cycle, and the diagonal line separates "Inshore" Cycles from "Offshore" Cycles.*

2.2. Sample Collection and Analysis

2.2.1. Nutrient and Chlorophyll-a Concentrations

Samples for dissolved inorganic nutrients ([NO_3^-], [NO_2^-], [NH_4^+]) and chlorophyll-*a* concentrations were collected on upcasts from CTD Niskin bottles triggered at 10 discrete depths. These depths purposely spanned different light levels and Chl-*a* distributions as estimated from CTD fluorometer profiles. Samples collected for nutrients were filtered through GF/F (47 mm, Whatman), frozen, and analyzed by flow injection analysis at UC Santa Barbara. Chl-*a* concentrations were determined from GF/F (25 mm, Whatman) filters extracted with 90% acetone, and measured onboard using a Turner Designs10AU Fluorometer after storage for 24 h at -18°C [*Goericke*, 2002].

2.2.2. δ^{15}N and δ^{18}O of Nitrate

Nitrate $\delta^{15}N_{NO3}$ and $\delta^{18}O_{NO3}$ were measured on 0.7 μm-filtered (precombusted GF/F, 47mm, Whatman) seawater collected directly from Niskin bottles and stored in 60 mL HDPE bottles at -80°C until analysis. Samples were analyzed on an IsoPrime mass spectrometer following the denitrifier method [*Sigman et al.*, 2001; *Casciotti et al.*, 2002], with nitrite removed (sulfamic acid method [*Granger et al.*, 2006]). Typical error for $\delta^{15}N_{NO3}$ and $\delta^{18}O_{NO3}$ on duplicate measurements of the same nitrate sample was 0.2‰, which was similar to the 0.3‰ precision of internal quality control nitrate standards.

2.2.3. Stable Isotopes of Suspended and Sinking POM

Seawater for suspended particulate organic matter (POM) isolation was collected from Niskin bottles into 4 L acid-washed Nalgene bottles that were wrapped in black plastic to minimize the influence of light. Between two to four liters was immediately filtered under low vacuum (<50 mm Hg) onto pre-combusted GF/F filters (47 mm, Whatman). The volume filtered depended on Chl-*a* and the sampling location. Similar samples have been collected in the CalCOFI region since 2004, and so, particulate organic carbon and nitrogen concentrations ([POC] and [PON], respectively) distributions in the region are very well constrained (see dissertation author's Chapter II;

Stephens et al., in prep). At the end of the filtration, each filter was wrapped in pre-combusted foil, placed inside sealed plastic bags, and stored at -80 °C until processing for stable isotopes.

Sinking POM was collected from 2 to 3 discrete depths in Vertex-style drifting sediment traps as described previously [*Stukel et al.*, 2013]. Sediment trap tubes contained a slurry of 0.1 μm-filtered seawater mixed with 50 g L^{-1} NaCl, to reduce resuspension of particles, and 4% formaldehyde to reduce biological degradation of organic matter. Particles were filtered onto pre-combusted GF/F filters (25 mm, Whatman) and stored in pre-combusted foil and zip locks bags at -80 °C until further processing for stable isotopes. Visible organisms and animal parts were picked off the filter prior to freezing.

For $\delta^{15}N$ measurements, suspended and sinking POM samples were processed for POM isotope and [POC] measurements [*Sharp*, 1974; *Altabet*, 1990]. Filters were first oven dried overnight at 60 °C and acid fumed in a desiccator the second night to minimize inorganic carbon contamination of $\delta^{13}C$ signatures (needed for a separate analysis). Following fumigation, samples were briefly heated again at 60 °C to dry the filters and provide consistent initial weights. The filters were folded into quarters and the centers were extracted and placed into pre-weighed tin cups. Tin cups were stored in a sample tray inside a desiccator for at least 24 h but not longer than 14 d, until analysis. Blank filters were prepped in the same manner.

POM samples were analyzed on a coupled elemental analyzer-isotope ratio mass spectrometer (EA-IRMS) at SIO's unified laboratory facility. The measured isotope value is a function of the area response of the sample, and can dramatically influence the perceived isotope signatures at low N concentrations. To correct for this bias, nine different quantities of finely powdered acetanilide standards (Baker AO68-03) were dispersed throughout each run. Absolute isotopic values were then estimated using a mixture of acetanilide and calcium carbonate (MK) of known isotopic value. When sample quantities reached the limit of detection (4 μg N and 50 μg C), additional acetanilide standards spanning the 2 to 30 μg N range were added to better constrain the instrument response for low mass samples. The isotopic error for each measurement was then determined as a function of the area response. Reported error bars when averaged across multiple samples were propagated using a sum of square error procedure. Reported errors combined the instrument error as above and the standard deviation of measurements.

2.2.4. Ammonia Oxidizing Archaea and *amo*A genes

During CCE P1604, depth profiles for microbial community composition (i.e., 16s) were isolated from CTD Niskin bottles. Approximately 1.8 L of seawater was collected into opaque HDPE bottles and filtered with a peristaltic pump through 0.1 μm-size cut off sterivex filters (EMD Millipore). Sample collection and processing time did not exceed 45 min. Dry filters were capped with putty and immediately flash frozen in Whirlpak bags prior to storage at -80 °C until further processing. RNA was extracted following protocols developed in Dr. Andrew Allen’s lab by Ariel Rabines (JCVI), where sterivex filters were first cracked open using pipe cutters. RNA was then purified using Macherey-Nagel’s NucleoMag 96 RNA Kit (Ref # 744350.1). The quality and quantity of RNA were subsequently determined using an Agilent RNA ScreenTape System. cDNA was then extracted using Life Technology's SuperScript III First-Strand Synthesis System (Cat. #: 18080-051) and was used as the template for 16s PCRs. Products of the PCR were analyzed for community composition at the Institute for Genomic Medicine at UCSD. Extracts of cDNA were also analyzed for ammonia monooxygenase subunit A (*amo*A) gene activity using optimized primers as in [*Beman et al.*, 2008, 2010] in the lab of Dr. J. Michael Beman (UC Merced).

2.3. Multiple Linear Regression Analysis

A stepwise multiple linear regression analysis (MLRA) was performed on the long-term California Cooperative Oceanic Fisheries Investigations (CalCOFI) dataset from stations nearest the Inshore CCE Cycles exhibiting elevated [NO_2^-] and nitrification. These CalCOFI stations were classified as "Inshore" (lines 076.0 and 080.0, and stations 055.0 and 060.0) and "Midshore" (lines 076.0 and 080.0, and stations 070.0 and 080.0), similar to the regions classified in Figure 3.1. A table of variables tested in the stepwise regression analysis is presented in Appendix Table S3.1. The discussion of this analysis primarily focuses on the model that used 16 parameters collected on CalCOFI cruises between 2004 and 2016, but a subsequent analysis was also performed using a longer time frame (1990 - 2016) on 13 parameters, in order to extend the analysis to cover additional strong climatic events (e.g., 1997 - 1998 El Niño).

Because the parameters tested in the stepwise MLRA ranged in magnitude and skew the distribution of each parameter was first normalized by using the cube root of observations. Cube root-normalized parameters were centered by subtracting the mean and dividing by the standard deviation of cube root values. Centering brought the mean value of each parameter close to 0.0 and allowed for a more direct comparison among predictors in the multiple regression model. The regression model improved significantly by cube-root normalizing and centering from an adjusted r^2 of 26.2% to 34.9%, and this was also reflected by a shift from skewed to normal distributions of residuals (not shown).

The best predictors of the primary maxima of [NO_2^-] were first identified using a stepwise MLRA approach in Minitab version 17.1.0 (Minitab, Inc., State College, PA, USA). The number of variables used in a generalized linear model was determined by stepwise regression analysis based on the Mallows' *Cp* statistic, a value estimated from the mean squared error of the prediction. The Mallows' *Cp* value closest to the number of predictors (plus the intercept) was used to determine the model best fit [*Mallows*, 1973]. A comparative analysis of model performance based on the Akaike Information criterion resulted in a similar outcome, but given that Mallows' *Cp* is built into the stepwise linear regression output from Minitab, this value is presented here. Appendix Figure S3.1 illustrates how the Mallows' *Cp* reaches a minimum point and then increases due to contributions from dataset noise, exhibiting a pattern similar to the adjusted r^2 values by incorporation of additional model parameters.

The stepwise MLRA above was first performed by correlating data collected from each of the eight CalCOFI stations identified above (47 cruises x8 stations, n=746 data points). And the model performance was subsequently compared with that of taking the cruise means of the four stations within each Inshore and Midshore region (47 cruises x2 regions, n=94 data points). The effect of averaging across stations improved the model performance, and the following analysis only focuses on cruise averages for each region (n=94 for 2004 to 2016). A similar outcome was found for the longer time series, and regional and cruise averages were analyzed for that dataset as well (n=212 for 1990 to 2016).

The MLRA resulted in a model containing 4 variables in the CalCOFI dataset covering 2004 to 2016 and resulted in a model containing 6 variables in the 1990 to 2016 CalCOFI dataset (Figure S3.1). The relative weight of individual variables to the generalized linear model parameters was compared based on beta coefficients (or slope values; Table S3.2). The relative contributions of each variable to the MLRA can be directly compared when variables are transformed and centered prior to model evaluation [*Sokal* and *Rohlf*, 1995]. While the beta coefficients presented in Table S3.2 are based on transformed data, in order to present values/concentrations of biogeochemical relevance the figures comparing observed NO_2^- and generalized linear model predicted-NO_2^- did not use transformed data. However, the beta coefficients and adjusted correlation values necessarily change when direct values and concentrations are used in a generalized linear model, and so the correlation values of the linear best fit lines in Figure 3.9 are based on observed values.

Linear regressions presented here determined the slope and intercept based on Type II model fits. Type II linear fits were determined using Matlab code provided by Edward Peltzer (Monterey Bay Aquarium Research Institute, Monterey, CA, USA).

Matlab version R2017b (The Mathworks, Inc., Natick, MA, USA) was used to generate these values.

3. Results

3.1. Cruise and Cycle Context

As is typical for CCE process cruises, each 2 to 4 day Cycle of P1408 and P1604 followed different water masses as determined by proximity to shore (20-300 km from shore), salinity, temperature, and chlorophyll (e.g., [*Landry et al.*, 2009; *Goericke* and *Ohman*, 2015]). Surface water (10 - 50 m) was anomalously warm by 0.8 - 1.5° C for all cycles during these two cruises [*Zaba* and *Rudnick*, 2016]. P1408 occurred just after the onset of the anomalous warming of surface waters in the California Current region [*Bond et al.*, 2015], which may have been mediated by the encroachment of the North Pacific warm pool from the northwest into the CCE [*Zaba* and *Rudnick*, 2016]. P1604 caught the tail end of a strong El Niño and at that time, the CCE was still a system in recovery from the warm anomaly [*Jacox et al.*, 2016b].

For the following presentation of study results, concentrations of chemical quantities are designated without brackets to increase readability but isotopic compositions include the delta notation. During P1408, NO_3^- was nearly undetectable for most surface depths (Figure 3.2). Overall, surface mean (10 - 50 m) values were ~4 μM lower than the long-term average for summer months at regional CalCOFI stations in the time period spanning 1990 - 2016 (determined for CalCOFI stations <75km of Pt. Conception (Figure S3.2)). Anomalously high NO_2^- at the primary nitrite max was also observed for Inshore Cycles 1 - 3 during P1408, increasing to about double the summer average (0.50 vs. 0.25 μM; Figure S3.3). During P1604 Inshore Cycles 3 and 4 had higher surface NO_3^- (10 - 50 m) relative to Inshore Cycles sampled during P1408 (Figure 3.2), but seasonal mean surface NO_3^- for P1604 was still 3 - 5 μM less than the long-term mean spring values (Figure S3.2). At Inshore Cycles 3 and 4 of P1604, maximum NH_4^+ and NO_2^- were nearly double that of the long-term spring mean concentration (1.0 vs. 0.5 μM and 0.4 vs. 0.2 μM, respectively; Figure S3.3). Despite low NO_3^- and anomalously warm temperatures at the surface during 2014 - 2016, mean surface Chl-*a* was not anomalously low in all regions sampled by CCE-LTER cruises (Figure S3.2).

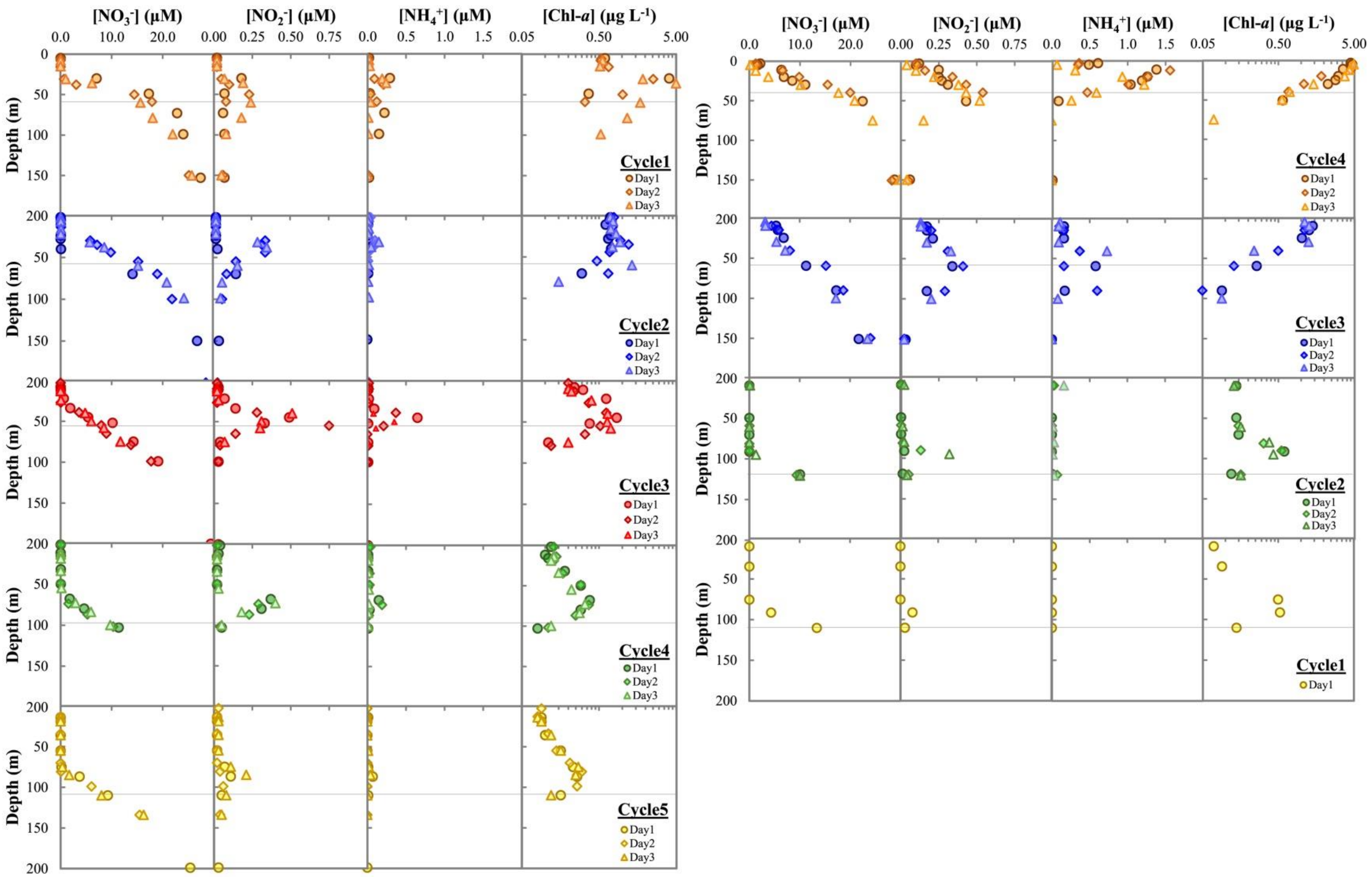

Figure 3.2. *CCE Cruise P1408 (left) and P1604 (right) profiles of NO_3^-, NH_4^+, NO_2^- and Chl-a. Note the relative increase in NO_2^- for Cycle 3 P1408 and Cycle 4 P1604. The horizontal gray line inside each set of figures denotes the remnant mixed layer depth.*

3.2. Dual Isotope Nitrification Model

The dual isotopes of nitrate, $\delta^{15}N_{NO3}$ and $\delta^{18}O_{NO3}$, can be used to examine nitrogen transformations [*Sigman et al.*, 2010; *Casciotti*, 2016]. In particular, the variability of these isotopic signatures with respect to an established source signature can be used to identify upper ocean N transformation processes such as nitrification. This deviation in isotope signatures can be expressed as Δ(15,18) above a reference depth, where Δ(15,18) is calculated as:

$$\Delta(15{,}18) = \left(\delta^{15}N_{NO3\_measured} - \delta^{15}N_{NO3\_source}\right) - \left(\frac{^{15}\varepsilon_p}{^{18}\varepsilon_p}\right) * \left(\delta^{18}O_{NO3\_measured} - \delta^{18}O_{NO3\_source}\right) \tag{1}$$

where $\delta^{15}N_{NO3}$ and $\delta^{18}O_{NO3}$ are the stable isotope compositions of N and O in nitrate, respectively. Source $\delta^{15}N_{NO3}$ and $\delta^{18}O_{NO3}$ values are assigned to the remnant mixed layer reference depth for each profile (as described in the following paragraph), and $^{15}\varepsilon_p$ and $^{18}\varepsilon_p$ are the fractionation factors associated with NO_3^- assimilation by phytoplankton.

Wintertime mixing of the water column resets vertical physical characteristics, but seasonal warming leads to a surface mixed layer that isolates the winter mixed layer from the atmosphere. This feature has been referred to as the remnant mixed layer and is present across the central and eastern North Pacific [*Cole et al.*, 2010; *Todd et al.*, 2012]. Inside the CCE these waters are typically of northern origin associated with Pacific Subarctic waters [*Todd et al.*, 2012]. The vertical structure of the remnant mixed layer can be identified using changes in surface salinity [*Cole et al.*, 2010], and the base of the remnant mixed layer depth was identified here using departures from surface salinity exceeding 0.03 units per meter (Figure S3.4). The vertical mixing between the remnant mixed layer and depths below it are likely reduced (e.g., [*Todd et al.*, 2012]). Therefore, the influence of NO_3^- and its isotopes in waters below the remnant mixed layer exert only minimal influence on nitrate in the seasonal mixed layer. The $\delta^{15}N_{NO3}$ and $\delta^{18}O_{NO3}$ at the remnant mixed layer depth (or slightly below this depth if no samples were collected there) are taken to be the upwelling "source" signature. A similar argument was made based on wintertime resetting to identify the source nitrate isotope signature in the Subantarctic Zone [*DiFiore et al.*, 2006].

Incubation studies with phytoplankton have found values of $^{15}\varepsilon_p$:$^{18}\varepsilon_p$ very close to 1.0 [*Granger et al.*, 2004, 2010]. Phytoplankton exhibiting this behavior included *Thalassiosira* sp., *Emiliana huxleyi, Psuedo-nitzschia hemii, Phaeodactylum tricornutum,* and two *Synechococcus* species. If $^{15}\varepsilon_p/^{18}\varepsilon_p$ ~ 1.0 then according to Eq (1) partial nitrate assimilation would produce $\delta^{15}N_{NO3}$ and $\delta^{18}O_{NO3}$ values that fall along a 1:1 line in a plot of $\delta^{15}N_{NO3}$ versus $\delta^{18}O_{NO3}$, and $\Delta(15,18)$ would ~ 0.0 [*Sigman et al*., 2005]. Any deviation of $\Delta(15,18)$ from 0.0 would indicate either unexpected assimilation $^{15}\varepsilon_p/^{18}\varepsilon_p$ or other N cycle processes occurring in the euphotic zone. Data in the current study were located within the depths of detected Chl-*a* (above the grey line in Figures 3.2 and 3.3) given the focus here on estimating contributions of euphotic zone-based nitrification.

During nitrification, $\delta^{15}N_{NO3}$ and $\delta^{18}O_{NO3}$ do not shift proportionally in the same direction as they typically do during nitrate assimilation. In fact, $\delta^{18}O_{NO3}$ becomes enriched relative $\delta^{15}N_{NO3}$ due to the incorporation of ^{18}O into the nitrate reservoir during nitrification (e.g., [*Wankel et al.*, 2007]), and such a positive excursion was observed in the $\delta^{18}O_{NO3}$ over the 1:1 line here (Figure S3.5). In contrast, if ammonia and nitrite accumulate during nitrification then a slight depletion is expected for $\delta^{15}N_{NO3}$ (a combined isotope effect of +22‰ for ammonia oxidation and -9 to -20‰ for nitrite oxidation; [*Buchwald* and *Casciotti*, 2010; *Santoro* and *Casciotti*, 2011], respectively). Thus, negative values are expected for $\Delta(15,18)$ when nitrification contributes to nitrate in the euphotic zone, and they were generally observed for most cycles (Figure 3.3).

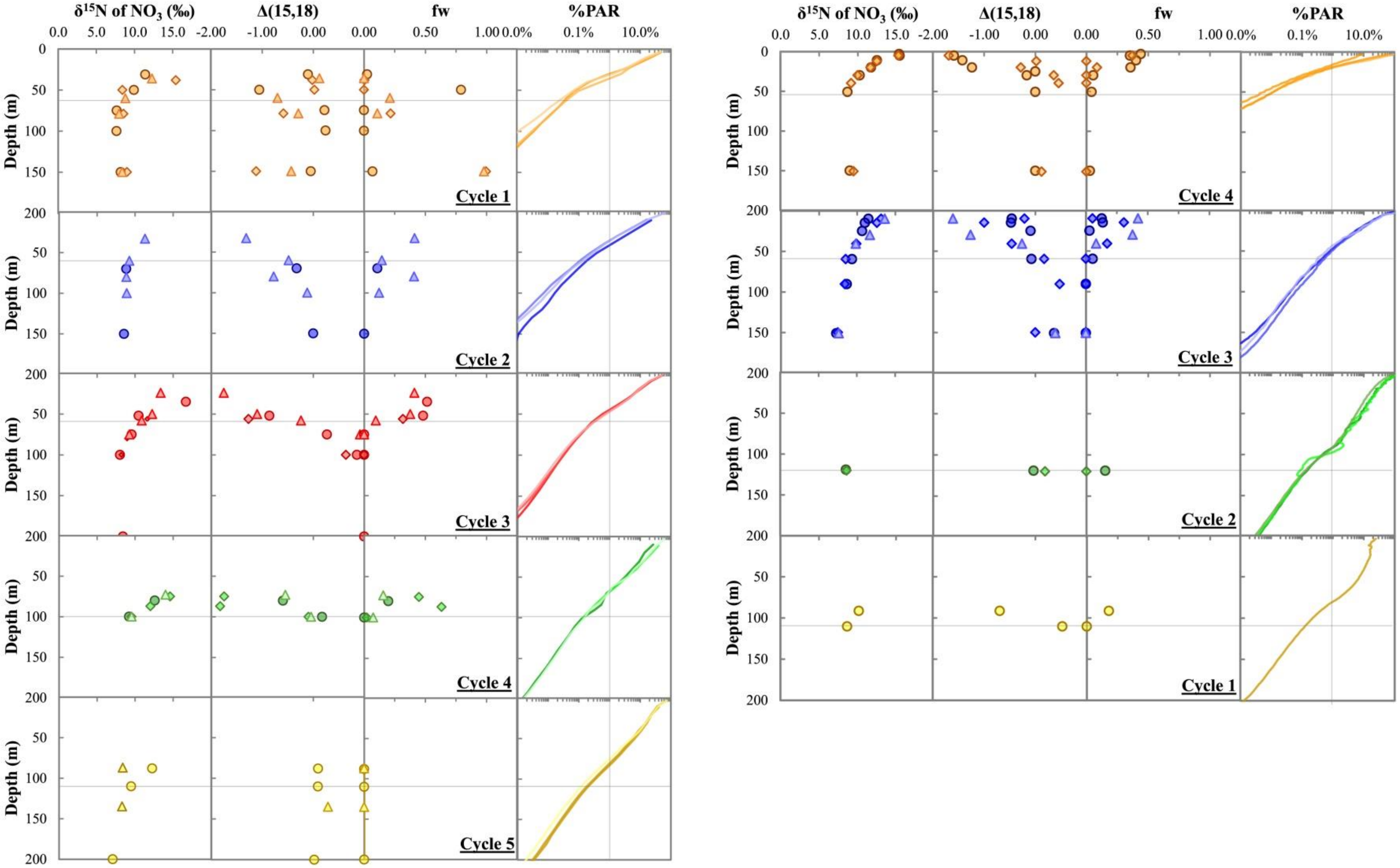

Figure 3.3. *Profiles of P1408 (left) and P1604 (right)* $\delta^{15}N_{NO3}$, *Δ(15,18)*, f_w *(or the contribution of nitrification to nitrate uptake), and % surface PAR. Legends and the horizontal gray lines are the same as for Figure 3.2. The vertical gray line in the %PAR figures represents the 1% light level. Model parameters used to estimate* f_w *in this figure represented a range of tested parameters* as *can be found in Table 3.1.*

Nitrate $\delta^{15}N_{NO3}$ became enriched as NO_3^- decreased for CCE cruises P1408 and P1604 throughout the region. In addition, an increasingly negative Δ(15,18) was calculated (Figure 3.3). Together these trends indicated that euphotic zone nitrate was being influenced both by partial nitrate assimilation and nitrification [*Sigman et al.*, 2010; *Casciotti*, 2016]. Negative Δ(15,18) values were more prominent during Inshore Cycles and indicated that nitrification contributed strongly to N cycle processes in the euphotic zone at these locations. The coarser sampling in offshore Cycles may have masked isotopic deviations associated with euphotic zone nitrification at those locations.

The values of Δ(15,18) calculated in Eq (1) can then be used to estimate the contribution of euphotic zone nitrification to nitrate uptake. Proportional contributions of EZ nitrification to nitrate are estimated by modeling Δ(15,18) in:

$$\begin{gathered}\Delta(15{,}18) = \\ f_n * \left(\varepsilon_p - f_a * f_w * (\varepsilon_{ntr} - \varepsilon_a)\right) - \\ \left(\frac{\delta^{18}O_{source} - \delta^{18}O_{source} * f_w + (\varepsilon_p * f_n) + (\delta^{18}O_{ntr} * f_n * f_w)}{1 - f_w + (f_n * f_w)}\right) + \delta^{18}O_{source},\end{gathered} \tag{2}$$

where f_n is the fraction of NO_3^- remaining relative to the source NO_3^-, ε_p is the fractionation factor for phytoplankton uptake of nitrate, f_a is the fraction of ammonia assimilated by phytoplankton, f_w is the fraction of assimilated nitrate contributed by euphotic zone nitrification, ε_{ntr} is the net isotope effect of ammonia and nitrite oxidation, ε_a is the isotope effect of ammonia assimilation, and $\delta^{18}O_{ntr}$ is the $\delta^{18}O$ resulting from nitrification.

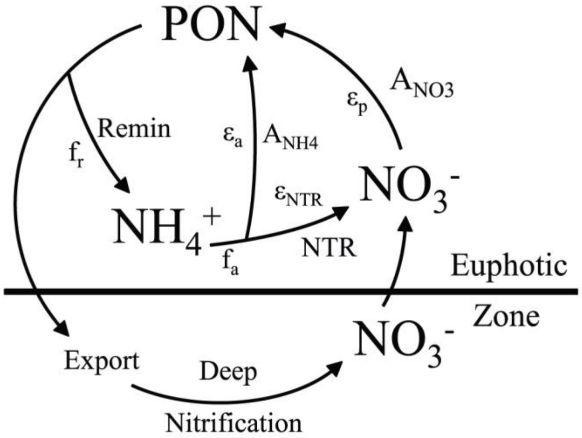

Figure 3.4. *Processes included in the euphotic zone-based nitrification model in Eq (2), after* [*Wankel et al.*, 2007]. *The concentration and isotope signature of nitrate (NO_3^-) in the euphotic zone can be influenced by assimilation (A_{NO3}) into biomass (PON) with isotope effect ε_p. As it is assimilated, this nitrate becomes isotopically enriched relative to the source nitrate associated with the base of the euphotic zone (remnant mixed layer). NO_3^- can also be generated from ammonium (NH_4^+) via nitrification (NTR) with isotope effect ε_{NTR}. NH_4^+ is derived from secondary production (e.g., remineralization, 'Remin'), and some fraction (f_a) is assimilated into PON (A_{NH4}) with isotope effect (ε_a) while the remainder is nitrified. PON not remineralized is assumed to be exported out of the euphotic zone, and ammonia generated from its degradation will contribute to nitrification in the dark ocean.*

In the model presented in Eq (2), the parameters (ε_{ntr}, f_a, etc.) are held constant and the f_w (% of assimilated nitrate derived from nitrifcation) values are adjusted using a solver-based approach to minimize the difference between Δ(15,18) estimated from Eq (1) and Δ(15,18) calculated from Eq (2). Profiles in Figure 3.3 showed that more negative Δ(15,18) values were associated with greater f_w values. As discussed in [*Wankel et al.*, 2007], the model is sensitive to the values used for both $\delta^{18}O_{NO3}$ resulting from nitrification ($\delta^{18}O_{ntr}$) and the fraction of ammonia directly assimilated by microbes (f_a). It is also particularly sensitive to the difference between fractionation factors associated with ammonia assimilation and nitrification (ε_{ntr} - ε_a) (and not to the absolute values).

Table 3.1. *Tested nitrification model parameters and associated references.*

Model Parameter	**Range Tested**	**Values Observed**	**Reference**
ε_a *(Isotope effect of* NH_4^+ *assimilation)*	*+4 to +8‰*	*+9.1‰* *+7.2±0.8‰* *+7.5±2.5‰*	[*Cifuentes et al.*, 1989] [*Montoya et al.*, 1991] [*Pennock et al.*, 1996]
ε_{ntr} *(Isotope effect of nitrification)*	*+14 to +24‰*	 *+22±5‰* *+26±12‰* *+15±2.5‰* *+20±5‰*	*Archaeal Ammonia Oxidation:* [*Santoro* and *Casciotti*, 2011] *Bacterial Ammonia Oxidation:* [*Casciotti et al.*, 2003] [*Horrigan et al.*, 1990] [*Miyake* and *Wada*, 1971]
		 -12.8‰ *-9±2‰* *-20±3‰*	*Nitrite Oxidation:* *Nitrococcus m.* [*Casciotti*, 2009] *Nitrospira m.* [*Buchwald* and *Casciotti*, 2010] *Nitrococcus m. and Nitrobacter sp.*[*Buchwald* and *Casciotti*, 2010]
		 +20±5‰ *+16‰*	*Net Nitrification:* *Coastal water column* [*Sugimoto et al.*, 2009] *Nitrification model optimized* [*Wankel et al.*, 2007]
f_a *(fract.* NH_4^+ *assim. by phyto.)*	*0.50 to 0.95*	*0.73±0.06*	[*Ward*, 2005]
$\delta^{18}O_{ntr}$ *(*^{18}O *in* NO_3^- *by nitrification)*	*0 to +2‰*	*0±1‰* *+1±1‰*	*Co-cultures of Nitrosomonas sp., Nitrococcus m. and AOA (CN25):* [*Buchwald et al.*, 2012] *Natural communities of Woods Hole, Costa Rica Dome, and Eastern Tropical South Pacific:*[*Buchwald et al.*, 2012]
f_n *(fract.* $[NO_3^-]$ *remaining)*	*Profile-based*	-	
$\delta^{18}O_{source}$ *(Source* ^{18}O*)*	*Profile-based*	-	
ε_p *(*NO_3 *Uptake)*	*Profile-based*	-	*(based on Rayleigh model fit of* $\delta^{15}NO_3$ *vs.* f_n*)*
f_w	*Solved for*	-	

Model parameters in Eq (2) were previously optimized for the central California Current in [*Wankel et al.*, 2007] using an iterative approach by testing the range of known (and unknown but potential) values. A similar approach is adopted here for the CCE region. All of the parameters that were tested are listed in Table 3.1, and the median of these tested values was used to estimate f_w in Figure 3.3.

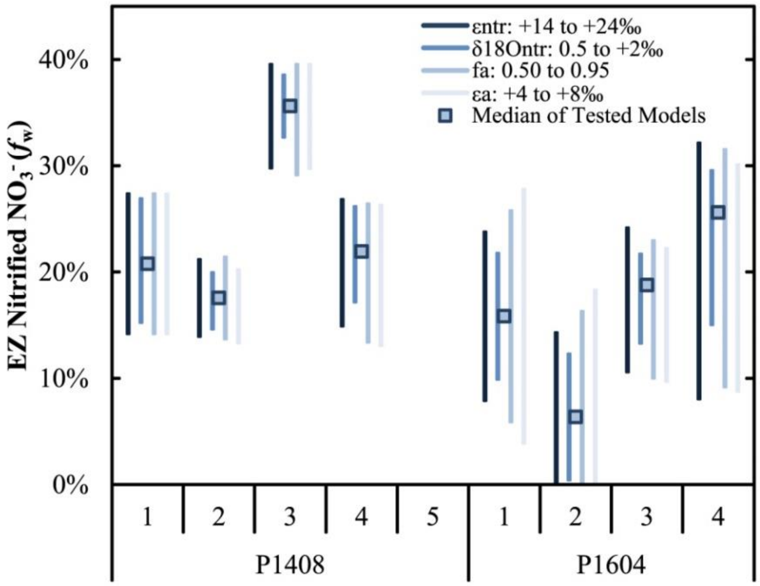

Figure 3.5. M*odel parameters were tested by comparing integrated % nitrification, where the square symbol represents* f_w *derived from using the median values of all tested parameters (n = 26 model variations). The length of the line extends from the 25th to the 75th percentile value for each tested parameter (n = 6 models tested for most parameters).*

Median f_w values for the euphotic zone varied from 6% to 36% with most Cycles falling between 15 - 23% (Figure 3.5 and Table 3.2). The range of these f_w values for the CCE is similar to that reported for Monterey Bay, where average f_w values between 15 - 27% were reported [*Wankel et al.*, 2007]. Such correspondence is not surprising given that the ranges of tested parameters and observed Δ(15,18) values were relatively similar between these sites. Across the Cycles, the 25th and 75th percentile values for f_w were on average 6 - 8% away from the median (n=26 tested model variations). Even after accounting for the significant range among tested model parameters, f_w values for P1408

Cycle 3 and P1604 Cycle 4 (or 2) were significantly greater (or less) (Mann-Whitney, $p<0.01$) than values for all other Cycles.

Nitrification most likely proceeds as a two-step process from ammonia oxidation to nitrite and nitrite oxidation to nitrate [*Ward*, 2008]. Archaeal ammonia oxidation (AOA) is widespread and the isotope effect for AOA in the California Current has been estimated to be +22 ± 5‰ [*Santoro* and *Casciotti*, 2011]. The second step is carried out by nitrite oxidizing bacteria (NOB), and cultured NOB and field populations have isotope effects between -9 ± 2‰ and -20 ± 3 [*Buchwald* and *Casciotti*, 2010]. The combined net isotope effect could be between +2 to +22‰; however, any $\varepsilon_{ntr} < +14$‰ resulted in no model solutions. An $\varepsilon_{ntr} < +14$‰ is only possible if $\varepsilon_a < +1$‰. However, empirical determinations of ε_a have indicated preferential uptake of the lighter ammonium isotope, with $\varepsilon_a > +6$‰ (e.g., [*Montoya et al.*, 1991]). This indicates that model solutions with $\varepsilon_{ntr} > +14$‰ are more likely, which is more in line with field studies of [*Sugimoto et al.*, 2009] (+20 ± 5‰) and the optimized values in the model of [*Wankel et al.*, 2007] (+19‰). Additionally, though not included in Figure 3.5, varying the isotope effect of nitrate uptake (ε_p) had little effect on f_w. For example, a typical open ocean ε_p of 5‰ [*Sigman et al.*, 1999; *Altabet*, 2001] instead of ~ 3‰, decreased median euphotic zone f_w by 2%, on average.

Table 3.2. *Summary of parameters used to estimate nitrification contribution to euphotic zone nitrate (f_w).*

Cruise	Cycle	Remnant Mixed Layer Depth (m)	$[NO_3^-]$ source (µM)	$\delta^{18}O$ NO_3 source (‰)	ε_p (‰)	f_w (Euphotic Zone Integrated)
P1408	*1*	*60*	*17.6±1.7*	*4.3*	*3.20*	*21%*
	2	*60*	*14.1±2.2*	*5.1*	*3.20*	*18%*
	3	*60*	*10.0±1.8*	*5.5*	*3.75*	*36%*
	4	*100*	*8.5±2.0*	*5.3*	*3.50*	*22%*
	5	*115*	*10.1±1.2*	*5.2*	*2.50*	-
P1604	*1*	*110*	*12.7±3.1*	*4.0*	*1.50*	*16%*
	2	*120*	*12.9±3.9*	*4.4*	*1.50*	*6%*
	3	*55*	*12.9±1.5*	*4.7*	*3.00*	*19%*
	4	*50*	*23.5±2.7*	*4.9*	*2.75*	*26%*

4. Discussion

Aerobic nitrification is an essential process in the oxidation of inorganic nutrients to nitrate. Many studies have shown that nitrification can be restricted to regions in the water column with low light levels [*Ward et al.*, 1984; *Ward*, 1985]. However, ammonia oxidation (considered the rate limiting step in nitrification) has been detected in the euphotic zone extending up to surface depths [*Ward*, 2005, 2008; *Smith et al.*, 2016]. The location of nitrification is particularly relevant to evaluating the role of "new" versus "recycled" nitrate in supporting primary production and examining the *f-ratio* (e.g., [*Dugdale* and *Goering*, 1967; *Eppley* and *Peterson*, 1979]). This study attempted to provide quantitative and qualitative bounds on the fraction of nitrate assimilation that was provided by euphotic zone nitrification in the CCE. The dataset discussed here was collected during two anomalously warm years in the eastern North Pacific Ocean, and so, to make these findings more relevant, they were placed in the context of the more extensive CalCOFI program, which has routinely surveyed nutrient dynamics in this region since the mid-1980s.

4.1. Nitrification Rates

The dual isotope method estimated that nitrification contributed a median of 6% to 36% (Figure 3.5 and Table 3.2) of total NO_3^- assimilated in the euphotic zone. This value refers only to the proportion of assimilated NO_3^- contributed by nitrification and provides no information on rates and magnitudes of nitrification. However, if nitrate uptake rates are known then nitrification rates can be inferred by multiplying the nitrate uptake rate by the f_w parameter (Table 3.3).

Two estimates of nitrate "assimilation" rates are presented here. The first is a traditional estimate, where the incorporation rate of $^{15}N_{NO3}$ into suspended particles (i.e., phytoplankton) was determined, after incubating unfiltered seawater spiked with ^{15}N-labelled NO_3^-, at ambient light and temperature levels in an *in-situ* array (e.g., [*Landry* et al., 2009], specific methods and data available at http://cce.lternet.edu/data). However, direct uptake measurements were only available for P1604. Therefore, a second method based on depth profiles of NO_3^- was also developed (similar in form to that presented in the dissertation author's Chapter II).

In the second method, NO_3^- supplied to the euphotic zone (source nitrate) was represented by the remnant mixed layer NO_3^- (the N and O isotope signatures of this "source" reservoir were used in Eq (1) and Eq (2)). Mean euphotic zone nitrate was then subtracted from this source concentration to determine the amount of nitrate utilized at each location. In order to convert this utilized NO_3^- into a rate, we assume that nitrate was assimilated by euphotic zone organisms at the same rate as it is supplied by vertical advection from the remnant mixed layer. This assumption was evaluated in the dissertation author's Chapter II where nitrate-based production rates by this method resulted in reasonable values when concurrent estimates of net primary production were used to compute *f*-ratios. Nitrate supply was based on model-derived vertical advection rates (*w*) as obtained from the California State Estimate (available at http://sose.ucsd.edu/CASE/). Advection rates were averaged over ±10 m surrounding the source depth, and ±10 d and ±20 km within sampling time and location, respectively.

The $^{15}N_{NO3}$-labelled incubation experiments likely captured the instantaneous nitrate assimilation rate whereas the euphotic zone NO_3^- deficit method captured a longer time window. During P1604, the NO_3^- deficit approach could not be applied at two of the four Cycles because values for *w* at these two sites were negative, which implied that no new NO_3^- was transported by vertical advection into the surface at that time. As a result, both estimates of nitrate assimilation were only available at two Cycles of P1604 (Cycles 3 & 4), and there was little agreement between methods (Table 3.3). The disagreement is not unexpected given the possible difference in timescale between methods (instantaneous versus integrated over longer timescales); however, the dataset is too small for a more meaningful comparison of these methods here.

Table 3.3. *Integrated nitrate uptake estimates that were used to convert f_w into euphotic zone nitrification rates. Nitrification rates were estimated by multiplying the fraction of nitrate uptake derived from nitrification (f_w) by nitrate uptake rates. Vertical velocities (w) were determined based on the California State Estimate for ±10m around the source depth for ±10 days surrounding Cycle locations. Standard deviations for these values were calculated based on this temporal and spatial variability. Standard deviations for other terms represent ±1σ over the 2 - 4 days of each cycle. If w exhibited negative values (downwelling conditions) then nitrification rates were not estimated from the transport-based method.*

Cruise	Cycle	Remnant MLD	$[NO_3^-]$ at Remnant MLD	$[NO_3^-]$ Surface Avg	*w* at Remnant MLD	$^{15}NO_3$ Uptake Rate (1)	*w*-NO_3 Uptake Rate (2)	Integ EZ Nitrif Rate (1)	Integ EZ Nitrif Rate (2)
		(m)	(μM)		(m d^{-1})	(mmol N m^{-2} d^{-1})			
P1408	1	*60*	*17.6±1.7*	*4.8±0.9*	*0.18±0.05*	-	*2.2±0.2*	-	*0.47±0.15*
	2	*60*	*14.1±2.2*	*3.8±2.0*	*0.18±0.18*	-	*1.9±0.2*	-	*0.33±0.05*
	3	*60*	*10.0±1.8*	*3.3±0.7*	*0.39±0.02*	-	*2.6±0.6*	-	*0.93±0.10*
	4	*100*	*8.5±2.0*	*1.8±0.5*	*0.31±0.13*	-	*2.1±0.5*	-	*0.46±0.10*
	5	*115*	*10.1±1.2*	*1.8±0.6*	*0.29±0.02*	-	*2.4±0.2*	-	-
P1604	1	*110*	*12.7±3.1*	*3.6±0.9*	*-0.34±0.13*	*1.3±0.0*	-	*0.21±0.04*	-
	2	*120*	*12.9±3.9*	*2.7±1.1*	*-0.06±0.06*	*1.9±1.0*	-	*0.12±0.06*	-
	3	*55*	*12.9±1.5*	*6.7±1.2*	*0.30±0.11*	*5.4±2.9*	*1.8±0.3*	*1.02±0.35*	*0.34±0.12*
	4	*50*	*23.5±2.7*	*9.6±1.8*	*0.58±0.10*	*3.6±1.0*	*8.1±0.7*	*0.93±0.43*	*2.07±0.95*

Depth-integrated assimilation rates that were estimated by the [NO_3^-] deficit method ranged from 1.8 to 8.1 mmol N m^{-2} d^{-1}, whereas results from the $^{15}N_{NO3}$ uptake experiments were between 1.3 and 5.4 mmol N m^{-2} d^{-1} (Table 3.3). Multiplying median f_w values (Table 3.2) by these nitrate assimilation rates resulted in integrated euphotic zone nitrification rates of 0.1 to 2.0 ± 0.95 mmol N m^{-2} d^{-1} (Table 3.3). Integrated nitrification rate estimates are in the range of integrated ammonia oxidation rates of 1.1 to 3.4 mmol N m^{-2} d^{-1} previously reported for the CCE and central California Current region by [*Ward et al.*, 1982; *Ward*, 1987; *Santoro et al.*, 2010; *Smith et al.*, 2016].

4.2. Vertical Profiles of Nitrification

The previous discussion compared nitrification rates that were integrated over the euphotic zone, where the bottom of the euphotic zone was defined as the depth of the remnant mixed layer [*Cole et al.*, 2010; *Todd et al.*, 2012]. However, the vertical distribution of nitrification can also be informative. Estimated rates of nitrification in the California Current region tend to be close to the detection limit at the surface (~0 m), increase with depth to peak near the primary nitrite maximum (often positioned at the base of the euphotic zone) and then decrease into the mesopelagic [*Ward et al.*, 1982; *Santoro et al.*, 2010; *Smith et al.*, 2016]. Yet, in the northern CCE, appreciable nitrification rates (1 - 20 nmol N L^{-1} d^{-1}) have been reported at light levels nearing 100% of photosynthetically active radiation [*Ward*, 2005, 2008; *Smith et al.*, 2016]. The vertical distribution of nitrification rate often mirrors the distribution of AOA and NOB [*Santoro et al.*, 2010], but some studies have reported a vertical offset between the peak abundance of nitrifier genes and the rate of nitrification [Smith *et al.*, 2016]. Nitrifiers can also outcompete phytoplankton for ammonia and nitrite at surface depths during twilight hours when photosynthetic activity is reduced [*Smith et al.*, 2014a]. Taken together, these studies indicate that active populations of nitrifiers exist throughout the euphotic zone even though the majority of existing data point to a fairly consistent pattern of peak nitrification rates at depths near the base of the euphotic zone. In this study, the dual isotope model indicated that nitrification contributed to assimilated NO_3^- throughout the euphotic zone and extended into surface water during two cycles in 2016 (P1604 Cycles 3 and 4; Figure 3.3).

4.2.1. Ammonia Oxidizing Microorganisms and Associated Genes

During P1604, RNA and DNA samples were available to examine the vertical distribution of nitrifiers (as AOA and NOB) and the expression of the gene encoding for subunit A of the ammonia monooxygenase enzyme (*amo*A). The abundance of AOA and NOB for Cycles 3 and 4 increased with depth (Figure 3.6). At P1604 Cycle 3 both AOA and NOB peaked at 80 m, which is about 30 m below the remnant mixed layer depth. The vertical distribution of AOA and NOB did not match that of f_w. Similar to other studies [*Santoro et al.*, 2010; *Smith et al.*, 2016], the subsurface peak in abundance was more similar to the vertical distribution of nitrite, but even in this case, the depths of each peak were not correlated.

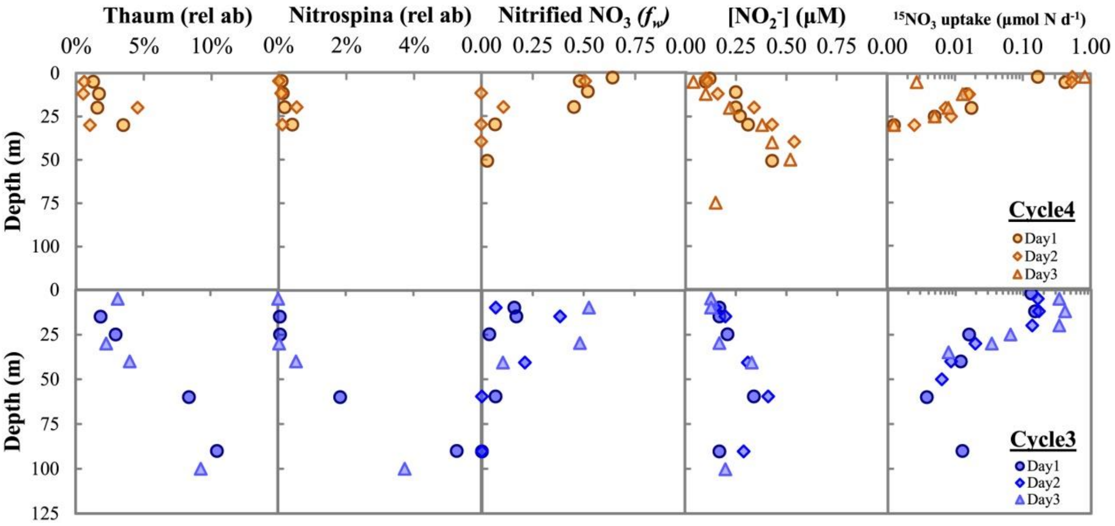

Figure 3.6. *Vertical profiles of the 16s rRNA gene abundances of ammonia oxidizing archaea (AOA) and nitrite oxidizing bacteria (NOB) at P1604 inshore cycles.*

Previous work in the central California Current region found that depth profiles of archaeal *amo*A gene expression and rates of ammonia oxidation were offset, where nitrification rates peaked ~90 m above the maximum peak in *amo*A gene expression [*Smith et al.*, 2016]. The shallower f_w peak found for this study (Figure 3.6) may reflect similar offsets between nitrification rates and gene abundance [*Smith et al.*, 2016]. However, the isotope approach may not actually reflect instantaneous nitrification activity (whereas gene expression should track active populations). Unfortunately, *in-situ* nitrification rates were not available from CCE cruises to test this correspondence. Thus, it cannot be ruled out that the observed negative departures in Δ(15,18) within the surface ocean were caused by processes other than local nitrification (e.g., [*Wankel et al.*, 2007]).

In the CCE region, negative departures in Δ(15,18) could be a result of deeper nitrification, but the isotopic signature of this nitrification is detected in surface waters once it gets mixed upward via vertical advection, [*Fripiat et al.*, 2015]. For instance, an isotope model for the Southern Ocean demonstrated that vertical advection left a detectable imprint of nitrification on the nitrate isotope reservoir in a region where wind-driven mixing brought nitrified waters from just below the euphotic zone up to surface depths [*Fripiat et al.*, 2015]. Also, a limited number of heterotrophic bacteria have been shown to produce negative Δ(15,18) values during nitrate uptake in culture studies [*Granger et al.*, 2010].

4.2.2. Physical Transport

To examine the role of mixing in structuring the vertical distribution of f_w, a simple three-box model was constructed for cycles of P1604 where both gene abundance data and Δ(15,18) data were available. Three light levels were used: (1) surface to 5% PAR, (2) 5% to 1% PAR and (3) 1% PAR to the remnant mixed layer depth. The model assumed that lateral mixing (e.g., salt fingering described in [*Todd et al.*, 2012] for the CCE) was minimal and that any departures in the Δ(15,18) signature were either from local nitrification or vertical transport of the nitrification signal into shallower depth. In other words, nitrification contributions estimated by f_w for the CCE are assumed to be unaffected by lateral inputs of nitrate.

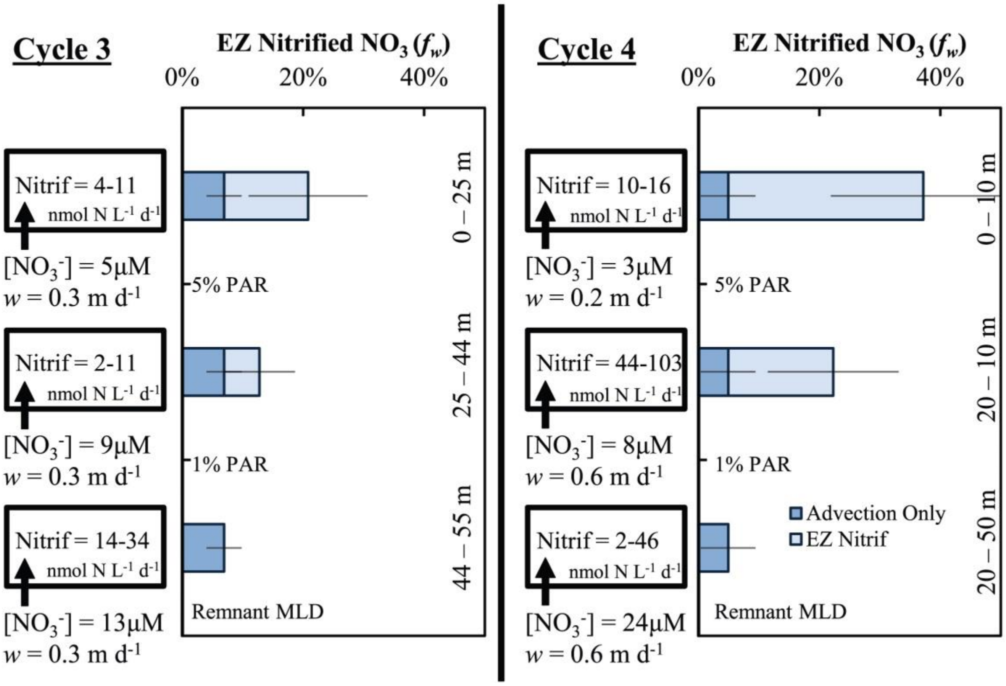

Figure 3.7. *The relative contribution of (1) the nitrification signal transported from the remnant mixed layer depth (MLD) by advection (dark blue bars) and (2) local nitrification (light blue bars), to f_w determined for P1604 Cycles 3 and 4 from Equation (2). Nitrification rates are presented within the boxes to the left of each chart and were estimated based on multiplying f_w values by vertical nitrate transport (from w and nitrate concentration data) into the boxes. Because the source nitrate for the f_w-based approach is at the remnant mixed layer depth, typically located above the 0.1% PAR level (Figures 3.2 and 3.3), any f_w observed above this would be associated with local nitrification.*

The first vertical trend that must be acknowledged in this context is that f_w estimated using the dual isotope model (e.g., Figure 3.3), is significantly lower ($p<0.01$, Mann Whitney) in the remnant mixed layer box than it is in the surface box (blue bar Figure 3.7). This shows that a greater proportion of NO_3^- utilized by phytoplankton in the surface box is derived from nitrification than can be explained by vertical supply alone. Since nitrified nitrate is neither preferentially transported nor discriminated against during nitrate uptake by phytoplankton, the calculated increase in f_w with increasing light level must be a result of local (i.e., above the remnant mixed layer) nitrification and simple vertical mixing alone cannot explain the observed trend. The three-box model in Figure 3.7 was thus used to estimate rates of local nitrification necessary to reproduce the observed trend in f_w. The model recreated each f_w profile using a combination of advection of nitrified nitrate from the remnant mixed layer box (light blue bars in Figure 3.7) and local nitrification within each box (darker blue bars, Figure 3.7). Nitrification rates in each box encompassed the range of published rates for the central California Current for similar light regimes [*Ward et al.*, 1982; *Santoro et al.*, 2010; *Smith et al.*, 2014a, 2016].

The observed increase of f_w up toward the surface is linked to locally nitrified nitrate in the model. To account for these processes, % nitrified nitrate (f_w) was first converted into nitrification rates by multiplying the f_w values by nitrate transport (vertical velocities were obtained from the CASE model as described earlier; relevant nitrate concentrations were directly measured). However, the nitrification contribution (f_w) that was transported by advection from the boxes immediately below the 1 to 5% PAR and 5% PAR to 0 m boxes was subtracted from the f_w within that box prior to estimating the nitrification rate. For example, for the 1 - 5% PAR box for P1604 Cycle 3, 9 µM of NO_3^- was transported into the box at a rate of 0.3 m d^{-1} resulting in 2.6 mmol NO_3^- m^{-2} d^{-1} by vertical advection (Figure 3.7). If no nitrification was taking place in this box the f_w should remain at 7 ± 2%, which is the f_w for the box below (remnant mixed layer depth). But f_w was estimated to be 13 ± 7% for this 1 - 5% PAR box, which would require a local nitrification rate of 2 - 11 nmol L^{-1} d^{-1} (or 0.04 - 0.24 mmol N m^{-2} d^{-1} when integrated over 25 to 44m depths). This would then indicate that 46 ± 6% of the $\Delta(15,18)$-based f_w within this box (i.e., ~6% of 13 ± 7%) was derived from local nitrification processes.

Overall, for P1604 Cycles 3 and 4, vertical advection of nitrified water from the lower part of the euphotic zone (~from the remnant mixed layer depth up to the 1% PAR level) was responsible for just over half of the surface nitrified nitrate. The low range of nitrification rates observed here for the surface-most boxes (2 - 16 nmol N L^{-1} d^{-1}; Figure 3.7) are also consistent with those reported for the central California Current from similar light levels of surface to 1% PAR depths (15 - 30 nmol N L^{-1} d^{-1}) [*Ward*, 2005].

4.3. Modeled Organic Matter Export

In addition to estimating nitrification contributions in the surface ocean, the nitrification model developed in [*Wankel et al.*, 2007] can be used to estimate the isotopic composition of exported PON. This was estimated from a derivation of Eq (2) above (see Text S1 for derivation):

$$\delta^{15}N_{PON\_export} = \delta^{15}N_{NO3\_surface} - \varepsilon_p + f_w * (\varepsilon_{ntr} - \varepsilon_{cons}), \tag{3}$$

where $\delta^{15}N_{PON\_export}$ is the stable isotope of organic nitrogen exported locally from the surface box, $\delta^{15}N_{NO3\_surface}$ is the mean surface mixed layer $\delta^{15}N_{NO3}$, ε_{cons} is the net isotope effect of ammonia oxidation (ε_{ntr}) and assimilation (ε_a) based on the proportion of ammonia assimilated by phytoplankton (f_a), and f_w is the fraction of assimilated nitrate that is derived from euphotic zone nitrification (from Table 3.2). When an independent measure of $\delta^{15}N_{PON\_export}$ is available, measured values and values calculated using Eq (3) can be used to confirm the validity of f_w. Measured $\delta^{15}N$ PON values were determined on $\delta^{15}N_{Sinking\ PON}$ collected in drifting sediment trap arrays (at 100m) and on median suspended PON ($\delta^{15}N_{\text{Suspended PON}}$) for depths over the surface remnant mixed layer (Table 3.4).

Table 3.4. *The isotope composition of* $\delta^{15}N_{PON}$ *exported from the surface ocean as calculated from Eq (3). The* $\delta^{15}N_{NO3}$ *and* $\delta^{15}N_{susp}$ *represent median measured values from the surface to the remnant mixed layer, and* $\delta^{15}N_{sink}$ *was measured on material collected at 100 m from a drifting sediment trap array. The Δ(15,18)-predicted* f_w *can also be found in Table 3.2 and represents the surface median estimate from Eq (2).*

Cruise	Cycle	$\delta^{15}NO_3$ EZ to Rem MLD (‰)	$\delta^{15}N$ Susp PON EZ to Rem MLD (‰)	$\delta^{15}N$ Sink PON at 100m (‰)	Δ(15,18) predicted f_w	$\delta^{15}N$ of Modeled Export (‰)
P1408	**1**	*10.6±1.9*	*6.5±1.0*	*8.9±0.2*	*21%*	*8.7±0.1*
	2	*10.7±1.8*	*8.7±0.6*	*10.2±0.6*	*18%*	*8.5±0.2*
	3	*11.7±1.2*	*8.3±0.5*	*10.6±0.7*	*36%*	*10.0±0.4*
	4	*10.8±0.3*	*7.1±0.6*	*9.6±0.8*	*22%*	*8.6±0.2*
	5	*11.9±1.0*	*6.5±0.4*	*9.6±0.3*	-	-
P1604	**1**	*10.8±0.4*	*5.4±1.2*	*11.0±1.3*	*16%*	*10.2±0.3*
	2	*9.3*	*6.3±0.8*	*9.0±0.6*	*6%*	*8.2±0.4*
	3	*10.9±0.4*	*6.3±1.0*	*8.0±0.6*	*19%*	*9.0±0.4*
	4	*10.0±1.2*	*7.1±0.6*	*8.1±1.2*	*26%*	*8.7±0.5*

The formulation of Eq (3) essentially predicts the net δ15N of PON as autotrophic biomass that utilized a combination of surface ammonium, advected deep nitrate, and surface nitrified nitrate. On average, exported $\delta^{15}N$ of PON predicted from Eq (3) was 9.0 ± 0.7‰ and more closely resembled measured $\delta^{15}N_{\text{Sinking PON}}$, particularly for P1408 Cycle 1 and 3 and P1604 Cycle 3 and 4. Instances where modeled PON export matched sinking PON suggest that contributions from primary producers and associated detritus may have contributed a significant fraction of sinking POM. However, in other cases, the measured values exceeded those predicted by Eq (3) and such a finding would be consistent with $\delta^{15}N_{\text{Sinking PON}}$ being comprised of products from secondary consumers (e.g., fecal pellets; [*Stukel et al.*, 2013]), which are expected to be isotopically enriched [*Mingawa et al.*, 1984; *Wada et al.*, 1987], a process is not accounted for in Eq (3). $\delta^{15}N_{\text{Suspended PON}}$ was most often depleted relative to modeled estimates of exported PON $\delta^{15}N$ in Eq (3) and could be due to other nutrient sources contributing to the $\delta^{15}N_{\text{Suspended PON}}$ not accounted for here (e.g., surface ammonia or interactions with accumulating dissolved organic nitrogen [*Knapp et al.*, 2011]).

4.4. Correlations with Nitrified Nitrate

As discussed previously, integrated contributions of nitrified nitrate in the euphotic zone were significantly ($p<0.01$; Mann-Whitney) greater(less) for P1408 Cycle 3 and P1604 Cycle 4(2). A simple correlation analysis with water column properties found a strong positive correlation ($r^2=0.81$, $p<0.01$) between f_w and NO_2^- at the primary nitrite max depth (Figure 3.8). Prior studies based in the California Current showed that ammonia oxidation rates can be positively correlated with ammonium concentrations (e.g., [*Smith et al.*, 2014a]) but that AOA *amo*A gene expression can also be decoupled in time from inorganic nutrient concentrations (e.g., [*Beman et al.*, 2010]). A better relationship between nitrification contributions and NO_2^- found here is similar to a correlation between NO_2^- and nitrite oxidation found further south in the eastern tropical North Pacific [*Beman et al.*, 2013].

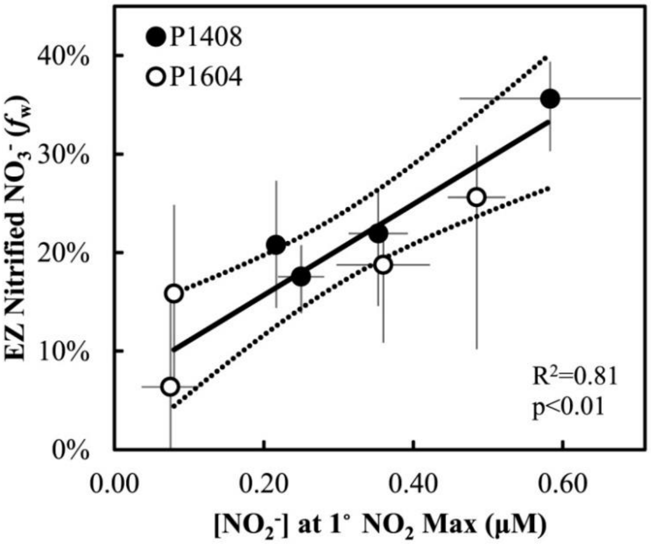

Figure 3.8. *Median euphotic zone (EZ) nitrified* f_w *is positively correlated with* NO_2^- *from the primary nitrite maximum depth. Error bars for* NO_2^- *represent ±1σ across the Cycle days and for* f_w *represent the 25th and 75th quartiles across the days and 26 model variations. The best fit line in bold was calculated using a Type II linear fit and the dotted lines surrounding the best fit line are the ±95% confidence intervals.*

4.4.1. Nitrite in CalCOFI

During P1408 and P1604, the nitrite concentration at the primary nitrite maximum was significantly greater ($p<0.01$, Mann-Whitney) than the long-term seasonal mean for nearby CalCOFI stations (~080.0 55.0 and 080.0 060.0; Figure S3.3). Factors contributing to nitrite accumulation in the surface ocean have been extensively reviewed (e.g., [*Lomas* and *Lipschultz*, 2006]), and there are several, not mutually exclusive, hypotheses for the widespread recurrence of the primary nitrite maximum as a water column feature. The most common explanation for the recurrence of a nitrite maximum near the 0.1% PAR light level is that light inhibition of autotrophs (too little) and nitrite oxidizing bacteria (too much) may lead to nitrite accumulation at this depth [*Lomas* and *Lipschultz*, 2006]. A recent study based in the California Current found that the residence time of nitrite at the nitrite maximum can range widely (8 - 470 d), and the study further noted that nitrite production is primarily from ammonia oxidation rather than nitrite release during assimilatory nitrate reduction by light-limited phytoplankton [*Santoro et al.*, 2013]. Formation of the primary nitrite maximum feature in the Red Sea was also hypothesized to be due to ammonia oxidation, particularly during enhanced stratification [*Meeder et al.*, 2012]. A brief analysis of the Δ(15,18)-based estimates of nitrification (f_w) from a longer-term (2010 - 2013) CalCOFI record found that median nitrification contributions of 12 - 19% to be common. CalCOFI samples collected during the 2015 - 2016 strong El Niño were also slightly elevated in f_w (median of 27%), and suggested that the increase in nitrification during the two warm anomaly CCE cruises reflected anomalous climate conditions during 2014 - 2016.

4.4.2. CalCOFI Nitrite Correlations

The correlation between f_w and NO_2^- could be linked to substrate-limitation of the last step in nitrification. Positive linear correlations between inorganic nutrients and nitrification rates have previously been identified in the central and southern California Current [*Smith et al.*, 2014a]. Processes that influence the buildup of NO_2^- can thus influence f_w, and so, the long-term CalCOFI dataset was used to examine controls on NO_2^- and by extension, f_w. A combination of stepwise linear regression analyses with NO_2^- followed by a multiple linear regression analysis (MLRA) was carried out for long-term data collected from CalCOFI stations (2004 - 2016) close to the inshore CCE Cycles. A stepwise regression of 16 parameters (Table S3.1) isolated four predictors (in order of importance based on Mallows' Cp, Figure S3.1): mean [PON] (0-50m), mean

POC:Chl-a (0 - 50m), mean O_2 saturation (0 - 30m), and the North Pacific Gyre Oscillation (NPGO) index. Of the four parameters, [PON] and POC:Chl-a together accounted for the majority of the linear prediction (an adjusted $R^2 = 24.3\%$ for the two parameters compared to 34.9% by including all four).

A general linear model for CalCOFI stations predicted that $NO_2^- > +1\delta$ above the mean typically occurred during summer months, and elevated NO_2^- was typically associated with either high PON in the Inshore (4 out of 6 Inshore) or high POC:Chl-a in the Midshore (9 out of 12 Midshore; Figure 3.9). Most of the stations with elevated PON were low in POC:Chl-a and vice versa (15 out of the 18 combined Inshore and Midshore stations). This characteristic was also the case for CCE Cycles with elevated NO_2^-, where P1408 Cycle 3 NO_2^- was effectively predicted by high POC:Chl-a (and low [PON]) and P1604 Cycle 4 was predicted by high PON (and low POC:Chl-a; Figure 3.9). Based on these relationships, one hypothesis is that when PON is elevated, the rates of ammonia production and oxidation are enhanced (producing nitrite). When Chl-a is low (i.e., when POC:Chl-a is high), the competition for nitrite from phytoplankton is reduced and NO_2^- can accumulate. Both scenarios allow NO_2^- to accumulate as a substrate for nitrite oxidation. Figure 3.10 presents potential competing pathways influencing NO_2^- accumulation in the CCE.

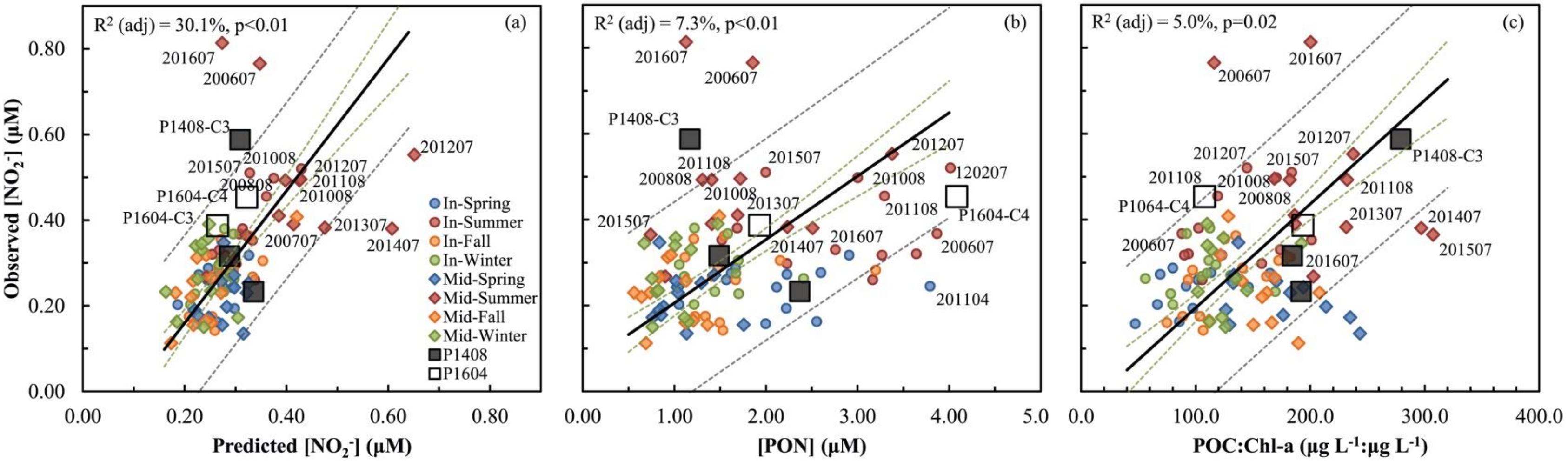

Figure 3.9. *Cube-root transformed NO_2^- at the primary nitrite maximum was predicted using a multiple linear regression analysis of PON, POC:Chl-a, O_2 saturation and the NPGO index (adjusted $R^2=0.301$; $n=94$). The relationship of NO_2^- to [PON] (b) and POC:Chl-a (c) is also shown to highlight conditions leading to elevated [NO_2^-] for CalCOFI stations and CCE Cycles. Data from CalCOFI 2004-2016 Inshore stations ('In'; Lines 076.0 and 080.0 and stations 055.0 and 060.0; circles) and Midshore stations ('Mid'; Lines 076.0 and 080.0 and stations 070.0 and 080.0; diamonds) were included in the analysis. Overlain are mean observed and predicted Inshore CCE cruise Cycles (large squares). A Type II model fit is shown in bold line with the ±95% confidence intervals (dashed green lines nearest the solid line) and ±95% prediction intervals (dashed grey lines furthest from the solid line.*

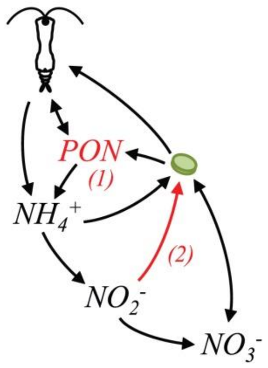

Figure 3.10. *Generalized linear model predicts that nitrite accumulates in the ocean due either to (1) an accumulation of particulate organic nitrogen (PON) supply or (2) reduced nitrite uptake by phytoplankton (where Chl-a is a proxy for phytoplankton abundance).*

A recent study in the central California Current that sampled a range of ecosystems conditions suggested that nitrite release by phytoplankton (via the assimilatory nitrate reductase pathway) is an order of magnitude lower near the primary nitrite max depths [*Santoro et al.*, 2013], and so, this process has relatively little influence on NO_2^- accumulation at the PNM and is not included in Figure 3.10. Reduced competition with phytoplankton for nitrite (i.e., pathway 2) was estimated to be the dominant contributor to nitrification in the central California Current based on concurrent estimates of nitrification rates, community composition data, and hydrography [*Smith et al.*, 2014a]. Increased PON can represent an increased biomass that is ultimately consumed by heterotrophic bacteria, zooplankton or other organisms, producing inorganic nutrients (NH_4^+ and NO_2^-) as byproducts. Based on these two potential pathways, elevated NO_2^- (and therefore contributions of nitrification) for P1604 Cycle 4 are likely due to increased organic supply as inferred by elevated PON (pathway 1 in Figure 3.10) and for P1408 Cycle 3 to be due to reduced competition with phytoplankton as inferred by elevated POC:Chl-a (pathway 2 in Figure 3.10).

The above analysis was limited to CalCOFI cruises between 2004 and 2016 in order to include POM concentration data, but relevant CalCOFI data were also available covering a longer time range (1990 - 2016) and included climate events of similar magnitude to 2014 - 2016 (e.g., 1997 - 1998 El Niño). A stepwise regression analysis for this longer dataset was performed on 13 parameters, identifying six predictors that correlated with NO_2^- (in order of importance): mean O_2 saturation (0-30m), dynamic height, integrated Chl-a (0m to base of euphotic zone), Si* (±10m of primary nitrite max depth), NPGO and Julian day (Table S3.1). The adjusted R^2 from this analysis was only slightly improved (adjusted $R^2 = 36.1\%$; Figure S3.6) relative to the analysis for 2004-2016 above (30.1%). For the 1990 - 2016 analysis, NO_2^- was inversely correlated with dynamic height and integrated chlorophyll and directly correlated with O_2 saturation (Table S3.2). Based on these relationships, increased NO_2^- was associated with either periods of reduced phytoplankton activity or a post-production signature if O_2 saturation is interpreted to lag peak productivity. The best example to support these hypotheses is CalCOFI cruise 201207, where high NO_2^- was associated with high [PON] (Figure 3.9), but also elevated high O_2 saturation, low dynamic height, and low integrated chlorophyll in the longer term model.

Several cruises with elevated NO_2^- cannot be adequately explained by either of the linear regression models presented here, for example, Midshore 200607 and 201607 CalCOFI cruises (Figure 3.9). However, these cruises had significantly elevated Inshore [PON] over the mean (>2.0 μM), and this excess PON could have been transported offshore, contributing to NO_2^- in the Midshore. Some of the most anomalous NO_2^- (i.e.,

> 0.5 μM) also followed strong El Niño events (e.g., CalCOFI cruises 199908 and 201607), where stratification may have contributed to increased nitrification in the water column and reduced competition for nitrite. While other biogeochemically relevant parameters like Si*, an indicator of iron limitation [*King* and *Barbeau*, 2011], moderately contributed to the long-term model (Table S3.2), no clear relationship could be established between nitrite and these parameters.

When observed over climate event scales, smoothed seasonally-corrected [NO_2^-] anomalies are positively correlated ($r^2=0.39$, $p<0.01$) with the North Pacific Gyre Oscillation (NPGO) index (Figure S3.7). NPGO is indicative of basin scale circulation patterns and nutrient delivery, where positive NPGO corresponds to enhanced upwelling and productivity in the region [*Di Lorenzo et al.*, 2008]. A positive correlation between the long-term record of [NO_2^-] and indices of primary production could reflect a dependence on substrate availability (e.g., as inferred by Figure 3.9); however, the available data did not allow clear mechanisms to be discerned.

5. Conclusions

The contribution of euphotic zone-based nitrification was estimated from two California Current Ecosystem (CCE) cruises using concurrent measurements of the $\delta^{15}N$ and $\delta^{18}O$ of nitrate. Results indicated that nitrification could contribute between 6% and 36% to the nitrate reservoir above the remnant mixed layer (~50 - 60m for Cycles <75 km from shore). A comparison to new production estimates allowed these percentages to be converted to integrated nitrification rates, which ranged from 0.1 to 2.0 mmol N m^{-2} d^-

^{1}. These estimated rates were comparable to the range of integrated nitrification rates previously reported for the central California Current (e.g., [*Santoro et al.*, 2010; *Smith et al.*, 2016]).

Nitrification in the euphotic zone could influence certain formulations of New Production. For example, when New Production is estimated from nitrate uptake rates, then New Production would be overestimated when euphotic zone nitrification is detectable. However, when NO_3^- at a fixed depth below the euphotic zone is used in combination with a vertical advection rate to calculate New Production then euphotic zone nitrification is not relevant. In other words, a calculation of New Production based on subsurface NO_3^- does not detect euphotic zone nitrifcation. If gradients in the vertical profile of NO_3^- in the euphotic zone are used to estimate New Production then New Production may be underestimated.

Vertical abundances of genes associated with nitrifying organisms suggested that maximal rates of nitrification would be found at depths deeper than the 1% PAR light level. In fact, profiles of nitrification by stable isotopes exhibited inverse patterns compared to nitrifier abundance/activity. In accordance with these findings, a simple vertical advection box-model for the same profiles required nitrification to occur up to the high light, surface depths. Stable isotope data presented here indicated that nitrification was occurring in surface waters at rates of 4 - 16 nmol L^{-1} d^{-1}. A similar finding was discussed in [*Ward*, 2008]. The discrepancy between the two measures of activity was also discussed in [*Smith et al.*, 2016], where authors demonstrated peak nitrification rates ~90 m shallower than AOA and associated *amo*A gene abundances.

The nitrification model presented here was also used to estimate the isotopic composition of particulate organic matter (POM) exported from the euphotic zone. Patterns of modeled $\delta^{15}N$ of PON export most often approximated the $\delta^{15}N_{\text{Sinking PON}}$ captured at 100 m, and differences between the modeled and measured values could have been due to additional sources contributing to sinking POM. Surface average $\delta^{15}N_{\text{Suspended PON}}$ was often depleted relative to modeled PON export suggesting this pool to have not contributed to export.

Integrated nitrification contributions to the nitrate reservoir were positively correlated with $[NO_2^-]$ at the primary nitrite maximum depth across CCE Cycles. A correlation analysis of $[NO_2^-]$ from the larger CalCOFI database (for stations near Pt. Conception) found that nitrite accumulation was positively correlated with PON and/or POC:Chl-a. In the first case, excessive PON could serve as an important substrate for nitrification when ammonia is released from this pool during heterotrophic activity. In the second case, reduced Chl-a could indicate reduced competition with phytoplankton for NO_2^-. Overall, these processes led to higher nitrite, which could thereby lead to increased nitrite oxidation/nitrification in the euphotic zone.

An analysis based on the natural abundance of $\delta^{15}N$ and $\delta^{18}O$ of nitrate provided evidence that nitrification within the euphotic zone of the CCE can contribute to the nitrate reservoir. Future studies that collect samples for natural abundance stable isotopes of nitrate would benefit from concurrent estimates of the activity of nitrifiers and measure ammonia oxidation and nitrite oxidation rates. In addition, identifying the role of PON and nitrite uptake by phytoplankton in controlling nitrite accumulation and by extension, nitrification should be a priority because it would allow nitrification to be better parameterized in models of nitrogen cycling in these climatically sensitive environments.

APPENDIX

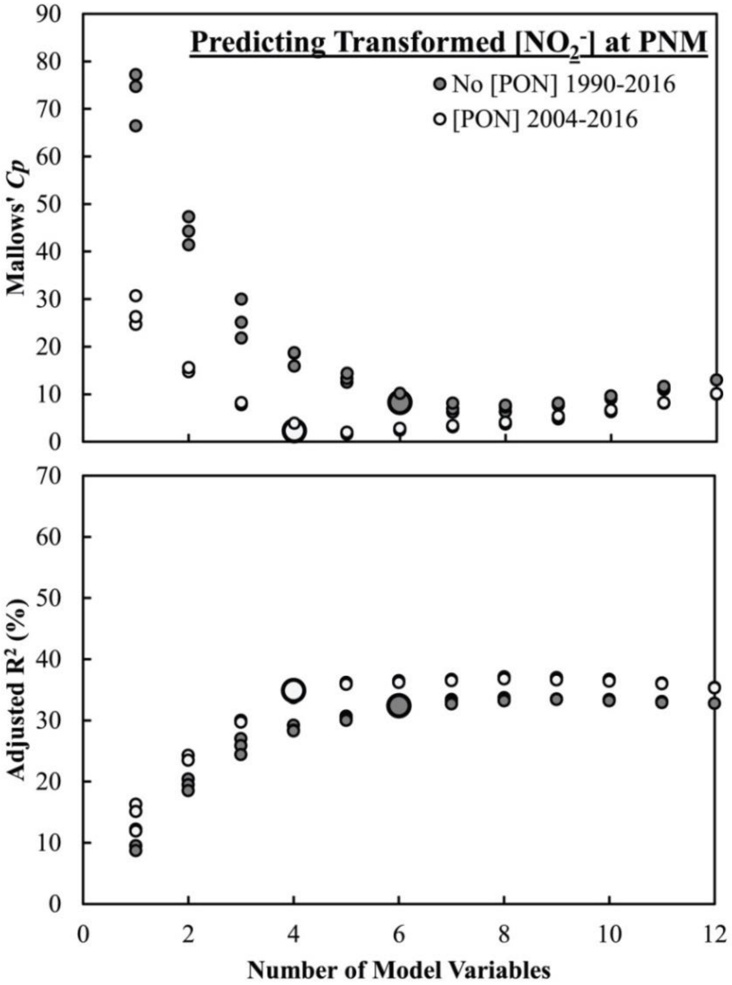

Figure S3.1. *The influence of increasing variables in a stepwise regression model is apparent by evaluating the Mallows' Cp (top panel) and the adjusted* R^2 *values (bottom panel). The most appropriate number of variables in a multiple regression minimizes the Mallows' Cp statistic while maximizing the adjusted* R^2*. These models are highlighted by the larger dot size with bold outline in two CalCOFI datasets (2004 - 2016 that included POM data, white circles) and (1990 - 2016 that did not include POM data, grey circles). The model output was evaluated based on cube-root transformed and centered data.*

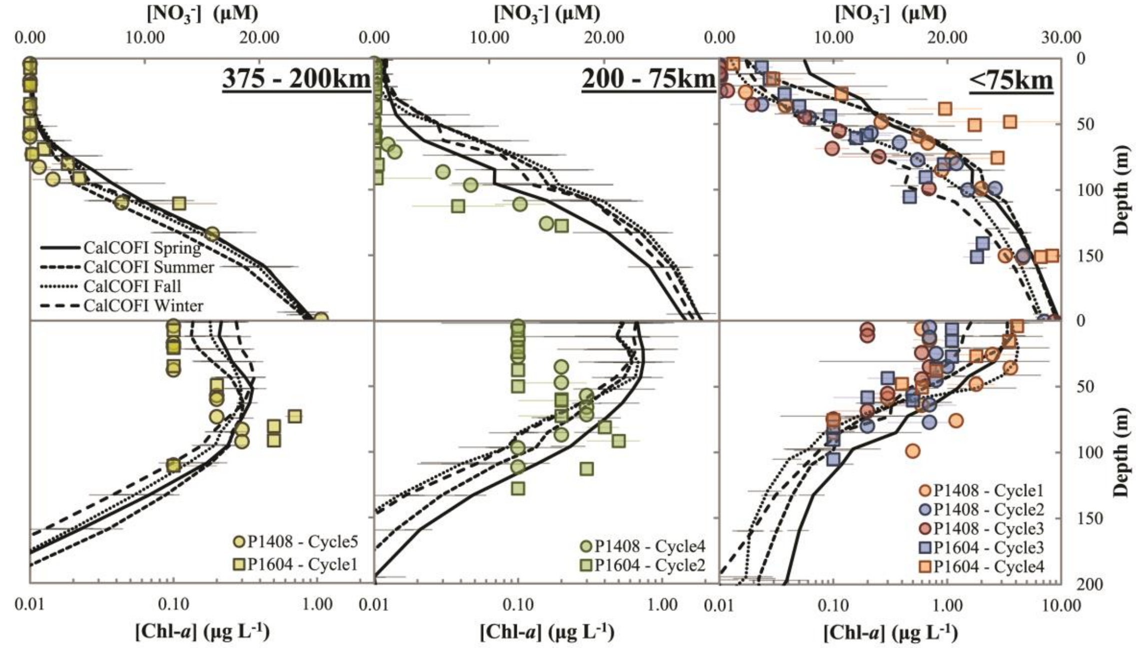

Figure S3.2. *CCE LTER Cruise mean Cycle [NO$_3^-$] (top panels) and [Chl-a] (bottom panels) depth profiles compared with long-term (1990-2016) seasonal mean CalCOFI profiles. Note the relative decrease in surface [NO$_3^-$] and [Chl-a] for most Cycles (all but P1408 Cycle 1 and P1604 Cycle 4 are reduced in [NO$_3^-$] and [Chl-a] over the surface 0-50m). Error bars represent the ±1σ standard deviation of the measured concentration within a 10 meter depth bin. CalCOFI stations used for these average profiles include northern lines 076.0 and 080.0 for stations less than 055.0 (<75 km), 060.0 to 080.0 (200-75 km) and 090.0 to 100.0 (375-200 km).*

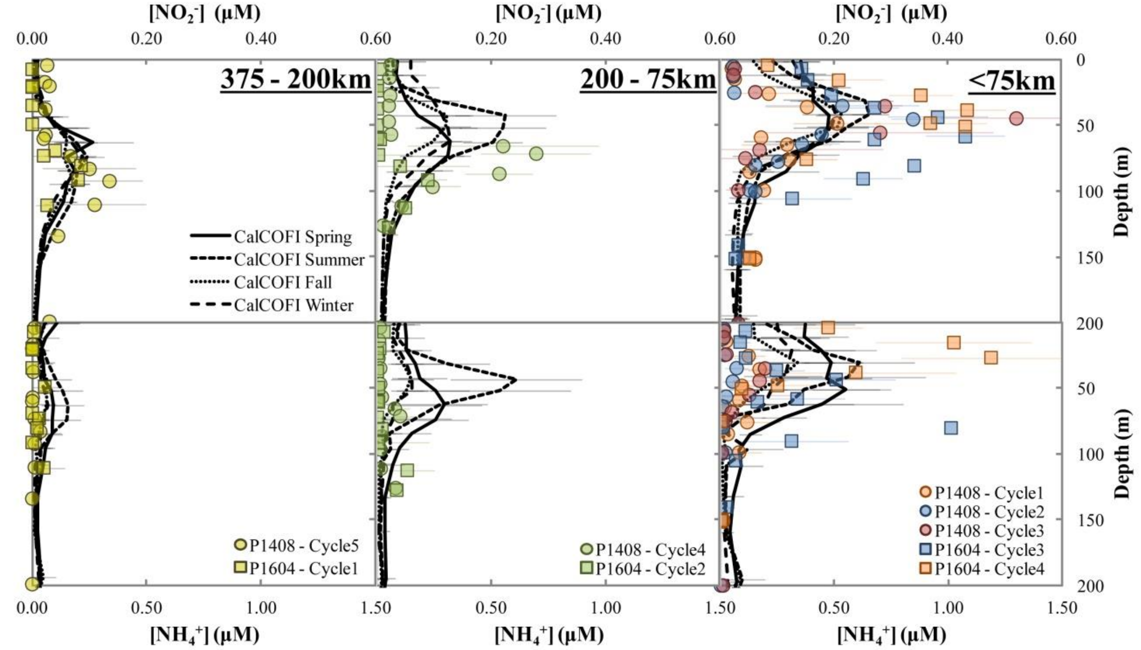

Figure S3.3. *Mean profile comparison as found in Figure S3.2 but now for [NO$_2^-$] (top panels) and [NH$_4^+$] (bottom panels). Note for both P1408 and P1604 Cycles <75 km from shore increase significantly in [NO$_2^-$] yet increase in [NH$_4^+$] only for P1604. Figures are arranged from Inshore (<75 km from shore) on the right to Offshore toward the left (375-200 km).*

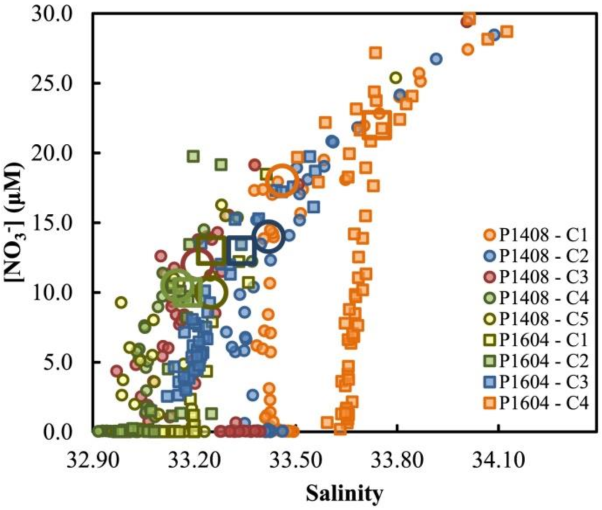

Figure S3.4. *Source nitrate to the surface ocean was determined based on the wintertime mixed layer depth salinity and on changes in salinity with depth. This location is also reflected in changes to nitrate concentration,* NO_3^-*, for a relatively fixed salinity, and is identified by the open symbols in this figure. The effects of Ekman-driven upwelling can also be observed here where coastal waters of higher salinity also have greater source* $[NO_3^-]$.

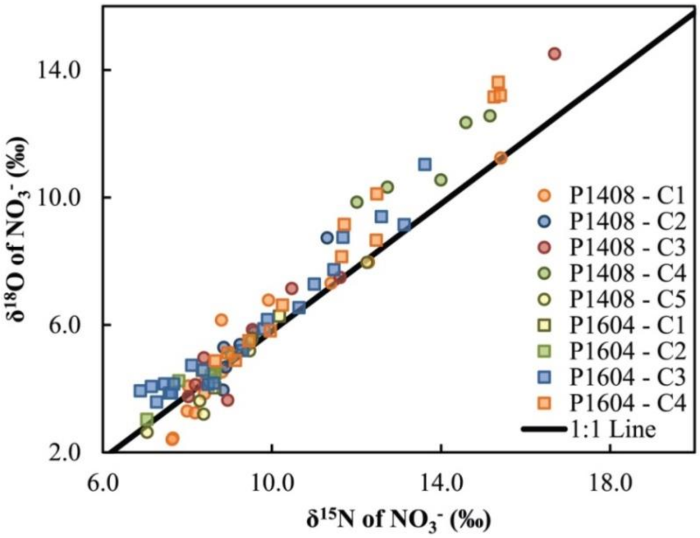

Figure S3.5. *Nitrate isotopes* $\delta^{15}N_{NO3}$ *and* $\delta^{18}O_{NO3}$ *depart from the isotopic composition of source waters suggesting nitrification to have imprinted the isotope signature on this reservoir. Source waters were determined for each Cycle and had an average* $\delta^{15}N_{NO3}$ *of 8.9‰ and* $\delta^{18}O_{NO3}$ *of 4.7‰.*

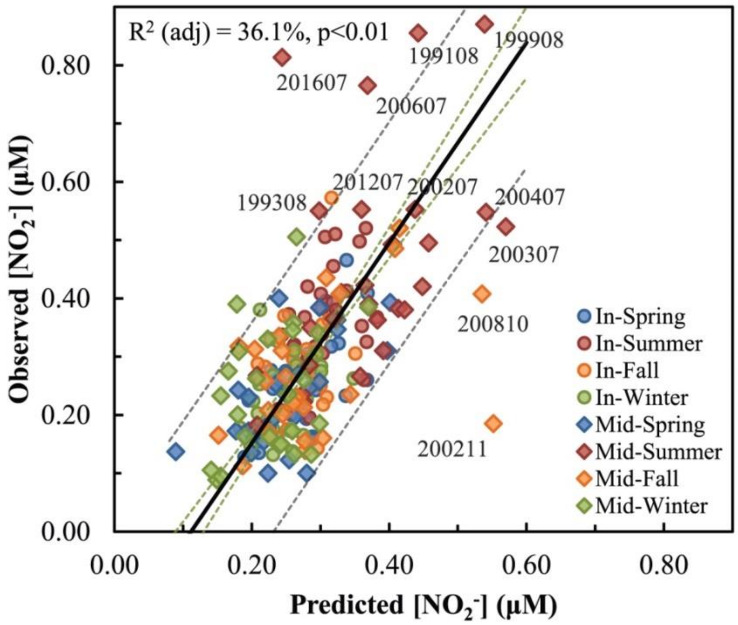

Figure S3.6. *Generalized linear regression model [NO$_2^-$] at the primary nitrite maximum depths were predicted by a combination of O$_2$ saturation, dynamic height, integrated chlorophyll, [NO$_3^-$] at base of the Chl-a max depth, Si* and the NPGO index (adjusted R^2=0.361; n=212). CalCOFI 1990-2016 Inshore stations ('In'; Lines 076.0 and 080.0 and stations 055.0 and 060.0; circles) and Midshore stations ('Mid'; Lines 076.0 and 080.0 and stations 070.0 and 080.0; diamonds). Type II model fit is shown in bold line with the ±95% confidence intervals (dashed green lines nearest the solid line) and ±95% prediction intervals (dashed grey lines furthest from the solid line. Overlain are mean observed and predicted Inshore CCE cruise Cycles (large squares).*

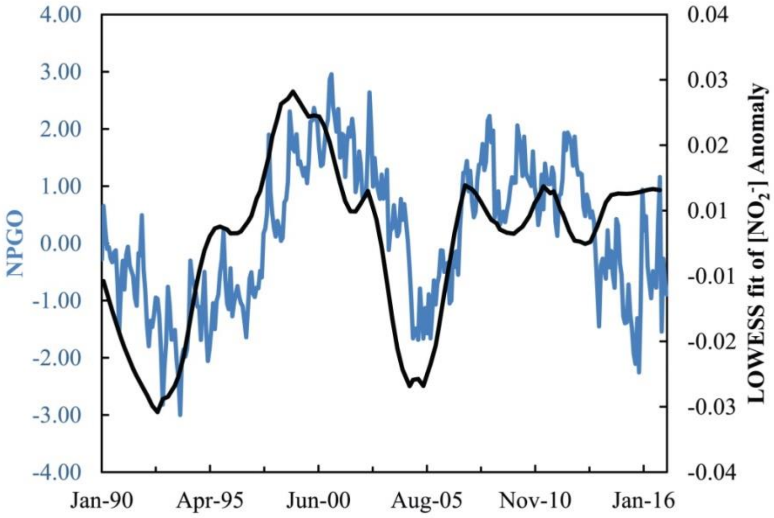

Figure S3.7. *North Pacific Gyre Oscillation (NPGO) indices (blue) are positively correlated (r^2=0.39, p<0.01) with seasonally corrected [NO_2^-] anomalies for stations <75 km from Pt. Conception ('Inshore') LOWESS smoothing was applied using a span of 20%, a length scale that approximated the typical span of NPGO peaks/troughs (~5 years). NPGO values obtained from http://www.o3d.org/npgo/, courtesy Manu Di Lorenzo.*

Table S3.1. *Cube-root transformed and centered variables used in stepwise regressions where [NO_2^-] near the primary nitrite max depth (±10 m) is the dependent variable. Variables with (*) were selected for a model based on CalCOFI data collected between 2004 and 2016. Variables with (**) were selected for a model based on CalCOFI data collected between 1990 and 2016. The p-values used in a generalized linear model associated with these variables can be found in Table S2.*

Multivariate ENSO Index (MEI)
North Pacific Gyre Oscillation (NPGO)*, **
Pacific Decadal Oscillation (PDO)
Wind Speed (knots)
Distance from coast (naut miles)
Julian Day
Buoyancy Frequency (N2; surface)
Dynamic Height (m)**
Mixed layer depth (m)
Integrated Chl-a (mg m^{-2}; 0m to base of euphotic zone)**
Avg Surface Oxygen Saturation (%; 0-30m)*, **
Avg Si* near Primary Nitrite Max (μM; ±10m)**
Avg [NO_3^-] near remnant mixed layer depth (μM; ±10m)**
Avg [PON] (μM; 0-50m)*
Avg molar POC:PON (μM; 0-50m)
Avg POC:Chl-a (μg C L^{-1}: μg Chl-a L^{-1}; 0-50m)*

Table S3.2. *Shown here are beta coefficients and p-values determined for generalized linear models based on cube-root transformed and centered variables from CalCOFI data collected (1) 1990 to 2016 and for data collected (2) 2004 to 2016. Selection of variables for the generalized linear models was based on evaluation of the Mallows' Cp and adjusted R^2 statistics from a stepwise linear regression analysis (Figure S3.1). See Table S3.1 for a list of tested variables.*

Model	Variable	β Coefficient	p-value
(1) 1990 - 2016	*O2 Saturation*	*0.3604*	*<0.001*
	Dynamic Ht	*-0.2229*	*0.003*
	Int [Chl-a]	*-0.2143*	*0.001*
	$[NO_3^-]$	*0.1938*	*0.005*
	*Si**	*-0.1688*	*0.014*
	NPGO	*0.1464*	*0.003*
	Intercept	*-0.0186*	*0.743*
(2) 2004-2016	*[PON]*	*0.3043*	*<0.001*
	POC:Chl-a	*0.2295*	*0.005*
	O_2 *Saturation*	*0.2250*	*0.003*
	NPGO	*0.2115*	*0.003*
	Intercept	*0.0679*	*0.396*

Supplemental Text S3.1

The following is a derivation of the PON export equation Eq (3) discussed in the main text (Section 4.2), and the derivation is built on model equations presented in [*Wankel et al.*, 2007]. The PON model in the main text Eq (3) is directly taken from Eq (10) in the Supplemental text of [*Wankel et al.*, 2007]:

$$\delta^{15}N_{PON\_export} = \frac{A_{NO3} * (\delta^{15}N_{surf} - \varepsilon_p) + NTR * (\varepsilon_{NTR} - \varepsilon_{consum})}{EXP + NTR}, \quad (4)$$

where $\delta^{15}N_{PON\_export}$ is the $\delta^{15}N$ of PON exported from the surface ocean, A_{NO3} refers to the nitrate uptake rate, $\delta^{15}N_{surf}$ refers to the mean surface nitrate $\delta^{15}N$, ε_p is the isotope effect of phytoplankton uptake of nitrate, NTR is the nitrification rate, ε_{NTR} is the net isotope effect of nitrification, ε_{consum} is the net isotope effect associated with the branching reaction of ammonium uptake and nitrification, and EXP is the export rate of PON from the surface ocean.

Eq (4) can be simplified using two other equations presented in the supplemental text in [*Wankel et al.*, 2007]. The first from supplemental Eq (3) in [*Wankel et al.*, 2007] is:

$$\delta^{15}N_{NH4} = \delta^{15}N_{PON} + \varepsilon_{consum} * f, \quad (5)$$

where $\delta^{15}N_{NH4}$ is the $\delta^{15}N$ of ammonium and *f* is the fraction of the ammonium pool that is consumed and is assumed to be equal to 1 for the surface California Current. The second equation used to reduce Eq (4) above is Eq (6) from the supplemental text in [*Wankel et al.*, 2007]:

$$A_{NH4} * (\delta^{15}N_{NH4} - \varepsilon_a) + A_{NO3} * \left(\delta^{15}N_{surf} - \varepsilon_p\right) = (EXP * \delta^{15}N_{PON}) + (Remin * \delta^{15}N_{PON}), \tag{6}$$

where A_{NH4} refers to the uptake rate of ammonium, ε_a is the isotope effect of ammonium uptake, $\delta^{15}N_{PON}$ is the $\delta^{15}N$ of the surface particulate pool, $\delta^{15}N_{surf}$ is the mean $\delta^{15}N$ of the surface nitrate reservoir, *and Remin* refers to the remineralization rate of PON.

As stated in [*Wankel et al.,* 2007], inherent in the combination of the above equations Eq (6) and Eq (5) to reduce Eq (4) is the idea that the system is at steady state. This means that the phytoplankton pool is not changing in size and all assimilated N into the PON pool is either exported or remineralized. Based on inclusion of the above parameters to derive the PON isotope export equation in the main text (Eq 3), the exported PON is likely to reflect autotrophic biomass.

REFERENCES

Altabet, M. A. (2001). Nitrogen isotopic evidence for micronutrient control of fractional NO3- utilization in the equatorial Pacific. *Limnology and Oceanography*, *46*(2), 368–380.

Beman, J. M., Popp, B. N., and Alford, S. E. (2012). Quantification of ammonia oxidation rates and ammonia-oxidizing archaea and bacteria at high resolution in the Gulf of California and eastern tropical North Pacific Ocean. *Limnology and Oceanography*, *57*(3), 711–726.

Beman, J. M., Popp, B. N., and Francis, C. A. (2008). Molecular and biogeochemical evidence for ammonia oxidation by marine Crenarchaeota in the Gulf of California. *ISME Journal*, *2*(4), 429–441.

Beman, J. M., Sachdeva, R., and Fuhrman, J. A. (2010). Population ecology of nitrifying Archaea and Bacteria in the Southern California Bight. *Environmental Microbiology*, *12*(5), 1282–1292.

Beman, J. M., Leilei Shih, J., and Popp, B. N. (2013). Nitrite oxidation in the upper water column and oxygen minimum zone of the eastern tropical North Pacific Ocean. *ISME Journal*, *7*(11), 2192–2205.

Bond, N. A., Cronin, M. F., Freeland, H., and Mantua, N. (2015). Causes and impacts of the 2014 warm anomaly in the NE Pacific. *Geophysical Research Letters*, *42*(9), 3414–3420.

Buchwald, C., and Casciotti, K. L. (2010). Oxygen isotopic fractionation and exchange during bacterial nitrite oxidation. *Limnology and Oceanography*, *55*(3), 1064–1074.

Buchwald, C., Santoro, A. E., McIlvin, M. R., and Casciotti, K. L. (2012). Oxygen isotopic composition of nitrate and nitrite produced by nitrifying cocultures and natural marine assemblages. *Limnology and Oceanography*, *57*(3), 1361–1375.

Casciotti, K. L. (2009). Inverse kinetic isotope fractionation during bacterial nitrite oxidation. *Geochimica et Cosmochimica Acta*, *73*(7), 2061–2076.

Casciotti, K. L. (2016). Nitrogen and Oxygen Isotopic Studies of the Marine Nitrogen Cycle. *Annual Review of Marine Science*.

Casciotti, K. L., Sigman, D. M., Hastings, M. G., Böhlke, J. K., and Hilkert, A. (2002). Measurement of the oxygen isotopic composition of nitrate in seawater and freshwater using the denitrifier method. *Analytical Chemistry*, *74*(19), 4905–4912.

Casciotti, K. L., Sigman, D. M., and Ward, B. B. (2003). Linking Diversity and Stable Isotope Fractionation in Ammonia-Oxidizing Bacteria Linking Diversity and Stable Isotope Fractionation in Ammonia-Oxidizing Bacteria. *Geomicrobiology Journal*, *20*(2002), 37–41.

Chavez, F. P., Barber, R. T., and Sanderson, M. P. (1989). The potential primary production of the Peruvian upwelling ecosystem, 1953-1984. *The Peruvian Upwelling Ecosystem: Dynamics and Interactions*, *18*, 50–63.

Cifuentes, L. A., Fogel, M. L., Pennock, J. R., and Sharp, J. H. (1989). Biogeochemical factors that influence the stable nitrogen isotope ratio of dissolved ammonium in the Delaware Estuary. *Geochimica et Cosmochimica Acta*, *53*(10), 2713–2721.

Cole, S. T., Rudnick, D. L., and Colosi, J. A. (2010). Seasonal evolution of upper-ocean horizontal structure and the remnant mixed layer. *Journal of Geophysical Research: Oceans*, *115*(4), 1–15.

Daims, H., Lebedeva, E. V., Pjevac, P., Han, P., Herbold, C., Albertsen, M., Jehmlich, N., Palatinszky, M., Vierheilig, J., Bulaev, A., Kirkegaard, R. H., Bergen, M. von, Rattei, T., Wagner, M. (2015).

Complete nitrification by Nitrospira bacteria. *Nature*, *528*(7583), 504–509.

Daims, H., Lücker, S., and Wagner, M. (2016). A New Perspective on Microbes Formerly Known as Nitrite-Oxidizing Bacteria. *Trends in Microbiology*, *24*(9), 699–712.

DiFiore, P. J., Sigman, D. M., Trull, T. W., Lourey, M. J., Karsh, K., Cane, G., and Ho, R. (2006). Nitrogen isotope constraints on subantarctic biogeochemistry. *Journal of Geophysical Research: Oceans*, *111*(8).

Dugdale, R. C., and Goering, J. J. (1967). Uptake of New and Regenerated Forms of Nitrogen in Primary Productivity. *Limnology and Oceanography*, *12*(2), 196–206.

Eppley, R. W., and Peterson, B. J. (1979). Particulate organic matter flux and planktonic new production in the deep ocean. *Nature*, *282*(5740), 677–680.

Fripiat, F., Elskens, M., Trull, T. W., Blain, S., Cavagna, A. J., Fernandez, C., Fonseca-Batista, D., Planchon, F., Raimbault, P., Roukaerts, A., and Dehairs, F. (2015). Significant mixed layer nitrification in a natural iron-fertilized bloom of the Southern Ocean. *Global Biogeochemical Cycles*, *29*(11), 1929–1943.

Goericke, R. (2002). Top-down control of phytoplankton biomass and community structure in the monsoonal Arabian Sea. *Limnology and Oceanography*, *47*(5), 1307–1323.

Goericke, R., and Ohman, M. D. (2015). Introduction to CCE-LTER: Responses of the California Current Ecosystem to climate forcing. *Deep-Sea Research Part II: Topical Studies in Oceanography*, *112*, 1–5.

Granger, J., Sigman, D. M., Needoba, J. A., and Harrison, P. J. (2004). Coupled nitrogen and oxygen isotope fractionation of nitrate during assimilation by cultures of marine phytoplankton. *Limnol. Oceanogr*, *49*(5), 1763–1773.

Granger, J., Sigman, D. M., Prokopenko, M. G., Lehmann, M. F., and Tortell, P. D. (2006). A method for nitrite removal in nitrate N and O isotope analyses. *Limnology and Oceanography: Methods*, *4*(7), 205–212.

Granger, J., Sigman, D. M., Rohde, M. M., Maldonado, M. T., and Tortell, P. D. (2010). N and O isotope effects during nitrate assimilation by unicellular prokaryotic and eukaryotic plankton cultures. *Geochimica et Cosmochimica Acta*, *74*(3), 1030–1040.

Horrigan, S. G., Montoya, J. P., Nevins, J. L., and McCarthy, J. J. (1990). Natural isotopic composition of dissolved inorganic nitrogen in the Chesapeake Bay. *Estuarine, Coastal and Shelf Science*, *30*(4), 393–410.

Jacox, M. G., Hazen, E. L., Zaba, K. D., Rudnick, D. L., Edwards, C. A., Moore, A. M., and Bograd, S. J. (2016). Impacts of the 2015–2016 El Niño on the California Current System: Early assessment and comparison to past events. *Geophysical Research Letters*, *43*(13), 7072–7080.

King, A. L., and Barbeau, K. A. (2011). Dissolved iron and macronutrient distributions in the southern California Current System. *Journal of Geophysical Research: Oceans*, *116*(3).

Knapp, A. N., Sigman, D. M., Lipschultz, F., Kustka, A. B., and Capone, D. G. (2011). Interbasin isotopic correspondence between upper-ocean bulk DON and subsurface nitrate and its implications for marine nitrogen cycling. *Global Biogeochemical Cycles*, *25*(4).

Könneke, M., Bernhard, A. E., De La Torre, J. R., Walker, C. B., Waterbury, J. B., and Stahl, D. A. (2005). Isolation of an autotrophic ammonia-oxidizing marine archaeon. *Nature*, *437*(7058), 543–546.

Landry, M. R., Ohman, M. D., Goericke, R., Stukel, M. R., and Tsyrklevich, K. (2009). Lagrangian studies of phytoplankton growth and grazing relationships in a coastal upwelling ecosystem off Southern California. *Progress in Oceanography*, *83*(1–4), 208–216.

Lipschultz, F. (2001). A time-series assessment of the nitrogen cycle at BATS. *Deep-Sea Research Part II: Topical Studies in Oceanography*, *48*(8–9), 1897–1924.

Lomas, M. W., and Lipschultz, F. (2006). Forming the primary nitrite maximum: Nitrifiers or phytoplankton? *Limnology and Oceanography*, *51*(5), 2453–2467.

Di Lorenzo, E., Schneider, N., Cobb, K. M., Franks, P. J. S., Chhak, K., Miller, A. J., McWilliams, J. C., Bograd, S. J., Arango, H., Curchitser, E., Powell, T. M., and Rivière, P. (2008). North Pacific Gyre Oscillation links ocean climate and ecosystem change. *Geophysical Research Letters*, *35*(8).

Lücker, S., Nowka, B., Rattei, T., Spieck, E., and Daims, H. (2013). The genome of Nitrospina gracilis illuminates the metabolism and evolution of the major marine nitrite oxidizer. *Frontiers in Microbiology*, *4*(FEB), 1–19.

Mallows, C. L. (1973). Some Comments on Cp. *Technometrics*, *15*(4), 661.

Meeder, E., MacKey, K. R. M., Paytan, A., Shaked, Y., Iluz, D., Stambler, N., Rivlin, T., Post, A. F., and Lazar, B. (2012). Nitrite dynamics in the open ocean-clues from seasonal and diurnal variations. *Marine Ecology Progress Series*, *453*(2), 11–26.

Messié, M., Ledesma, J., Kolber, D. D., Michisaki, R. P., Foley, D. G., and Chavez, F. P. (2009). Potential new production estimates in four eastern boundary upwelling ecosystems. *Progress in Oceanography*, *83*(1–4), 151–158.

Mincer, T. J., Church, M. J., Taylor, L. T., Preston, C., Karl, D. M., and DeLong, E. F. (2007). Quantitative distribution of presumptive archaeal and bacterial nitrifiers in Monterey Bay and the North Pacific Subtropical Gyre. *Environmental Microbiology*, *9*(5), 1162–1175.

Mingawa, M., Winter, D. A., and Kaplan, I. R. (1984). Comparison of Kjeldahl and Combustion Methods for Measurement of Nitrogen Isotope Ratios in Organic Matter. *Anal. Chem*, *56*, 1859–1861.

Miyake, Y., and Wada, E. (1971). The isotope effect on the nitrogen in biochemical, oxidation-reduction reactions. *Records of Oceanographic Works in Japan*.

Montoya, J. P., Korrigan, S. G., and McCarthy, J. J. (1991). Rapid, storm-induced changes in the natural abundance of 15N in a planktonic ecosystem, Chesapeake Bay, USA. *Geochimica et Cosmochimica Acta*, *55*(12), 3627–3638.

Pennock, J. R., Velinsky, D. J., Ludlam, J. M., Sharp, J. H., and Fogel, M. L. (1996). Isotopic fractionation of ammonium and nitrate during uptake by Skeletonema costatum: Implications for d15N dynamics under bloom conditions. *Limnology and Oceanography*, *41*(3), 451–459.

Santoro, A. E., and Casciotti, K. L. (2011). Enrichment and characterization of ammonia-oxidizing archaea from the open ocean: Phylogeny, physiology and stable isotope fractionation. *ISME Journal*, *5*(11), 1796–1808.

Santoro, A. E., Sakamoto, C. M., Smith, J. M., Plant, J. N., Gehman, A. L., Worden, A. Z., Johnson, K. S., Francis, C. A., and Casciotti, K. L. (2013). Measurements of nitrite production in and around the primary nitrite maximum in the central California Current. *Biogeosciences*, *10*(11), 7395–7410.

Santoro, A. E., Casciotti, K. L., and Francis, C. A. (2010). Activity, abundance and diversity of nitrifying archaea and bacteria in the central California Current. *Environmental Microbiology*, *12*(7), 1989–

2006.

Schleper, C., Jurgens, G., and Jonuscheit, M. (2005). Genomic studies of uncultivated archaea. *Nature Reviews Microbiology*, *3*(6), 479–488.

Sharp, J. H. (1974). Improved analysis for "particulate" organic carbon and nitrogen from seawater. *Limnology and Oceanography*, *19*(6), 984–989.

Sigman, D. M., Casciotti, K. L., Andreani, M., Barford, C., Galanter, M., and Böhlke, J. K. (2001). A bacterial method for the nitrogen isotopic analysis of nitrate in seawater and freshwater. *Analytical Chemistry*, *73*(17), 4145–4153.

Sigman, D. M., Karsh, K. L., and Casciotti, K. L. (2010). Nitrogen Isotopes in the Ocean. In *Encyclopedia of Ocean Sciences* (pp. 40–54).

Sigman, D. M., Altabet, M. A., McCorkle, D. C., Francois, R., and Fischer, G. (1999). The δ15N of nitrate in the Southern Ocean: Consumption of nitrate in surface waters. *Global Biogeochemical Cycles*, *13*(4), 1149–1166.

Smith, J. M., Chavez, F. P., and Francis, C. A. (2014a). Ammonium uptake by phytoplankton regulates nitrification in the sunlit ocean. *PLoS ONE*, *9*(9).

Smith, J. M., Casciotti, K. L., Chavez, F. P., and Francis, C. A. (2014b). Differential contributions of archaeal ammonia oxidizer ecotypes to nitrification in coastal surface waters. *ISME Journal*, *8*(8), 1704–1714.

Smith, J. M., Damashek, J., Chavez, F. P., and Francis, C. A. (2016). Factors influencing nitrification rates and the abundance and transcriptional activity of ammonia-oxidizing microorganisms in the dark northeast Pacific Ocean. *Limnology and Oceanography*, *61*(2), 596–609.

Sokal, R. R., and Rohlf, F. J. (1995). *Biometry*. W. H. Freeman.

Stukel, M. R., Ohman, M. D., Benitez-Nelson, C. R., and Landry, M. R. (2013). Contributions of mesozooplankton to vertical carbon export in a coastal upwelling system. *Marine Ecology Progress Series*, *491*, 47–65.

Sugimoto, R., Kasai, A., Miyajima, T., and Fujita, K. (2009). Controlling factors of seasonal variation in the nitrogen isotope ratio of nitrate in a eutrophic coastal environment. *Estuarine, Coastal and Shelf Science*, *85*(2), 231–240.

Todd, R. E., Rudnick, D. L., Mazloff, M. R., Cornuelle, B. D., and Davis, R. E. (2012). Thermohaline structure in the California Current System: Observations and modeling of spice variance. *Journal of Geophysical Research: Oceans*, *117*(2).

Wada, E., Terazaki, M., Kabaya, Y., and Nemoto, T. (1987). 15N and 13C abundances in the Antartic Ocean with emphasis on the biogeochemical structure of the food web. *Deep Sea Research Part A, Oceanographic Research Papers*, *34*(5–6), 829–841.

Wankel, S. D., Kendall, C., Pennington, J. T., Chavez, F. P., and Paytan, A. (2007). Nitrification in the euphotic zone as evidenced by nitrate dual isotopic composition: Observations from Monterey Bay, California. *Global Biogeochemical Cycles*, *21*(2).

Ward, B. B. (1985). Light and substrate concentration relationships with marine ammonium assimilation and oxidation rates. *Marine Chemistry*, *16*(4), 301–316.

Ward, B. B. (1987). Nitrogen transformations in the Southern California Bight. *Deep Sea Research Part A*, *Oceanographic Research Papers*, *34*(5–6), 785–805.

Ward, B. B. (2005). Temporal variability in nitrification rates and related biogeochemical factors in Monterey Bay, California, USA. *Marine Ecology Progress Series*, *292*, 97–109.

Ward, B. B. (2008). Nitrification in Marine Systems. In *Nitrogen in the Marine Environment* (pp. 199–261).

Ward, B. B., and Carlucci, A. F. (1985). Marine ammonia- and nitrite-oxidizing bacteria: Serological diversity determined by immunofluorescence in culture and in the environment. *Applied and Environmental Microbiology*, *50*(2), 194–201.

Ward, B. B., Olson, R. J., and Perry, M. J. (1982). Microbial nitrification rates in the primary nitrite maximum off southern California. *Deep Sea Research Part A, Oceanographic Research Papers*, *29*(2), 247–255.

Ward, B. B., Talbot, M. C., and Perry, M. J. (1984). Contributions of phytoplankton and nitrifying bacteria to ammonium and nitrite dynamics in coastal waters. *Continental Shelf Research*, *3*(4), 383–398.

Watson, S. W., and Waterbury, J. B. (1971). Characteristics of two marine nitrite oxidizing bacteria, Nitrospina gracilis nov. gen. nov. sp. and Nitrococcus mobilis nov. gen. nov. sp. *Archiv Für Mikrobiologie*, *77*(3), 203–230.

Yool, A., Martin, A. P., Fernández, C., and Clark, D. R. (2007). The significance of nitrification for oceanic new production. *Nature*, *447*(7147), 999–1002.

Zaba, K. D., and Rudnick, D. L. (2016). The 2014-2015 warming anomaly in the Southern California Current System observed by underwater gliders. *Geophysical Research Letters*, *43*(3), 1241–1248.

Chapter IV

Nitrate Utilization in the California Current Ecosystem

Abstract

The California Current Ecosystem (CCE) experienced anomalous climate conditions during the North Pacific warm pool of 2014-15 and strong El Niño of 2015-16, conditions that led to a significant reduction in both nitrate supply and surface ocean productivity relative to long-term means. The stable isotopes of nitrogen ($\delta^{15}N$) have been used in archive-based studies of the CCE to infer changes in surface nitrate utilization and in the nitrate isotopic composition of source waters, yet both of these can impart an isotopic fingerprint on the surface reservoirs. To assess the influence of source and utilization on the food web, the stable isotopes of nitrate ($\delta^{15}N_{NO3}$), suspended and sinking particulate organic matter ($\delta^{15}N_{Susp}$ and $\delta^{15}N_{Sink}$, respectively), and *Calanus pacificus* copepods ($\delta^{15}N_{Cp}$) were measured across the euphotic zone of different productivity regimes in the CCE in August 2014 and April 2016. The euphotic zone source nitrate was identified as the remnant mixed layer. This surface source often did not correspond with the $\delta^{15}N_{NO3}$ of waters 200 - 400 m immediately below ($\delta^{15}N_{NO3}$ ranged 7.0 - 9.1‰, exhibiting a direct correlation with spiciness), but the remnant mixed layer was slightly enriched on average ($\delta^{15}N_{NO3}$ of 8.9 ± 0.4‰) suggesting that this source was influenced by the memory of nitrate utilization. A closed system Rayleigh model best fit the surface $\delta^{15}N_{NO3}$ behavior for cruises spanning the anomalous surface conditions with a nitrate uptake isotope fractionation factor of 3.0 ± 0.5‰. This relatively low fractionation factor was possibly linked to greater proportions of smaller-sized and/or flagellated phytoplankton communities, or could also been linked to the growth-limiting conditions that developed during this time. The nitrate isotope model also estimated that the extent of inshore nitrate utilization was 52 ± 15% on average indicating that water frequently leaves Inshore CCE regions with excess NO_3^-, the extent of which may be influenced by iron limitation on nitrate uptake by diatoms. However, nitrate utilization was enhanced during the North Pacific warm pool of 2014 (~65%) and during the peak of the 2015-16

El Niño (up to 85%), a nitrate utilization signature that was detected across the $\delta^{15}N$ reservoirs measured here. In particular, $\delta^{15}N_{Sink}$ at 100 m exhibited a strong positive correlation with nitrate utilization, which reinforced the intimate connection between upwelling N and sinking N. Though $\delta^{15}N_{Cp}$ and $\delta^{15}N_{Susp}$ were less correlated with nitrate utilization, the average difference between these reservoirs was ~3.7 ± 0.8‰ resulting in an average trophic position of 2.1 ± 0.3. The agreement with trophic position estimated here with prior studies suggests the $\delta^{15}N_{Susp}$ to be an important link between surface nutrients and primary consumers in the CCE. On average, the $\delta^{15}N_{Sink}$ exhibited a ~2‰ enrichment over $\delta^{15}N_{Susp}$ and a ~2‰ depletion from $\delta^{15}N_{Cp}$, and concurrently isolated fecal pellets fell between $\delta^{15}N_{Sink}$ and $\delta^{15}N_{Cp}$, suggesting that lighter $\delta^{15}N$ sources other than the fecal pellets of *Cp* (and similar consumers) contributed to the sinking flux at that time. This is the first study in the CCE that has simultaneously compared the cycling of suspended, sinking POM and copepod $\delta^{15}N$ with nitrate $\delta^{15}N$ values, addressing assumptions associated with nitrate source and utilization on archival-based N cycling studies.

1. Introduction

Eastern boundary current systems exhibit some of the highest rates of production in the oceans [*Quiñones*, 2010]. In these regions, high rates of primary productivity are maintained by alongshore winds that drive Ekman transport and coastal upwelling, which brings nutrient-rich waters to the surface ocean [*Di Lorenzo et al.*, 2008; *Messié et al.*, 2009; *Messié* and *Chavez*, 2015]. The seasonality and magnitude of upwelling-associated winds can vary spatially and interannually, and periods with stronger winds are positively correlated with net primary and secondary production [*Chavez* and *Messié*, 2009; *Chavez et al.*, 2011].

The California Current System (CCS) is a moderately productive eastern boundary current system [*Messié* and *Chavez*, 2015], where the extent of its productivity is strongly linked to nitrate uptake (e.g., [*Eppley* and *Peterson*, 1979; *Eppley et al.*, 1979]). The role of nitrate as the limiting macronutrient in upwelling waters of the CCS is further confirmed by nitrate to phosphate ratios lower than the Redfield ratio of 15 - 16 (e.g., [*Mills* and *Arrigo*, 2010; *Deutsch* and *Weber*, 2012]). Concentrations of nitrate (denoted as NO_3^-, throughout) can serve as a general indicator of primary production potential in the CCS (e.g., [*Messié* and *Chavez*, 2015]), and the stable isotopes of nitrate ($\delta^{15}N_{NO3}$) provide insight into the source and fate of nitrate supplied to the surface ocean (e.g., [*Sigman et al.*, 1999, 2005]). Previously published studies of $\delta^{15}N_{NO3}$ in the CCS region exhibit the expected isotopic enrichment of nitrate due to kinetic fractionation of nitrogen isotopes during assimilation in the euphotic zone [*Liu* and *Kaplan*, 1989; *Altabet et al.*, 1999; *Sigman et al.*, 2005]. These studies also remarked on the enriched $\delta^{15}N_{NO3}$ of subsurface nitrate and linked this elevated signature to the California Undercurrent that flows poleward along the shelf and originates in the eastern tropical Pacific Ocean.

An enriched $\delta^{15}N$ signal in the CCS propagates into upper ocean food webs first following uptake and incorporation into phytoplankton and detritus [*Rau et al.*, 1998; *Altabet et al.*, 1999] and this isotope signature can subsequently appear in the $\delta^{15}N$ signature of zooplankton [*Rau et al.*, 2003; *Ohman et al.*, 2012]. This $\delta^{15}N$ is then exported into underlying sediments via sinking particles [*Altabet et al.*, 1999; *Collins et al.*, 2011] such that well-preserved sediments provide a record of $\delta^{15}N_{NO3}$ variability in the upper ocean. Long-term records for the region include $\delta^{15}N$ in archived zooplankton biomass [*Rau et al.*, 2003; *Ohman et al.*, 2012] and in sinking particles and sediments of the Santa Barbara, Santa Monica and San Pedro Basins [*Collins et al.*, 2011; *Deutsch et al.*, 2014; *Tems et al.*, 2015]. These records exhibit interannual variability as well as long-term decadal variability, where longer term variations have been linked to changes in $\delta^{15}N_{NO3}$ of source waters supplying nitrate to regional food webs (e.g., [*Deutsch et al.*, 2014; *Tems et al.*, 2015]). Yet, shorter term, interannual variations are more enigmatic as changes in both $\delta^{15}N_{NO3}$ source signature and the extent of nitrate utilization could drive the observed changes. In addition, archived zooplankton records indicate that changes in trophic position could influence interpretations of $\delta^{15}N$ variability for this reservoir [*Hannides et al.*, 2009]. It is further possible that kinetic isotope effects associated with changes in phytoplankton species composition could impart some interannual variability [*Montoya* and *Mccarthy,* 1995; *Needoba et al.*, 2003].

Although $\delta^{15}N$ records exist for the region, there have been no studies that have systematically examined $\delta^{15}N$ relationships between upper ocean nitrogen reservoirs. In this study, $\delta^{15}N$ was used to examine the depth from which nitrate was delivered to the euphotic zone, which was used to delineate the competing influences of source isotope signature and the extent of utilization on biomass nitrogen. The fractionation factor associated with nitrate uptake was also established, and by using this isotope-based model the food web processes contributing to the sinking organic matter flux were estimated. This study was conducted in the CCS during 2014-16, a time period spanning anomalous climate conditions (e.g., [*Bond et al.*, 2015; *Jacox et al.*, 2016; *Frischknecht et al.*, 2017]), and so, the conclusions presented provide insight into how the CCS behaves during warm, stratified conditions. By comparing to other available datasets for the region the behavior of $\delta^{15}N$ nitrate-based during more normal climate periods was also briefly examined.

2. Materials and Methods

2.1. Study Location

The following study was embedded in the southern CCS region of the eastern North Pacific Ocean as part of the California Current Ecosystem (CCE) Long-Term Ecological Research (LTER) program. Sample locations, termed “Cycles”, typically extended from within 20 km of Point Conception to as far as 350 km from shore (Figure 4.1). Inshore locations close to Point Conception experience persistent upwelling conditions whereas Offshore locations resemble conditions of the North Pacific

Subtropical Gyre. Between these extremes is the southward flowing California Current [*Checkley* and *Barth*, 2009].

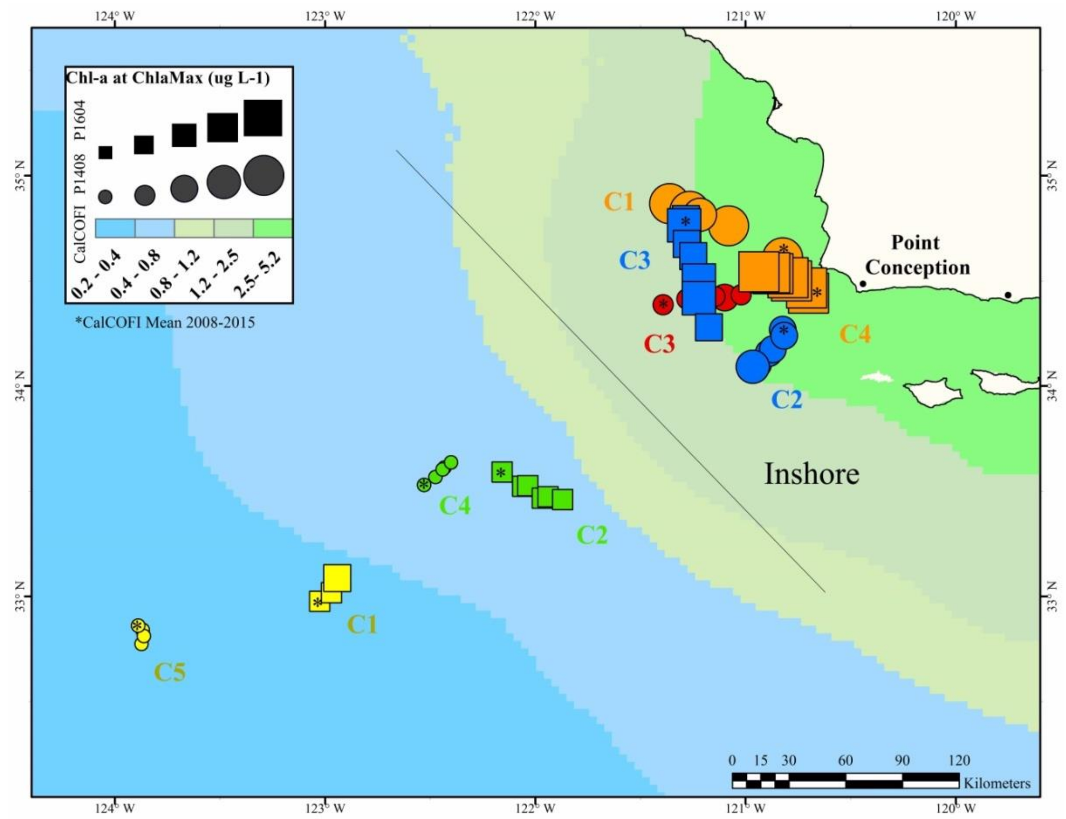

Figure 4.1. *Map of individual Cycles (C1, C2, etc.) for P1408 (circles) and P1604 (squares) cruises. Background blue-green colors coarsely delineate regions by Chl-a concentrations based on the long-term (2008 - 2015) interpolated CalCOFI mean Chl-a at the Chl-a maximum depth. The size of each Cycle symbol is scaled to Chl-a concentrations as indicated in the legend. Cycle colors are conserved throughout the document. An asterisk inside a Cycle symbol marks the starting location for each Cycle, and the diagonal line separates "Inshore" Cycles from "Offshore" Cycles.*

Samples for this study were collected during CCE process cruises P1408 and P1604, which took place during August 8 to September 9, 2014 and April 22 to May 10, 2016, respectively. Samples were collected daily for each Cycle from noontime casts via Niskin bottles. Each Cycle lasted between 2 to 4 days, and a drifter array with a subsurface drogue centered around 15 m enabled the ship to nominally follow the same surface water mass throughout each Cycle. Depth profiles extended from the surface to the 0.01% light level, typically <150 - 200 m, and at least one sample was collected from >200 m for each Cycle.

2.2. Sample Collection and Analysis

2.2.1. Nutrient and Chlorophyll-a Concentrations

Samples for dissolved inorganic nutrients ($[NO_3^-]$, $[NO_2^-]$, $[NH_4^+]$) and chlorophyll-*a* concentrations were collected on upcasts from CTD Niskin bottles triggered at 10 discrete depths. These depths purposely spanned different light levels and chlorophyll-*a* distributions as estimated from CTD fluorometer profiles. Samples collected for nutrients were filtered through GF/F filters (47 mm, Whatman), frozen, and analyzed by flow injection analysis at UC Santa Barbara. Chlorophyll concentrations, hereafter Chl-*a*, were determined from GF/F (25 mm, Whatman) filters extracted into 90% acetone, and measured onboard using a Turner Designs10AU Fluorometer after storage for 24 hours at -18° C [*Goericke*, 2002].

2.2.2. δ^{15}N and δ^{18}O of Nitrate

Nitrate $\delta^{15}N_{NO3}$ and $\delta^{18}O_{NO3}$ were measured on 0.7 μm-filtered (precombusted GF/F, 47 mm, Whatman) seawater collected directly from Niskin bottles and stored in 60 mL HDPE bottles at -80° C until analysis. Samples were analyzed on an IsoPrime mass spectrometer following the denitrifier method [*Sigman et al.*, 2001; *Casciotti et al.*, 2002], with nitrite removed (sulfamic acid method [*Granger et al.*, 2006]). Typical error for $\delta^{15}N_{NO3}$ and $\delta^{18}O_{NO3}$ on duplicate measurements of the same nitrate sample was

0.2‰, which was similar to the 0.3‰ precision of internal quality control nitrate standards.

2.2.3. Stable Isotopes of Suspended and Sinking POM

Seawater for suspended particulate organic matter (POM) isolation was collected from Niskin bottles into 4 L acid-washed Nalgene bottles that were wrapped in black plastic to minimize the influence of light. Between two to four liters of this water was immediately filtered under low vacuum (<50 mm Hg) onto pre-combusted GF/F filters (47 mm, Whatman). Predicting the amount of water necessary to provide adequate carbon and nitrogen for isotope measurements from each region was fairly straightforward as particulate organic carbon and nitrogen concentrations ([POC] and [PON], respectively) and their relationship to Chl-*a* in the region are very well constrained due to regular sampling by the CalCOFI program (see dissertation author's Chapter II; *Stephens et al.*, in prep). After filtration, each filter was wrapped in pre-combusted foil, sealed in plastic bags and stored at -80° C until processing for stable isotopes.

Sinking POM was collected from 2 to 3 discrete depths into a Vertex-style drifting sediment trap array as described previously in *Stukel et al.* (2013). Sediment trap tubes contained a slurry of 0.1 μm-filtered seawater mixed with 50 g L^{-1} NaCl, to reduce resuspension of particles, and 4% formaldehyde to reduce biological degradation of organic matter. Particles were filtered onto pre-combusted GF/F filters (25 mm, Whatman) and stored in pre-combusted foil and zip locks bags at -80 °C until further processing for stable isotopes. Visible organisms and animal parts were picked off the filter prior to freezing.

Suspended and sinking POM samples were processed for $\delta^{15}N$ and $\delta^{13}C$ measurements after prior methods for [POC] and POM stable isotope measurements [*Sharp*, 1974; *Altabet*, 1990]. Filters were first oven-dried overnight at 60° C and then acid fumigated in a desiccator the second night to minimize inorganic carbon contamination of $\delta^{13}C$ signatures. Following fumigation, samples were briefly (~1 - 2 hr) heated again at 60° C to dry the filters and provide consistent initial weights. The filter was folded into quarter folds and the center of each filter was extracted and placed into pre-weighed tin cups. Tin cups were stored in a sample tray inside a desiccator for at least 24 hr but not longer than 14 d, until analysis. Blank filters were prepped in the same manner to constrain process blanks.

Filter material was analyzed for N and C mass and stable isotopes on an elemental analyzer (Costech, model ECS 4010) coupled to an isotope ratio mass spectrometer (Thermo, model Delta Plus XP) at Scripps Institution of Oceanography’s unified laboratory facility. The measured isotope value varies as a function of the area response of the sample, and at low N concentrations the response deviates dramatically from a linear relationship. To correct for this bias, nine different quantities of finely powdered acetanilide standards (Baker AO68-03, Lot A15467) of constrained isotopic value were dispersed throughout each run. Absolute isotopic values were then estimated using a mixture of acetanilide and calcium carbonate of known isotopic value. Standards were cross-calibrated to NBS-19 limestone in terms of Vienna Pee Dee Belemnite and IAEA-

N1 (USGS 8547) ammonium sulfate in terms of pure N_2 gas from air. When sample quantities began to approach the limit of detection (~1 μg N and 10 μg C), additional acetanilide standards spanning the 2 to 30 μg N range were added to better constrain the instrument response for low mass samples. The isotopic error for each measurement was then determined as a function of the area response. Reported error bars combined the instrumental error as above and the standard deviation of measurements, and when averaged across multiple samples were propagated using a sum of square error procedure.

2.2.4. Collection and Analysis of *Calanus pacificus* Copepods

For a single day of each Cycle, adult female *Calanus pacificus* (*Cp*) were collected by 0.5 mm double oblique tows with a 1 m diameter ring net. Samples were collected for depths 0 to 200 m and preserved in formaldehyde-seawater buffered with sodium tetraborate. To prepare *Cp* samples for stable isotope analysis, organisms were first washed three times with filtered seawater then washed three times with MQ and finally dried at 60°C overnight. For each cycle, triplicate analyses were performed on tins containing three individuals, and so the error shown here represents ±1σ across the three replicate samples for each cycle.

Carbon isotope data are used for some discussions throughout this chapter, and prior isotopic analyses of *Calanus pacificus* (and similar organisms) preserved in formaldehyde have identified a substantial decrease in $\delta^{13}C$ compared to frozen samples [*Sarakinos et al.*, 2002; *Rau et al.*, 2003]. In this study, *Cp* samples were preserved in formaldehyde and stored for less than one year prior to analysis but were also compared with concurrently collected and subsequently frozen *Cp* samples. The decrease in $\delta^{13}C$ of preserved samples when compared with frozen *Cp* was less than 0.4‰ on average but up to 0.8‰ for one sample. *Sarakinos et al.* (2002) found an average decrease in $\delta^{13}C$ of 1.65‰ for formalin preserved samples as compared to frozen samples. Their data indicated that the isotopic shift occurred within a few days of storage but was stable thereafter with time. Overall, the available data support the conclusion that differences between samples documented in the current study could be influenced by formaldehyde but *Cp* $\delta^{13}C$ offsets between study regions likely represent real environmental differences. For example, the $\delta^{13}C$ difference between study regions (2 - 3‰) exceeded the offset due to preservatives alone (up to 0.8‰).

2.2.5. Nucleic Acid Isolation for Phylogenetic Analyses

During P1604 surface samples (~12 m depths) for DNA-based estimations of eukaryotic community composition (i.e., 18s) were isolated from CTD Niskin bottles. Approximately 1.8 L of seawater were collected into opaque HDPE bottles and immediately filtered through 0.1 µm-size cut off sterivex filters (EMD Millipore) with a peristaltic pump. Sample collection and processing time did not exceed 45 minutes. Dry filters were capped with putty, immediately flash frozen in Whirlpak bags and stored at -80 °C until further processing. RNA was extracted following protocols developed in Dr. Andrew Allen’s lab by Ariel Rabines (JCVI), where sterivex filters were first cracked open using pipe cutters. The RNA was then purified using Macherey-Nagel’s NucleoMag 96 RNA Kit (Ref # 744350.1). The quality and quantity of RNA were determined using an Agilent RNA ScreenTape System. cDNA was then extracted using Life Technology’s SuperScript III First-Strand Synthesis System (Cat. #: 18080-051) and was used as the template for 18s PCR experiments. Products of the PCR were analyzed for community composition at the Institute for Genomic Medicine at the University of California-San Diego. Operational taxonomic unit (OTU) reads were based on the V4 hypervariable region of the 18s rRNA gene for all samples.

3. Results

Cruises P1408 and P1604 sampled anomalously warm (up to 2 - 4° C warmer within the surface 100 m) conditions in the CCE [*Zaba* and *Rudnick*, 2016; *Frischknecht et al.*, 2017]. Surface NO_3^- at the time of sampling were also anomalously low (up to 4 μM lower in the surface 10 - 50 m) compared to the long-term record of NO_3^- from California Current Cooperative Oceanic Fisheries Investigation (CalCOFI) survey cruises (dissertation author's Chapter III Figure S3.2; [*McClatchie et al.*, 2016]). Surface NO_3^- was below detection (<0.02 μM) at the immediate surface for all Cycles of P1408 and near the detection limit for most Cycles of P1604 (Figure 4.2). Near the depth where Chl-*a* peaked NO_3^- was 3 - 10 μM, with Offshore Cycles having lower surface concentrations (Figure 4.2).

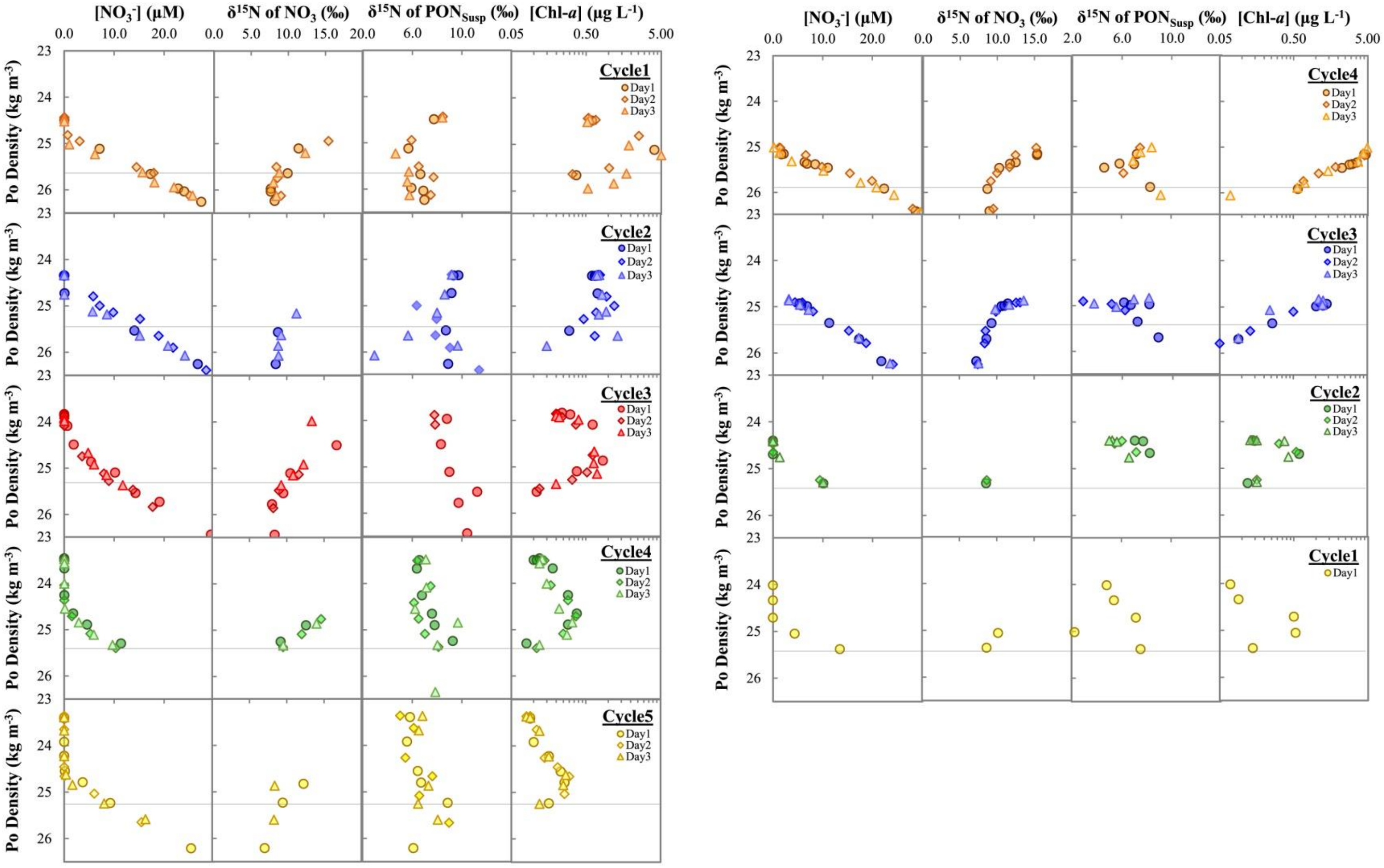

Figure 4.2. *Profiles on the left panel were collected during CCE cruise P1408 and the set on the right were collected during P1604. The horizontal gray line in the figures is the remnant mixed layer depth, or the location of 'source' nitrate as discussed in Sec 3.1.*

The average deep water $\delta^{15}N_{NO3}$ during P1408 and P1604 was 8.2 ± 0.7‰ (n=23) for NO_3^- between 22 and 40 μM and potential densities between 25.9 and 26.8 kg m^{-3}. Vertical profiles of NO_3^- showed drawdown in the surface ocean at all Cycles and $\delta^{15}N_{NO3}$ became enriched as NO_3^- decreased. This observation is consistent with the expected fractionation of N isotopes during nitrate uptake by phytoplankton [*Sigman et al.,* 2010]. For example, detectable $\delta^{15}N_{NO3}$ enrichment over the deep water isotope value was often observed at the depth where Chl-a was first detected (Figure 4.2), and $\delta^{15}N_{NO3}$ was significantly (Mann-Whitney, $p<0.01$) enriched by 2 - 3‰ within the Chl-*a* maximum depth relative to deeper waters.

3.1. Source Nitrate to the Euphotic Zone

Prior studies in the CCS demonstrated that the $\delta^{15}N_{NO3}$ of deep waters (>200 m) increases moving southward along the coast from 8.0‰ near Monterey Bay to 9.0‰ within the Southern California Bight to 10.0‰ off of Baja California [*Liu* and *Kaplan*, 1989; *Altabet et al.*, 1999; *Sigman et al.*, 2005; *Wankel et al.*, 2007; *Santoro et al.*, 2010]. Due to coastal upwelling and mesoscale activity the $\delta^{15}N_{NO3}$ entering the euphotic zone at any given location along this gradient can be variable. For instance, the vertical structure of the water column includes water masses of alternating northern and southern origin [*Checkley* and *Barth*, 2009] with markedly different physical and chemical characteristics. Interannual and decadal climate variability can also impact the strength of these water masses of differing northern and southern origins, which in turn can influence the $\delta^{15}N_{NO3}$ of source nitrate entering the food web [*Deutsch et al.*, 2014; *Tems et al.*, 2015].

The water column structure at the time of each CCE cruise had to be examined in order to establish the characteristics of nitrate upwelling into the surface ocean, and the combination of temperature and salinity can be used to distinguish the physical structure of surface waters in the CCE. In winter, the surface water column becomes well-mixed, but as surface warming proceeds a seasonal, surface mixed layer develops [*Cole et al.*, 2010; *Todd et al.*, 2012]. Below this seasonal mixed layer, a more stable feature termed the remnant mixed layer is distinguished by the salinity signature of the wintertime mixed layer [*Cole et al.*, 2010]. This remnant mixed layer feature is present throughout the central and eastern North Pacific [*Cole et al.*, 2010; *Todd et al.*, 2012].

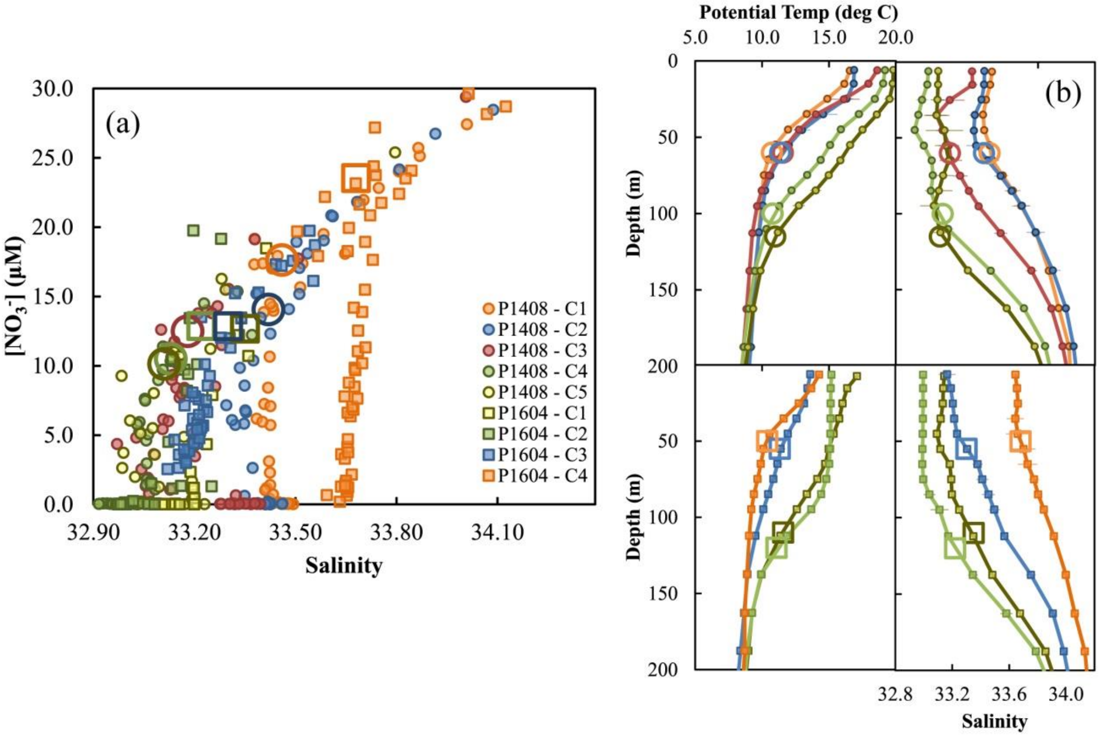

Figure 4.3. *Nitrate versus salinity for P1408 and P1604 Cycles (a), and associated depth profiles of potential temperature and salinity with P1408 properties on top and P1604 properties on the bottom (b). Large open symbols identify source waters for each Cycle as determined based on wintertime mixed layer salinity values and a prescribed vertical gradient in salinity. Above these depths, NO_3^- concentrations typically begin to decrease rapidly.*

The remnant mixed layer presents a stratification barrier to mixing with waters below it (e.g., [*Cole et al.*, 2010; *Todd et al.*, 2012]), and so, properties of the remnant mixed layer should represent the primary concentration and isotopic signature of NO_3^- delivered to the euphotic zone during spring and summer. A similar argument was made based on wintertime resetting to identify source $\delta^{15}N_{NO3}$ in the Subantarctic Zone [*DiFiore et al.*, 2006]. The base of the remnant mixed layer was identifiable here for cruises P1408 and P1604 using mixed layer salinities recorded for the preceding fall (November of 2013, no winter values were available) and winter (January 2016) by CalCOFI cruises on line 080.0 (Figure S4.1). The bottom of the remnant mixed layer also corresponded to a depth where the salinity gradient began to exceed 0.03 salinity units per meter (Figure 4.3).

Table 4.1. *Water mass properties that were used to establish source NO_3^- depth and characteristics. The isotope effect (ε_p) was estimated based on a Rayleigh model fit to $\delta^{15}N_{NO3}$ data from each Cycle as shown in Figure 4.6 and Table S4.1.*

Cruise	Cycle	Remnant Mixed Layer Depth (m)	Salinity (psu)	Temp (deg C)	Density (kg m^{-3})	[NO_3^-] source (μM)	δ^{15}N NO_3 source (‰)	ε_p (‰)
P1408	1	*60*	*33.5±0.06*	*10.7±0.3*	*25.6±0.09*	*17.6±1.7*	8.5	3.20
	2	*60*	*33.4±0.08*	*11.6±0.5*	*25.4±0.14*	*14.1±2.2*	9.0	3.20
	3	*60*	*33.2±0.06*	*11.4±0.5*	*25.3±0.07*	*10.0±1.8*	9.5	3.75
	4	*100*	*33.2±0.02*	*10.8±0.3*	*25.3±0.06*	*8.5±2.0*	9.3	3.50
	5	*115*	*33.3±0.04*	*11.0±0.3*	*25.3±0.05*	*10.1±1.2*	9.4	2.50
P1604	1	*110*	*33.3±0.03*	*11.6±0.3*	*25.4±0.07*	*12.7±3.1*	8.6	1.50
	2	*120*	*33.2±0.03*	*11.1±0.3*	*25.4±0.08*	*12.9±3.9*	8.6	1.50
	3	*55*	*33.3±0.04*	*11.3±0.5*	*25.4±0.10*	*12.9±1.5*	8.9	3.00
	4	*50*	*33.7±0.06*	*10.4±0.3*	*25.9±0.05*	*23.5±2.7*	8.7	2.75

During CCE cruises the density at the base of the remnant mixed layer was between 25.3 ± 0.1 and 25.9 ± 0.1 kg m^{-3} (Table 4.1). For comparison, the remnant mixed layer density identified previously for the eastern North Pacific was 25.4 kg m^{-3} [*Cole et al.*, 2010]. At these densities, NO_3^- was between a low of 8.5 ± 2.0 µM (P1408 Cycle 4, an Offshore Cycle) and a high of 23.5 ± 2.7 µM (P1604 Cycle 4, an Inshore Cycle). For most Cycles of P1408 and P1604, remnant mixed layer NO_3^- was between 14 and 17 µM (Table 4.1). The higher density at the base of the remnant mixed layer during P1604 Cycle 4 was indicative of enhanced upwelling conditions and the influence of a more saline, deeper water mass.

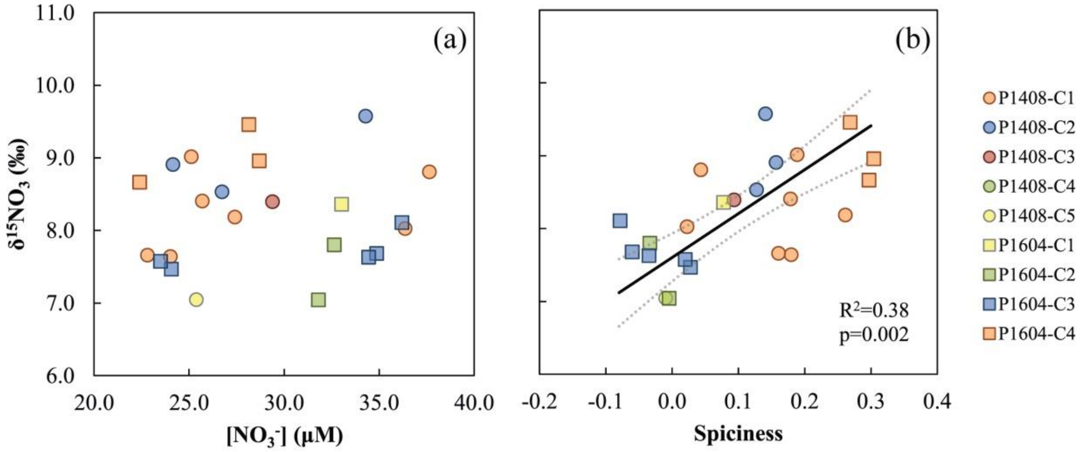

Figure 4.4. *CCE deep water* $\delta^{15}N_{NO3}$ *versus* NO_3^- *(a) and* $\delta^{15}N_{NO3}$ *versus spiciness (b). Only samples with* NO_3^- *between 22 and 40 µM are shown here to illustrate differences in deep water* $\delta^{15}N_{NO3}$ *across the CCE study region.*

The $\delta^{15}N_{NO3}$ of deeper waters across the CCE (densities between 25.9 - 26.8 kg m^{-3} and NO_3^- between 22 and 40 µM; n=23) was largely separated based on spiciness (Figure 4.4) [*Munk*, 1981], a measure that can serve as an indicator for waters of northern (less spicy) or southern (more spicy) origin [*Todd et al.*, 2012; *McClatchie et al.*, 2016]. Inshore Cycle 4 of P1604 had the highest $\delta^{15}N_{NO3}$ (9.0 ± 0.4‰) and spiciness values

(0.29 ± 0.02) (Figure 4.4), consistent with a deep water signature influenced by southern component waters. However, this Cycle exhibited a remnant mixed layer $\delta^{15}N_{NO3}$ that was slightly depleted (8.7‰; Table 4.1) relative to the associated deeper waters. Other Inshore sites showed similarly complex source signatures between deep waters and the remnant mixed layer depth. For example, at P1408 Cycle 1, $\delta^{15}N_{NO3}$ was depleted at for some deep waters (7.7‰ for NO_3^- of 23 μM) and slightly enriched elsewhere (8.5 ± 0.4‰ for NO_3^- of 30 ± 6 μM), potentially highlighting the complex layering of water masses at this site. Deep water for Cycle 2 of P1408 exhibited a stronger influence of southern component water as inferred by spiciness (0.14 ± 0.01) and $\delta^{15}N_{NO3}$ (9.0 ± 0.5‰), an isotopic value that was similar to its remnant mixed layer depth. During P1604 Cycle 3, despite being an Inshore Cycle with relatively enriched remnant source isotope (8.9‰), deep water plotted more closely to California Current waters (7.7 ± 0.2‰), which are sourced from the north.

As described above for most cases, the remnant mixed layer signatures (Table 4.1) were distinct from those of deeper waters (Figure 4.4), which indicated that the remnant mixed layer was isolated from waters below it. On average, $\delta^{15}N_{NO3}$ at remnant mixed layer source depths have a composition of 8.9 ± 0.4‰ (ranging between 8.5 and 9.5‰ for $NO_3^- < 25$ μM; Table 4.1) whereas the $\delta^{15}N_{NO3}$ of deeper waters was 8.2 ± 0.7‰ at these locations (densities between 25.9 - 26.8 kg m^{-3} and NO_3^- between 22 and 40 μM; n=23). Similar depleted deep values ~8.0‰ have been previously reported for Monterey Bay [*Altabet et al.*, 1999; *Wankel et al.*, 2007; *Santoro et al.*, 2010].

The overall lower NO_3^- and higher $\delta^{15}N_{NO3}$ of the remnant mixed layer was consistent with a residual signature of nitrate utilization (lower NO_3^- but higher $\delta^{15}N_{NO3}$ than deeper waters). This is the layer that directly supplies nitrate to the seasonal mixed layer and such a connection was confirmed by the Rayleigh model discussed below. Below the remnant mixed layer, changes in physical and chemical characteristics are most likely a function of diapycnal and diffusion-based mixing [*Todd et al.*, 2012]. Mixing, as identified by changes in salinity, adequately explained gradients in NO_3^- and $\delta^{15}N_{NO3}$ below the remnant mixed layer depth.

3.2. Surface Nitrate Behavior

Regardless of the history of source $\delta^{15}N_{NO3}$, the behavior of surface $\delta^{15}N_{NO3}$ can now be modeled using the endmember values in Table 4.1 and either Rayleigh or open system isotope dynamics (e.g. [*Altabet et al.*, 1999; *Sigman et al.*, 2010]). In this formulation, phytoplankton preferentially utilize the lighter isotope of nitrate (^{14}N). The rate-limiting step in the conversion of nitrate to biomass is the intracellular reduction of nitrate to nitrite [*Granger et al.*, 2010]. At this step, the partially reduced, isotopically enriched (^{15}N) nitrate can exit the cell. As a result, as the nutrient concentration decreases the $\delta^{15}N_{NO3}$ in the surrounding medium (i.e., seawater) increases [*Granger et al.*, 2004, 2010; *Needoba et al.*, 2004]. If nitrate is not re-supplied (or only slowly supplied) to the surface ocean as it is depleted during photosynthesis then the isotopic behavior of nitrate can be modeled using a closed system Rayleigh model. However, if upwelling is ongoing, then an open system model has been shown to be more appropriate (e.g., [*Hayes*, 2002; *Sigman et al.*, 2010]). In an open system, a linear enrichment of

$\delta^{15}N_{NO3}$ accompanies the decrease in NO_3^- Eq (1), and in a Rayleigh formulation, the $\delta^{15}N_{NO3}$ reservoir becomes exponentially enriched as concentration decreases Eq (2):

$$\delta^{15}NO_{3_{observed}} = \delta^{15}NO_{3_{source}} + \varepsilon_p\{u\}, \quad (1)$$

$$\delta^{15}NO_{3_{observed}} = \delta^{15}NO_{3_{source}} - \varepsilon_p\{ln(1-u)\}, \quad (2)$$

where $\delta^{15}NO_{3observed}$ is the $\delta^{15}N_{NO3}$ of the sample from the euphotic zone, $\delta^{15}NO_{3source}$ is the estimated $\delta^{15}N_{NO3}$ of upwelling nitrate, ε_p is the kinetic fractionation factor for nitrate uptake by the community (i.e., the slope of a linear fit to data plotted as either *u* or *ln*(1-*u*) versus $\delta^{15}NO_{3observed}$), and *u* is the fraction of source NO_3^- that has been utilized.

Upwelling conditions of spring and summer in the CCE (e.g., 30 to 35°N; [*Bakun* and *Nelson*, 1991]) may enrich $\delta^{15}N_{NO3}$ in an open system manner. Samples collected during 2010-2013 from nearby Inshore CalCOFI stations (line 080.0 stations 051.0 (34.45°N 120.53°W), 055.0 (34.32°N 120.8°W), and 060.0 (34.15°N 121.15°W) exhibited open system $\delta\ ^{15}N_{NO3}$ enrichment with decreasing in NO_3^- (Figure 4.5 open circles; *Rafter et al*., unpublished; *White et al.* unpublished). However, samples collected in 2014 (North Pacific warm pool) and 2016 (following the strong El Niño of 2015 - 2016) when anomalously warm conditions prevailed, exhibited a pattern of $\delta^{15}N_{NO3}$ enrichment that fit better to a Rayleigh, closed system model (Figure 4.5, CalCOFI cruises and CCE cruises).

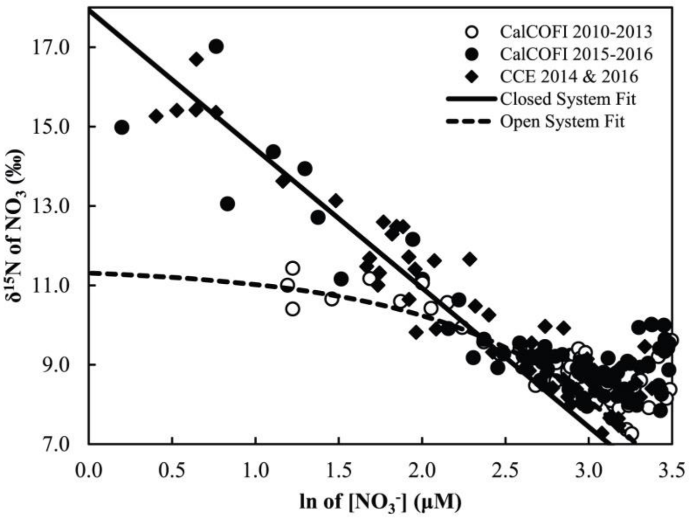

Figure 4.5. *Nitrate isotope signatures in the surface ocean fit either with an open system model (open circles, CalCOFI cruises between 2010-2013) or closed system Rayleigh model (CCE P1408 and P1604, closed diamonds; CalCOFI 2015 - 2016, closed circles). For simplicity, we only show a single open model fit (data from CalCOFI Cruise 201010 stations 080.0 051.0 and 080.0 055.0 using source N characteristics of 17.9 μM* NO_3^-*,* $\delta^{15}N_{NO3}$ *of 8.5‰ and* ε_p *of 3.0‰) and a single closed system model fit (CalCOFI Cruise 201601 with a source [*NO_3^-*] of 12.6 μM,* $\delta^{15}N_{NO3}$ *of 9.1‰, and* ε_p *of 3.5‰).*

A model fitting exercise was then carried out to identify cycle-specific fractionation factors for nitrate uptake (ε_p). In this case, the ε_p was varied and source $\delta^{15}N_{NO3}$ and NO_3^- were kept constant (Table 4.1) to identify the ε_p that resulted in the lowest mean absolute difference between predicted and observed $\delta^{15}N_{NO3}$ values ($\delta^{15}NO_{3observed}$) for each Cycle. Models that were ultimately selected had a mean difference from observations of ±0.3‰ for all Cycles, and the range was 0.09 - 1.70‰ (Table S4.1). The average fractionation factor was 3.0 ± 0.5‰ for Inshore cycles, but these values were generally lower in the Offshore, ranging from 1.5 to 3.0‰ (Figure 4.6; Tables 4.1 and S4.1). An isotope effect of 3.0 ± 0.3‰ was also estimated for 2015 - 16 CalCOFI samples based on a similar approach but using individual CalCOFI profiles.

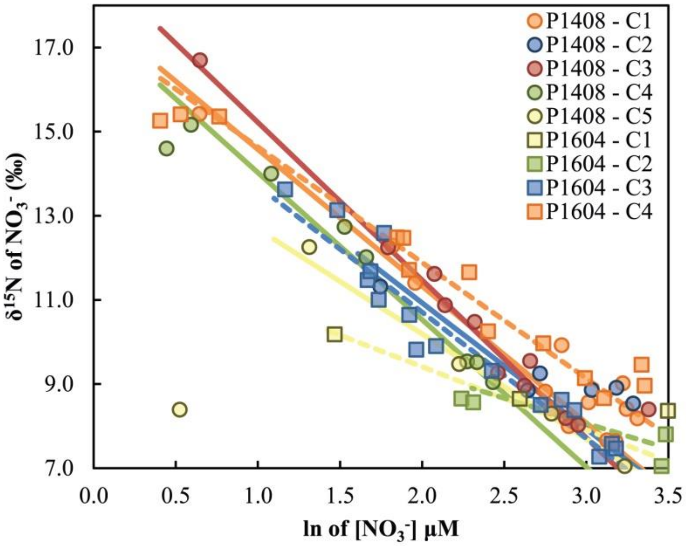

Figure 4.6. *Rayleigh model curve fits to CCE* $\delta^{15}N_{NO3}$ *observations where solid lines are for P1408 and dashed lines are P1604 (model constants are provided in Table 4.1).*

In a closed system, surface $\delta^{15}N_{NO3}$ becomes exponentially enriched (i.e., Figures 4.5 and 4.6) because the rate of vertical nitrate exchange by physical processes is lower than the rate of uptake by phytoplankton. Typical vertical transport rates for Point Conception are between 0.5 and 1.5 m d^{-1} (e.g., [*Rykaczewski* and *Checkley*, 2008; *Haskell et al.*, 2016]), but California Current state estimates for locations near the P1408 and P1604 Inshore Cycles were an average of 0.32 ± 0.17 m d^{-1} near the remnant mixed layer depth (Figure S4.2). At these rates it would take several weeks to move water from the remnant mixed layer into the chlorophyll maximum as compared to an estimated 7 - 10 days for phototrophic biomass turn over (e.g., [*Falkowski et al.*, 2003]). For comparison, complete nitrate uptake during an upwelling pulse took approximately 3 to 7 days [*Zimmerman et al.*, 1987; *Wilkerson et al.*, 2006]).

3.3. Organic Matter and the Food Web

In the current study, suspended and sinking POM, and an abundant copepod in the CCE, *Calanus pacificus*, were collected to examine the isotopic relationship between $\delta^{15}N_{NO3}$ and other N reservoirs in the regional food web. Previous studies in the region have examined nutrient cycling on short and long timescales, but in many cases they had to assume values to define connections to $\delta^{15}N_{NO3}$ (e.g., [*Rau et al.*, 1998, 2003; *Ohman et al.*, 2012; *Deutsch et al.*, 2014]).

3.3.1. δ^{15}N of Suspended POM

The average δ^{15}N of suspended POM ($\delta^{15}N_{Susp}$; ~>0.7 µm) of all CCE P1408 and P1604 samples collected over 0 - 100 m depths was 7.0 ± 1.6‰ (range of 2.3 - 11.2‰, n = 110) (see Figure 4.2 for profiles). For comparison, $\delta^{15}N_{Susp}$ collected from surface waters off Monterey Bay had mean values of ~6‰ (range 1.3 - 7.6‰) between 1993 - 1997 [*Rau et al.*, 1998] and 5.9 ± 1.3‰,(3.5 - 9.7‰) between 2007 - 2009 [*Walker* and *McCarthy*, 2012]. With depth, $\delta^{15}N_{Susp}$ increased by an average of 1.6 ± 0.8‰ beneath the euphotic zone, similar to previously published profiles in the North Pacific [*Saino* and *Hattori*, 1980, 1987]. P1408 Cycles 2 and 3 exhibited a significant (Mann-Whitney, $p<0.01$) enrichment of 1.5 - 2.0‰ across all densities compared to other Cycles (Figure 4.2). At P1408 Cycle 3 this observed enrichment was consistent with strongly enriched surface $\delta^{15}N_{NO3}$ (Figure 4.2) and suggests a transfer of source nutrient isotope signatures into the suspended pool.

Table 4.2. *Stable isotope signatures of suspended PON ($\delta^{15}N_{Susp}$) averaged within ±10 m of the Chl-a max depths (see Figure 4.1 for locations), sinking PON ($\delta^{15}N_{Sink}$) captured in floating sediment traps at 100m and adult female Calanus pacificus (Cp; $\delta^{15}N_{Cp}$) copepods. All values are in units of per mil and the error is a propagation of instrumental error and the deviation across multiple measured samples.*

Cruise	Cycle	$\delta^{15}N_{Susp}$ ±10m Chl-a Max (‰)	$\delta^{15}N_{Sink}$ at 100m (‰)	$\delta^{15}N$ of *Cp* (‰)
P1408	1	*5.4±0.9*	*8.9±0.2*	*9.7±0.6*
	2	*8.2±1.4*	*10.2±0.6*	*10.3±0.4*
	3	*8.1±0.3*	*10.6±0.7*	*12.2±0.4*
	4	*7.8±1.4*	*9.6±0.8*	*11.8±0.2*
	5	*7.0±0.5*	*9.6±0.3*	*11.4±0.6*
P1604	1	*2.3±0.5*	*11.0±1.3*	*11.4±0.3*
	2	*7.3±0.8*	*9.0±0.6*	*10.5±0.3*
	3	*6.5±1.1*	*8.0±0.6*	*9.4±0.6*
	4	*5.9±1.2*	*8.1±1.2*	*10.3±0.4*

For each Cycle, the $\delta^{15}N_{Susp}$ at the depth of the Chl-*a* maximum was significantly (Mann-Whitney, $p<0.02$) depleted by ~0.9 ± 0.5‰ (Figure 4.2) compared to suspended POM from other depths. Averaged across all CCE Cycles, $\delta^{15}N_{Susp}$ (averaged ±10m within the Chl-*a* maximum depth) was 6.5 ± 0.4‰ (Table 4.2; range of 2.3 to 8.2‰). A brief study in the summer of 2015 based on size-fractionated Chl-a demonstrated that a greater proportion of the Chl-*a* was contributed by larger cell sizes near the Chl-*a* max depth (Figure S4.3). This size distribution was reminiscent of the observed increase in larger cell sizes with increasing Chl-*a* in the CalCOFI domain [*Goericke*, 2011]. Taken together, the contribution of more depleted $\delta^{15}N_{Susp}$ near the Chl-*a* maximum depth and the greater proportion of larger cell sizes at these depths indicated that actively growing, large phytoplankton may have contributed disproportionately to POM at these depths

[*Eppley et al.*, 1977]. A similar argument based on $\delta^{15}N_{Susp}$ was presented for the western North Pacific [*Saino* and *Hattori*, 1987].

3.3.2. δ^{15}N of Sinking POM

Sinking POM was collected from drifting sediment trap arrays typically deployed for three to four days during each Cycle (see methods described in *Stukel et al.* (2013)). The average δ^{15}N of sinking POM ($\delta^{15}N_{Sink}$) from 100 m trap depths across all Cycles was 9.5 ± 1.0‰ (ranges 8.9 - 11.0‰; Table 4.2). Bi-weekly $\delta^{15}N_{Sink}$ collected at a depth of 450 m off Monterey Bay from 1989 to 1992 was 7.8‰ on average but was 6 - 7‰ during spring periods of enhanced nitrate delivery and 8 - 9‰ during other seasons [*Altabet et al.*, 1999]. Inside the Southern California Bight, near the San Pedro Basin, the $\delta^{15}N_{Sink}$ of sediment trap material collected in May 1983 at 100 m was 7.8 - 8.0‰ [*Nelson et al.*, 1987], similar to material collected at 500 m near San Pedro from January to July 1988 averaging 8.0‰ (range 6.9 to 10.7‰) [*Altabet et al.*, 1999]. A longer term study of weekly samples collected near San Pedro at 550 m averaged 8.9‰ (range 6.8 to 12.0‰) during January 2004 to December 2007 but was also slightly depleted during spring and summer months [*Collins et al.*, 2011]. These values are similar to recent (2005 - 2010) sediment trap $\delta^{15}N_{Sink}$ of ~7.8 - 8.4‰ collected at 500 m in the nearby Santa Barbara Basin [*Deutsch et al.*, 2014].

Available evidence suggests that the sinking organic matter collected during short-term deployments of floating sediment traps in the CCE to primarily derive from zooplankton fecal pellets, with little evidence that sinking phytoplankton contribute directly to this flux (e.g., [*Stukel et al.*, 2013]). Microscopic enumeration has shown sediment traps to primarily contain a combination of amorphous processed particulate aggregates or intact fecal pellets [*Stukel et al.*, 2013]. The $\delta^{15}N_{Sink}$ at 100 m was 2 - 3‰ more enriched than $\delta^{15}N_{Susp}$ from the Chl-*a* maximum (Table 4.2). If $\delta^{15}N_{Susp}$ from Chl-*a* max depths reflected the isotope composition of primary producers, as argued previously, then these data would suggest that phytoplankton biomass did not directly contribute to the sinking flux at this time. Additionally, three depths were used to capture sinking POM in the CCE (trap depths at 60 m, 100 m, and 150 m), and a comparison across these depths showed no systematic change in $\delta^{15}N_{Sink}$ and trap C:N indicating that there was no major reworking of sinking organic matter during sinking (Figure S4.4).

3.3.3. δ^{15}N of *Calanus pacificus*

The copepod *Calanus pacificus* (*Cp*), an abundant primary consumer in the CCE [*Ohman et al.*, 1998], was collected here by early morning surface net tows for each Cycle. The isotopic signature of adult female *Cp* from Inshore Cycles was 10.4 ± 0.3‰ (Table 4.2), similar to the long-term median of CalCOFI archived *Cp* (10.7 ± 0.5‰; [*Ohman et al.*, 2012]). In the Offshore CCE, the average $\delta^{15}N_{Cp}$ was 11.3 ± 0.3‰ (Table 4.2). One Cycle, P1408 Cycle 3, exhibited a significantly ($p<0.01$, Mann-Whitney) enriched $\delta^{15}N_{Cp}$ of 12.2 ± 0.4‰ compared to long-term means for the region [*Ohman et al.*, 2012]. This Cycle also exhibited enriched $\delta^{15}N_{Sink}$ and $\delta^{15}N_{Susp}$ (Table 4.2), suggesting a coherence across these reservoirs at that time.

Cp is found within the upper 100 m of the water column and migrates daily between the surface and the base of the euphotic zone [*Ohman et al.*, 1998]. Their primary prey are larger-sized autotrophic organisms [*Frost*, 1972, 1977] but as filter feeders they can also ingest smaller heterotrophic organisms [*Landry*, 1981] and non-living organic particles [*Dilling et al.*, 1998]. Given its wide range of habitat and potential diet, Chl-a max (±10 m) $\delta^{15}N_{Susp}$ should reflect the isotopic composition of *Cp*'s diet. On average, $\delta^{15}N_{Cp}$ was elevated by $3.7 \pm 0.8‰$ relative to $\delta^{15}N_{Susp}$ (Table 4.2; excluding P1604 Cycle 1), an offset that is consistent with the expected isotopic enrichment associated with new biosynthesis of peptides [*Bada et al.*, 1989] and preferential excretion of isotopically-depleted nitrogen [*Gannes et al.*, 2007] by mesozooplankton.

4. Discussion

Overall, the observed $\delta^{15}N_{NO3}$ of deep waters (> 200 m) in the CCE region, 7.0 - 9.5‰, spanned the range measured in previous studies (e.g., [*Liu* and *Kaplan*, 1989; *Altabet et al.*, 1999; *Sigman et al.*, 2005; *Wankel et al.*, 2007; *Santoro et al.*, 2010]). The lowest deep water $\delta^{15}N_{NO3}$ values were linked to Offshore sites (P1408 Cycles 4 and 5 and P1604 Cycle 2) and higher values were observed for P1408 Cycles 1, and 2 and P1604 Cycle 4 (Figure 4.4). Long-term trends across multiple records, have shown that the source $\delta^{15}N_{NO3}$ off of the Central and Southern California coasts has become enriched by ~1.0‰ since the late 1990's (from 7.0 to 8.0‰ in [*Deutsch et al.*, 2014; *Tems et al.*, 2015]). Waters in the 200 - 400m range (~California Undercurrent; [*Checkley* and *Barth,* 2009]) for the CCE Cycles were on average similar (~8.2 ± 0.7‰) to samples collected off Monterey Bay (~8‰) between 1997 and 2007 [*Altabet et al.*, 1999; *Wankel et al.*, 2007; *Santoro et al.*, 2010], and so, such trends suggest that there has been no obvious change in Undercurrent $\delta^{15}N_{NO3}$ off of Point Conception and northward.

The $\delta^{15}N_{NO3}$ at the base of the remnant mixed layer was 8.9 ± 0.4‰ (data in Table 4.1), which was enriched in $\delta^{15}N_{NO3}$ relative to deeper local waters and its NO_3^- was reduced. It is likely that nitrate at these depths bore the memory of prior nitrate utilization, which had not been reset by mixing with deeper waters due to the stratification gradient that existed below the remnant mixed layer [*Cole et al.*, 2010]. The remnant source $\delta^{15}N_{NO3}$ at Inshore sites during P1408 was 0.2 - 0.4‰ more enriched than similar locations sampled during P1604, which is consistent with the observed anomalous climatology to be strongly expressed during P1408 but to have dissipated by the spring of 2016 [*Jacox et al.*, 2016; *Zaba* and *Rudnick*, 2016; *Frischknecht et al.*, 2017].

For samples collected at nearby CalCOFI stations (Line 080.0, stations 051.0, 055.0 and 060.0) spanning climatologically distinct periods from 2010 to 2016, the remnant mixed layer had a mean $\delta^{15}N_{NO3}$ of 8.9 ± 0.3‰ (range of 8.3 to 9.4‰) and an average NO_3^- of 17 ± 3 μM (range of 13 to 22 μM). Across this record, the most enriched source $\delta^{15}N_{NO3}$ values ($\delta^{15}N_{NO3}$ of 9.2‰ and NO_3^- of 21 μM) for the Inshore CalCOFI record were observed during a relatively strong La Niña in the spring of 2010 [*Bjorkstedt et al.*, 2011] when upwelling near the coast was likely enhanced. The isotopic similarity between CalCOFI and CCE samples collected prior to the anomalous climate conditions of 2013 - 2016 indicated that there was not a broad scale change in source-water $\delta^{15}N_{NO3}$ spanning the 2010 - 2016 time period.

For CCE samples collected during cruises P1408 and P1604, a closed system Rayleigh model provided the closest fit of $\delta^{15}N_{NO3}$ whereas an open system model for nitrate uptake was often more appropriate at other times (Figure 4.5) when vigorous upwelling was re-supplying nitrate to the euphotic zone [*Sigman et al.*, 2010]. This behavior was observed at Inshore CalCOFI stations in previous sampling years but not during the anomalously warm conditions experienced during 2014 and 2016 (Figure 4.5). The Rayleigh system model found that a fractionation factor of ~ 3.0 ± 0.5‰ for nitrate utilization by phytoplankton was most common for Inshore Cycles. This value is lower than the mean oceanic fractionation factor of 4.0 to 6.0‰ [*Sigman et al.*, 1999; *Altabet,* 2001].

Using a closed system Rayleigh model, *Altabet et al.* (1999) estimated an ε_p of 3‰ based on all available $\delta^{15}N_{NO3}$ for Monterey Bay and a sub-euphotic $\delta^{15}N_{NO3\_source}$ of 8‰. Based on a break in $\delta^{15}N_{NO3}$ linearity *vs*. NO_3^- they then binned their dataset into two separate groups and reported an ε_p of ~5‰ for each group, arguing that each bin was associated with unique water masses. A similar approach was taken in the current study, where remnant mixed layer depths (~60 m) provided an analog for the shallower data bin from Monterey Bay (~80 m depth). Directly plotting the Monterey Bay data over CCE data revealed that the fractionation factor for nitrate uptake in Monterey Bay was higher than for the CCE (i.e., exhibiting a steeper slope in Figure S4.5). This difference in fractionation factor could be a result of distinct phytoplankton communities [*Needoba et al.*, 2003; *Granger et al.*, 2010] or differences in growth rate and nutrient limitation [*Montoya* and *Mccarthy*, 1995; *Difiore et al.*, 2010].

While a net fractionation factor of ~3.0‰ is less common for the open ocean (see summary table in [*Sigman et al.*, 1999]), low fractionation factors have been observed in cultures of some phytoplankton species. For example, dinoflagellates, some diatoms, and some chlorophytes have exhibited fractionation factors (2 - 4‰) similar to those observed during CCE cruises [*Montoya* and *Mccarthy*, 1995; *Waser et al.*, 2000; *Needoba et al., 2003; Granger et al.*, 2010]. However, environmental factors such as micronutrient or light limitation that slow down growth rates could also be responsible for lower fractionation factors.

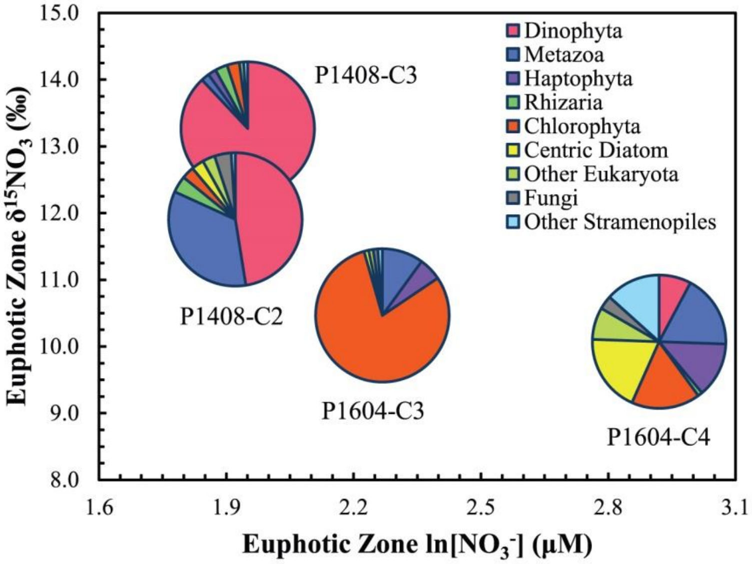

Figure 4.7. *Surface (~12m) Inshore eukaryotic community as determined based on the V4 region of 18s rRNA. Groups shown in the legend represent broad operational taxonomic units (OTUs) containing ~10k reads on average for the P1408 cruise and ~60k reads for the P1604 cruise. P1408 Cycle 1, with an* $\ln NO_3$ *of ~2.5 µM, was only processed for the V9 region but primarily contained Dinophyta (P1408 data courtesy A. Freibott and M. Landry).*

Eukaryotic community composition during each Inshore Cycle was examined by sequencing the hypervariable V4 region of the 18s rRNA gene. A relatively recent upwelling pulse at Inshore Cycle 4 of P1604 resulted in the highest euphotic zone NO_3^- and lowest euphotic zone $\delta^{15}N_{NO3}$ at this site and these conditions may have favored a relative increase the proportion of diatoms (i.e., other stramenopiles and centric diatoms; Figure 4.7). P1604 Cycle 3, with nearly 50% less surface NO_3^- as Cycle 4, exhibited a composition dominated by chlorophytes. During P1408 Cycles 2 and 3 (and Cycle 1, data not shown) dinoflagellates were prominent members of the phytoplankton community.

Overall, despite variations in the composition of the surface 12 m phytoplankton community for both CCE cruises across surface NO_3^- gradients (Figure 4.7), the fractionation factor of nitrate uptake remained fairly constant (Figure 4.6 and Table 4.1). The general composition of the phytoplankton community, which included chlorophytes and dinoflagellates, may have contributed to the low fractionation factors observed for this dataset [*Fawcett et al.*, 2011]. Even lower fractionation factors were determined for Offshore Cycles, but nutrient limitation for these Cycles likely contributed to low isotope discrimination during nitrate uptake by phytoplankton [*Fawcett et al.*, 2011].

4.1. Nitrate Utilization by $\delta^{15}N_{NO3}$

The stable isotopes of nitrate ($\delta^{15}N_{NO3}$) can be a sensitive indicator to detect nitrate utilization (e.g., [*Altabet*, 2001]). In the CCE and broader CCS regions, the extent of primary productivity is related to the extent of nitrogen supply [*Di Lorenzo et al.*, 2008; *Chavez* and *Messié*, 2009; *Messié* and *Chavez*, 2015], and the extent of nitrate utilization can illuminate whether other factors limit productivity in the euphotic zone when nitrate is available. While NO_3^- often accurately predicts primary production potential in the CCE (dissertation author's Chapter II, Figure S4.5) residual surface concentrations cannot always accurately predict the extent of nitrate utilization [*DiFiore et al.*, 2006]. Using the characteristics of source nitrate, the isotope fractionation factor and Rayleigh systematics, it is possible to estimate the extent of nitrate utilized during each Cycle. However, this calculation only estimates the fraction of upwelled nitrate that is utilized and does not provide a direct measure of the magnitude of nitrate that was consumed.

For this study, the fraction of upwelled nitrate that was consumed/utilized near the Chl-a maximum depth was determined by rearranging the Rayleigh model formulation in Eq (2) after *Altabet* (2001), taking the form:

$$\%\ NO_3\ utilization = 1 - e^{\frac{\delta^{15}N_{NO3\_surface} - \delta^{15}N_{NO3\_source}}{\varepsilon_p}}, \tag{3}$$

where values for $\delta^{15}N_{NO3\_source}$ and ε_p are provided in Table 4.1, and $\delta^{15}N_{NO3\_surface}$ values were averaged ±10 m over the Chl-a max depth to estimate the amount of nitrate available at the peak depth of the primary phototrophic biomass (Table 4.3). Secondary peaks in [Chl-a] (i.e., deep Chl-a max) do frequently occur in the CCE but were not observed during these CCE cruises (Figure 4.2). If $\delta^{15}N_{NO3}$ samples were not available from the Chl-a max depth then values were interpolated based on the cycle-specific Rayleigh fits from Figure 4.6. Interpolated profiles were then used to determine the mean $\delta^{15}N_{NO3}$ surface around (±10 m) the Chl-a maximum depth (Figure S4.7).

Near-complete utilization was estimated for Offshore P1408 Cycles 4 and 5 and P1604 Cycles 1 and 2, with values ranging 79 ± 30% to 92 ± 6% (Table 4.3). Nitrate utilization for Inshore Cycles spanned a larger range, between 37 ± 29% and 68 ± 9%, which was consistent with the greater hydrographic variability for this region [*Mantyla et al.*, 2008]. If a single surface NO_3^- was used, a similar percentage of nitrate utilization at P1604 Cycles 3 and 4 (Table 4.3) would not have been predicted because residual NO_3^-

was nearly double for Cycle 4. By dividing the mean Chl-a max NO_3^- by the remnant mixed layer depth NO_3^- a relatively similar utilization pattern is observed as found in Table 4.3, but the utilization values by NO_3^- are lower by 15% on average.

Table 4.3. *Nitrate utilization was calculated using Equation (3) and the constants shown below and in Table 4.1. Surface* NO_3 *and* $\delta^{15}N_{NO3}$ *are represented by the ±10 m averages surrounding the Chl-a max depths. The Chl-a max depth was on average 20 - 30 m shallower than the remnant mixed layer.*

Cruise	Cycle	Chl-a Max Density (kg m^{-3})	Surface [NO_3^-] (µM)	Surface NO_3 $\delta^{15}N$ (‰)	Source NO_3 $\delta^{15}N$ (‰)	Nitrate Utilization (%)
P1408	1	*25.1*	*12.5±6*	*10.5±1*	*8.5*	*46±30*
	2	*24.8*	*6.8±1*	*11.9±1*	*9.0*	*59±13*
	3	*24.7*	*5.4±2*	*13.8±1*	*9.5*	*68±9*
	4	*24.9*	*3.5±4*	*14.8±4*	*9.3*	*79±30*
	5	*24.6*	*1.0±1*	*15.6±2*	*9.4*	*92±6*
P1604	1	*25.1*	*4.4±5*	*11.0±2*	*8.6*	*80±31*
	2	*24.8*	*2.6±4*	*11.4±2*	*8.6*	*85±23*
	3	*25.1*	*9.8±2*	*10.3±1*	*8.9*	*38±26*
	4	*25.5*	*18.6±6*	*10.0±1*	*8.7*	*37±29*

Cycles 2 and 3 of P1408 exhibited the highest nitrate utilization (60 - 70%) for Inshore stations. Expanding the $\delta^{15}N_{NO3}$ dataset to include samples collected for nearby CalCOFI stations (sampled between 2010 and 2016) showed that Inshore (i.e., <50 km from shore) nitrate utilization was generally enhanced during the recent warm anomalies (Figure 4.8). For example, Inshore CalCOFI sites showed 80 - 85% utilization during November 2015 and January of 2016 (Figure 4.8). These time periods coincided with peak anomalous climate conditions in the region during that time (e.g., [*Jacox et al.*, 2016]). Broad scale reductions in sea surface Chl-*a* in the central and southern CCS were also reported for this time [*McClatchie et al.*, 2016; *Frischknecht et al.*, 2017].

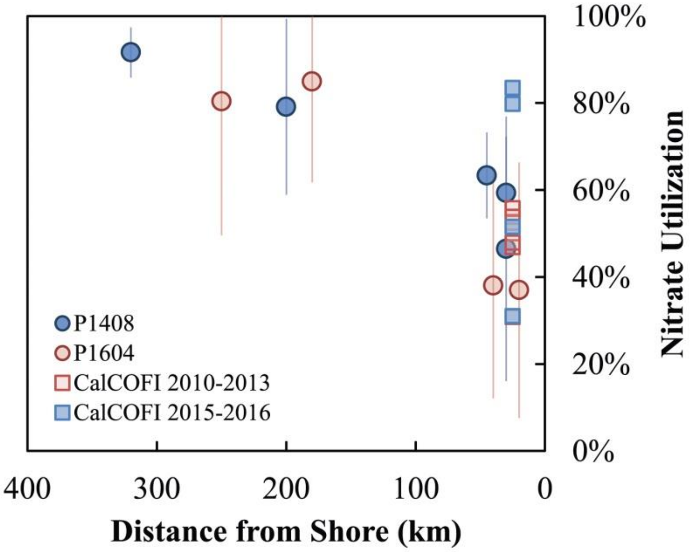

Figure 4.8. *Nitrate utilization by the* $\delta^{15}N_{NO3}$*-based Rayleigh model (or open system for CalCOFI 2010-2013 as discussed in Results Section 3.1) vs. distance from shore. CalCOFI samples shown in this figure were taken either from 080.0 051.0 or 080.0 055.0, located within 50km of CCE Inshore stations.*

Together, these observations indicated that nitrate supply in the region was limited (as evidenced by decreased Chl-*a*), perhaps due to enhanced stratification [*Frischknecht et al.*, 2017], and that the available nitrate was heavily utilized during this period. Relaxed alongshore winds and reduced upwelling, which therefore reduced nitrate transport into the surface ocean is consistent with the enhanced stratification observed in the region at the time (e.g., [*Jacox et al.*, 2015; *Zaba* and *Rudnick*, 2016; *Frischknecht et al.*, 2017]). By spring of 2016 (CCE Cruise P1604), while still behaving as a closed isotope system, Inshore nitrate utilization appeared to have returned to more mean conditions detected during prior El Niño-neutral years.

Mean nitrate utilization of all available Inshore (<50 km from shore) CCE and CalCOFI $\delta^{15}N_{NO3}$ records was 52 ± 15% (Figure 4.8) and suggest that nitrate frequently leaves the coastal zone without being fully drawn down. Excess nitrate leftover in coastal surface water due to underutilization can be laterally exported away from the coast [*Plattner et al.*, 2005; *Gruber et al.*, 2011]. On average, about 15% of excess nitrate that is transported laterally is subsequently subducted out of the euphotic zone [*Messié* and *Chavez*, 2015]. When the spatial distribution of estimated nitrate utilization was compared for all cruises, it was clear that very little of the upwelled nitrate remained in the surface by 200 km offshore of Point Conception (Figure 4.8). This finding is consistent with the modeling outcome of [*Plattner et al.*, 2005].

One potential mechanism leading to incomplete nitrate utilization in the CCS can be due to iron (Fe) limitation of phytoplankton productivity [*Hutchins* and *Bruland*, 1998; *Bruland et al.*, 2001; *King* and *Barbeau*, 2011; *Messié* and *Chavez*, 2015]. Iron limitation is a common phenomenon in the CalCOFI region, often observed in spring and summer months near the coast [*King* and *Barbeau*, 2011]. Fe limitation was observed during CCE P1408 Cycles 2 and 3 (Cycle 1 was not tested) during on-deck Fe-enrichment experiments (*K. Barbeau,* unpublished). Another measure of Fe limitation is the presence of excess NO_3^- over silicic acid ($Si(OH)_4$) relative to their upwelling ratio, given that nitrate uptake becomes inhibiting for Fe-limited diatoms [*Cohen et al.*, 2017]. This difference between $Si(OH)_4$ and NO_3^- relative to the upwelling ratio, can be expressed by Si* [*King* and *Barbeau*, 2011], which has been previously used to identify iron limitation in the region.

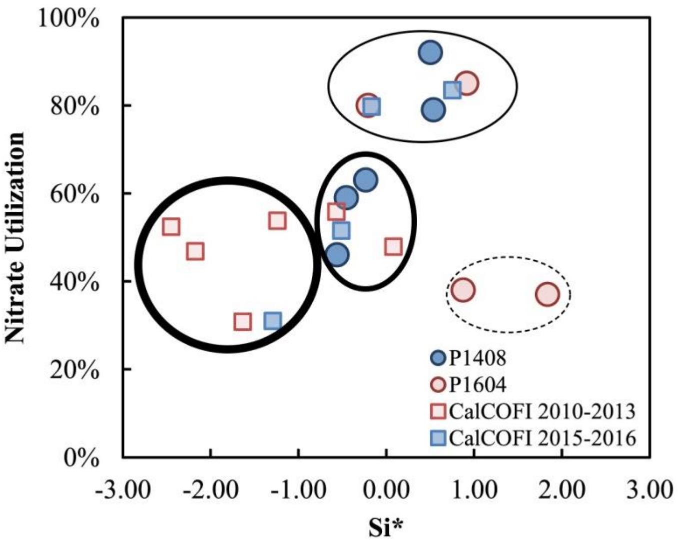

Figure 4.9. *Nitrate utilization shown in Table 4.3 vs. Si*, an indicator of iron limitation* [*King* and *Barbeau*, 2011]. *CalCOFI data are shown only for Line 080.0, stations 051.0, 055.0 and 060.0. Highlighted are conditions as discussed in the text (Sec 4.1).*

Nitrate utilization calculated for CCE and CalCOFI cruises was compared with the mean of the lowest 25th percentile Si* values at each site (Figure 4.9) to determine if Fe limitation was relevant to the trends in nitrate utilization. For locations where nitrate utilization was high, there was no evidence of iron limitation (Si*>0, thinnest circle in Figure 4.9), as might be expected when nitrate is drawn down to completion. At other locations, evidence of Fe limitation (Si*< 0) was coupled to moderate nitrate utilization values (e.g., darkest circle in Figure 4.9). However, P1408 Cycles 1, 2 and 3 exhibited subtle evidence for Fe limitation based on the Si* proxy (filled blue circles inside the dark oval in Figure 4.9). Iron limitation localized to one or two depths at these Cycles, like the Chl-a maximum, cannot be discounted (e.g., Figure S4.8), but a conservative approach using minimum 25th percentile values for Si* was adopted here to reproduce the general status of the water column. At these sites, the phytoplankton community was dominated by *Dinophyta* and because they don't have a $Si(OH)_4$ requirement, Si* may not be an appropriate tracer of Fe limitation.

In the absence of strong indicators of Fe limitation other factors related to nutrient status must be considered. For example, the dashed oval in Figure 4.9 encompasses the two Inshore stations from P1604 that had low utilization (~37%) and no Fe limitation by the Si* proxy. At these sites, communities other than diatoms must have also been contributing to nitrate uptake because $Si(OH)_4$ was present at excess concentrations relative to the upwelling ratio. For P1604 Cycle 3, *Chlorophyta* dominated the surface community and processes such as increased grazing could have kept nitrate utilization low at this site. At P1604 Cycle 4, a mixed assemblage that included diatoms was observed. Here, the sampling of early bloom conditions may have led to the estimated low nitrate utilization (Figure 4.8). Enhanced Chl-*a* (Figure 4.2) and increased particle flux at Cycle 4 instead of Cycle 3 both indicated that the absolute magnitude of nitrate consumed in the euphotic zone of Cycle 4 was significantly higher even though the extent of utilization was comparable. Overall, no consistent explanation for low nitrate utilization could be discerned across the Inshore stations, and a combination of Fe limitation, phytoplankton community composition, grazing, early bloom conditions, and other factors not explored here such as limitation by other micronutrients (e.g., vitamins), reduced surface light penetration or enhanced viral activity could have contributed to distributions of nitrate utilization.

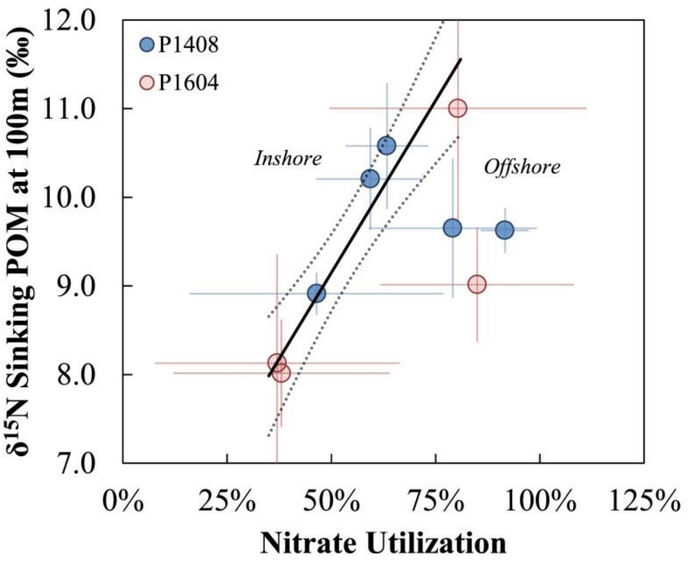

Figure 4.10. *Sinking POM $\delta^{15}N$ at 100m and nitrate utilization estimated from Equation (3). Line of best fit represents the Type II regression and dotted lines outside of this are the ±95% confidence intervals.*

4.1.1. Nitrate Utilization and the Food Web

To independently assess the nitrate utilization estimated here, the percent of nitrate utilized was compared with $\delta^{15}N_{Sink}$ and $\delta^{15}N_{Cp}$. The comparison with $\delta^{15}N_{Sink}$ showed a positive linear relationship for P1408 Cycles 1,2 and 3 and P1604 Cycles 1, 3, and 4 (r^2= 0.93, p<0.01; Figure 4.10) where an increase in utilization was coupled to an increase in $\delta\ ^{15}N_{Sink}$. For example, $\delta^{15}N_{Sink}$ was significantly enriched for Inshore P1408 Cycles 2 and 3 (10.0 - 11.0‰), and Figure 4.10 would suggest that this was due to an enhanced nitrate utilization that was propagated from phytoplankton into sinking particles via grazing. At the other end of the relationship, an average $\delta\ ^{15}N_{Sink}$ of 8.0 ± 0.7‰ collected during Inshore Cycles 3 and 4 of the productive spring cruise P1604 corresponded to relatively low nitrate utilization (Figure 4.10). A similar $\delta^{15}N_{Sink}$ was also measured during a recent CCE cruise that followed a highly productive bloom just north of Point Conception during the summer of 2017 (mean of 8.0 ± 0.5‰; Figure S4.9). Based on prior trap data and POM collected during the CCE cruises and average trap data described for the CCS in the Results Sec 3.3.2, a $\delta^{15}N_{Sink}$ of ~8.0‰ is likely common for the area.

The observed correspondence with nitrate utilization suggests that exported N is tightly linked to nitrate N and that the isotopic composition of nitrate is transferred relatively consistently to the sinking N reservoir (Figure 4.10). The short-term deployment (2 - 3 days) of these sediment traps likely meant that N utilization and sinking N production were tightly linked in the Inshore. However, the $\delta^{15}N_{Sink}$ at Offshore P1408 Cycles 4 and 5 and P1604 Cycle 2, was more depleted than would be predicted by the relationship to utilization that described the remaining cycles (Figure 4.10). This would be more consistent with source $\delta^{15}N_{NO3}$ is more depleted Offshore than Inshore (see Figure 4.4, for example).

In the comparison of $\delta^{15}N_{Cp}$ to nitrate utilization two populations of data were apparent (Figure S4.10), where Cycles with high nitrate utilization and higher $\delta^{15}N_{Cp}$ were differentiated from Cycles that had lower nitrate utilization and lower $\delta^{15}N_{Cp}$ (Figure S4.10). However, the linear fit to all this data had a comparatively reduced r^2 of 0.44 ($p=0.05$) relative to the relationship with $\delta^{15}N_{Sink}$, and this correlation was not substantially different from that of $\delta^{15}N_{Cp}$ and $\delta^{15}N_{NO3}$ in source waters (r^2 of 0.46; $p=0.04$). However, the outliers in each case were different, which highlights the complicated relationship of $\delta^{15}N_{Cp}$ to both the extent of utilization and the isotopic signature of upwelling nitrate.

4.2. Predicting the Products of $\delta^{15}N_{NO3}$

In Rayleigh systems, the products of nutrient uptake, in this case biomass, should ultimately reflect the isotopic composition of source nutrients (e.g., [*Hayes*, 2002; *Montoya*, 2008; *Sigman et al.*, 2010]). Accordingly, the isotopic composition of sinking and suspended POM has been shown to track the isotopic signature of surface nitrate in several locations [*Altabet* and *Deuser*, 1985; *Altabet* and *McCarthy*, 1985]. In these cases, Rayleigh fractionation, when $\delta^{15}N_{NO3}$ and NO_3^- is available, can predict the $\delta^{15}N$ of instantaneous and integrated products (i.e., biomass) [e.g., *Altabet et al.* 1999]. The instantaneous product is predicted as:

$$\delta^{15}N_{PON\_Instantaneous} = \delta^{15}N_{NO3\_surface} - \varepsilon_p\ , \tag{4}$$

where $\delta^{15}N_{NO3\_surface}$ is the average value from around the Chl-*a* maximum depth as found in Table 4.3 and ε_p is from the Rayleigh best fit model (Table 4.1). The integrated product can be estimated by:

$$\delta^{15}N_{PON\_Integrated} = \delta^{15}N_{NO3\_source} + \varepsilon_p \left\{\frac{(1-u)}{u}\right\} ln(1-u)\ , \tag{5}$$

where $\delta^{15}N_{NO3\_source}$ is the $\delta^{15}N_{NO3}$ from the base of the mixed layer (Table 4.1), and *u* is the nitrate utilization estimated in Table 4.3.

4.2.1. Nitrate-based Production and the $\delta^{15}N$ of Suspended PON

Bulk suspended particulate organic matter (POM) from the water column was used in this study as a proxy for recently living phytoplankton as previously considered for marine systems [*Eppley et al.*, 1977; *Altabet* and *McCarthy*, 1986; *Montoya et al.*, 1990; *Waser et al.*, 2000; *Altabet*, 2001; *Mercado et al.*, 2010; *Wannicke et al.*, 2010; *Zhang et al.*, 2011; *Landrum et al.*, 2011; *Martiny et al.*, 2013; *Fernández et al.*, 2014]. However, $\delta^{15}N_{Susp}$ is notoriously difficult to interpret in the context of $\delta^{15}N_{NO3}$. For example, *Altabet et al.* [1999] noted that the observed ranges in $\delta^{15}N_{Susp}$ (2 - 8‰) and $\delta^{15}N_{Sink}$ (6 - 9.5‰) for samples collected off Monterey Bay were smaller than the possible range of biomass values predicted by the range in $\delta^{15}N_{NO3}$ (3 - 15‰). If suspended POM only reflected the instantaneous products of nitrate assimilation then these isotopic signatures should track each other closely. However, $\delta^{15}N_{Susp}$ and $\delta^{15}N_{Sink}$ samples collected near the surface ocean during the current study generally fell between 5 and 11‰ (Figures 4.2 and S4.6), despite a range in $\delta^{15}N_{NO3}$ of 7 - 17‰ (Figure 4.6).

One potential reason an enriched PON $\delta^{15}N$ up to 14 - 16‰ is not observed in the CCE and broader CCS regions could be due to longer residence times for surface suspended POM compared with the timeframe over which nitrate consumption takes place [*Altabet et al.*, 1999]. In this case, suspended POM behaves more like the accumulated product of nitrate assimilation. Furthermore, any contribution from recycled nitrogen to the phytoplankton reservoir, particularly when NO_3^- is low (a condition which corresponds to the highest endmember $\delta^{15}N_{NO3}$), would dampen the imprint of isotopically enriched nitrate on the surface POM reservoir.

Suspended POM isolated onto 0.7 μm size-cutoff filters (GF/F) could capture a combination of detritus (up to 50% non-living material for CalCOFI may be possible as reported in [*Taylor et al.*, 2015]) and heterotrophic and autotrophic microbes (including a large proportion of bacteria, [*Pedler et al.*, 2014]). However, the depletion in $\delta^{15}N_{Susp}$ at Chl-*a* maximum depths relative to depths above and below, was consistent with a more rapidly cycling fraction of PON and thus, an enhanced contribution of fresh, phototrophic biomass to POM as argued previously [*Eppley et al.*, 1977]. Such a trend has also been reported in prior studies for the North Pacific [*Saino* and *Hattori*, 1987; *Montoya et al.*, 1992] and North Atlantic [*Altabet* and *McCarthy*, 1986]. For example, in a comprehensive study tracking a warm core eddy in the North Atlantic, 23 out of 33 profiles exhibited a $\delta^{15}N_{Susp}$ minima near the region of greatest PON and where NO_3^- had the greatest rate of change [*Altabet* and *McCarthy*, 1986].

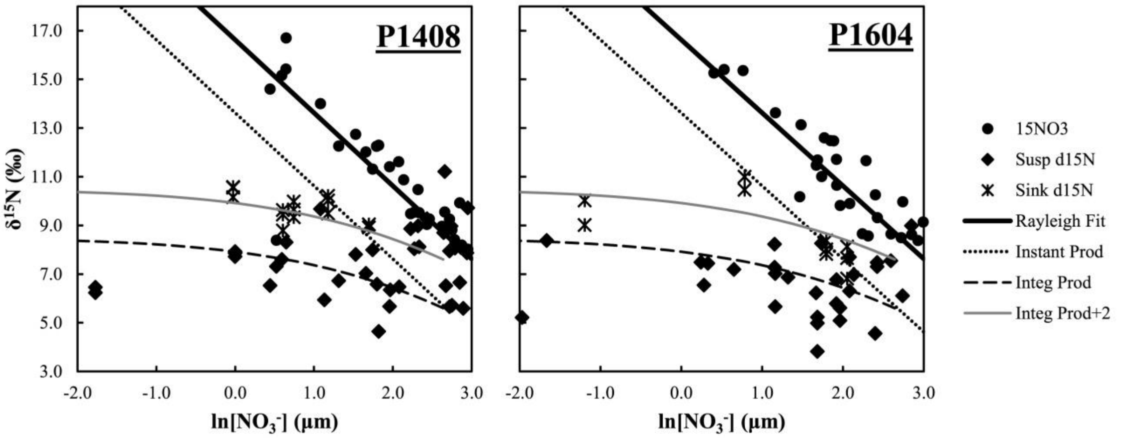

Figure 4.11. *Rayleigh-predicted fit line ('Rayleigh Fit', dark solid), and the associated instantaneous ('Instant Prod', dotted) and integrated ('Integ Prod', dashed) products are plotted over observations for cruises P1408 and P1604. A predicted integrated product +2‰ ('Integ Prod+2'; grey solid) is also shown for reference to sinking POM. Fits use a source* $\delta^{15}N_{NO3}$ *of 8.5‰,* NO_3^- *of 15 μM and* ε_p *of 3.0‰.*

When all $\delta^{15}N_{Susp}$ from each Cycle were compared against predicted instantaneous and integrated product relationships it became clear that $\delta^{15}N_{Susp}$ was better represented as the integrated product (diamonds in Figure 4.11 compared to the dashed line). Thus, the residence time of suspended POM in the euphotic zone was long enough to enable it to integrate over the variations in $\delta^{15}N_{NO3}$. For Cycles 2 and 3 of P1408, some $\delta^{15}N_{Susp}$ fell between the predicted instantaneous and integrated products but increasing the source $\delta^{15}N_{NO3}$ to 9.2‰ (see Table 4.1) in the Rayleigh fit shifted the integrated product line up to incorporate several of these datapoints (source $\delta^{15}N_{NO3}$ adjusted fit not shown). However, it is important to recognize that the overall timescale of these relationships is still short. For $\delta^{15}N_{Susp}$ to reflect any of the dynamics of $\delta^{15}N_{NO3}$ the residence time cannot be much longer than the time it takes for an upwelled nitrate pulse to be utilized by the existing phytoplankton community [*Zimmerman et al.*, 1987; *Wilkerson et al.*, 2006].

As expected, the $\delta^{15}N_{Susp}$ of deeper high nitrate waters (ln[NO_3^-] >2.5 μM, on the far right of each plot in Figure 4.11), where Chl-a begins to decline, do not conform to these expectations and are typically enriched due to their much longer residence times in the ocean. Such a trend in deep water $\delta^{15}N_{Susp}$ enrichment is likely influenced by processes such as degradation (e.g., [*Guo et al.*, 2004]). *Altabet* (1988) also suggested that deeper $\delta^{15}N_{Susp}$ is supplied from sinking particles and thus should reflect $\delta^{15}N_{Sink}$, which is often enriched relative to $\delta^{15}N_{Susp}$ (see below). The outlier $\delta^{15}N_{Sink}$ value in this case was P1604 Cycle 1, which was substantially enriched over the predicted fit. One explanation is that at this site, the food web was more elongated such that organisms that occupied a higher trophic position contributed sinking POM.

4.2.2. Nitrate-based Production and the $\delta^{15}N$ of Sinking PON

At all sites, $\delta^{15}N_{Sink}$ was enriched relative to $\delta^{15}N_{Susp}$, and in some cases $\delta^{15}N_{Sink}$ plotted with the predicted instantaneous product dynamics (crosses on Figure 4.11 versus dotted line). However, $\delta^{15}N_{Sink}$ should reflect the combination of upper ocean food web processes and not simply nitrate assimilation into phytoplankton. Previous CCE studies have estimated that the waste products of consumers contributing to sinking flux to be relatively high [*Landry et al.*, 2009; *Stukel et al.*, 2011, 2013]. Additionally, prior studies have found that the bodies of copepods become enriched in $\delta^{15}N$ by 3.3‰ on average relative to their food source [*Mingawa et al.*, 1984; *Checkley* and *Entzeroth*, 1985; *Wada et al.*, 1987; *Fry*, 1988], due to the excretion of isotopically- depleted nitrogen (see discussion below). So, $\delta^{15}N_{Sink}$ might track $\delta^{15}N_{Susp}$ (food source) but should also be elevated by up to 3.3‰. In Figure 4.11, if the integrated product line was shifted upward by ~2‰ (thin grey line) it could reproduce many of the $\delta^{15}N_{Sink}$ values that were observed. Just as for $\delta^{15}N_{Susp}$ during P1408 Cycles 2 and 3, an upward shift of the adjusted integrated product line ("Integ Prod+2‰" fit) associated with a more enriched source $\delta^{15}N_{NO3}$ was reflected in the observed enriched $\delta^{15}N_{Sink}$ (not shown).

To evaluate contributions of fecal pellet $\delta^{15}N$ to $\delta^{15}N_{Sink}$, fecal pellets were collected from short incubations (4 - 6 hours) of early morning surface waters (nominally $\delta^{15}N_{\mathit{Cp}\text{-fecal}}$). Pellets that fell through a 100 μm mesh screen were isolated under a microscope using a modified glass pipette. Many of the fecal pellets observed under the microscope during these experiments were cylindrical and similar in size and shape to those of copepod origin previously isolated from the CCE (e.g., [*Stukel et al.*, 2013]). Measured $\delta^{15}N_{\mathit{Cp}\text{-fecal}}$ was variable but often depleted with respect to $\delta^{15}N_{\mathit{Cp}}$ and enriched with respect to $\delta^{15}N_{Sink}$ (Figure S4.9). However, $\delta^{13}C_{\mathit{Cp}\text{-fecal}}$ was also depleted by ~1‰ on average compared with $\delta^{13}C_{Sink}$ and $\delta^{13}C_{\mathit{Cp}}$ suggesting that fecal pellets alone cannot explain sediment trap isotopes. For instance, a more depleted $\delta^{13}C_{Cp\text{-}fecal}$ could reflect an increased proportion of lipid or pigment-like material [*Prahl et al.*, 1984; *Close et al.*, 2013]. Overall, results were consistent with $\delta^{15}N_{Sink}$ having some contribution from fecal pellets of mesozooplankton (e.g. [*Montoya*, 2008; *Stukel et al.*, 2013]) and consistent with measured $\delta^{15}N_{Sink}$ being elevated with respect to phytoplankton, which would serve as the food source for mesozooplankton. Such a hypothesis requires very close temporal coupling between phytoplankton production, grazing, and egestion [*Landry et al.*, 2009].

4.2.3. Using the *f*-ratio to Estimate Alternate N Sources

Integrated rates of nitrate-based ("new") production were estimated for the CCE P1408 and P1604 cruises (dissertation author's Chapter III, Table 4.3), and integrated rates of net primary production were also available (Table S4.2). Together, these parameters were used to determine the '*f*-ratio [*Eppley* and *Peterson*, 1979]), which was on average 45 ± 9% for all cycles (Table S4.2). Production fueled by other forms of nitrogen would impact $\delta^{15}N_{Susp}$ but would not be reflected in Rayleigh predictions of integrated or instantaneous products. For example, several $\delta^{15}N_{Susp}$ values in Figure 4.11 fell below the predicted integrated product line. A two-endmember $\delta^{15}N$ and N mass balance can be used to calculate $\delta^{15}N_{non\text{-}nitrateN}$. In such a formulation, the isotope signature of non-nitrate nitrogen contributes to measured $\delta^{15}N_{Susp}$ but has an unknown isotope signature. The signature of $\delta^{15}N_{non\text{-}nitrateN}$ can be constrained using the *f*-ratio, which is an expression of the relative contribution of nitrate versus non-nitrate nitrogen to primary production. Such a calculation yields a $\delta^{15}N$ value between 4.0 and 5.0‰. This value is significantly more depleted than $\delta^{15}N_{NO3}$ and more similar to recycled forms of N (e.g., [*Checkley* and *Miller*, 1989; *Montoya et al.*, 1990; *Knapp et al.*, 2011]). Such a mass balance indicates that a depleted $\delta^{15}N_{Susp}$ relative to estimated instantaneous or integrated products may have been influenced by inorganic nitrogen sources other than nitrate.

4.2.4. δ^{15}N Reservoir Interconnections

The δ^{15}N interconnection among reservoirs was at times straightforward but more difficult to discern at others from the available data. For instance, P1408 Cycle 3 exhibited evidence across the organic reservoirs to suggest conditions sampled were more reflective of Offshore Cycles than Inshore Cycles. The $\delta^{15}N_{Susp}$, $\delta^{15}N_{Sink}$ and $\delta^{15}N_{Cp}$ were all enriched over other Cycles (Table 4.2). However, $\delta^{15}N_{Cp}$ was only enriched for P1408 Cycle 3 (12.2 ± 0.4‰; Table 4.2) over long-term median δ^{15}N values (10.7 ± 0.5‰ spanning 1951 to 2004 from CalCOFI [*Ohman et al.*, 2012]). Physical state estimates for the period surrounding the P1408 cruise suggest that Cycle 3 sampled warmer surface water that was moving inshore (Figure S4.11). In addition, the δ^{13}C of suspended and sinking POM, and *Cp* for Cycle 3 cluster with Offshore samples (Figure S4.6) in agreement with the physical model that suggested this Cycle to represent an Offshore water mass. A relative depletion in δ^{13}C could be a reflection of smaller slower growing cells Offshore fractionating more strongly against a source dissolved inorganic carbon of ~0.0‰ (e.g. [*Goericke et al.*, 1994]).

Conversely, $\delta^{15}N_{Cp}$ for Cycle 1 of P1604 exhibited little connection to the other N reservoirs (Table 4.1). P1604 Cycle 1 had the lowest $\delta^{15}N_{Susp}$ (2.3 ± 0.5‰), and $\delta^{15}N_{Cp}$ and $\delta^{15}N_{Sink}$ were identical (~11‰). At this site, the sinking N flux at 100 m was also elevated (i.e., 0.94 ± 0.15 mmol N m^{-2} d^{-1}) with respect to other Offshore Cycles (e.g., 0.37 ± 0.04 0.50 ± 0.04 mmol N m^{-2} d^{-1}), and the material in the 100 m trap for this Cycle had a low C:N ratio (6.3). Consistent with higher fluxes of material to this trap, the $\delta^{13}C_{Sink}$ was also elevated (by ~1.5‰) compared with other Offshore Cycles. It is relevant to note that only one day of profile data was available for this Cycle but sediment traps were deployed for 5 days (typically 3-day deployments); however, all of the various measurements discussed above isolated this site as unique. The observed mismatch may have resulted from elongation of the food web specific to this site or perhaps that the copepods isolated were not local residents. Biomass turnover time for copepods likely exceeds 3 to 5 weeks [*Tamelander et al.*, 2006], suggesting that offsets among the reservoirs could reflect offsets between the time scales relevant to each reservoir. Such a finding serves to caution studies that attempt to use archived nitrogen reservoirs to infer $\delta^{15}N_{NO3}$ variability in the past.

4.2.5. Using δ^{15}N to Predict Trophic Position

As stated previously, *Cp* preferentially feed on larger diatoms but may ingest small heterotrophs and detritus [*Frost*, 1977; *Landry*, 1981; *Dilling et al.*, 1998]. Prior studies have found that the bodies of animals become enriched in δ^{15}N by 3.3‰ on average [*Mingawa et al.*, 1984; *Checkley* and *Entzeroth*, 1985; *Wada et al.*, 1987; *Fry*, 1988], where the following formula can then be used to predict trophic position:

$$\delta^{15}N_{Animal} = 3.3(trophic\ level - 1) + \delta^{15}N_{Food} \qquad (6)$$

Solving for the trophic level in Eq (6) using the $\delta^{15}N_{Susp}$ and *Cp* values in Table 4.2 predicted a trophic position (TP) of 2.1 ± 0.3 for *Cp* across all but one Cycle (P1604 Cycle 1 had a $\delta^{15}N_{Susp}$ of 2.3‰ resulting in a predicted TP of 3.8, but $\delta^{15}N_{Susp}$ was only available from one samples at this site). A TP of around 2.0 is consistent with a diet of primary producers and is similar to that estimated previously for primary copepod consumers for the North Pacific [*Hannides et al.*, 2009]. No change in the TP during strong climate events is also in agreement with estimated TP based on compound-specific amino acid analysis for *Cp* samples collected across the 1997 - 1998 El Niño [*Décima et al.*, 2013]. Use of bulk $\delta^{15}N_{Susp}$ from the Chl-a max depths as representative of *Cp*'s diet could either suggest that the of $\delta^{15}N_{Susp}$ at this location contains proportionally greater fresh biomass or that *Cp* also ingests living and detrital material represented by the bulk PON pools (e.g., [*Dilling et al.*, 1998]). However, without sorting and isolating intact cells (e.g., flow cytometry [*Fawcett et al.*, 2011]), it is difficult to speculate much beyond this observation.

5. Conclusions

Anomalously warm and stratified conditions prevailed in the California Current System during the North Pacific warm pool anomaly of 2014-15 and the El Niño period of fall 2015 through spring 2016. Such conditions provided a unique opportunity to study nitrogen dynamics in the upper ocean in a region strongly dependent on vertical NO_3^- delivery to support its ecosystem. Systematic investigations of the connections between various N reservoirs was facilitated by $\delta^{15}N$ measurements made on nitrate, suspended POM, sinking POM and copepods during CCE Process Cruises in 2014 and

2016. Validation of the observed trends and context was provided by $\delta^{15}N_{NO3}$ samples collected at spatially similar locations during CalCOFI cruises (2010 - 2016).

Previous physical oceanographic studies in the region had identified the importance of the remnant mixed layer in providing a stratification barrier to mixing between surface waters and deep water, and the $\delta^{15}N_{NO3}$ data supported this view of surface-subsurface interaction. The remnant mixed layer $\delta^{15}N_{NO3}$, which appears to serve as the immediate source of NO_3^- to the seasonal mixed layer, was consistently enriched (average $\delta^{15}N_{NO3}$ of 8.9 ± 0.4‰) relative to waters below it suggesting the memory of nitrate uptake to have remained at these depths. The $\delta^{15}N_{NO3}$ found in deeper waters (NO_3^- >20 µM) was 8.2 ± 0.7‰ and was enriched for spicier Inshore waters likely associated with southerly origins. However, the $\delta^{15}N_{NO3}$ of remnant source waters only occasionally matched the patterns of $\delta^{15}N_{NO3}$ in deeper waters below.

Using the source characteristics of the remnant mixed layer nitrate, an isotope fractionation model was used to examine the relationships between nitrate and the associated organic N reservoirs. Using a closed system Rayleigh model, the isotope fractionation factor for phytoplankton uptake, $\varepsilon_{p,}$ was determined to be ~3.0 ± 0.5‰ for Inshore locations. This value was lower than values previously measured or assumed for the region. However, similar ε_p values were calculated for both CCE and CalCOFI cruise, indicating that these low values were not unique to the anomalous conditions sampled by CCE. In addition, similar fractionation factors were identified for locations with fairly disparate eukaryotic communities, though the communities during 2014 - 2016 may have either been an increased proportion of smaller-sized/flagellated cells or could have been impacted by surface stratified nutrient conditions. Further study into how nitrate uptake fractionation factors vary under diatom *versus* dinoflagellate or cholorophyte populations should be further explored in order to better understand interannual variations in $\delta^{15}N_{NO3}$ and biomass.

The Rayleigh closed system nitrate model was also used to examine the extent of nitrate utilization across the CCE. Consistent with previous studies, it was found that surface waters are routinely exported away from inshore sites with excess nitrate (52 ± 15% on average). However, nitrate utilization was nearly complete for some Inshore stations that were sampled during stratified time periods of 2014 and 2015. An enrichment in $\delta^{15}N_{NO3}$ that resulted from enhanced nitrate utilization was detected as an enriched $\delta^{15}N$ throughout the food web, from surface nitrate to suspended and sinking POM to *Calanus p*.

Moderate levels of nitrate utilization (~50%) Inshore were associated with an indicator of iron limitation (Si*) on nitrate uptake by diatoms, suggesting that nitrate utilization under these conditions could otherwise have been greater. The highest levels of Inshore nitrate utilization (80%) were associated with slightly negative to positive values of Si*; however, utilization was slightly lower than this during the CCE P1408 cruise (~60%) and associated with moderate levels of iron limitation (Si* of -0.5).

Contributions to the isotopic composition of suspended POM, $\delta^{15}N_{Susp}$, can be difficult to constrain given that its signature can be impacted by a range of processes including incorporation of various N sources into biomass, and preferential degradation of certain organic compounds and their associated range in mean residence times.

However, the $\delta^{15}N_{Susp}$ presented here exhibited an overall correspondence with the integrated product predicted from the Rayleigh closed system nitrate uptake model. This correspondence suggested that suspended POM largely followed the isotope dynamics of nitrate but also that its residence time in the euphotic zone was long enough to integrate the variability of $\delta^{15}N_{NO3}$.

A connection between $\delta^{15}N_{Susp}$ and $\delta^{15}N_{NO3}$ is an important finding given that higher trophic level organisms like copepods, a class of organisms that likely ingests N from this suspended reservoir, have been used to infer long-term trends in nitrate utilization for the CCS. These data confirm that there must be a connection between $\delta^{15}N_{Cp}$ and $\delta^{15}N_{NO3}$, a connection that is carried out via the $\delta^{15}N_{Susp}$ reservoir and is dependent on the extent of nitrate utilization. In accordance with this finding, Inshore $\delta^{15}N_{Sink}$ was also correlated with the extent of nitrate utilization, again showing the direct connection between $\delta^{15}N_{NO3}$ and $\delta^{15}N_{Sink}$ and one that must involve the surface $\delta^{15}N_{Susp}$ reservoir.

The $\delta^{15}N_{Sink}$ at each CCE location was reproduced from a closed system Rayleigh fit where a 2‰ enrichment of the integrated product prediction was applied across the range of observed NO_3^- and $\delta^{15}N_{NO3}$ values. A fixed relationship between these reservoirs could be coincidental, but the interpretation provided here is that $\delta^{15}N_{Sink}$ is connected to the $\delta^{15}N_{Susp}$ reservoir through copepods, whose fecal pellets are routinely found in sediment traps. Therefore, a ~2‰ enrichment in the $\delta^{15}N_{Sink}$ over $\delta^{15}N_{Susp}$ would be consistent with the trophic level $\delta^{15}N$ enrichment expected for copepods relative to their food source, but may also be smaller in magnitude (hence ~2‰ versus

~3.3‰) because excreted products, such as fecal pellets, are expected to be depleted relative to biomass. A limited number of experiments were conducted to determine the $\delta^{15}N$ of copepod fecal pellets and in several experiments, and the $\delta^{15}N$ of fecal pellets was lower than $\delta^{15}N_{Cp}$. However, comparison of $\delta^{15}N$ and $\delta^{13}C$ signatures across these reservoirs suggests that an organic N source more similar to $\delta^{15}N_{\mathrm{Susp}}$ (or phytoplankton) in addition to copepod-derived waste products directly contribute to the sinking N flux.

Overall, the results presented in this chapter helped to validate relationships between $\delta^{15}N_{\mathrm{NO3}}$ and several reservoirs that are used to examine past variations in the ocean's N cycle. The extent of nitrate utilization likely drives interannual variations in the $\delta^{15}N_{Cp}$ and $\delta^{15}N_{\mathrm{Sink}}$ at specific locations. Further study of the interconnection of these reservoirs across the CCE and broader CCS regions could help to more clearly discern among the competing influences of changes in $\delta^{15}N_{\mathrm{NO3}}$ source and $\delta^{15}N_{\mathrm{NO3}}$ uptake fractionation factors exhibited across phytoplankton groups.

APPENDIX

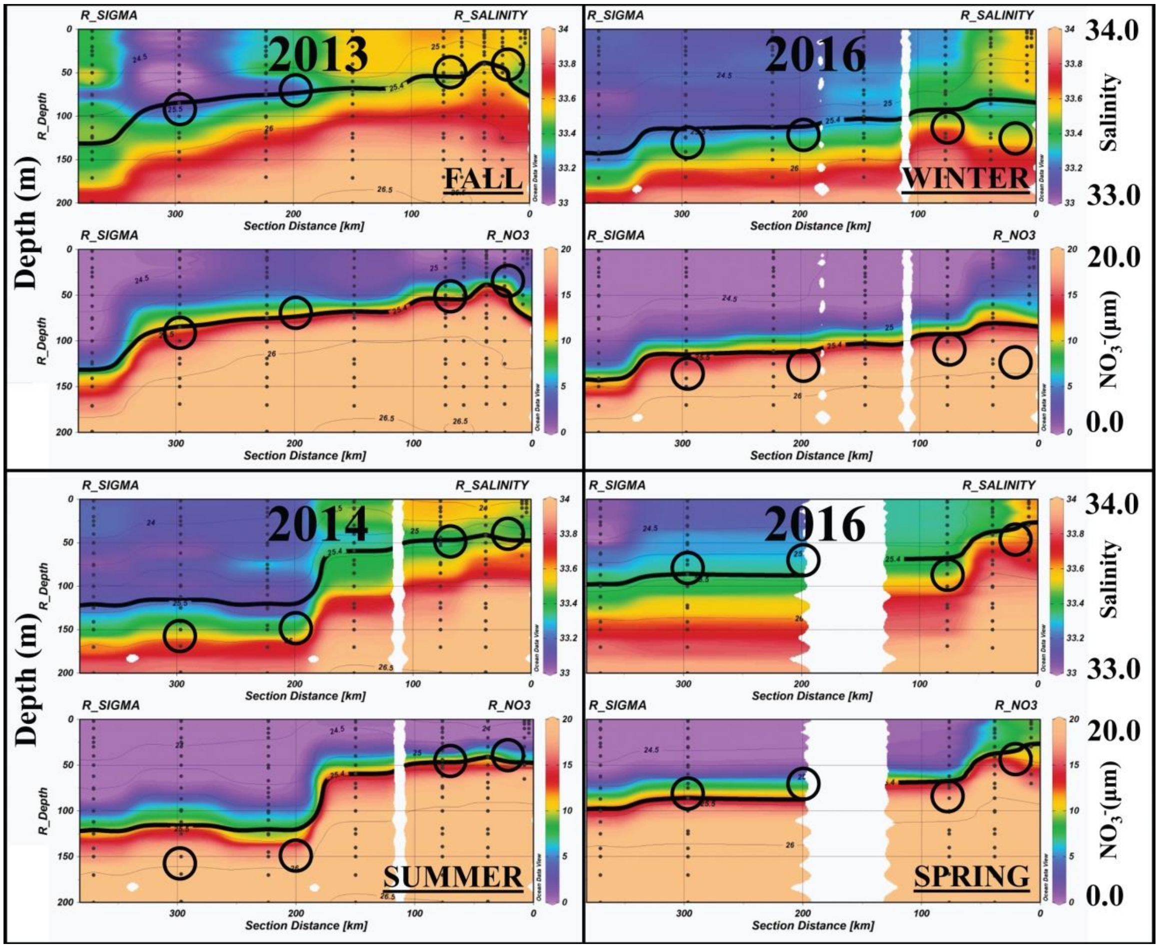

Figure S4.1. *CalCOFI Line 080,0 salinity (top) and nitrate (bottom) for 2014 (left) and 2016 (right). The nearest CalCOFI cruise (201407 and 201604) to CCE P1408 and P1604 cruises is shown at the bottom set of figures. The nearest wintertime cruise is shown in the upper set of figures (201311 and 201601). The bold black line represents the 25.4 isopycnal which was previously identified as nearest the remnant mixed layer depth* [*Cole et al.*, 2010]. *And the circles represent the approximate lateral location of CCE Cycles with a depth associated with the wintertime mixed layer.*

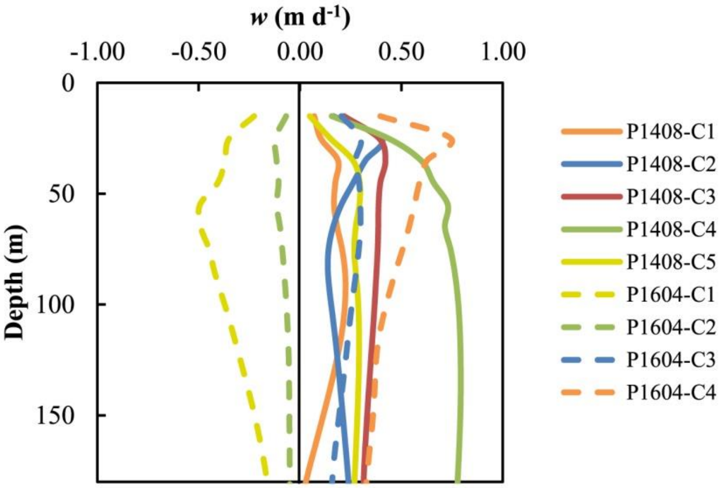

Figure S4.2. *Average California Current state estimated vertical velocities for the ±10 days and within ±10km surrounding each Cycle. Data obtained courtesy of the CASE site: at http://sose.ucsd.edu/CASE/.*

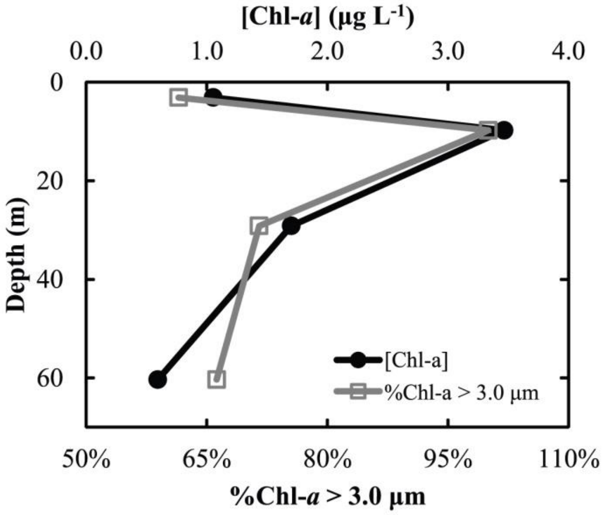

Figure S4.3. *Size-fractionated Chl-a collected near Pt. Conception during oc1507b illustrating the correspondence of an increasing proportion of larger Chl-a-containing cells near the Chl-a max depth.*

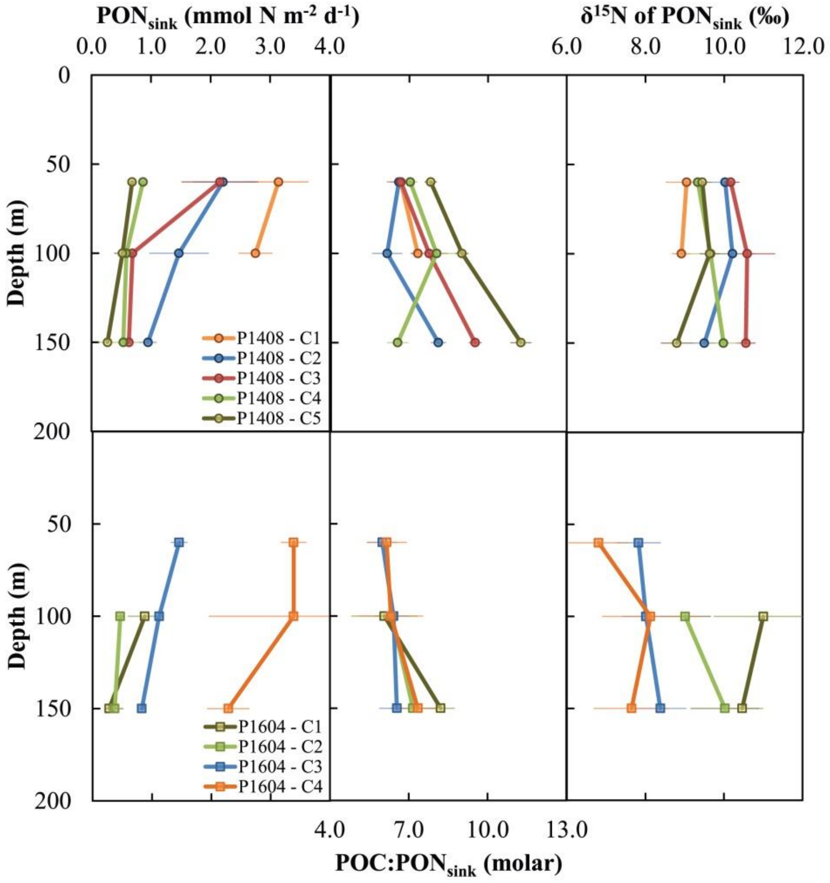

Figure S4.4. *POM sinking rates, POC:PON molar ratio and* $\delta^{15}N$ *collected from up to three depths for P1408 (top) and P1604 (bottom). The relatively low change in POC:PON molar ratio and* $\delta^{15}N$ *from the 60m to 100m trap depths suggest that the* $\delta^{15}N$ *observed at 100m is not due any preferential removal of high N-containing isotopically-lighter POM during sinking.*

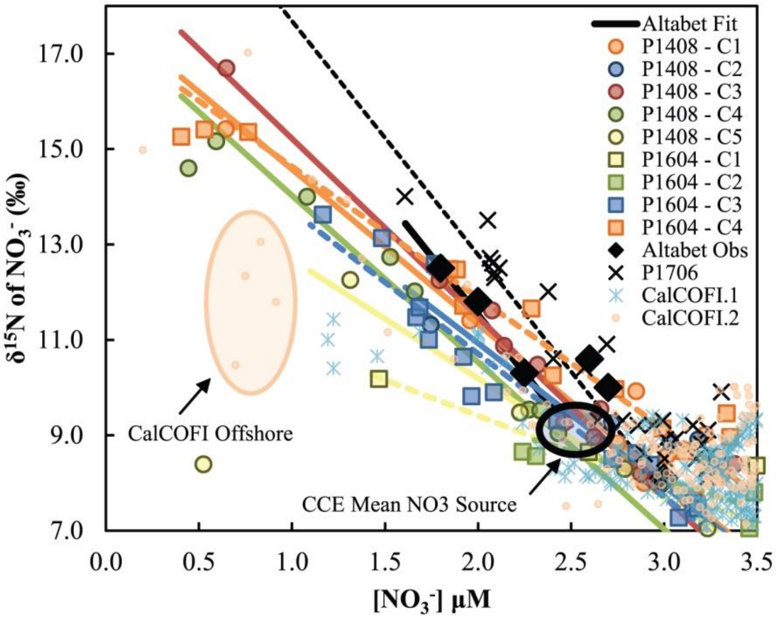

Figure S4.5. *Rayleigh model comparison of available nitrate isotope data. The darker solid fit line was estimated for Monterey Bay in Altabet et al.* (1999) *and the dotted line above this uses a similar isotope effect (4.9‰) for the CCE cruise P1706 (x's).*

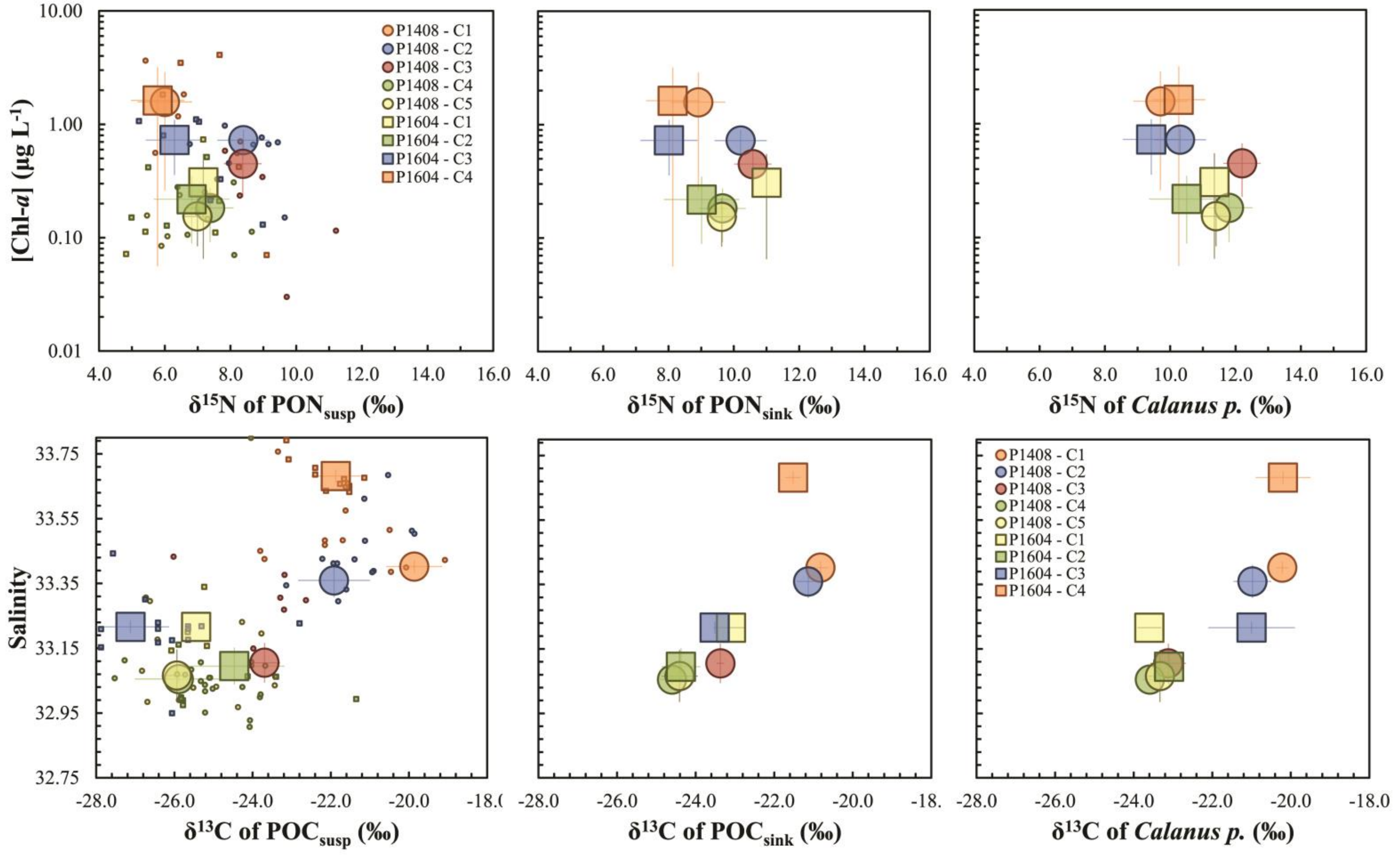

Figure S4.6. *Mean δ^{15}N and δ^{13}C separate Inshore Cycles from Offshore, where Inshore Cycle 3 P1408 tends to group with Offshore Cycles.*

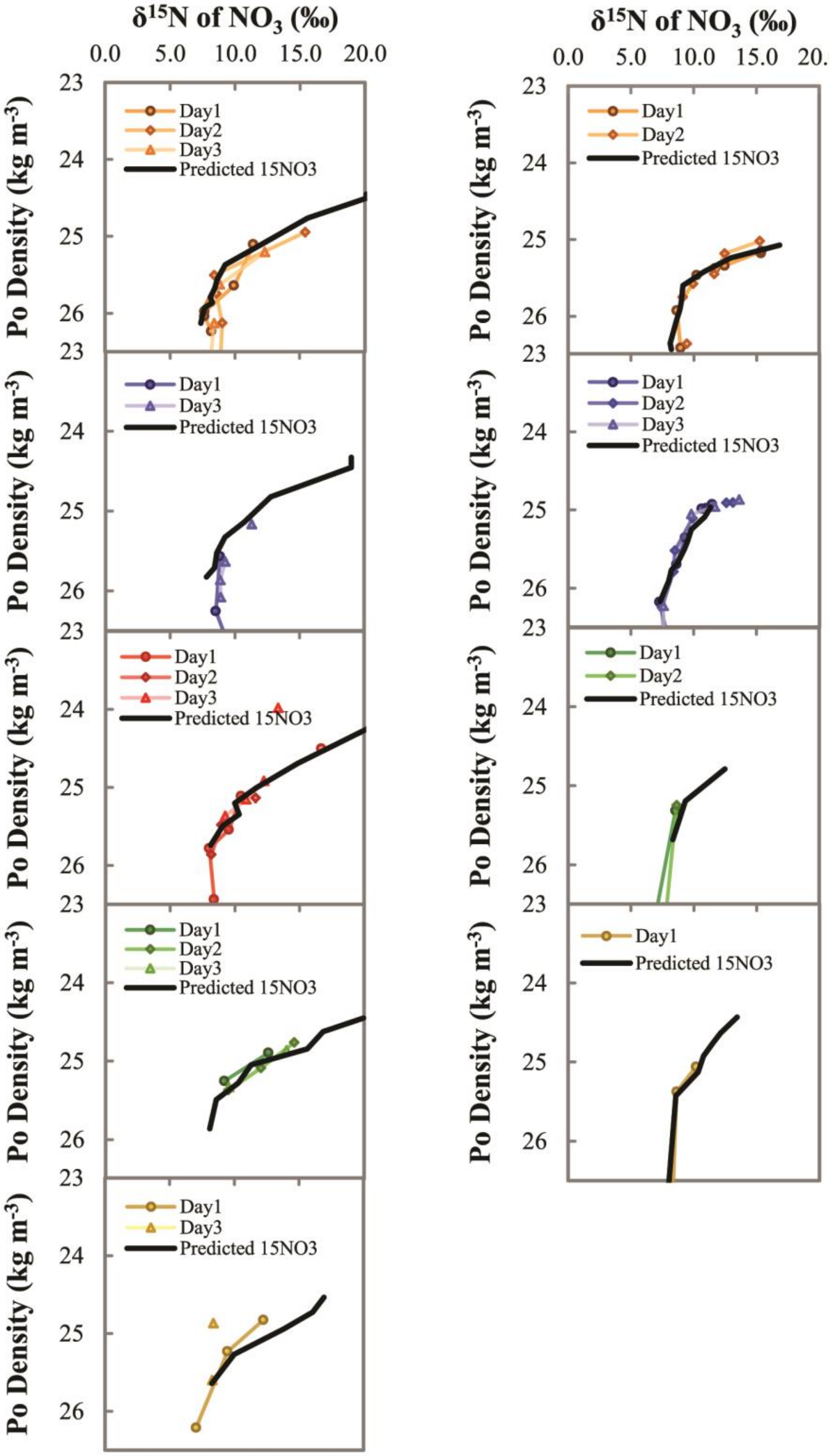

Figure S4.7. *Rayleigh best fits were used to interpolate across locations in the water column where* $\delta^{15}N_{NO3}$ *observations were not available. P1408 Cycles are on the left and P1604 on the right, as for Figure 4.2.*

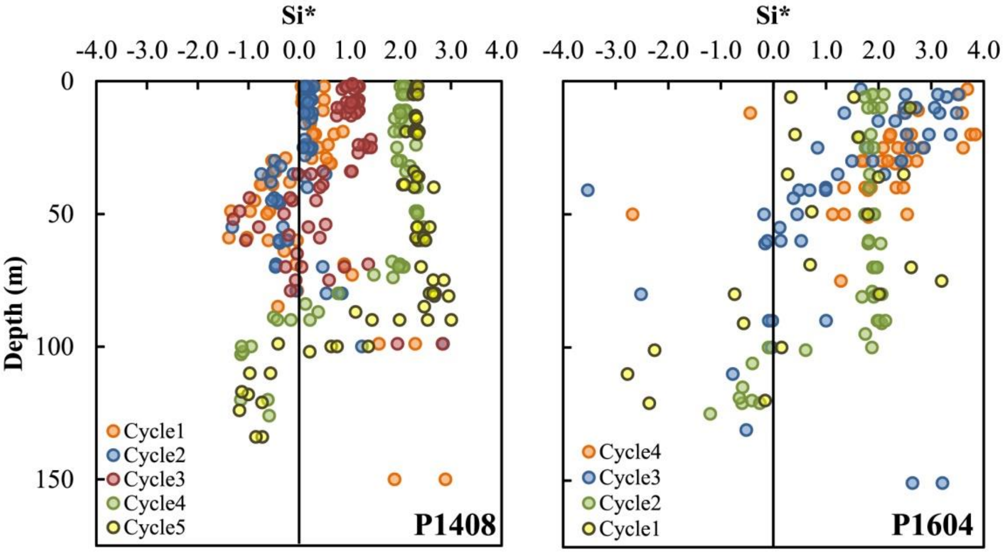

Figure S4.8. *Si* estimated after King and Barbeau (2011), using the mean deep ocean* $Si(OH)_4$*:*NO_3^- *ratio over 50 - 100 m depths associated with each Cycle.*

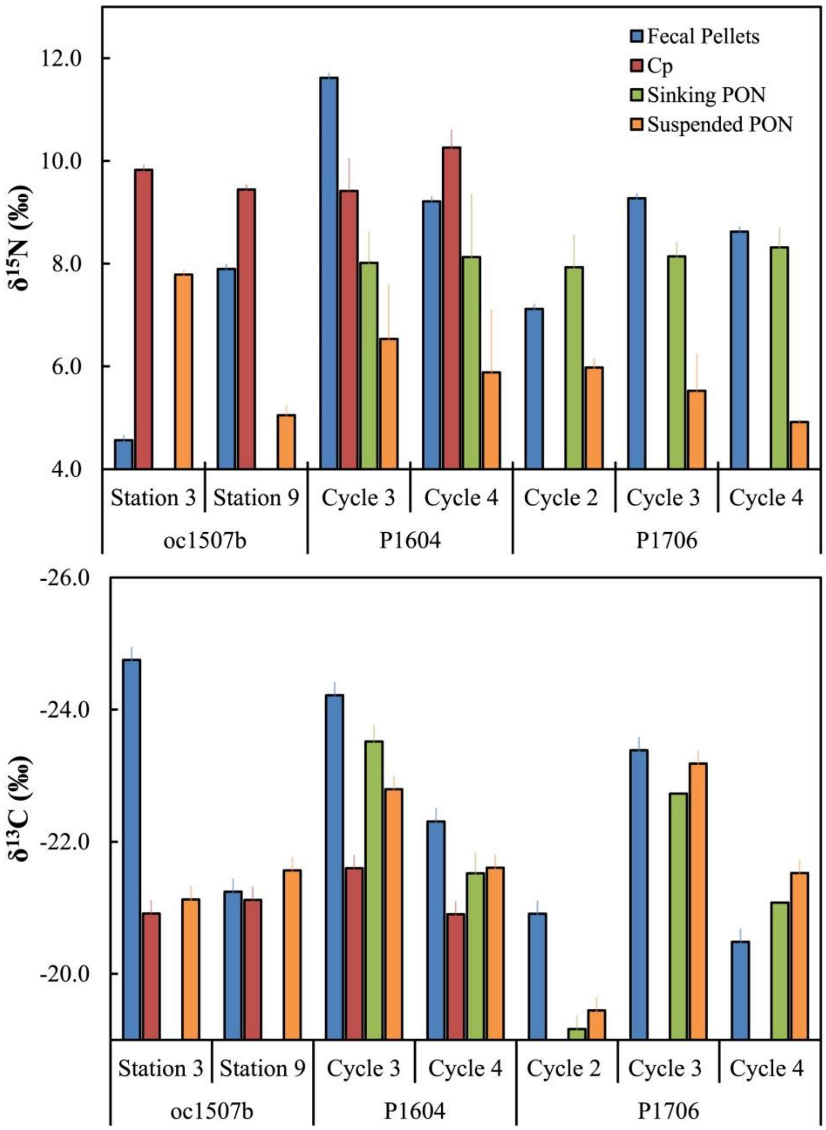

Figure S4.9. *δ^{15}N (top) and δ^{13}C (bottom) of fecal pellets collected from three CCE cruises carried out near Point Conception compared with the copepod Calanus pacificus (Cp), sinking PON at 100m and suspended PON averaged over ±10m within Chl-a max depths. Fecal pellets are nearly always enriched in δ^{15}N and more depleted in δ^{13}C than suspended PON, and almost always more depleted in δ^{15}N and δ^{13}C than average Cp (i.e., <10 per mil) and within ±1 per mil of sinking PON.*

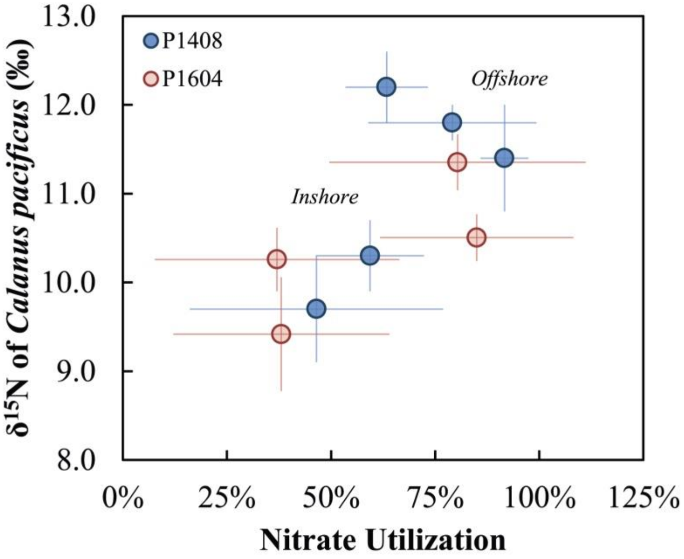

Figure S4.10. *δ^{15}N of Cp vs. nitrate utilization as presented in Figure 4.9.*

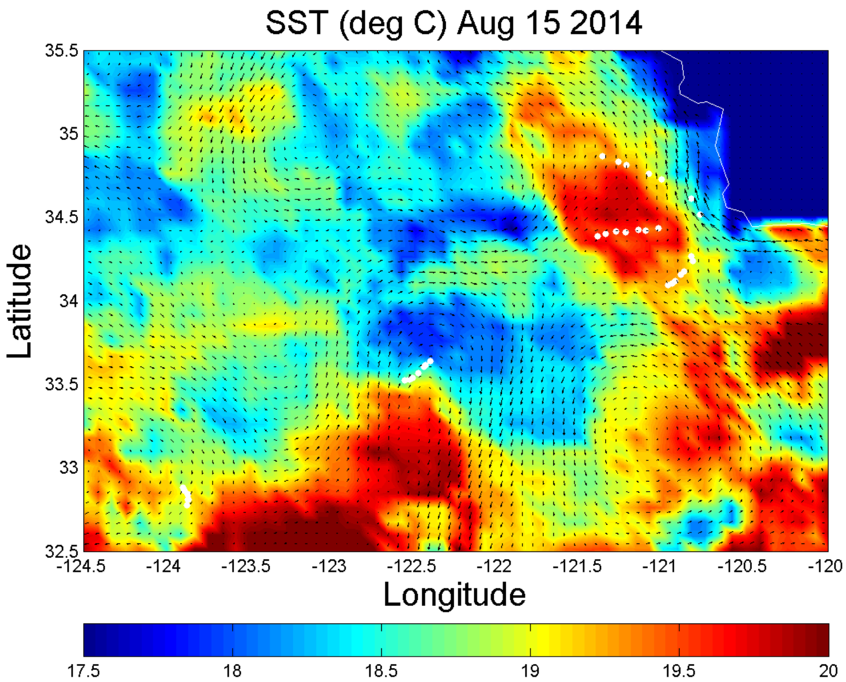

Figure S4.11. *California State Estimate model velocities (arrows) at 60m depths averaged over ±10 days around August 15th 2014, plotted over average sea surface temperatures (SeaWIFS). White dots indicate sampling locations.*

Table S4.1. *Mean (absolute) difference of closed model (Rayleigh) fit from observations (in units of ‰), where the nitrate isotope effect (ε_p) resulting in the best fit for a particular Cycle is highlighted with an outline. P1408 Cycle 2 and P1604 Cycles 1 and 2 are not shown here as the number of data points in the euphotic zone determining the isotopic difference for these Cycles was too low (i.e., n<3), and so the ε_p was estimated for these Cycles based on their behavior relative to other nearby Cycles. Excluding P1408 Cycle 5, the mean model difference from observations across Cycles was ±0.3‰. Using the same approach to estimate the mean isotope effect for CalCOFI stations near Point Conception collected from several cruises across 2010 – 2013 found an ε_p of 3.0 ± 1.5‰ using an open system model and an ε_p of 2.8 ± 0.8‰ for 2015-2016 using a closed system model.*

		ε_p (‰)→								
Cruise	Cycle	1.50	2.25	2.75	3.00	3.25	3.50	3.75	4.00	4.25
P1408	1	1.52	0.99	0.64	0.47	**0.42**	0.52	0.66	0.84	1.02
	2									
	3	2.16	1.53	1.10	0.89	0.68	0.47	**0.26**	0.26	0.37
	4	1.60	0.98	0.56	0.46	0.38	**0.37**	0.42	0.55	0.72
	5	**1.70**	1.91	2.06	2.21	2.44	2.68	2.92	3.15	3.39
P1604	1									
	2									
	3	1.12	0.67	0.49	**0.48**	0.50	0.59	0.68	0.83	0.98
	4	1.47	0.55	**0.35**	0.51	0.78	1.07	1.39	1.70	2.01

Table S4.2. *Integrated rates of nitrate-based and net primary production. Nitrate-based uptake rates are from the* dissertation *author's Chapter III Table 3.3. Rates of nitrate-based production are converted into carbon units using canonical Redfield ratio (C:N of 106:16). The f-ratio (determined here as net primary production divided by nitrate-based production) represents a combination of the four rate-based estimates, depending available data for a particular Cycle.*

Cruise	Cycle	*w*-NO_3 Uptake Rate	$^{15}NO_3$ Uptake Rate	^{14}C-based Net Primary Production	Satellite-based Net Primary Production	*f*-ratio
		(mmol N m^{-2} d^{-1})		**(mmol C m^{-2} d^{-1})**		
P1408	1	*2.2±0.2*	-	*34±9*	*59.4*	*0.34±0.13*
	2	*1.9±0.2*	-	*28±1*	*59.4*	*0.33±0.17*
	3	*2.6±0.6*	-	*25±1*	*59.4*	*0.49±0.28*
	4	*2.1±0.5*	-	*10±1*	*29.2*	*0.48*
	5	*2.4±0.2*	-	*11±0*	*27.4*	*0.59*
P1604	1	-	*1.3±0.0*	*19*	*25.0*	*0.40±0.08*
	2	-	*1.9±1.0*	*22±5*	*27.7*	*0.52±0.07*
	3	*1.8±0.3*	*5.4±2.9*	*67±13*	*59.0*	*0.40±0.28*
	4	*8.1±0.7*	*3.6±1.0*	*134±29*	*59.0*	*0.47±0.31*

REFERENCES

Altabet, M. A. (1988). Variations in nitrogen isotopic composition between sinking and suspended particles: implications for nitrogen cycling and particle transformation in the open ocean. *Deep Sea Research Part A, Oceanographic Research Papers*, *35*(4), 535–554.

Altabet, M. A. (1990). Organic C, N, and stable isotopic composition of particulate matter collected on glass-fiber and aluminum oxide filters. *Limnology and Oceanography*, *35*(4), 902–909.

Altabet, M. A. (2001). Nitrogen isotopic evidence for micronutrient control of fractional NO3- utilization in the equatorial Pacific. *Limnology and Oceanography*, *46*(2), 368–380.

Altabet, M. A., and Deuser, W. G. (1985). Seasonal variations in natural abundance of 15n in particles sinking to the deep sargasso sea. *Nature*, *315*(6016), 218–219.

Altabet, M. A., Pilskaln, C., Thunell, R., Pride, C., Sigman, D., Chavez, F., and Francois, R. (1999). The nitrogen isotope biogeochemistry of sinking particles from the margin of the eastern North Pacific. *Deep-Sea Research Part I: Oceanographic Research Papers*, *46*(4), 655–679.

Altabet, M. A., and McCarthy, J. J. (1985). Temporal and spatial variations in the natural abundance of 15N in PON from a warm-core ring. *Deep Sea Research Part A, Oceanographic Research Papers*, *32*(7), 755–772.

Altabet, M. A., and McCarthy, J. J. (1986). Vertical patterns in 15N natural abundance in PON from the surface waters of warm-core rings. *Journal of Marine Research*, *44*(1980), 185–201.

Bada, J. L., Schoeninger, M. J., and Schimmelmann, A. (1989). Isotopic fractionation during peptide bond hydrolysis. *Geochimica et Cosmochimica Acta*, *53*(12), 3337–3341.

Bakun, A., and Nelson, C. S. (1991). The seasonal cycle of wind-stress curl in subtropical eastern boundary current regions. *Journal of Physical Oceanography*, *21*(12), 1815–1834.

Bjorkstedt, E. P., Goericke, R., McClatchie, S., Weber, E., Watson, W., Lo, N., Peterson, B., Emmett, B., Brodeur, R., Peterson, J., Litz, M., Gomez-Valdes, J., Gaxiola-Castro, G., Collins, C. A. (2011). State of the California Current 2010-2011: Regionally Variable Responses to a Strong (But Fleeting) La Nina.

Bond, N. A., Cronin, M. F., Freeland, H., and Mantua, N. (2015). Causes and impacts of the 2014 warm anomaly in the NE Pacific. *Geophysical Research Letters*, *42*(9), 3414–3420.

Bruland, K. W., Rue, E. L., and Smith, G. J. (2001). Iron and macronutrients in California coastal upwelling regimes: Implications for diatom blooms. *Limnol. Oceanogr*, *46*(7), 1661–1674.

Casciotti, K. L., Sigman, D. M., Hastings, M. G., Böhlke, J. K., and Hilkert, A. (2002). Measurement of the oxygen isotopic composition of nitrate in seawater and freshwater using the denitrifier method. *Analytical Chemistry*, *74*(19), 4905–4912.

Chavez, F. P., and Messié, M. (2009). A comparison of Eastern Boundary Upwelling Ecosystems. *Progress in Oceanography*, *83*(1–4), 80–96.

Chavez, F. P., Messié, M., and Pennington, J. T. (2011). Marine Primary Production in Relation to Climate Variability and Change. *Annual Review of Marine Science*, *3*(1), 227–260.

Checkley, D. M., and Barth, J. A. (2009). Patterns and processes in the California Current System. *Progress in Oceanography*, *83*(1–4), 49–64.

Checkley, D. M., and Entzeroth, L. C. (1985). Elemental and isotopic fractionation of carbon and nitrogen by marine, planktonic copepods and implications to the marine nitrogen cycle. *Journal of Plankton Research*, *7*(4), 553–568.

Checkley, D. M., and Miller, C. A. (1989). Nitrogen isotope fractionation by oceanic zooplankton. *Deep Sea Research Part A, Oceanographic Research Papers*, *36*(10), 1449–1456.

Close, H. G., Shah, S. R., Ingalls, A. E., Diefendorf, A. F., Brodie, E. L., Hansman, R. L., Freeman, K. H., Aluwihare, L. I., and Pearson, A. (2013). Export of submicron particulate organic matter to mesopelagic depth in an oligotrophic gyre. *Proceedings of the National Academy of Sciences*, *110*(31), 12565–12570.

Cohen, N. R., Ellis, K. A., Lampe, R. H., McNair, H., Twining, B. S., Maldonado, M. T., Brzezinski, M. A., Kuzminov, F. I., Thamatrakoln, K., Till, C. P., Bruland, K. W., Sunda, W. G., Bargu, S., and Marchetti, A. (2017). Diatom Transcriptional and Physiological Responses to Changes in Iron Bioavailability across Ocean Provinces. *Frontiers in Marine Science*, *4*, 360.

Cole, S. T., Rudnick, D. L., and Colosi, J. A. (2010). Seasonal evolution of upper-ocean horizontal structure and the remnant mixed layer. *Journal of Geophysical Research: Oceans*, *115*(4), 1–15.

Collins, L. E., Berelson, W., Hammond, D. E., Knapp, A., Schwartz, R., and Capone, D. (2011). Particle fluxes in San Pedro Basin, California: A four-year record of sedimentation and physical forcing. *Deep-Sea Research Part I: Oceanographic Research Papers*, *58*(8), 898–914.

Décima, M., Landry, M. R., and Popp, B. N. (2013). Environmental perturbation effects on baseline δ15N values and zooplankton trophic flexibility in the southern California current ecosystem. *Limnology and Oceanography*, *58*(2), 624–634.

Deutsch, C., Berelson, W., Thunell, R., Weber, T., Tems, C., McManus, J., Crusius, J., Ito, T., Baumgartner, T., Ferreira, V., Mey, J., and Van Geen, A. (2014). Centennial changes in North Pacific anoxia linked to tropical trade winds. *Science*, *345*(6197), 665–668.

Deutsch, C., and Weber, T. (2012). Nutrient Ratios as a Tracer and Driver of Ocean Biogeochemistry. *Annual Review of Marine Science*, *4*(1), 113–141.

DiFiore, P. J., Sigman, D. M., Trull, T. W., Lourey, M. J., Karsh, K., Cane, G., and Ho, R. (2006). Nitrogen isotope constraints on subantarctic biogeochemistry. *Journal of Geophysical Research: Oceans*, *111*(8).

Difiore, P. J., Sigman, D. M., Karsh, K. L., Trull, T. W., Dunbar, R. B., and Robinson, R. S. (2010). Poleward decrease in the isotope effect of nitrate assimilation across the Southern Ocean. *Geophysical Research Letters*, *37*(17).

Dilling, L., Wilson, J., Steinberg, D., and Alldredge, A. (1998). Feeding by the euphausiid Euphausia pacifica and the copepod Calanus pacificus on marine snow. *Marine Ecology Progress Series*, *170*, 189–201.

Eppley, R. W., Renger, E. H., and Harrison, W. G. (1979). Nitrate and phytoplankton production in southern California coastal waters. *Limnology and Oceanography*, *24*(3), 483–494.

Eppley, R. W., and Peterson, B. J. (1979). Particulate organic matter flux and planktonic new production in the deep ocean. *Nature*, *282*(5740), 677–680.

Eppley, R. W., Harrison, W. G., Chisholm, S. W., and Stewart, E. (1977). Particulate organic matter in surface waters off Southern California and its relationship to phytoplankton. *Journal of Marine Research*, *35*, 671–691.

Falkowski, P. G., Laws, E. A., Barber, R. T., and Murray, J. W. (2003). Phytoplankton and Their Role in Primary, New, and Export Production. In *Ocean Biogeochemistry* (pp. 99–121). Berlin, Heidelberg: Springer Berlin Heidelberg.

Fawcett, S. E., Lomas, M. W., Casey, J. R., Ward, B. B., and Sigman, D. M. (2011). Assimilation of upwelled nitrate by small eukaryotes in the Sargasso Sea. *Nature Geoscience*, *4*(10), 717–722.

Fernández, A., Marañón, E., and Bode, A. (2014). Large-scale meridional and zonal variability in the nitrogen isotopic composition of plankton in the Atlantic Ocean. *Journal of Plankton Research*, *36*(4), 1060–1073.

Frischknecht, M., Münnich, M., and Gruber, N. (2017). Local atmospheric forcing driving an unexpected California Current System response during the 2015–2016 El Niño. *Geophysical Research Letters*, *44*(1), 304–311.

Frost, B. W. (1972). Effects of Size and Concentration of Food Particles on the Feeding Behavior of the Marine Planktonic Copepod Calanus Pacificus1. *Limnology and Oceanography*, *17*(6), 805–815.

Frost, B. W. (1977). Feeding behavior of Calanus pacificus in mixtures of food particles. *Limnology and Oceanography*, *22*(3), 472–491.

Fry, B. (1988). Food web structure on Georges Bank from stable C, N, and S isotopic compositions. *Limnology and Oceanography*, *33*(5), 1182–1190.

Gannes, L. Z., Brien, D. M. O., Martinez, C., and Jun, N. (2007). Stable Isotopes in Animal Ecology : Assumptions , Caveats , and a Call for More Laboratory Experiments. *Ecology*, *78*(4), 1271–1276.

Goericke, R. (2002). Top-down control of phytoplankton biomass and community structure in the monsoonal Arabian Sea. *Limnology and Oceanography*, *47*(5), 1307–1323.

Goericke, R. (2011). The Size Structure of Marine Phytoplankton— What Are the Rules? *CalCOFI Rep*, *52*, 198–204.

Goericke, R., Montoya, J. P., and Fry, B. (1994). Physiology of isotope fractionation in algae and cyanobacteria. In K. Lajtha & R. Michener (Eds.), *Stable isototopes in ecology and environmental science* (pp. 187–221). Oxford; Boston: Blackwell Scientific Publications.

Granger, J., Sigman, D. M., Needoba, J. A., and Harrison, P. J. (2004). Coupled nitrogen and oxygen isotope fractionation of nitrate during assimilation by cultures of marine phytoplankton. *Limnol. Oceanogr*, *49*(5), 1763–1773.

Granger, J., Sigman, D. M., Prokopenko, M. G., Lehmann, M. F., and Tortell, P. D. (2006). A method for nitrite removal in nitrate N and O isotope analyses. *Limnology and Oceanography: Methods*, *4*(7), 205–212.

Granger, J., Sigman, D. M., Rohde, M. M., Maldonado, M. T., and Tortell, P. D. (2010). N and O isotope effects during nitrate assimilation by unicellular prokaryotic and eukaryotic plankton cultures. *Geochimica et Cosmochimica Acta*, *74*(3), 1030–1040.

Gruber, N., Lachkar, Z., Frenzel, H., Marchesiello, P., Münnich, M., McWilliams, J. C., Nagai, T., and Plattner, G.-K. (2011). Eddy-induced reduction of biological production in eastern boundary upwelling systems. *Nature Geoscience*, *4*(11), 787–792.

Guo, L., Tanaka, T., Wang, D., Tanaka, N., and Murata, A. (2004). Distributions, speciation and stable isotope composition of organic matter in the southeastern Bering Sea. *Marine Chemistry*, *91*(1–4), 211–226.

Hannides, C. C. S., Popp, B. N., Landry, M. R., and Graham, B. S. (2009). Quantification of zooplankton trophic position in the North Pacific Subtropical Gyre using stable nitrogen isotopes. *Limnology and Oceanography*, *54*(1), 50–61.

Haskell, W. Z., Prokopenko, M. G., Hammond, D. E., Stanley, R. H. R., Berelson, W. M., Baronas, J. J., Fleming, J. C., and Aluwihare, L. I. (2016). An organic carbon budget for coastal Southern California determined by estimates of vertical nutrient flux, net community production and export. *Deep-Sea Research Part I: Oceanographic Research Papers*, *116*, 49–76.

Hayes, J. M. (2002). *Practice and Principles of Isotopic Measurements in Organic Geochemistry (Revision 2)*.

Hutchins, D. A., and Bruland, K. W. (1998). Iron-limited diatom growth and Si:N uptake ratios in a coastal upwelling regime. *Nature*, *393*(6685), 561–564.

Jacox, M. G., Hazen, E. L., Zaba, K. D., Rudnick, D. L., Edwards, C. A., Moore, A. M., and Bograd, S. J. (2016). Impacts of the 2015–2016 El Niño on the California Current System: Early assessment and comparison to past events. *Geophysical Research Letters*, *43*(13), 7072–7080.

Jacox, M. G., Fiechter, J., Moore, A. M., and Edwards, C. A. (2015). ENSO and the California current coastal upwelling response. *Journal of Geophysical Research: Oceans*, *120*(3), 1691–1702.

King, A. L., and Barbeau, K. A. (2011). Dissolved iron and macronutrient distributions in the southern California Current System. *Journal of Geophysical Research: Oceans*, *116*(3).

Knapp, A. N., Sigman, D. M., Lipschultz, F., Kustka, A. B., and Capone, D. G. (2011). Interbasin isotopic correspondence between upper-ocean bulk DON and subsurface nitrate and its implications for marine nitrogen cycling. *Global Biogeochemical Cycles*, *25*(4).

Landrum, J. P., Altabet, M. A., and Montoya, J. P. (2011). Basin-scale distributions of stable nitrogen isotopes in the subtropical North Atlantic Ocean: Contribution of diazotroph nitrogen to particulate organic matter and mesozooplankton. *Deep-Sea Research Part I: Oceanographic Research Papers*, *58*(5), 615–625.

Landry, M. R. (1981). Switching between herbivory and carnivory by the planktonic marine copepod Calanus pacificus. *Marine Biology*, *65*(1), 77–82.

Landry, M. R., Ohman, M. D., Goericke, R., Stukel, M. R., and Tsyrklevich, K. (2009). Lagrangian studies of phytoplankton growth and grazing relationships in a coastal upwelling ecosystem off Southern California. *Progress in Oceanography*, *83*(1–4), 208–216.

Liu, K., and Kaplan, I. R. (1989). The eastern tropical Pacific as a source of 15N-enriched nitrate in seawater off southern California. *Limnology and Oceanography*, *34*(5), 820–830.

Di Lorenzo, E., Schneider, N., Cobb, K. M., Franks, P. J. S., Chhak, K., Miller, A. J., McWilliams, J. C., Bograd, S. J., Arango, H., Curchitser, E., Powell, T. M., and Rivière, P. (2008). North Pacific Gyre Oscillation links ocean climate and ecosystem change. *Geophysical Research Letters*, *35*(8).

Mantyla, A. W., Bograd, S. J., and Venrick, E. L. (2008). Patterns and controls of chlorophyll-a and primary productivity cycles in the Southern California Bight. *Journal of Marine Systems*, *73*(1–2), 48–60.

Martiny, A. C., Pham, C. T. A., Primeau, F. W., Vrugt, J. A., Moore, J. K., Levin, S. A., and Lomas, M. W. (2013). Strong latitudinal patterns in the elemental ratios of marine plankton and organic matter. *Nature Geoscience*, *6*(4), 279–283.

McClatchie, S., Goericke, R., Leising, A., Auth, T., Bjorkstedt, E. P., Robertson, R., Brodeur, R., Du, X., Daly, E., Morgan, C., Chavez, F. P., Debich, A., Hildebrand, J., Jahncke, J. (2016). State of the California Current 2015-16: Comparisons with the 1997–98 El Nino, *57*, 61.

Mercado, J. M., Ramíohmrez, T., Cortésand, D., and Liger, E. (2010). Isotopic composition of particulate organic nitrogen and its relationship to nitrate assimilation in the Mediterranean Sea. *Scientia Marina*, *74*(4), 745–753.

Messié, M., Ledesma, J., Kolber, D. D., Michisaki, R. P., Foley, D. G., and Chavez, F. P. (2009). Potential new production estimates in four eastern boundary upwelling ecosystems. *Progress in Oceanography*, *83*(1–4), 151–158.

Messié, M., and Chavez, F. P. (2015). Seasonal regulation of primary production in eastern boundary upwelling systems. *Progress in Oceanography*, *134*, 1–18.

Mills, M. M., and Arrigo, K. R. (2010). Magnitude of oceanic nitrogen fixation influenced by the nutrient uptake ratio of phytoplankton. *Nature Geoscience*, *3*(6), 412–416.

Mingawa, M., Winter, D. A., and Kaplan, I. R. (1984). Comparison of Kjeldahl and Combustion Methods for Measurement of Nitrogen Isotope Ratios in Organic Matter. *Anal. Chem*, *56*, 1859–1861.

Montoya, J. P. (2008). Nitrogen Stable Isotopes in Marine Environments. In *Nitrogen in the Marine Environment* (pp. 1277–1302).

Montoya, J. P., and Mccarthy, J. J. (1995). Isotopic fractionation during nitrate uptake by phytoplankton grown in continuous culture. *Journal of Plankton Research*, *17*(3), 439–464.

Montoya, J. P., Horrigan, S. G., and McCarthy, J. J. (1990). Natural abundance of ^{15}N in particulate nitrogen and zooplankton in the Chesapeake Bay. *Marine Ecology Progress Series*, *65*, 35–61.

Montoya, J. P., Wiebe, P. H., and McCarthy, J. J. (1992). Natural abundance of 15N in particulate nitrogen and zooplankton in the Gulf Stream region and warm-core ring 86A. *Deep Sea Research Part A. Oceanographic Research Papers*, *39*(Supplement 1), S363–S392.

Munk, W. (1981). Internal Waves and Small-Scale Processes. In *Evolution of physical oceanography* (pp. 264–291).

Needoba, J. A., Waser, N. A., Harrison, P. J., and Calvert, S. E. (2003). Nitrogen isotope fractionation in 12 species of marine phytoplankton during growth on nitrate. *Marine Ecology Progress Series*, *255*, 81–91.

Needoba, J. A., Sigman, D. M., and Harrison, P. J. (2004). The mechanism of isotope fractionation during algal nitrate assimilation as illuminated by the 15N/14N of intracellular nitrate. *Journal of Phycology*, *40*(3), 517–522.

Nelson, J. R., Beers, J. R., Eppley, R. W., Jackson, G. A., McCarthy, J. J., and Soutar, A. (1987). A particle flux study in the Santa Monica-San Pedro Basin off Los Angeles: particle flux, primary production, and transmissometer survey. *Continental Shelf Research*, *7*(3), 307–328.

Ohman, M. D., Rau, G. H., and Hull, P. M. (2012). Multi-decadal variations in stable N isotopes of California Current zooplankton. *Deep-Sea Research Part I: Oceanographic Research Papers*, *60*, 46–55.

Ohman, M. D., Drits, A. V., Clarke, M. E., and Plourde, S. (1998). Differential dormancy of co-occurring copepods. *Deep-Sea Research Part II: Topical Studies in Oceanography*, *45*(8–9), 1709–1740.

Pedler, B. E., Aluwihare, L. I., and Azam, F. (2014). Single bacterial strain capable of significant contribution to carbon cycling in the surface ocean. *Proceedings of the National Academy of Sciences*, *111*(20), 7202–7207.

Plattner, G.-K., Gruber, N., Frenzel, H., and McWilliams, J. C. (2005). Decoupling marine export production from new production. *Geophysical Research Letters*, *32*(11), L11612.

Prahl, F. G., Eglinton, G., Corner, E. D. S., O'Hara, S. C. M., and Forsberg, T. E. V. (1984). Changes in plant lipids during passage through the gut of calanus. *Journal of the Marine Biological Association of the United Kingdom*, *64*(2), 317–334.

Quiñones, R. A. (2010). Eastern Boundary Current Systems (pp. 25–120). Springer, Berlin, Heidelberg.

Rau, G. H., Low, C., and Chavez, F. P. (1998). Suspended particle nitrogen delta 15 N versus nitrate ultilization: observations in Monterey Bay, CA. *Deep-Sea Research*, *45*(8 / 9), 1603.

Rau, G. H., Ohman, M. D., and Pierrot-Bults, A. (2003). Linking nitrogen dynamics to climate variability off central California: A 51 year record based on 15N/14N in CalCOFI zooplankton. *Deep-Sea Research Part II: Topical Studies in Oceanography*, *50*(14–16), 2431–2447.

Rykaczewski, R. R., and Checkley, D. M. (2008). Influence of ocean winds on the pelagic ecosystem in upwelling regions. *Proceedings of the National Academy of Sciences*, *105*(6), 1965–1970.

Saino, T., and Hattori, A. (1980). 15N natural abundance in oceanic suspended particulate matter [6]. *Nature*.

Saino, T., and Hattori, A. (1987). Geographical variation of the water column distribution of suspended particulate organic nitrogen and its ~SN natural abundance in the Pacific and its marginal seas. *Deep-Sea Research*, *346*(5), 807–827.

Santoro, A. E., Casciotti, K. L., and Francis, C. A. (2010). Activity, abundance and diversity of nitrifying archaea and bacteria in the central California Current. *Environmental Microbiology*, *12*(7), 1989–2006.

Sarakinos, H. C., Johnson, M. L., and Zanden, M. J. Vander. (2002). A synthesis of tissue-preservation effects on carbon and nitrogen stable isotope signatures. *Canadian Journal of Zoology*, *80*(2), 381–387.

Sharp, J. H. (1974). Improved analysis for "particulate" organic carbon and nitrogen from seawater. *Limnology and Oceanography*, *19*(6), 984–989.

Sigman, D. M., Casciotti, K. L., Andreani, M., Barford, C., Galanter, M., and Böhlke, J. K. (2001). A bacterial method for the nitrogen isotopic analysis of nitrate in seawater and freshwater. *Analytical Chemistry*, *73*(17), 4145–4153.

Sigman, D. M., Karsh, K. L., and Casciotti, K. L. (2010). Nitrogen Isotopes in the Ocean. In *Encyclopedia of Ocean Sciences* (pp. 40–54).

Sigman, D. M., Altabet, M. A., McCorkle, D. C., Francois, R., and Fischer, G. (1999). The δ15N of nitrate in the Southern Ocean: Consumption of nitrate in surface waters. *Global Biogeochemical Cycles*, *13*(4), 1149–1166.

Sigman, D. M., Granger, J., DiFiore, P. J., Lehmann, M. M., Ho, R., Cane, G., and van Geen, A. (2005). Coupled nitrogen and oxygen isotope measurements of nitrate along the eastern North Pacific margin. *Global Biogeochemical Cycles*, *19*(4).

Stukel, M. R., Landry, M. R., Benitez-Nelson, C. R., and Goericke, R. (2011). Trophic cycling and carbon export relationships in the California Current Ecosystem. *Limnology and Oceanography*, *56*(5), 1866–1878.

Stukel, M. R., Ohman, M. D., Benitez-Nelson, C. R., and Landry, M. R. (2013). Contributions of mesozooplankton to vertical carbon export in a coastal upwelling system. *Marine Ecology Progress Series*, *491*, 47–65.

Tamelander, T., Søreide, J. E., Hop, H., and Carroll, M. L. (2006). Fractionation of stable isotopes in the Arctic marine copepod Calanus glacialis: Effects on the isotopic composition of marine particulate organic matter. *Journal of Experimental Marine Biology and Ecology*, *333*(2), 231–240.

Taylor, A. G., Landry, M. R., Selph, K. E., and Wokuluk, J. J. (2015). Temporal and spatial patterns of microbial community biomass and composition in the Southern California Current Ecosystem. *Deep Sea Research Part II: Topical Studies in Oceanography*, *112*, 117–128.

Tems, C. E., Berelson, W. M., and Prokopenko, M. G. (2015). Particulate δ15N in laminated marine sediments as a proxy for mixing between the California Undercurrent and the California Current: A proof of concept. *Geophysical Research Letters*, *42*(2), 419–427.

Todd, R. E., Rudnick, D. L., Mazloff, M. R., Cornuelle, B. D., and Davis, R. E. (2012). Thermohaline structure in the California Current System: Observations and modeling of spice variance. *Journal of Geophysical Research: Oceans*, *117*(2).

Wada, E., Terazaki, M., Kabaya, Y., and Nemoto, T. (1987). 15N and 13C abundances in the Antartic Ocean with emphasis on the biogeochemical structure of the food web. *Deep Sea Research Part A, Oceanographic Research Papers*, *34*(5–6), 829–841.

Walker, B. D., and McCarthy, M. D. (2012). Elemental and isotopic characterization of dissolved and particulate organic matter in a unique California upwelling system: Importance of size and composition in the export of labile material. *Limnology and Oceanography*, *57*(6), 1757–1774.

Wankel, S. D., Kendall, C., Pennington, J. T., Chavez, F. P., and Paytan, A. (2007). Nitrification in the euphotic zone as evidenced by nitrate dual isotopic composition: Observations from Monterey Bay, California. *Global Biogeochemical Cycles*, *21*(2).

Wannicke, N., Liskow, I., and Voss, M. (2010). Impact of diazotrophy on N stable isotope signatures of nitrate and particulate organic nitrogen: Case studies in the north-eastern tropical Atlantic Ocean. *Isotopes in Environmental and Health Studies*, *46*(3), 337–354.

Waser, N. A., Harrison, W. G., Head, E. J. H., Nielsen, B., Lutz, V. a, and E Calvert, S. (2000). Geographic variations in the nitrogen isotope composition of surface particulate nitrogen and new production across the North Atlantic Ocean. *Deep Sea Research Part I: Oceanographic Research Papers*, *47*(7), 1207–1226.

Wilkerson, F. P., Lassiter, A. M., Dugdale, R. C., Marchi, A., and Hogue, V. E. (2006). The phytoplankton bloom response to wind events and upwelled nutrients during the CoOP WEST study. *Deep-Sea Research Part II: Topical Studies in Oceanography*, *53*(25–26), 3023–3048.

Zaba, K. D., and Rudnick, D. L. (2016). The 2014-2015 warming anomaly in the Southern California Current System observed by underwater gliders. *Geophysical Research Letters*, *43*(3), 1241–1248.

Zhang, R., Chen, M., Ma, Q., Cao, J., and Qiu, Y. (2011). Latitudinal distribution of nitrogen isotopic composition in suspended particulate organic matter in tropical/subtropical seas. *Isotopes in Environmental and Health Studies*, *47*(4), 489–497.

Zimmerman, R. C., Kremer, J. N., and Dugdale, R. C. (1987). Acceleration of nutrient uptake by phytoplankton in a coastal upwelling ecosystem: A modeling analysis. *Limnology and Oceanography*, *32*(2), 359–367.

Chapter V

Conclusions

1.1 Summary of Dissertation Chapters

As presented in the introduction **Chapter I**, eastern boundary current systems, including the California Current System (CCS), are highly productive regions limited primarily by the supply of nitrate into the surface ocean. It is therefore in the context of nitrate supply that **Chapters II** to **IV** present new observational data for the CCS. Anomalous climatological conditions sampled for **Chapters III** and **IV** led to enhanced nitrate utilization at the coast, allowing for these chapters to explore impacts of surface stratified and nutrient-limited conditions on the organic reservoirs.

Chapter II presents one of the most spatially-resolved time series analyses of net primary (NPP), new (i.e., nitrate-based, NP) and dissolved organic carbon (DOC) production for the oceans. Data were collected as profiles from 9 cruises conducted between the years 2008 and 2010 from ~72 stations per cruise as associated with the California Cooperative Oceanic Fisheries Investigations (CalCOFI) program. Partitioning of NPP and NP into DOC ranged 8 to 26% and 16 to 56%, respectively, covering a range of coastal to oligotrophic gyre production conditions. Periods of enhanced production (i.e., 'bloom') exhibited greater partitioning into DOC: 16 ± 8% of NPP and 28 ± 15% of NP. Periods of post-bloom, DOC accumulation also exhibited elevated DOC concentrations (10 - 20 μM over baseline) and partitioning ratios (>10% of NPP and >25% of NP). Periods of surface stratification and iron limitation were implicated as mechanisms leading to increased surface accumulation and partitioning ratios during post-bloom conditions. The DOC to NPP ratio was on average similar to the sinking export:NPP ratio (i.e, *e*-ratios; [*Stukel et al.*, 2011]), and the combination of these reservoirs was similar to average net oxygen to gross oxygen ratios presented for the region [*Munro et al.*, 2013]. The data presented in this chapter provides quantitative bounds on DOC production, and discusses the potential for this pool to be laterally transported between ecologically distinct regions of the California Current.

Chapter III uses an established model [*Wankel et al.*, 2007] based on the isotopes of nitrate (δ^{15}N and δ^{18}O) to estimate the contribution of recycled nitrogen into nitrate (i.e., nitrification) within the euphotic zone. These are the first nitrification estimates covering the coastal to open ocean productivity gradient as part of the California Current Ecosystem (CCE) long-term ecological research program. Nitrification contributions to euphotic zone nitrate spanned 6% to 36% and were positively correlated with concentrations of nitrite, a relationship that suggests substrate quantity to be a limiting factor for nitrification as previously hypothesized for the northern CCS [*Ward*, 1985]. A linear regression model of nitrite concentrations for the CalCOFI record (1990 - 2016) suggested organic substrate supply or competition with phytoplankton were the strongest determinants to nitrite accumulation in the CCE. The latter process was recently implicated as influencing nitrification rates off Monterey Bay [*Smith et al.*, 2016]. Integrated nitrate uptake rates were used here to convert nitrification contributions to rates, where integrated rates of nitrifcation were estimated to span from 0.1 to 2.0 mmol N m^{-2} d^{-1}, rates that were similar to those reported previously across the broader CCS region [*Ward et al.*, 1982; *Santoro et al.*, 2010; *Smith et al.*, 2016]. A three-box model suggested nitrification rates of up to 10 - 20 nmol N L d^{-1} must have occurred at the immediate high light surface ocean, a range also measured for the surface waters of

Monterey Bay [*Ward*, 2005]. Estimated nitrification rates presented here provide bounds for studies that use nitrate concentration gradients in the surface euphotic zone to estimate nitrate-based production rates.

Chapter IV presents $\delta^{15}N$ data for the CCE study region and estimates potential influences of nitrate supply on sinking and suspended particulate organic matter (POM) and the copepod *Calanus pacificus*. Four key products using a closed-system nitrate isotope model were generated for the CCE: (1) source nitrate concentration and $\delta^{15}N$, (2) the fractionation factor associated with nitrate uptake, (3) $\delta^{15}N$-based estimates of nitrate utilization, and (4) instantaneous and integrated products of nitrate uptake. Nitrate source waters based on the remnant mixed layer were slightly elevated relative to immediate deep sources, which could have been due either to increased contributions from enriched southerly California Undercurrent (as detected in inshore regions) or to phytoplankton uptake processes (as detected further from shore with a depleted deep water). Using the remnant mixed layer, a closed system model was found to be the best fit to $\delta^{15}N$ nitrate observations. The isotope fractionation factor was on average 3.0 ± 0.5‰, a relatively low value that may have been influenced by an increase in smaller-sized and/or flagellated phytoplankton.

Nitrate utilization was strongly correlated with sinking POM $\delta^{15}N$, suggesting that sinking POM $\delta^{15}N$ directly reflected surface nitrate drawdown processes. The $\delta^{15}N$ of sinking POM was also often related to the integrated product of nitrate uptake (and occasionally related to suspended POM) but enriched by 2‰, supporting the idea that sinking POM is linked to nitrate utilization via the suspended POM reservoir that is supported by nitrate uptake. Additionally, δ^{15}N of the primary consumer, *Calanus pacificus* (*Cp*), was 3.7 ± 0.8‰ enriched compared to suspended POM, providing further evidence that suspended POM plays a key role in linking nutrients to *Cp*. Nitrate utilization was on 51 ± 15% on average, the extent of which was likely at times limited by iron availability. However, nitrate utilization was enhanced during the anomalous climate conditions of 2014 to 2016, the effect of which was observed in all of the reservoirs measured here. Concurrently collected fecal pellets were depleted in δ^{15}N relative to sinking POM, suggesting that sinking POM is comprised of detrital or recent phytoplankton sources in addition to the waste products of primary (and secondary) consumers.

While several studies using δ^{15}N in the CCS are available, there has yet to be a systematic examination of the isotopic interconnection of upper ocean N reservoirs. Data suggest the surface CCE to be strongly influenced by surface nitrate utilization, but caution is taken given that subsurface δ^{15}N nitrate was isotopically enriched at some locations by a similar magnitude as observed across other related surface δ^{15}N reservoirs.

1.2 Future Directions

The data presented in **Chapter II** suggest DOC to accumulate at the surface ocean, and a brief modeling effort using average DOC profiles from the CalCOFI grid suggested that this pool could be transported from productive coastal zones into the oligotrophic gyre. Studies that use biogeochemical models incorporating DOC for the central CCS and suggest DOC to be transported offshore and later subducted [*Gruber et* *al.*, 2011; *Letscher et al.*, 2013; *Nagai et al.*, 2015]; however, these are based on few observations and assumptions about DOC lifetimes. Given the expansive area of the CalCOFI grid, CalCOFI DOC time series data offer a unique opportunity to validate DOC turnover times inherently assumed by biogeochemical models (e.g. [*Letscher et al.*, 2015]). Preliminary modeling efforts associated with biogeochemical property state estimates of the California Current (http://sose.ucsd.edu/CASE/) suggest this to be a useful model construct. In addition, the unique ecosystem conditions associated with DOC production and accumulation identified in **Chapter II** provide conditions and bounds under which DOC might accumulate.

The distribution of nitrification rates estimated in **Chapter III** were decoupled from 16s-based profiles of nitrifying bacteria and archaea, a finding similar to that reported off of Monterey Bay [*Smith et al.*, 2016]. Future studies using natural abundance stable isotopes to estimate nitrification in the CCE should concurrently estimate the vertical distribution of stable-isotopes of nitrate, and ammonia and nitrite oxidation rates [*Beman et al.*, 2013]. In addition, **Chapter III** found nitrite concentrations to be a prominent determinant to nitrification contributions in the euphotic zone, and use of the long-term CalCOFI record generated two hypotheses (PON accumulation *vs.* competition with phytoplankton) that might lead to the accumulation of nitrite. These hypotheses could be tested by – in addition to collecting sample for the nitrification – estimating nitrite uptake rates by phytoplankton and quantifying the organic N reservoirs.

Chapter IV demonstrated that the stratified surface ocean conditions sampled during the CCE cruises were best modeled by a closed-system Rayleigh model to arrive at nitrate uptake isotope effects. This was compared to samples collected as part of the longer-term CalCOFI record that suggested an open system model to normally be appropriate for the CCE region. However, samples of the various other N reservoirs were not available during the CalCOFI cruises to compare with CCE. Community composition, and nitrate and POM $\delta^{15}N$ samples that cover the progression of a bloom and across various surface nitrate drawdown conditions could be used to better contrast the apparently unusual closed-system nitrate model behavior sampled during 2014 and 2016. Further, it was hypothesized in **Chapter IV** that the nitrate isotope of waters supplied to the euphotic zone of the CCE was not always reflective of the deeper waters immediately below. Samples collected across the CalCOFI station grid and for different time periods could more carefully evaluate the influence of subsurface nitrate on surface $\delta^{15}N$. A transport-based model that incorporated nitrogen isotopes could be useful in this effort to constrain deep source influences on surface production.

REFERENCES

Beman, J. M., Leilei Shih, J., and Popp, B. N. (2013). Nitrite oxidation in the upper water column and oxygen minimum zone of the eastern tropical North Pacific Ocean. *ISME Journal*, *7*(11), 2192–2205.

Gruber, N., Lachkar, Z., Frenzel, H., Marchesiello, P., Münnich, M., McWilliams, J. C., Nagai, T., and Plattner, G.-K. (2011). Eddy-induced reduction of biological production in eastern boundary upwelling systems. *Nature Geoscience, 4*(11), 787–792.

Letscher, R. T., Hansell, D. A., Carlson, C. A., Lumpkin, R., and Knapp, A. N. (2013). Dissolved organic nitrogen in the global surface ocean: Distribution and fate. *Global Biogeochemical Cycles*, *27*(1), 141–153.

Letscher, R. T., Moore, J. K., Teng, Y. C., and Primeau, F. W. (2015). Variable C : N : P stoichiometry of dissolved organic matter cycling in the Community Earth System Model. *Biogeosciences*, *12*(1), 209–221.

Munro, D. R., Quay, P. D., Juranek, L. W., and Goericke, R. (2013). Biological production rates off the Southern California coast estimated from triple O 2 isotopes and O 2 : Ar gas ratios. *Limnol. Oceanogr.*, *58*(4), 1312–1328.

Nagai, T., Gruber, N., Frenzel, H., Lachkar, Z., McWilliams, J. C., and Plattner, G. K. (2015). Dominant role of eddies and filaments in the offshore transport of carbon and nutrients in the California Current System. *Journal of Geophysical Research: Oceans*, *120*(8), 5318–5341.

Santoro, A. E., Casciotti, K. L., and Francis, C. A. (2010). Activity, abundance and diversity of nitrifying archaea and bacteria in the central California Current. *Environmental Microbiology*, *12*(7), 1989–2006.

Smith, J. M., Damashek, J., Chavez, F. P., and Francis, C. A. (2016). Factors influencing nitrification rates and the abundance and transcriptional activity of ammonia-oxidizing microorganisms in the dark northeast Pacific Ocean. *Limnology and Oceanography*, *61*(2), 596–609.

Stukel, M. R., Landry, M. R., Benitez-Nelson, C. R., and Goericke, R. (2011). Trophic cycling and carbon export relationships in the California Current Ecosystem. *Limnology and Oceanography*, *56*(5), 1866–1878.

Wankel, S. D., Kendall, C., Pennington, J. T., Chavez, F. P., and Paytan, A. (2007). Nitrification in the euphotic zone as evidenced by nitrate dual isotopic composition: Observations from Monterey Bay, California. *Global Biogeochemical Cycles*, *21*(2).

Ward, B. B. (1985). Light and substrate concentration relationships with marine ammonium assimilation and oxidation rates. *Marine Chemistry*, *16*(4), 301–316.

Ward, B. B. (2005). Temporal variability in nitrification rates and related biogeochemical factors in Monterey Bay, California, USA. *Marine Ecology Progress Series*, *292*, 97–109.

Ward, B. B., Olson, R. J., and Perry, M. J. (1982). Microbial nitrification rates in the primary nitrite maximum off southern California. *Deep Sea Research Part A, Oceanographic Research Papers*, *29*(2), 247–255.